Light quark jet quenching and the Gauge/Gravity duality

RAGURAM SUBRAMANIAM

Light quark jet quenching and the Gauge/Gravity duality

Raguram Subramaniam

A Thesis presented for the degree of
Doctor of Philosophy

Department of Mathematical Sciences
Durham University
United Kingdom

May 2019

Light quark jet quenching and the Gauge/Gravity duality

Raguram Subramaniam

Submitted for the degree of Doctor of Philosophy

May 2019

Abstract: In this dissertation, the gauge/gravity duality is used to study light quark jet quenching in the context of strongly coupled non-Abelian plasmas. In particular, we focus on using the so-called finite end point momentum strings to probe such plasmas. First, the Sakai-Sugimoto model is investigated using these strings. The stopping distance of thermalised light quarks and their rate of energy loss are computed. This stopping distance is then used to compute the transverse momentum broadening parameter $\hat{q}$. The Sakai-Sugimoto model shows less jet quenching than $\mathcal{N} = 4$ super Yang-Mills plasma. Both the super Yang-Mills and Sakai-Sugimoto cases over predict the jet quenching parameter relative to phenomenological models that extract $\hat{q}$ from experimental data. Next, the impact of non-zero chemical potentials within the plasma has on light probe quenching is investigated. The two cases of interest are the finite R-charged case and the finite baryon chemical potential. It is found that the baryon or flavour chemical potential has very little effect on the jet quenching relative to the R-charged case. Finally, small anisotropy is added to the plasma and it is found that for fixed temperature, the anisotropy increases jet quenching for motion in all directions. The longitudinal direction increases the jet quenching parameter the most. However, the parameter decreases in the transverse direction for fixed entropy density.

Declaration

The work in this thesis is based on research carried out in the Department of Mathematical Sciences at Durham University. No part of this thesis has been submitted elsewhere for any degree or qualification.

Acknowledgements

I would like to thank my supervisors Dr. Kasper Peeters and Dr. Marija Zamaklar for all their help and advice with this PhD. I would also like to thank my sisters, whom without this would have not been possible. I also appreciate all the support I received from the rest of my family. Lastly, I would like to thank the Engineering and Physical Sciences Research Council (EPSRC) for the studentship that allowed me to conduct this thesis.

Contents

Chapter 1

Introduction

The non-linearity of most interacting quantum field theories (QFT's) make them analytically unsolvable. In many cases one can use perturbation theory to compute physical observables such as scattering amplitudes. However the use of perturbation theory is only valid when the coupling, which characterises the strength of the interaction, is small. An important feature of QFT is renormalisation of UV divergences and the consequential running of the couplings. Whilst the running of the Electromagnetic and Weak force couplings is such that perturbation theory is valid at relatively low energies, this is not true for the Strong force. Thus, developing techniques to investigate this low energy regime of Quantum Chromodynamics (QCD) is very important. With the advent of string theory in the 1970's and the proposal of the AdS/CFT correspondence in the 1990's, the development of new techniques to probe strongly coupled theories such as QCD gained momentum [Sch10].

One of the key applications of the gauge/gravity duality has been the study of strongly coupled plasmas. It is well known that there exists a strongly coupled plasma phase known as the Quark-Gluon plasma (QGP) in the phase structure of QCD. Above a critical temperature, QCD systems are now deconfined; quarks and gluons may exist as unbound states. This phase is of particular interest due to its current experimental investigation and it is thought that the state of the early

Universe a few ms after the Big Bang is thought to be similar to that of the QGP phase - see [PŠ17], [BVS06]. It also proves a playground to further understand the so-called gauge/gravity duality.

Strongly coupled Physics is quite often investigated using lattice field theory. Unfortunately these lattice techniques cannot be used to study real time processes, as they cannot be computed from correlators. On the other hand, there has been much progress in the development of techniques via the gauge/gravity correspondence. This includes methods to compute many observables of interest in the QGP story. In this thesis, the study of light quarks traversing the QGP medium and the subsequent energy loss through their interactions with the medium are studied. A method developed by Ficnar and Gubser using so-called finite end point momentum strings is used to study a variety of gauge/gravity duals that model different strongly coupled plasmas.

In this chapter, QCD and the strongly coupled deconfined phase in particular are reviewed. In Sec. 1.2, the basics of the gauge/gravity duality are discussed and a few holographic descriptions of jet quenching are considered. Finally some of the issues faced by these models, along with how they match with certain phenomenological models that use data from experiment is described in Sec. 1.3. The data is obtained from the experiments at the Relativistic Heavy Ion Collider (RHIC) and the Large Hadron Collider (LHC).

1.1 Quantum Chromodynamics and the Quark-Gluon plasma

In 1964, the first indications that hadrons such as mesons and baryons are not fundamental particles was proposed ([Gel64], [Zwe64]). With the inclusion of gluons, it was soon proposed and accepted through experimental evidence that a non-Abelian

$SU(3)$ gauge theory best described these hadrons at a fundamental level. The first of these were the Deep Inelastic Scattering (DIS) experiments performed at SLAC in 1969 ([Blo+69], [Bre+69]).

The final gauge theory is characterised by the following Lagrangian:

$$\begin{aligned} \mathcal{L} &= -\frac{1}{4}F^a_{\mu\nu}F^{a\mu\nu} + (\overline{q}_L)^i \not{D} (q_L)_i + (\overline{q}_R)^i \not{D} (q_R)_i \\ &- M_j{}^i (\overline{q}_L)^j (q_R)_i - M_j{}^i (\overline{q}_R)^j (q_L)_i \end{aligned} \tag{1.1.1}$$

The field strength tensors $F^a_{\mu\nu}$ represent the gluons in the theory and are in the adjoint representation of the gauge group denoted by the index $a = 1, ..., 8$. The quarks are given by the fermions q and are in the fundamental representation of the colour gauge group. The indices i represent the different quark flavours present in the theory. It is also important to note the L/R index denotes whether the quark is left or right handed. The derivative $\not{D} = \gamma^\mu D_\mu$ is the covariant derivative with respect to the gauge group and acts on the quarks in the fundamental representation. Finally $M_j{}^i$ are diagonal mass matrices, whose non-zero components denote the masses of the quarks.

It is important to note that there are six flavours of quarks in QCD. These are usually split into two groups known as Up quarks and Down quarks. The Up and Down quarks form pairs that rotate into each through the $SU(2)$ gauge group of the standard model, however we will not be concerned by this in this discussion.

One can also split the 6 quarks in accordance with mass. The so called up, down and strange quarks are called light as their constituent masses are relatively small $(300 - 500MeV)$. The charm, bottom and top quarks have much larger constituent

masses $(1500 - 180000MeV)$ and so are called heavy quarks. It is the light quarks that are of interest in the context of this thesis and so the Lagrangian Eq. (1.1.1) is restricted to the three light quark flavours. However, the light quark computations are compared to heavy quark computations in order to discern the differences in holographic methods.

QCD has two important features of huge interest. The first is the confinement of quarks. The main reason that the constituent nature of hadrons was so difficult to identify in the 1950's and 1960's, is the fact that quarks are not observed as free states at suitably low temperatures. In other words, the quarks are always observed in bound colourless hadron states.

The first models of confinement involved strings as representations of bound meson states [Reg59]. It was found that the linear relationship between the mass and angular momentum of bound states could be modelled using relativistic strings. This provided an early glimpse at the relationship between strings and field theory states.

As one increases the temperature of the system, there reaches a critical temperature T_c above which the system undergoes a phase transition. The phase above this temperature is the deconfining phase, where quarks and gluons exist as free states. This phase is known as the Quark-Gluon plasma, as it exhibits certain features similar to electromagnetic plasmas. This is discussed later in the section.

The critical temperature, where the phase transition occurs, is given by $T_c \sim 160MeV$. One can also turn on a chemical potential associated to $U(1)_B$ Baryon symmetry. By increasing this chemical potential, one encounters a number of non-trivial phases, including the QGP and colour superconducting phases. Fig. 1.1 shows the full phase diagram of QCD [Bha14].

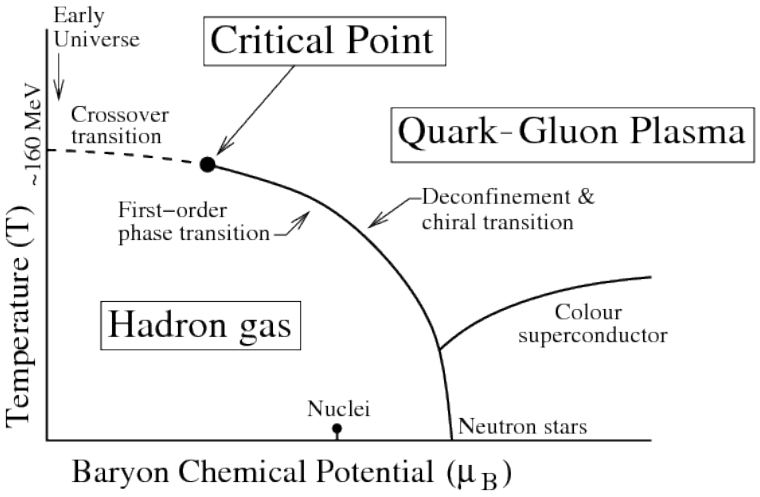

Figure 1.1: This shows the phase diagram of QCD for varying temperature and Baryon chemical potential μ_H [Bha14].

In order to easily discern whether the system is in either phase, the Polyakov loop is used as an order parameter [MS81]. The loop is defined as[1] :

$$\begin{aligned} \langle W_P \rangle &= \left\langle \frac{1}{N_c} \mathrm{Tr} \mathcal{P} \mathrm{exp} \left[\int_0^{\frac{1}{T}} A_0 dx^0 \right] \right\rangle \\ &\sim \exp\left[-\frac{F_q}{T} \right] \end{aligned} \tag{1.1.2}$$

The second line of Eq. (1.1.2) states that the Polyakov loop is related to the free energy of a free quark introduced into the system. The loop must vanish for the confinement phase, since it is not possible for free quarks to exist in this phase by definition. For non-zero values, the free quark exists and this is a determining sign of deconfinement.

One can also use closed static Wilson loops, representing static heavy quarks to

[1]The Boltzman constant has been set to 1.

see whether the confinement is present at zero temperature. The exponent of the loop obeys an area law if the phase is confining. This is because the potential between the two quarks is linear. This area law turns to a perimeter law in the case of deconfinement, since there is no potential between the quarks.

The second key feature of QCD that is important to discuss, is asymptotic freedom. The couplings of certain quantum field theories, like Quantum electrodynamics (QED), increase with energy. In other words, the QED coupling is small for low energies, but increases to a divergence as the energy is increased (Landau pole). In QCD, the reverse if true. The coupling is large for small energies, and decreases to 0 as the energy is increased to infinity. This can be seen explicitly in the 1 loop beta function:

$$\begin{aligned} \beta &= \frac{d\alpha_S}{d\log\Lambda} \\ &= -\frac{7\alpha_S^2}{2\pi} \end{aligned} \tag{1.1.3}$$

It is clear that the coupling $\alpha_S = \frac{g_{YM}^2}{4\pi}$, decreases with the energy scale Λ. This is important in the context of the deconfined phase of QCD. For the temperatures of interest ($200MeV < T < 500MeV$), the deconfined phase is strongly coupled. It is for this reason that the QGP is difficult to study, since the strong coupling prevents one to use perturbative methods to study this phase of QCD. The asymptotic freedom gives a small insight into the fact that only bound states are observed at low energy.

Throughout this section, the deconfined phase of QCD has been called the Quark-Gluon plasma. It is instructive to qualify how this phase relates to the usual plasma. The first important point of note is the neutrality of normal plasmas. The free electric charges in the plasma are screened, due to the effect of the other charges in

the plasma. This effect is similarly observed in the QGP phase, where the screening is associated to colour charge. In the deconfining phase, the interaction between the free quarks and gluons exponentially decays with a Debye screening effect taking place.

Non-relativistic plasmas are usually defined as a quasi-neutral state of matter, exhibiting collective behaviour. In particular, the deconfining phase is observed to behave like a liquid. The equation of state for this liquid is modelled using lattice QCD in [Ris+92], and a phenomenological model in [Ban95]. The lattice QCD analysis finds that only the high momentum gluons are free, and small momentum states form glueball states. This is the reason that the plasma is not an ideal plasma.

In order to characterise the plasma, the plasma parameter $\Gamma \propto \frac{\alpha_S}{a^2 T^2}$ is defined[2]. Physically one can interpret this, as the ratio of interaction energy to thermal energy. For the QGP, this parameter is much greater than 1 and provides further evidence that the QGP does not behave like an ideal gas but a strongly correlated plasma [PŠ17].

The final feature of the QGP that should be noted is the chiral symmetry breaking/restoration transitions that occur for light quarks. Since the constituent masses are so small, it is common to model light quark QCD with massless quarks. In this case, QCD exhibits $U_L(3) \times U_R(3)$ flavour and chiral symmetries. The fact the groups are $U(3)$ is because it is the three light flavours (u, d, s) that are begin rotated in the fundamental representation of the $U(3)$ groups. The $U_L(3)$ flavour symmetry rotates the three left handed fermions and the $U_R(3)$ group rotates the right handed fermions. It is important to note that one can rotate both left and right handed parts independently, because the mass term vanishes in the massless limit. The mass term breaks the symmetry to a subgroup, where the left and right handed fermions

[2] $a \sim 0.5fm$ is the interparton distance.

transform in a dependent manner - see Eq. (1.1.1).

In the low temperatures confining phase, the system undergoes spontaneous symmetry breaking, and the $U_L(3) \times U_R(3)$ group breaks to $U_B(1) \times U_A(1) \times SU_V(3)$. The $SU_V(3)$ group is the diagonal subgroup of $SU_L(3) \times SU_R(3)$. It is also important to note that the axial symmetry $U_A(1)$ is anomalous, so does not apply in the full quantum theory. This symmetry breaking is manifest through the development of a quark condensate $\langle \bar{\psi}\psi \rangle \neq 0$.

In the deconfining phase, the symmetry undergoes this same symmetry breaking for low temperatures. However, there exists a phase transition within the deconfining phase, where the symmetry is restored. In other words, the condensate developed in the symmetry breaking phase disappears. This is called the chiral restoration phase.

An important point of note is that lattice computations are not possible to capture non-zero baryon chemical potential due to the sign problem [HK83]. In most studies, the chemical potential is assumed to be zero. This is motivated by small baryon number chemical potentials observed at the RHIC $\mu_B = 45MeV \ll T = 280MeV$ [Ada+05a]. It is possible to include these effects using the gauge/gravity duality, as we will see in Chapter 3.

1.1.1 QGP in the Laboratory: Heavy ion experiments

Having introduced the theoretical concepts underlying the QGP phase of QCD, let us review the basics of creating such a phase in the laboratory. The two main experiments of interest are the experiments at the Relativistic Heavy Ion Collider (RHIC), at the Brookhaven National Laboratory, and the Large Hadron Collider (LHC) at CERN.

In order to create the plasma state, heavy ions are accelerated and collided in

order to create the high temperatures and densities required to enter the deconfining phase - see Fig. 1.1. At the RHIC, copper (Cu) and gold (Au) ions were the main nuclei involved in the experiment. The ions were accelerated to centre of mass energies of $\sqrt{s} = 200GeV$. At these energies, the high temperatures required to enter the QGP phase are achieved. It is also important to note that high densities are created, due to the fact that the beam undergoes contraction. The three experiments STAR [Ada+05a], PHENIX [Adc+05], PHOBOS [Bac+05] and BRAHMS [Ars+05] provided much experimental data from these collisions.

The second experiment of interest is at the LHC in CERN. In 2010, the first collisions of lead (Pb) ions were performed at centre of mass energies of around $\sqrt{s} = 2.67TeV$. The beam energy has been increased steadily and recently increased to $\sqrt{s} = 5TeV$.

Let us describe the evolution of the heavy ion collisions, and the resultant fireball. Upon collision, the heavy ion beam collisions begin to form the QGP fireball. The initial energy leads to a state in disequilibrium, however the system quickly reaches the state of equilibrium in a time of order $\tau_{eqb.} \sim 1\frac{\text{fm}}{c}$ [KSH00]. The fireball then expands according to the laws of hydrodynamics. When the fireball expands, it cools and reaches the so-called freezeout temperature $T_{FO.} = 155-180MeV$ [ABS06]. At this temperature hadronisation occurs, and the hydrodynamic description of the system is no longer valid.

It is important to note the small equilibrium time $\tau_{eqb.}$. This small time is important, as it allows for the observed almond shape that the fireball takes at equilibrium. This almond shape is a consequence of the anisotropy, that are caused by peripheral collisions. This anisotropy is measured through the elliptic flow parameter ν_2. This parameter characterises the asymmetry of particles observed in different directions along the reaction plane of the collisions. This parameter is extracted from experimental data, and compared to a variety of hydrodynamic models in [Ada+05b],

[Cha+12] and [Sir+18].

Finally, let us consider the impact that the QGP medium has on jets that have not thermalised into the medium. When the fireball has reached equilibrium, ongoing collisions within the plasma can be used to probe the medium. Jets that are produced as the result of the heavy ion collisions, must pass through the medium. These jets interact with the medium and hence undergo a procedure of energy loss that is not observed in nucleon-nucleon collisions. In fact, it is possible that entire jets lose all their energy, and are thermalised into the medium.

Consider two jets that are produced near the edge of the plasma medium, but are travelling in opposite directions. If one jet is travelling away from the centre of the medium, it does not have to travel far before it escapes the medium. However, the other jet must travel a large distance within the medium, as it is travelling in the opposite direction. Through its interaction with the medium, there is a chance that this jet does not emerge from the other side, and completely thermalises to form part of the medium. This process is known as jet quenching.

A useful measure of this process is known as the jet nuclear modification factor R_{AA}.

$$R_{AA} \propto \frac{d\sigma_{I-I\to H}/dp_T}{d\sigma_{p-p\to H}/dp_T} \tag{1.1.4}$$

$d\sigma_{I-I\to H}(p_T)/dp_T$ is the distribution of the produced hadron H from heavy ion collision from the medium, and is a function of the transverse momentum p_T. Similarly, $d\sigma_{p-p\to H}(p_T)/dp_T$ is the distribution of the same hadron H from proton-proton collisions, where there is no QGP medium for the jet to undergo quenching.

It is expected that this parameter yields a fractional result,s due to the fact that the

number of jets observed in the heavy ion case is suppressed from medium interaction. This is indeed observed in both the RHIC [Pło09] and LHC ([Col12], [Col18]) experiments.

The final observable that is important to mention in the context of jet quenching is the so-called jet quenching parameter $\hat{q}$. This concerns the momentum lost by the partons produced by the heavy ion collisions within the plasma. As the partons traverse the medium, they interact and gain momentum transverse to the longitudinal direction of travel. This momentum broadening is a key effect of the medium's impact on the parton. The transverse momentum broadening is characterised by the parameter $\hat{q}$, which is a measure of the change in transverse momentum squared per unit time that the parton undergoes as it traverses the medium [Bai+97]. This parameter can be extracted from R_{AA} data, by considering different phenomenological models of parton propagation [Ada+08], [Bur+14] and [CLQW18].

1.2 Review of the Gauge/Gravity duality and holographic models of jet quenching

Having discussed the basics of the QGP phase of QCD in Sec. 1.1, the basics of the gauge/gravity duality and a number of holographic models of jet quenching are reviewed in this section.

In 1997, Juan Maldacena proposed a connection between $\mathcal{N} = 4$ $SU(N_c)$ Superconformal Yang-Mills, and 10D Type IIB supergravity on $AdS_5 \times S^5$ [Mal98a]. The origin of this connection comes from the identification of particular solutions of 10D supergravity known as black p-branes, and the Dirichlet boundary conditions for open strings known as D-Branes [Pol95]. Maldacena showed by taking the low energy limit in a particular manner, there exists a duality between the gauge theory and the supergravity theory.

The particular case considered was a stack of extremal N_c D_3 branes. According to Polchinski, the branes are described by the fluctuations of open strings ending on the branes for $g_s N_c \ll 1$, where g_s is the string coupling constant. It is important to note that this is all within the perspective of perturbative string theory; that is the limit $g_s \ll 1$. To be more specific, the D_3 branes are described by open string excitations with the end points lying on the branes, closed string excitations traversing the bulk, and open/closed string interactions in which closed string are emitted/absorbed by the brane through closed $\rightarrow$ open string tree level interactions.

On the other hand, the stack of branes are described by the black 3-brane solution of Type IIB supergravity for $g_s N_c \gg 1$. The black brane solution is given by:

$$\begin{aligned} ds_{10}^2 &= f^{-\frac{1}{2}}(-dt^2 + dx^2 + dy^2 + dz^2) + f^{\frac{1}{2}}(dr^2 + r^2 d\Omega_5) \\ f(r) &= 1 + \frac{L^4}{r^4} \end{aligned} \tag{1.2.1}$$

where L is a length scale defining the curvature of this metric. The sub-space (t, x, y, z) spans the directions parallel to the D_3 branes, and $d\Omega_5$ represents the metric of a compact 5-sphere subspace. Also, the radial co-ordinate is a positive co-ordinate $r \geq 0$, where the black brane horizon is defined by $r = 0$. It is important to note that there exist a non-trivial self-dual 5-form field, and a scalar dilaton field turned on in this solution. However, this is not relevant to the discussion that follows.

It is well known that Type II supergravity is a low energy effective theory for closed superstring theory. This condition is best defined through the length scales in the theory as $\frac{\sqrt{\alpha'}}{L} \ll 1$, where α' is the square of the fundamental string length l_s. The connection between this supergravity solution and the D_3 brane open string

picture is made through the following identification of parameters:

$$L^4 = 4\pi g_s^2 N_c \alpha'^2 \tag{1.2.2}$$

One can see from Eq. (1.2.2) that the supergravity condition $\frac{\sqrt{\alpha'}}{L} \ll 1$ matches with the Polchinski brane condition $g_s N_c \gg 1$. It is also important to note that the supergravity description is valid for tree level interactions only i.e for $g_s \ll 1$.

In the low energy limit, the open string description ($g_s N_c \ll 1$) undergoes a decoupling effect. The interaction between closed and open strings scales with α', so this interaction no longer occurs in the low energy limit since $\alpha' \to 0$ defines this limit. One is left with two distinct effective low energy quantum field theories; $\mathcal{N} = 4$ superconformal $SU(N_c)$ Yang-Mills, which describe the open string excitations, and Type IIB supergravity in flat space describing the closed strings.

Moving to the black brane description ($g_s N_c \gg 1$), it is naive to only consider locally low energy excitations. Let us consider the Doppler shift that occurs when a local excitation at a position r with energy E_r, is observed by an asymptotic observer. An observer at $r = \infty$, would measure this excitation with energy:

$$E_\infty = f^{-\frac{1}{4}} E_r \tag{1.2.3}$$

It is clear to see that for arbitrary r, the excitations E_r must be small in accordance with the low energy limit. However, finite E_r excitations are permissible for $r \to 0$, as the Doppler shift reduces these excitations to low energy for the asymptotic observer.

In this sense, the low energy theory in the black brane background undergoes a similar decoupling effect to the open string description. On the one hand, one has

Type IIB supergravity at the boundary ($r \to \infty$). Eq. (1.2.1) shows that this is effectively just flat space supergravity. In the second case, one has Type IIB supergravity in the $r \to 0$ limit of the black brane background. It is trivial to see that this near horizon limit of the black brane background is $AdS_5 \times S^5$.

$$ds^2 = \frac{r^2}{L^2}\left[-dt^2 + dx^2 + dy^2 + dz^2\right] + \frac{L^2}{r^2}dr^2 + L^2 d\Omega_5 \tag{1.2.4}$$

Both descriptions undergo a similar decoupling and in each case, one of the decoupled theories is Type IIB supergravity in flat 10D space-time. It is thus natural to identify the duality between the gauge theory, describing the open strings on the branes, and the Type IIB supergravity in the $AdS_5 \times S^5$ background.

So Type IIB supergravity on $AdS_5 \times S^5$ can be used to describe $\mathcal{N} = 4$ super Yang-Mills in the limit of $g_s N_c \gg 1$ and $g_s \ll 1$. These limits intimate that colour number N_c must be large for this limit to hold. The final parameter that must be identified on the gauge theory side is the Yang-Mills coupling. This is given by $g_{YM}^2 = 4\pi g_s$, and means the limit in which the duality holds is the large $N_c \gg 1$ t'Hooft limit defined by $\lambda = g_{YM}^2 N_c \gg 1$. This limit is associated to the first indications that string theory and gauge theories are connected.

t'Hooft found in 1974 that in the large N_c limit, non-Abelian gauge theories arranged themselves into a double expansion [Hoo74a]. Rather than using the usual single line Feynman diagrams, t'Hooft proposed a double line system, where the double lines represent the adjoint representation indices of the fields involved. These 2D graphs can also be interpreted as string world sheets. In fact, t'Hooft realised that the perturbative series arranged itself in terms of the topology of these diagrams. A diagram of higher genus, carries a higher overall factor of $\frac{1}{N_c}$. This means that in the large colour limit only the planar (genus 0) diagrams remain. For each genus, the series becomes an expansion in $\lambda = g_{YM}^2 N_c$. This was the first hint

between the connection of gauge theory and string theory. So the limit in which the gauge/gravity duality has been described, matches the planar large λ case in t'Hooft's double line expansion.

It is important to note that it is assumed that the correspondence occurs outside of the large N_c t'Hooft limit. The most general statement of the correspondence is that $\mathcal{N} = 4$ super Yang-Mills is dual to closed superstring theory on $AdS_5 \times S^5$, for all values of the parameters. However, performing computations on either side of the duality for this general case is extremely non-trivial. For the purpose of our discussion, the simpler large N_c t'Hooft limit is always considered.

The specific case discussed above is an example of a top down model of the gauge/gravity duality. First, one can generalise this by extending this to other black p-branes. For an arbitrary black brane, the gauge theory content and dimensions change, along with the near horizon background metric of the black brane. One can construct a variety of models by introducing different stacks of branes, and taking the near horizon limit of the associated black brane configurations. It is also possible to further extend the system, by introducing fundamental matter to the system through probe branes.

From the gauge theory point of view, introducing a set of N_f branes at some separation from the N_c main stack of branes expands the types of open string excitations possible [KK02]. The open strings that live on the N_c colour branes and closed strings that propagate the bulk still exist, but they are supplemented by open strings on the probe branes and strings that stretch between each stack. When the Maldacena limit ($\alpha' \to 0$) is taken in the probe limit as defined by $g_s N_c \gg 1$ and $g_s N_f \ll 1$, the decoupling effect between closed strings in the bulk and open strings on the branes occurs once more. However, the open strings on the flavour probe branes also decouple from both the closed strings and the open strings on the N_c stack of branes.

On the other hand, the stretched strings between the stacks and the open strings on the colour branes remain. Since the stretched strings have end points that lie on each stack, they transform under the fundamental representation of both the gauge group $SU(N_c)$, and the flavour global symmetry group $U(N_f)$. The resulting decoupled theories are Type IIB supergravity in 10D flat space, and $SU(N_c)$ gauge theory coupled to fundamental matter fields in the fundamental representation of both gauge and global flavour symmetry groups. The mass of the fundamental matter is dependent on the separation of the two stacks of branes.

From the gravitational side, this system is described by treating the flavour branes as probes within the black brane solution of supergravity[3]. The flavour branes are described by the DBI action and the fields associated with this action. The symmetry itself is realised through the gauge fields living on the probe branes. Whilst this symmetry is a gauge symmetry in the gravitational system, it is realised as a global symmetry in the dual field theory. One can then construct models by setting up stack of appropriate colour branes and flavour branes with the particular desired features of interest, and use the weakly coupled gravitational dual to analyse the strongly coupled field theory. Some solutions describing D_7 flavour branes, for both the $T = 0$ and finite temperature cases, are shown in Appendix D.

It is possible to generalise even further and work from the so called bottom up approach ([GPR08], [GN08], [RFFN16]). In this case, one starts with gravitational theories and find solutions that can be written in general as $\mathcal{M} \times \mathcal{C}$. This is a 10D system, where $\mathcal{M}$ is a non-compact manifold with a boundary, and $\mathcal{C}$ is a compact subspace. One can then build gravitational theories with specific properties of interest in order to model strongly coupled dual gauge theories.

[3]The back reaction from the branes is negligible in the probe limit $g_s N_c \gg 1$, $g_s N_f \ll 1$.

1.2.1 Finite Temperature and Confinement/Deconfinement phase transition

So far, the zero temperature vacuum state of the field theory has been discussed in the context of the gauge/gravity duality. Continuing to Euclidean time and compactifying the time co-ordinate with periodicity $\frac{1}{T}$ in the gravitational theory, one can turn on a non-zero temperature in the dual theory. This mimics the canonical methodology of finite temperature field theory.

Since the deconfined phase of QCD is the state of interest in this thesis, it is important to discuss phase transitions in the context of the gauge/gravity duality. The first proposal for the confinement/deconfinement phase transition, was the Hawking-Page phase transition observed for the global AdS_5 background [Wit98b]. The AdS_5 black hole is found to be thermodynamically more favourable[4] than the AdS_5 vacuum state. However, the transition only occurs for the global, spherical topology background. The near horizon region of the black 3-branes described in Eq. (1.2.1) is the planar Poincaré patch of AdS_5. The planar black hole is always thermodynamically more favourable for finite temperatures, and hence there is no phase transition that occurs.

It is also important to note that the AdS_5 background is not dual to a confining phase. It is well known that the static Euclidean Wilson loop, representing heavy quarks, acts as an order parameter in the context of confinement/deconfinement. The exponent of the Wilson loop relates to the energy of the flux tube created by the Wilson line operator. If an area law is observed, the system is in a confining phase and if a perimeter law is observed, then the system is in a deconfining phase.

In 1998, Maldacena proposed the connection between classical strings in the gravitational theory and Wilson loops in the dual theory [Mal98b].

[4]This solution minimises the free energy over the AdS_5 vacuum state.

$$W_{\mathcal{C}} \sim e^{-S_{NG}} \tag{1.2.5}$$

S_{NG} is the on-shell Nambu-Goto action, which describes the dynamics of a relativistic string, whose end point follow the curve $\mathcal{C}$ that describes the loop contour. The radial value for the end point of the strings is taken to the boundary $r \to \infty$. One can then use this proposal to compute the Wilson loop for the static case, and hence determine whether confinement is present.

The first proposal to model the phase transition in the gravitational side of the duality, involves a hard wall that is imposed onto the system [Her07]. At some fixed r_0, an artificial cut off is imposed. The string required to compute the static Wilson loop to determine confinement/deconfinement, drops from the boundary and lies flat along this hard wall. This condition leads to a confining potential. As the temperature is increased past the critical temperature $T = \frac{2^{\frac{1}{4}} r_0}{L^2 \pi}$, the AdS_5 black hole is thermodynamically more favourable and a phase transition occurs. The string now drops from the boundary into the black hole and the potential is no longer confining. This model describes the confinement/deconfinement transition correctly, however it requires an artificial wall to be imposed onto the system.

Alternative methods involve a bottom up approach, in which additional scalar fields are added to the gravitational action ([Her07], [LYY17]). By choosing appropriate potentials for the scalar, one can obtain cutoffs similar to the hard wall, but occur naturally from the gravitational equations of motion. Once more, a black hole solution dominates past a critical temperature, and the lack of the wall leads to deconfining potentials as required.

The final model to mention are top down models, in which a modification of D_p

branes are considered [SS05b]. These are called D_4 solitons, where a cutoff is introduced through the metric itself. The extra dimension parallel to the brane is compactified to obtain a $4D$ gauge theory, and the background develops a confinement/deconfinement transition. Matter can be added to this model by the inclusion of D_8 probe branes and is called the Sakai-Sugimoto model. Further details of this are outlined in Appendix A.

A variety of gauge/gravity duality models that describe the confinement/deconfinement phase transition have been discussed. The high temperature phases, describing the deconfining plasma phase, all involve black holes. This is important in the context of the thermalisation of probes in strongly coupled plasmas, as will be discussed later in this chapter.

1.2.2 Field/Operator Correspondence and large energy excitations

Whilst a rough reasoning for the connection between the gravitational theory and gauge theory has been made, this was not made concrete until a connection between gauge theory and gravitational fields had been made. In [Wit98a], a proposal to make this relationship concrete was made by considering absorption and emission of closed string modes by branes [Kle97],[GK97] and [GKT97]. The identification can be made through:

$$\exp\left[-S^{cl.}_{grav}(\phi(\vec{x},r))\right] \sim \left\langle \int_{\Sigma} \phi_0(\vec{x})\mathcal{O}(\vec{x}) \right\rangle_{FT} \tag{1.2.6}$$

The field $\phi(\vec{x},r)$ is an on-shell supergravity field that behaves like:

$$\phi(\vec{x}, r \to \infty) \sim f(r)\phi_0(\vec{x}) \tag{1.2.7}$$

The field asymptotes to the field ϕ_0 up to a conformal factor. The operator $\mathcal{O}$ is an operator of the field theory that is dual to the supergravity field ϕ. The expectation value on the right hand side is on the field theory side and the integral is over the manifold Σ, which describes the conformal boundary to the non-compact part of the 10D supergravity background $\mathcal{M}$. One can use this correspondence to compute correlation functions of the various operators $\mathcal{O}_i$ in the gauge theory, by solving the classical supergravity equations of motion subject to the boundary conditions Eq. (1.2.7), substituting into the action, and taking functional derivatives with respect to ϕ_0.

The solutions to the classical gravity equations described above are known as non-normalisable, due to the fact that they do not vanish at the conformal boundary by definition. However, it is possible to add solutions that are normalisable i.e. vanish at the boundary. These solutions may be written as a superposition of normalisable modes. These modes are defined to be dual to field theory excitations of the dual operator $\mathcal{O}$. To be more specific, the glueballs associated to the operator $\mathcal{O}$ are dual to the normalisable modes associated to the dual operator ϕ [COOT99].

Whilst many of the field theory states are identified with these normalisable supergravity modes propagating in the gravity background, there exist certain large energy states which are not. The duality identifies these large energy states in the field theory with classical strings propagating in the gravity background[5]. In particular, the end points of these strings are identified with dressed quarks in the dual theory. This entry in the so called gauge/gravity dictionary arises from the Wilson loop conjecture by Maldacena [Mal98b], and was further elucidated in [GKP02].

[5]In the large colour and large t'Hooft coupling limit $N_c \to \infty$ and $\lambda \to \infty$, the strings are classical and the energy scales as $\sqrt{\lambda}$.

1.2.3 Large energy excitations and jet quenching probes

At the end of Sub. 1.2.2, it was noted that the normalisable modes of the supergravity and the probe brane world-volume fields, fully describe the normalisable modes of dual gauge theory operators. For example, the dilaton is dual to the $\mathrm{Tr}(F^2)$ operator, and its modes are dual to bound state glueballs.

However, there also exist heavy soliton states, which carry large charges in the gauge theory. The natural object to identify these states are 'solitons' of the non-linear sigma model, whose low energy states are described by sugergravity. These particular states are large macroscopic strings that end on the colour and probe branes [RY01]. Strings with one endpoint on each brane is dual to a quark, as it transforms under fundamental representations of both the flavour group $U(N_f)$ and the gauge group $SU(N_c)$. On the other hand, strings whose endpoints both end on the same brane are though of as meson states. There are also large R-charge and spin operators dual to large macroscopic spinning closed strings on the gravity side [GKP02].

These ideas were first put forward by Callan and Maldacena [CM98]. They showed that certain macroscopic strings attached to D_p branes, can excite BPS states on the world volume of the brane. The gauge fields of the brane look like those of a point charge. The orientation of the string determines the sign of the charge of the quark. In this case, a single brane is seperated from a stack of $N+1$ branes by an infinite distance. The effect is the spontaneous symmetry breaking $U(N+1) \to U(N) \times U(1)$ on the world volume theory. The quark is a soliton state associated with massive W bosons, caused by this spontaneous symmetry breaking. By putting together two strings of opposed orientation, one does not form a stable state. It turns out that by joining the two strings into a single connected string, one can represent a bound $q\bar{q}$ state [RY01]. In our case, the quarks are states associated to the hypermultiplet introduced via the probe branes.

This notion was used to motivate the computation of Wilson loops using AdS/CFT, as noted in Sub. 1.2.1. It was also shown that the gluon potential sourced by the quark, obeys a coulomb like potential[6]. This computation involves solving for the dilaton sourced by the static string, and using the bulk to boundary correspondence to compute $\langle \mathrm{Tr} F^2 \rangle$ [DKK99].

One of the key applications of the gauge/gravity duality has been the study of strongly coupled plasmas. As mentioned in the introduction of Chapter 1, strongly coupled Physics is quite often investigated using lattice field theory. Unfortunately these lattice techniques cannot be used to study real time processes, due to the fact that they require Wick rotation to Euclidean time. On the other hand, there has been much progress in the development of techniques via the gauge/gravity correspondence. This includes methods to compute many observables of interest in the QGP story. It also provides a playground to investigate the duality itself.

In order to investigate the QGP, let us use the gauge/gravity duality to review a number of different methods used to analyse how certain partons interact and lose energy to the QGP medium. These methods use the large charge, classical string states to describe the probes traversing the strongly coupled medium.

Heavy probes and the drag force

The first example of a direct application of the gauge/gravity duality, in the context of jet quenching, is the drag force for heavy quarks. This was first proposed and studied in 2006 in [Her+06]. In order to describe this system, one introduces probe D_7 branes into the AdS_5 black hole geometry. The black hole is chosen to describe the deconfinement phase of the dual field theory. For quarks with large masses, it can

[6]The modification is due to the finite width of the dual state at finite temperature. The dual quark is a quasi-particle with finite size. Far from the quasi particle the potential tends to Coulomb.

be shown that the probe branes drop from the boundary to a fixed radius $r_m > r_H$, where r_H is the location of the event horizon - see Appendix D. As explained in Sub. 1.2.3, the gravitational dual of the heavy quark is modelled by classical relativistic strings.

The Nambu-Goto action, describing the string dynamics, is just the pull back of the space-time metric $G_{\mu\nu}$ on to the world sheet of the string:

$$S = -T_0 \int \sqrt{-h} d\tau d\sigma \tag{1.2.8}$$

where $h_{ab} = G_{\mu\nu}\partial_a X^\mu \partial_b X^\nu$ is the volume element on the world sheet, h is the determinant of the metric h_{ab}, T_0 is the tension of the string and $\sigma^a = \{\tau, \sigma\}$ are the co-ordinates on the world-sheet. Let us first consider a static string in pure $AdS_5 \times S^5$ in static gauge.

The string in question has one end attached to the D_7 brane at a radial co-ordinate r_m and hangs down to $r = 0$. This is dual to a static heavy quark in the dual theory with mass $m_q \propto r_m$. One can reconcile this by considering the energy of the static string. The exponential of the energy of the string just gives us the static endpoint Wilson line in the gauge theory [Mal98b]. It is standard that the infinite time static Wilson line is just the exponential of the ground state energy of the quark on the gauge theory side. This is proportional to r_m. The mass parameter in the action for the elementary quarks m is determined from the brane embedding. It turns out that this mass is proportional to r_m as well. So the mass of the elementary perturbative quark states and the heavy soliton states are proportional to each other[7].

Now consider a similar string in the AdS_5 black hole background. The string has one endpoint at r_m, but the other lies at the horizon of the black hole r_h. The energy

[7]Remember the proportionality is $\sqrt{\lambda}$ and so is formally infinite in the t'Hooft limit.

of this string is now proportional to $(r_m - r_h)$. A similar look at the static Wilson line indicates that the string energy is actually dual to the free energy contribution from this probe quark. It includes contributions from the effect the quark has on the medium. So the total energy has two components; one from the internal energy of the quark and another from its interactions with the medium.

It is important to note that the relationship between r_m and m is no longer the same. Since the gravitational background has changed, the embedding of the D_7 is different. The flavour branes are introduced at some separation R in the directions perpendicular to the D_3 branes. In order to find the radius r_m, one extremises the world-volume action of the brane in the background of interest.

For a general asymptotically AdS background, the radius r_m is a non-trivial function of the separation R, however $r_m \propto R$ in the pure AdS case. Now the mass of elementary quark excitations m is proportional to R. So for the pure AdS case, m is proportional to R, R is proportional to r_m and r_m is proportional to the string energy. One can directly relate the string energy to the mass of the quark.

In general however, m is proportional to R, $r_m(R)$ is some non-trivial function of R, and the energy of the string depends on r_m. This means m and r_m, and hence m and the string energy have non-trivial relationships between them. For the AdS_5 black hole system, it can be shown that the relationship between m and r_m is given by:

$$\frac{T_0 r_m}{m} = 1 + g\Big(\frac{T_0 r_h}{m}\Big) \tag{1.2.9}$$

where $g(x)$ is a non trivial function determined as a truncated series, chosen at a suitable level of accuracy [Her+06]. $g(x)$ tends to 0 for small x, and so the relationship between m and r_m tends towards the $T = 0$ case for $m \to \infty$.

Now let us consider a trailing string solution. In [Her+06] and [Gub06], the authors find a particular solution to the string equations of motion in the black hole background. For this solution, the endpoint of the string travels in the x-direction at constant $\frac{dx}{dt} = v$. This solution violates standard Neumann boundary conditions, and thus one interprets this violation as the consequence of an external electric field. The dual quark is fed energy through the electric field at a rate equal to the energy it loses to the medium in order to maintain a constant speed. The energy of this string is formally divergent, due to a logarithmic factor that tends to ∞ as $r \to r_h$. By introducing a regulator near the horizon, the energy and momentum of the string can be written as follows:

$$E = T_0 L^2 \frac{(r_m - r_{min})}{\sqrt{1-v^2}} + \frac{1}{v}\pi_t^\sigma \Delta x(r_{min}) \tag{1.2.10}$$

$$P = T_0 L^2 \frac{v(r_m - r_{min})}{\sqrt{1-v^2}} + \frac{1}{v}\pi_x^\sigma \Delta x(r_{min}) \tag{1.2.11}$$

where r_{min} is an IR regulator controlling the divergence at $r = r_h$, $\Delta x(r_{min})$ is the difference in x between the string endpoint at r_m and the cut off at r_{min}, and π_μ^a are the conserved currents due to space-time translation symmetry. $\pi_{t(x)}^\sigma(t,\sigma)$ is just the rate at which energy (momentum) flows through the string at a point defined by σ along the string and at time t. The total energy (momentum) flowing through the point over some period Δt is just given by the following integral:

$$E_{\Delta t} = \int_{\Delta t} \pi_t^\sigma dt \tag{1.2.12}$$

It turns out that $\pi_{t(x)}^\sigma$ is a constant along the string. This means it is non-zero at the string end point, which is the manifestation of non-Neumann boundary conditions[8].

[8] $\pi_x^\sigma = 0$ at the end point for Neumann conditions.

The non-zero value is the rate at which energy and momentum is transferred from the dual external electric field to the quark. This is equal to the rate at which energy is lost by the quark, in order for it to maintain the constant speed. The string energy is no longer the correct exponent when computing the Wilson loop, because the string is now dynamical. One must evaluate the NG action on shell and exponentiate in order to find the Wilson line. On the dual side one cannot interpret the exponent as the free energy due to the dynamical characteristic of the line[9]. However it does seem intuitive to think that the string energy does contain contributions of both the quark energy and its interactions with the medium.

The first term of Eq. (1.2.10) looks very much like the energy of a relativistic particle of mass $T_0 L^2(r_m - r_{min})$. The second term goes like $\frac{dE}{dx}\Delta x(r_{min}) = \frac{1}{v}\frac{dE}{dt}\Delta x(r_{min})$, which looks like the energy lost by the quark as it travels the distance $\Delta x(r_{min})$. When $r_{min} \to r_h$, $\Delta x(r_{min})$ just becomes the difference in x between the end point at r_m and r_h. So the infinite term is the total energy lost (and gained from the external field) for the quark travelling at constant speed over an infinite time.

Also, the mass tends to the thermal mass $M(T)$ in this limit. The authors suggest that it is not correct to assume the first term correctly describes the quark energy. This is because the quark has a finite size and is not point like. Instead one should accelerate a static string over a small time scale, such that the energy lost in this time is negligible, and define the quark energy as the energy of the string at this time.

In order to correctly obtain the energy, one would have to use the bulk to boundary map in order to compute the dual stress tensor for the string[10]. In other words, one would compute the back reaction of the string, and then integrate the energy density

[9] The exponent of the Wilson loop tends to the ground state energy for non-dynamical infinite time loops. This is not the case if the line represents some non-trivial dynamics of a quark.

[10] One would remove the constant force and allow the string to stop in this case.

over a sphere representing the quasi-particle. This sphere would be centred about the string end point, and would have radius $\sim \frac{1}{T}$; the size of the quasi-particle is of order $\frac{1}{T}$.

In [Her+06], they model the energy loss via a toy model given by $\frac{dp}{dt} = -\mu p$, where μ is a constant. By also assuming a relativistic dispersion relation $p \propto \frac{v}{\sqrt{1-v^2}}$ (v is the end point speed), they numerically obtain values for μ by matching this model to strings. Whilst this model does seem to match fairly well, they have not used the full bulk to boundary mapping to compute the energy loss. They also obtain a dispersion relation, by assuming the energy and momentum of the string are dual to the quark energy and momenta. However, this is not true for reasons stated above.

Following the AdS_5 black hole case, a number of authors used this method and applied it to a variety of different holographic models, including models that add chemical potentials, anisotropy, angular momentum and more - see [SSPH09], [AS10], [CFMT12a] and [BL07].

Light quarks and the stopping distance

In Sub. 1.2.3, the probes considered were massive quarks i.e. those with mass larger than the temperature $\frac{m}{T} \gg 1$. Let us now consider so called light quarks, with masses far lower than the temperature scale $\frac{m}{T} \to 0$.

In this case, the probe brane fills the entire AdS_5 background, up to the black hole horizon - see Appendix D. Strings in this background are free to fall to the horizon and into the black hole. In the massive case, the string cannot fall into the black hole because the end point boundary condition, provided by the probe brane, forces the string end point to a minimum radius. In the small mass case this does not occur, due to the lack of a cut off.

In [CJKY09], falling strings in both AdS_5 and AdS_5 black hole backgrounds are analysed. Certain long lived string states are constructed and used to analyse the baryon density of the dual theory. These strings are initially point like, located near the boundary, and kicked in directions parallel to the boundary co-ordinate x. The baryon density is interpreted as the time component of the current associated to the $U(1)$ global flavour symmetry on the field theory side. This is realised via a $U(1)$ gauge field on the probe brane world volume on the gravity side.

The string end point is charged under this gauge field, and so sources the field. By computing the first order correction to the gauge field, one can use the field/operator correspondence (see Sub. 1.2.2) to compute the dual baryon current density. In particular, it is realised that certain strings resemble steady state strings, which travel almost entirely in the x direction over a time scale $\frac{L^2}{r_H} \ll t \ll \frac{r_0 L^2}{r_H^2}$. r_0 is the initial radial starting co-ordinate. As the end points of the string travel in opposite directions initially, the bulk of the string dips into the bulk of the geometry, and reaches the horizon in a time scale $t \sim \frac{L^2}{r_H}$.

For the near boundary strings, the baryon density is very local to the end point of the string. In other words, the closer the string is to the boundary, the more local the density is. For $t \gg \frac{r_0 L^2}{r_H^2}$, the density starts to spread out, and is now described by hydrodynamics [11].

The dual picture is as follows: the quark loses energy up to the thermalisation time $t_{therm} \sim \frac{r_0 L^2}{r_h^2}$. The quark then undergoes thermalisation i.e. it begins to disintegrate into a soup of gauge fields and quarks. This is the dispersing of the baryon density. The rest of the string evolution then describes the evolution of the resulting

[11] The time taken for the string to reach the black hole horizon is infinite and the distance x is finite. However, the thermalisation time is finite, but very close to the horizon in the $r_0 \gg r_H$ limit. In principle, we should compute the stopping distance at the thermalisation time. But since this event is very late time for this limit, one can use the finite stopping distance as calculated at the horizon. The difference between this and the distance at the thermalisation time is negligible.

soup, which occurs from t_{therm} to t_H and is formally infinite. One can consider strings representing suitably long lived quark states, where the thermalisation time and the time taken for the string to fall into the horizon are the same. Hence these states maximise the stopping distance of the quark, which occurs when the point of thermalistion is at $t \to \infty$.

In order to determine the dependence of the stopping distance on the initial energy of the quark, one needs to find a mapping between the string energy and the quark. In [CJK09], they argue that the quark energy can be extracted from the string energy, by identifying the UV contribution of the energy. By looking at the 1st order perturbations on the null steady state string, they extract an exact relationship between the energy and r_0.

Also, the authors approximate the trajectory of the end points of the string, by considering perturbations from geodesic motion - see [CJKY09]. This allows one to obtain a maximum stopping distance approximation, as a function of r_H and r_0. Eliminating r_0 for the energy and r_H for the temperature, the following approximation for the stopping distance is obtained:

$$\Delta x_{stop} = \frac{C}{T}\left(\frac{E}{T\sqrt{\lambda}}\right)^{1/3} \tag{1.2.13}$$

where Δx_{stop} is the stopping distance, T is the temperature of the plasma and E is the initial energy of the quark. The constant C is later computed numerically, by obtaining the stopping distance for various initial conditions of strings. Here the energy is computed as half the string energy. Whilst the assumption of large energy density near the end point means this is valid to some extent, there will be contributions from the interior of the string. These contributions will include quark-medium interactions.

Another observable of interest is the rate at which energy is lost to the plasma. Again, this can be computed from the dual stress tensor and considering the energy flux through a sphere of radius $\sim \frac{1}{T}$. Since the quark energy is identified with the high energy density at the string end point, it is argued that the flux of the string energy, flowing down the string evaluated near the string end point, is dual to the rate of quark energy loss. The plot obtained in [CJKY09] shows a late time burst of high energy loss. This picture is consistent with the evolution of the baryon density from highly local, to suddenly non-local through the thermalisation process.

It is important to note that the point along the string the flux is evaluated is not important when the rate is small. So the behaviour at late times described by this approximation may not be accurate. The Bragg peak behaviour is universal to all initial conditions for near boundary strings. The time at which the peak appears coincides with the thermalisation time, as one would expect.

Jet quenching parameter

The last methods of the gauge/gravity duality, used to study the strongly coupled plasma, are the light-like Wilson loop and time-like virtual gluon methods, used to compute the jet quenching parameter $\hat{q}$. This is a parameter that measures the energy loss of a parton produced in the QGP medium. To be more precise, it is the transverse momentum squared lost by the parton, traversing the medium per unit time.

In [Bai+97], Baier, Dokshitzer, Müeller, Peigne and Schiff (BDMPS), proposed a method to compute the process of gluon radiation in the context of a medium (e.g. QGP), considering both quarks and gluons as the partons initially involved in the scattering process. Using this formalism and by considering the energy distribution of the gluon radiation, it is possible to relate the jet quenching parameter to the Wilson loop of a closed light-like path that two quarks, seperated by a distance L_D

travel along ([LRW06], [LRW07]).

$$\left\langle W_C^A \right\rangle \approx \exp\left[-\frac{1}{4\sqrt{2}}\hat{q}L^- L_D^2\right] \tag{1.2.14}$$

Let us define the curve C more concretely, by firstly defining light-cone co-ordinates $x^{+/-} = \frac{1}{\sqrt{2}}(x_0 \pm x_1)$. The curve is constructed by considering two lines defined by $x^+ = \text{const.}$, $x_2 = \pm\frac{L_D}{2}$. The length L^- describes the path length traversed by the quark along the loop. It is important to note that it is assumed that $L^- \gg L_D$.

Using Eq. (1.2.14), the authors' in [LRW06] use the Wilson loop conjecture (see Sub. 1.2.3) to compute the jet quenching parameter. It is important to note that the expression in Eq. (1.2.14) is used as a non-perturbative definition of the jet quenching parameter itself.

In order to do this, the classical relativistic string, travelling in the AdS_5 black hole background, must be solved for. The boundary conditions for this string are defined by the light-like curve of the Wilson-loop; the end points of the string follow the trajectory of the loop in the co-ordinates parallel to the conformal boundary for $r \to \infty$. The final expression for the Wilson loop, and hence the jet quenching parameter is given by:

$$\begin{aligned}\left\langle W_C^A \right\rangle &= \exp\left[-\frac{\pi^{\frac{3}{2}}\Gamma\left[\frac{3}{4}\right]}{4\sqrt{2}\Gamma\left[\frac{5}{4}\right]}\sqrt{\lambda}T^3 L^- L_D^2 + \mathcal{O}\left(T^5 L^- L_D^4\right)\right] \\ \Rightarrow \hat{q} &= \frac{\pi^{\frac{3}{2}}\Gamma\left[\frac{3}{4}\right]}{\Gamma\left[\frac{5}{4}\right]}\sqrt{\lambda}T^3\end{aligned} \tag{1.2.15}$$

This method to compute the parameters was followed for a variety of different models, including finite chemical potential, anisotropy, and also for the case of adding next order terms for the finite λ expansion (see [FPS11], [GXZ06], [ZHR13], [WW16]

and [AEM06]).

There is a second method that is important to review in the context of this thesis. In [GGPR08], the jet quenching parameter for virtual gluons produced in the QGP soup is computed, using the gauge/gravity duality. In order to do so, Gubser et al. model the virtual gluon as a doubled closed string that falls into the AdS_5 black hole. The initial state of the falling string is set up, by considering the trailing string solution found in the drag string case - see Sub. 1.2.3. This trailing string defines the initial condition of the closed string configuration. The stopping distance is computed as the distance the falling string has travelled in the directions parallel to the boundary before it falls into the black hole.

The main problem for this model is related to how to define the quark energy from the string. This is similar to the heavy and light quark scenarios, and have been described in Sub. 1.2.3. In [GGPR08], the authors propose two different methods to define the energy. The total energy of the string must be divergent, as it includes the infinite energy contribution of the constant electric field required to reach the initial steady state trailing string. One method to define the energy is to introduce a finite cut off along the string, and define the quark energy by integrating up to this cut off. The second definition involves measuring the amount of energy flowing out of a fixed $x_1 = const.$ surface.

Rather than solving the string equations fully, the authors find upper and lower limit estimates, by considering space-time and world sheet geodesics to find the stopping distance. The next step is to convert these stopping distances into the jet-quenching parameter. In [Bai+97], the energy distribution is integrated to obtain an explicit expression for the jet quenching parameter in terms of the path length.

$$\Delta E = \frac{1}{4}\alpha_S C_R \hat{q} \frac{(L^-)^2}{2} \tag{1.2.16}$$

This is generalised for the virtual gluon case, by replacing the stopping distance Δx for the path length $\frac{\left(L^{-}\right)^{2}}{2} = (\Delta x)^2$. Since the gluon is fully thermalised, ΔE can be replaced with the initial energy of the quark E. The constants α_S and C_R are the strong coupling and Casimir of the gauge group associated to representation R. The gluon is in the adjoint representation and so one can write $C_A = N_c$. Inverting Eq. (1.2.16), one can find the jet quenching parameter.

The fundamental difference in this method is that the parton follows a time-like trajectory in this case. In this thesis, this method will be used to compute the jet quenching parameter for time-like light flavoured partons. This will be further elucidated in Chapter 2.

1.3 The energy problem, temperature scaling and phenomenological models for $\hat{q}$

So far in this chapter, the basic features of QCD, the gauge/gravity duality and holographic energy loss mechanisms have been reviewed. In this section, a few issues with the models considered so far are discussed. Also, we will discuss some of the issues observed in the context of some of the models used outside of the gauge/gravity correspondence. This will motivate the use of the so-called finite end point momentum strings, to investigate the energy loss of light probes. A variety of models that include factors that are not accounted for in the basic AdS_5 black hole model are considered - see Sec. 1.2.

In the three main probes described in Sec. 1.2, a common issue observed is with regards to identifying the energy of the dual probe from the energy of the string. The total energy of the string is conserved in backgrounds with time-translation symmetry. In the zero temperature static string case, the energy of the string has

a much more direct connection to the energy of the probe. As mentioned in Sub. 1.2.3, the energy of the string in the black hole background is dual to the free energy contribution of introducing the probe to the medium. Disentangling the probe energy from the effect the quark has on the medium is non-trivial from the gravity side of the duality.

In the trailing string scenario, the flux of energy flowing through the string is used to determine the energy loss. The authors in [Her+06] also numerically solve the string equations for a string, where both end points end on the probe brane - see Fig. 1.2.

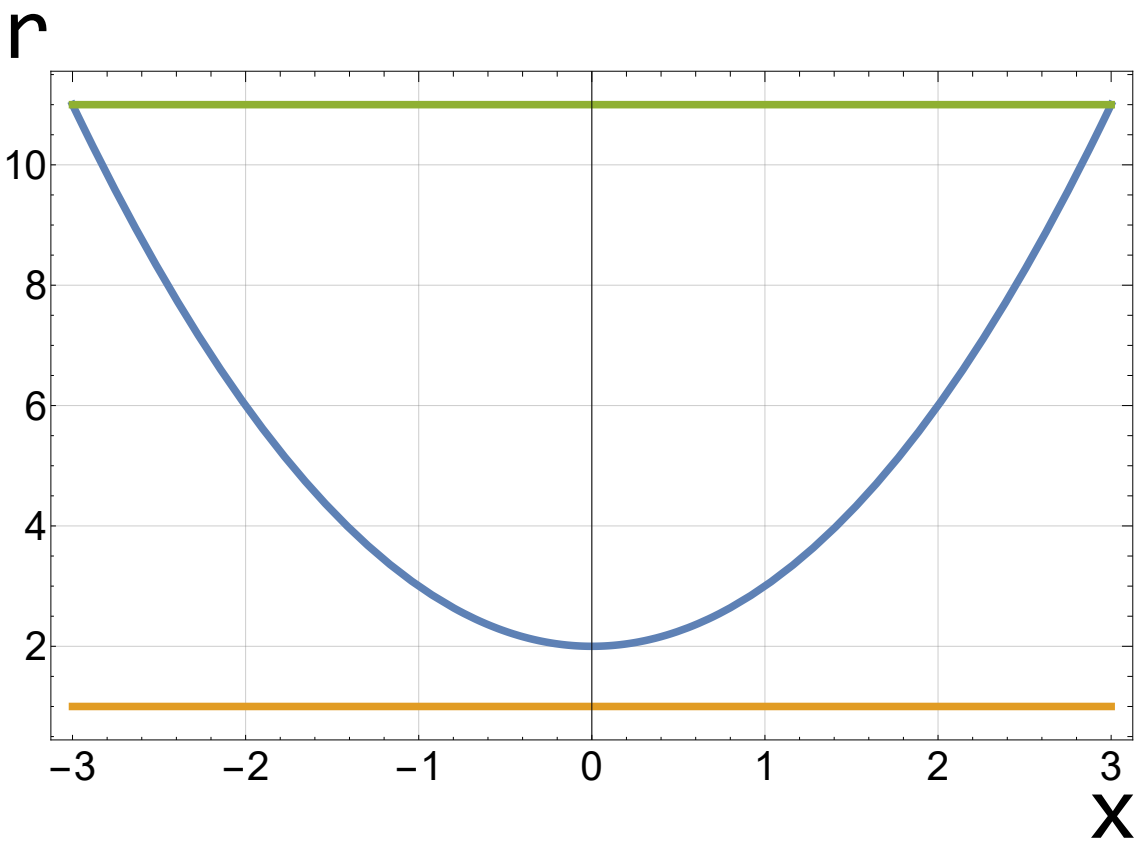

Figure 1.2: This plot shows the meson string used to describe heavy quarks, using gauge gravity duality. The horizon is marked by the orange curve $r_h = 1$ and the green line shows the probe brane for $r_0 = 11$.

For this moving string, it is even more difficult to truly discern the probe energy

from the system. In the paper, the authors' make the choice of cutting the string in half and assigning the energy contained in each half to each quark. This energy contains some of the energy lost to the medium, but provides an effective energy for each probe.

The same problem is observed for the light probe case, in which strings that start in a point-like state at the boundary, can now fall all the way into the black hole. The authors in [CJKY09] apply a similar principle, by assigning half the string energy to the quark. This is motivated by the fact that the energy density is localised around the string end point for the majority of the string trajectory.

Finally, the doubled closed string, that is dual to virtual gluons, has a divergent energy in a similar manner to the trailing string. A choice of cut off or choosing to measure the flux through a fixed x_1 surface is made in order to define a finite probe energy from this divergent energy.

In all three cases, there is no definitive manner to extract the probe energy from the string energy. This ambiguity was removed by the use of the so-called finite end point momentum strings, described by Ficnar and Gubser in [FG14]. By focussing on these longitudinal mode strings, the energy of the probe becomes simple to define from the string energy. To be more specific, the energy of the string is split into three distinct terms, including the energy associated to each end point and the energy of the bulk of the string. It is then logical to identify the energy associated to the string end points with the quarks, and the energy of the bulk string with the energy lost to the medium. This string solution is described in detail in Chapter 2.

Ficnar and Gubser go on to use these finite momentum strings to compute the jet nuclear modification factor R_{AA} [FGG14]. As explained in Sec. 1.1, this is just the ratio of the observed hadron jet seen in heavy ion collisions vs proton-proton

collisions. Using the Gauss-Bonnet extension of the AdS_5 black hole, a good fit to the RHIC data is obtained by tuning the t'Hooft coupling and the Gauss-Bonnet parameter. When this method is used to predict R_{AA} for the LHC experiments involving Pb-Pb collisions, the parameters for the RHIC Au-Au collisions lead to an under prediction for the LHC data.

In order to perform this computation, the authors use the Glauber model to represent the expanding fireball produced in the heavy ion collisions [GM70]. There is a potential uncertainty in the initial formation time t_i between the two experiments, that could account for the discrepancy in R_{AA}. Since the temperature dependence of the energy loss has a large power $\sim T^3(T^4)$ (see Chapter 2), small uncertainties in the temperature have a large impact on the energy loss. This feature is also observed in a phenomenological model, where the energy loss rate is predicted by a simple 'abc' model [HG11].

In this case, the energy loss is written in the form of a simple power law, with free parameters labelled a, b and c. These parameters are used to fit observables such as R_{AA} to data. This model leads to similar differences when the temperature is scaled up from RHIC to the LHC.

Another point of interest in our discussion, is the jet quenching parameter. As noted in Sec. 1.1, the jet quenching parameter $\hat{q}$ measures the transverse momentum squared per unit time that the probe and medium exchange, as the probe traverses the medium. The light-like Wilson loop method described in Sub. 1.2.3 has been used to investigate a number of different models for the QGP.

In most cases, this computation seems to over predict the parameter as observed by RHIC and LHC experiments ([Ada+08], [Bur+14] and [CLQW18]). The parameter in these cases is extracted from the experimental data, using phenomenological mod-

els considering energy loss interactions with the medium.

Another discrepancy with the gauge gravity duality is the temperature dependence for the AdS_5 black hole. The T^3 dependence seems unphysical because the dimensionless quantity $\frac{\hat{q}}{T^3}$, that is used quite commonly in the literature, is a constant. This is not observed by the data, and a clear decreasing effect of $\hat{q}$ is seen with increases of temperature.

It is also important to note that the phenomenological models tend to extract a jet quenching parameter that is dependent on the initial parton energy. For example, the $E = 20GeV$ partons in [Ada+08] lead to substantially different values for $\hat{q}$, relative to the $E = 10GeV$ partons studied in [Bur+14] and [CLQW18]. The light-like Wilson loop method does not lead to such dependencies, where $\hat{q}$ is a function of the t'Hooft coupling and temperature of the plasma only.

On the other hand, the virtual gluon jet quenching parameter, discussed in [GGPR08] (see Sub. 1.2.3), depends on the energy. And it has already been noted that this energy is not so clear in its definition from the string energy.

It is also interesting to note the difference in the jet quenching parameter seen in [CLQW18] for different types of parton. In this paper, the authors take into account gluons, heavy and light quarks, and thus observed different behaviours accordingly. Not only does the type of parton seem to have a difference, but effects such as scheme in which the coupling runs, and the chromo-electric and chromo-magnetic effects modify the extracted jet quenching parameter - see [XLG16]. In this paper, the CUJET 3.0 model that is used incorporates such effects, and it is seen to have significant changes to the temperature behaviour of $\hat{q}$.

In this thesis, so-called finite momentum strings are used to compute the stop-

ping distances and the rates of energy loss of light quarks in different models for the QGP. As it is explained in Chapter 2, the finite end point momentum strings provide a concrete prescription to define the quark energy from the string, and thus removes any ambiguity that exists for other probes discussed in this chapter. The model also allows for analytic solutions to be obtained due to a decoupling effect that occurs for these strings. An extension of the virtual gluon jet quenching parameter is used to convert the stopping distances into $\hat{q}$ - see Chapter 2.

A number of QGP models are analysed in this manner. Firstly, the AdS_5 black hole case studied in [FG14] and [FGG14] are computed as examples. The stopping distance, energy loss rate and jet quenching parameter are then computed for the Sakai-Sugimoto model; a QGP model that includes a concrete confinement/deconfinement transition, chiral symmetry breaking and restoration phase transition, and is both non-supersymmetric and non-conformal - see Chapter 2.

In Chapter 3, the addition of chemical potential is considered. First, the STU black hole solution, dual to $\mathcal{N} = 2$ supersymmetric gauge theory with a finite chemical potential associated to R-symmetry, is considered. In the second half of the chapter, the chemical potential associated to flavour symmetry or baryon number is considered. This is done by considering gauge fields propagating on the probe branes, and coupling these fields to the end points of string. In Chapter 4, anisotropy is added to the system, through the model Mateos et. al. found in [MMT07].

For all the models described above, the observables are compared to the heavy and light quarks and jet quenching parameters computed using the methods reviewed in Sec. 1.2.3. The models used to extract $\hat{q}$ from the experimental data is also compared to the results from the finite momentum strings, as a rough phenomenological test of the method. Whilst the full jet nuclear modification factor is not computed for any of the models, the analytic nature of the finite end point

momentum strings allow us to obtain explicit temperature and energy dependencies for the energy loss rates, and thus gives us an indication whether the potential scaling of temperature uncertainties are as significant.

Chapter 2

Method and light probe energy loss in the Sakai-Sugimoto Model

In Chapter 1, a variety of different holographic methods that describe the energy loss of probes traversing a deconfining medium have been described. In particular, drag strings, doubled closed string, and falling Nambu-Goto strings were considered. These strings are the holographic duals of heavy quarks, virtual gluons, and light quarks respectively. It was noted that in all three cases, there is some ambiguity in how the energy of the probe is defined from the string energy; how does one apportion the total string energy into probe energy, and the energy lost to the medium? In the falling string case, there is also a significant dependence on the initial conditions of the bulk of the string [CJKY09].

The authors of [FG14] proposed a new string action that provides a more definitive definition of the light probe energy. These strings essentially supplement the bulk string with end points that carry finite end point momenta. Effectively, this involves adding massless particles to the end points of the string. In addition to defining the energy of the light probe in a more robust way, a decoupling effect occurs, such that the bulk string has no impact on the motion of the end points of the string. This means the initial condition problems of the Nambu-Goto strings are not seen for

these strings. Finally, the string end points can be shown to follow null geodesics. This makes it possible to obtain analytic expressions for jet quenching observables, such as stopping distances.

In this chapter, the finite momentum end point strings proposed by [FG14] are examined, and the main methods used to compute light probe stopping distances and rates of energy loss are discussed. First, the relation of these strings to the longitudinal modes of Nambu-Goto strings and strings with massive end points is reviewed. The finite end point momentum string action is then analysed, including the explanation of the decoupling effect that occurs for these strings. The AdS_5 black hole case, as shown in [FG14], is reproduced as an example implementation of the method.

Having reviewed the work of Ficnar and Gubser, we proceed to apply this method to the Sakai-Sugimoto system. The stopping distance of falling strings and energy loss rates of shooting strings are compared with the AdS_5 black hole case, in order to see the differences obtained for this non-conformal theory that undergoes a confinement/deconfinement transition. Finally, these stopping distances are used to compute and analyse the jet quenching parameter $\hat{q}$, and compared to phenomenological models that use experimental data to extract $\hat{q}$.

2.1 Longitudinal modes and massive end points

Before proceeding to describe the finite end point momentum strings, let us first consider the origins of such strings. There are solutions of the Nambu-Goto string equations of motion with longitudinal modes, that are of particular interest in relation to finite end point momentum strings. These modes were first encountered by Patrascioiu [Pat74].

Patrascioiu was interested in showing that the canonical orthonormal light-cone gauge used to solve the Nambu-Goto action, does not contain all solutions to the system. The choice of orthonormal gauge does not uniquely specify the gauge; there exist residual gauge transformations that preserve the orthonormal condition. It is using this condition that the light-cone gauge is achieved. This assumes there exists a well-defined transformation from any starting orthonormal gauge. However, it is shown by Patrascioiu that there exists a starting gauge such that the transformation Jacobian is singular. The light-cone gauge itself restricts to transverse modes only. The existence of gauges that are disconnected from the light-cone gauge hints at the possibility of longitudinal motion. An example of these strings with longitudinal modes are explicitly found by in the paper [Pat74].

Fig. 2.1 shows the world sheet describing this string with longitudinal modes. The solution is obtained by fixing the gauge to orthonormal gauge and then using the residual gauge freedom to fix the gauge to the time-like gauge. At $x_0 = 0$ the string lies flat along the x_1 direction. As time evolves, the string shrinks to a point at $x_0 = \frac{\pi}{2}$ and then expands back to full length at $x_0 = \pi$. This motion repeats in an oscillatory manner.

Having described the existence of these longitudinal modes in the solutions of the Nambu-Goto strings equations of motion, it is interesting to consider the notion of adding mass to the end points of the string. In [BBHP76], the authors proposed to analyse such massive end point strings, in the context of longitudinal modes. The Nambu-Goto string action is supplemented with terms that represent massive particles at the end point.

$$S_{\text{massive}} = -\frac{1}{2\pi\alpha'}\int d\tau \int_0^{\pi} d\sigma \sqrt{-\det\left[G_{\mu\nu}(X)\partial_a X^{\mu}\partial_b X^{\nu}\right]}$$

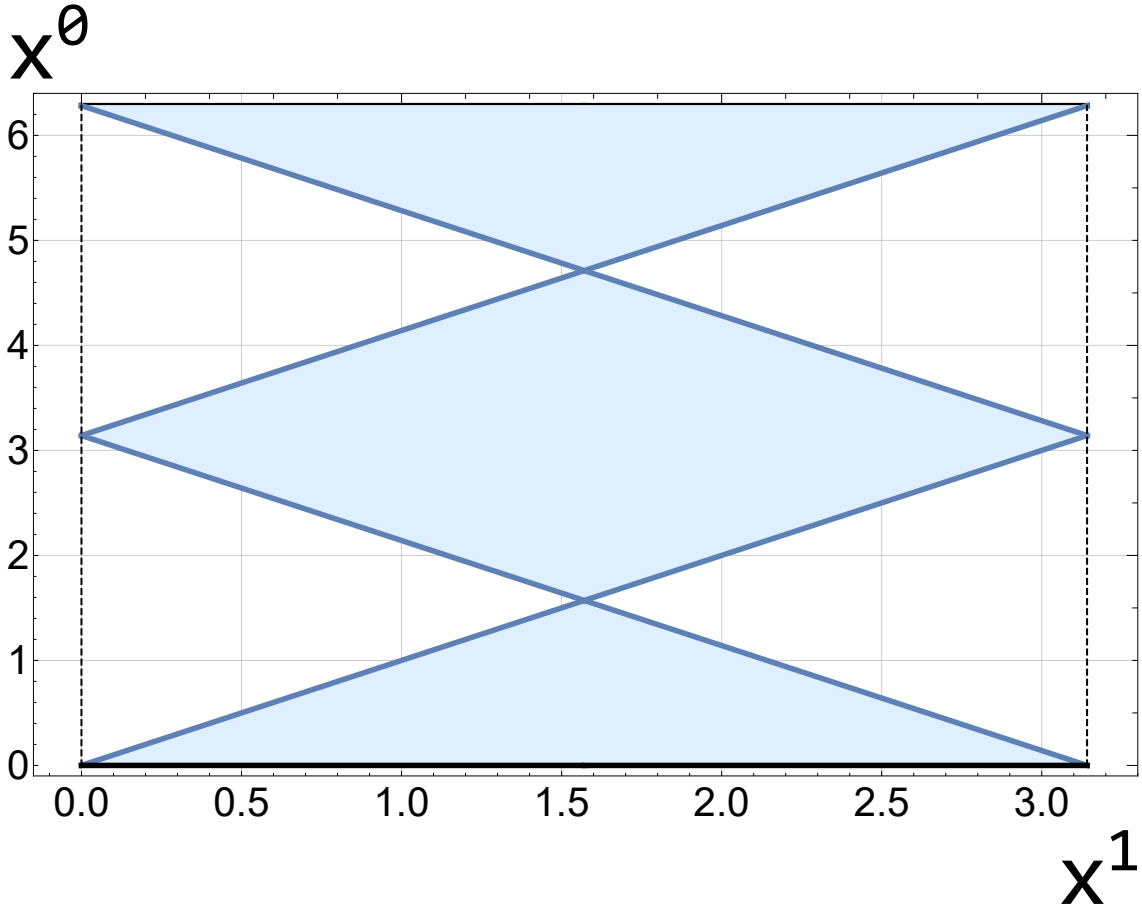

Figure 2.1: This is a plot of the string world sheet for the string with longitudinal modes. The shaded area represents the string world sheet.

$$- \int d\tau \int_0^\pi d\sigma m(\sigma) \sqrt{-\det\left[G_{\mu\nu}(X)\dot{X}^\mu \dot{X}^\nu\right]} \tag{2.1.1}$$

X^μ describes the world sheet embedding, $\dot{X}^\mu = \frac{dX^\mu}{d\tau}$, and partial derivatives are with respect to the world sheet co-ordinates $\sigma^a = (\tau, \sigma)$. The first term is the standard Nambu-Goto term, and the second term describes a mass term that apportions a mass distribution across the length of the string. The massive end point case is given by choosing the mass function $m(\sigma) = m\left(\delta(\sigma) + \delta(\sigma - \pi)\right)$. Upon this substitution, this term looks like the geodesic action for two massive particles of mass m.

When dealing with massless particles, the usual method involves using the geodesic

equation of motion for massive particles to solve the system, and then take the limit of zero mass. Taking the mass to zero a priori, takes the action to zero in a naive fashion. To be more precise, the limit of $m \to 0$ forces the momentum of the particle to zero. However solving for the system and then taking the mass to zero, allows one to keep the momentum of the particle finite.

In exactly the same way, the massive end point system is solved, and then the massless limit $m \to 0$ limit is taken. The solutions with longitudinal modes can be found in the time-like and uniform σ gauge, as shown in [BBHP76]. It is interesting to note that the world sheet of this solution looks identical to Fig. 2.1. In order to make this connection between the massless limit solution and the Patrascioiu string clearer, it is important to consider the conserved momenta of the two strings.

The momentum of the massive end point theory is clearly not the same as those of the pure Nambu-Goto action. It is decomposed into three terms; two terms denoting momentum associated with the end points, and a momentum associated with the bulk of the string.

$$\begin{aligned} P_\mu^{Total} &= P_\mu^{\text{bulk}} + p_\mu^{\sigma=0} + p_\mu^{\sigma=\pi} \\ P_\mu^{\text{bulk}} &= \int d\sigma_0^\pi \sqrt{-\gamma}\left[\left(\partial_\sigma X \cdot \partial_\sigma X\right)\partial_\tau X_\mu - \partial_\sigma X_\mu \left(\partial_\tau X \cdot \partial_\sigma X\right)\right] \\ \gamma &= \left(\partial_\tau X \cdot \partial_\tau X\right)\left(\partial_\sigma X \cdot \partial_\sigma X\right) - \left(\partial_\tau X \cdot \partial_\sigma X\right)^2 \\ p_\mu^\sigma &= m\frac{\dot{X}^\mu}{\sqrt{-\dot{X}\cdot\dot{X}}} \end{aligned} \tag{2.1.2}$$

Whilst the charges look different, it turns out particular solutions with longitudinal modes can be identified. In [BBHP76], the momentum density of the Patrasciouiu string is plotted for various times. The general form for the momentum density involves three plateaus over three finite regions of the string. One can see this explicitly in Fig. 2.2, where the momentum density has been plotted for three different times.

As noted previously, the gauge in which the Patrascioiu solution is solved in is the orthonormal, time-like gauge. On the other hand, the massive end point solution is obtained in the time-like, uniform σ gauge. In order to match the solutions, the appropriate gauge transformation must be performed. When this transformation is performed, it is found that finite portions of the Patrascioiu string map to the end points of the string. To be more precise, the momentum contained in two of the plateaus shown in the plots in Fig. 2.2, map to the end points of the massive end point strings. Thus, one can split the integral for the momenta in three terms, and identify the terms with the end point and bulk momenta of the other solutions.

2.2 Polyakov action with boundary term

Using the knowledge that certain solutions to the Nambu-Goto string action are physically identical to strings with finite end point momentum, the authors of [FG14] proposed a new method to compute stopping distances and energy losses of light probes in the QGP. In [BBHP76], the authors add finite momentum to the end points, by including the standard affine parameterisation geodesic action to the Nambu-Goto action - see Eq. (2.1.1). The limit of zero mass is taken, after solving for the equations of motion. Rather than work in this manner, it is simpler to use the Polyakov form of the string action and significantly, use the einbein form of the particle action for the end points. Not only does this allow the mass of the end

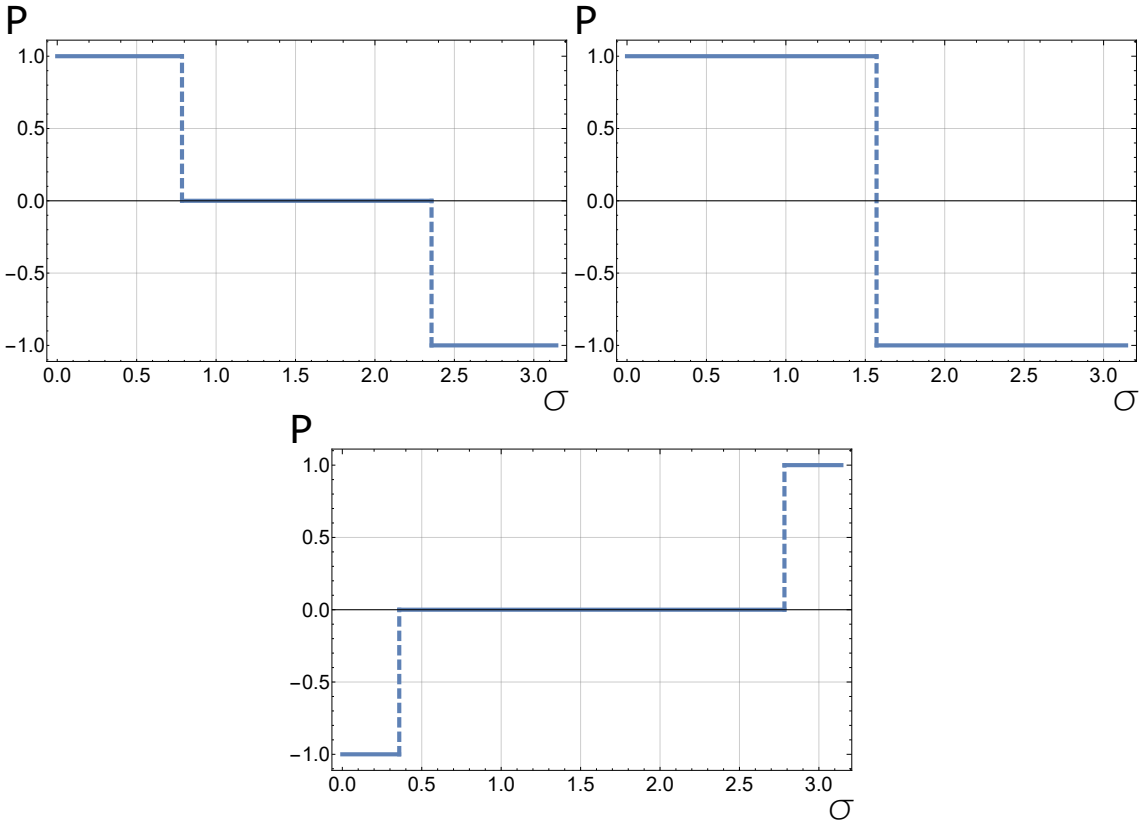

Figure 2.2: This is a plot of the momentum density along the Patrascioiu string along the σ direction for three different values of τ. The left plot is for $\tau = \frac{\pi}{4}$, the middle plot is for $\tau = \frac{\pi}{2}$ and the bottom plot is for $\tau = 3.5$.

points to be set to zero at the level of the action, but a decoupling effect occurs for the equations of motion [FG14].

In order to see this fully, let us first consider the action proposed by Ficnar and Gubser:

$$S_{bound} = -\frac{1}{4\pi\alpha'}\int \sqrt{-h}h^{ab}G_{\mu\nu}\partial_a X^\mu \partial_b X^\nu d\tau d\sigma + \frac{1}{\alpha'}\int \frac{1}{\eta}G_{\mu\nu}\dot{X}^\mu \dot{X}^\nu d\xi \qquad (2.2.1)$$

The first term is clearly just the usual Polyakov string action. This linear system reproduces the same dynamics as the Nambu-Goto string action, through the introduction of a dynamical metric h_{ab} on the world sheet. By finding the equations of motion for this metric, one can eliminate h_{ab} and obtain the Nambu-Goto action.

The second term adds massless particles to the end points of the string in a similar fashion. The introduction of the einbein η allows us to define a linear system for particles. Again, the affine parameterisation geodesic action for the end points can be obtained by solving the equations of motion for η and eliminating this dynamical metric for the world line. It is important to note that there is no mass dependence for the end points at the level of the action, and thus provides the first simplification to the method used in [BBHP76].

By extremising the action in the canonical way, the following equations of motion are obtained:

$$\partial_a P^a_\mu - \Gamma^\tau_{\mu\nu}\partial_a X^\nu P^a_\tau = 0 \tag{2.2.2}$$

$$\dot{p}_\mu - \Gamma^\tau_{\mu\nu}\dot{p_\tau}\dot{X}^\nu = \dot{\sigma}^a \epsilon_{ab} P^b_\mu \tag{2.2.3}$$

$$G_{\mu\nu}\dot{X}^\mu\dot{X}^\nu = 0 \tag{2.2.4}$$

$$T_{ab} = 0 \tag{2.2.5}$$

where:

$$P^a_\mu = -\frac{1}{2\pi\alpha'}\sqrt{-h}h^{ab}G_{\mu\nu}\partial_b X^\nu \tag{2.2.6}$$

$$p_\mu = \frac{1}{\eta\alpha'}G_{\mu\nu}\dot{X}^\nu \tag{2.2.7}$$

$$T_{ab} = G_{\mu\nu}\partial_a X^\mu \partial_b X^\nu - \frac{1}{2}h_{ab}h^{cd}G_{\mu\nu}\partial_c X^\mu \partial_d X^\nu \tag{2.2.8}$$

It is important to note that the einbein equation of motion Eq. (2.2.4) gives the constraint that the end points travel on null curves, which is of course expected for massless particles. The momentum of the string is found through the Nöether current of space-time translation symmetry, which the background of interest all obey. The total conserved momentum is given by:

$$P_\mu^{Total} = P_\mu^{bulk} + 2p_\mu \tag{2.2.9}$$

where P_μ^{bulk} is the usual conserved charge obtained by integrating P_μ^a along the string at some point in time. The form of P_μ^{Total} makes for a very intuitive physical interpretation.

As noted previously, the total energy of the string contains contributions from both the probes and the interaction with the medium. Since the end points are associated with the location of the probes, it is natural to identify the $2p_0$ term with the energy of the quarks. The remaining part of the energy, which is associated with the bulk of the string, is interpreted as the energy lost through the interaction with the medium. In this sense, a well defined notion of probe energy naturally arises from the action, unlike for the case of drag strings (heavy quarks), normal zero end point momentum strings (light quarks), and doubled closed strings (virtual gluons).

The system of equations (Eqs. (2.2.2) - (2.2.5)) appear to be a complicated set of non-linear coupled partial differential equations. However, it can be shown that a decoupling effect occurs and the end point moves independently of the bulk of the string. It can be shown that the source term of the end point equations of motion can be written by the following expression:

$$\dot{\sigma}^a \epsilon_{ab} P_\mu^b = \mp \frac{\eta}{2\pi} p_\mu \tag{2.2.10}$$

Let us show this now by first considering the following matrix and eigenvector equations:

$$M^a{}_c v^c = \Lambda v^a \tag{2.2.11}$$

$$M^a{}_c = \sqrt{-h} h^{ab} \epsilon_{bc} \tag{2.2.12}$$

This eigenvalue equation shall be the reference for a particular choice in parameterisation. If the end point parameterisation is such that $\dot{\sigma}^a$ is an eigenvector, the decoupling effect can be explicitly shown.

$$\begin{aligned}
\dot{\sigma}^a \epsilon_{ab} P^b_\mu &= -\frac{1}{2\pi\alpha'} G_{\mu\nu} \partial_c X^\nu \sqrt{-h} h^{cb} \epsilon_{ab} \dot{\sigma}^a \\
&= \frac{1}{2\pi\alpha'} G_{\mu\nu} \partial_c X^\nu M^c{}_a \dot{\sigma}^a \\
&= \frac{1}{2\pi\alpha'} \Lambda G_{\mu\nu} \partial_c X^\nu \dot{\sigma}^c \\
&= \frac{1}{2\pi\alpha'} \Lambda G_{\mu\nu} \dot{X}^\nu \\
&= \frac{\eta}{2\pi} \Lambda p_\mu
\end{aligned} \tag{2.2.13}$$

Let us explicitly solve the eigenvector equation Eq. (2.2.11) for the canonical choice of flat gauge $h_{ab} = \eta_{ab}$. In this gauge:

$$M^a{}_b = \begin{bmatrix} 0 & -1 \\ -1 & 0 \end{bmatrix} \tag{2.2.14}$$

and the eigenvectors are given by $\dot{\sigma}^a = (1, \pm 1)$, with eigenvalues $\Lambda = \mp 1$. Using this choice of gauge and substituting $\Lambda = \mp 1$ into Eq. (2.2.13), one finally ends with Eq. (2.2.10).

Clearly, $\dot{\sigma}^a = (1, 1)$ corresponds to outward motion of the string end point. Since this eigenvector corresponds to the eigenvalue -1, the negative sign in Eq. (2.2.10) corresponds to outward motion. On the other hand, $\dot{\sigma}^a = (1, -1)$ represents inward motion and has the $+1$ eigenvalue. This means the $+$ sign in Eq. (2.2.10) corresponds to inward motion.

Finally, the end point equation of motion may be re-written as:

$$\begin{aligned} \dot{p}_\mu - \Gamma^\tau_{\mu\nu} p_\tau \dot{X}^\nu &= \mp \frac{1}{2\pi\alpha'} G_{\mu\nu} \dot{X}^\nu \\ &= \mp \frac{\eta}{2\pi} p_\mu \end{aligned} \tag{2.2.15}$$

As explained previously, the end point equation of motion has decoupled from the bulk string. This is important in the context of light probe quenching. In [CJKY09], it is noted that the initial conditions of the string have a substantial impact on the dual light quark observables. The decoupling effect for the finite end point momentum strings means that this ambiguity is lost.

There is one further simplification that can be performed. Through an appropriate re-definition of the einbein, the end point equation of motion Eq. (2.2.3) simplifies to the geodesic equation. The einbein equation of motion constrains this to a light-like geodesic, to be more specific.

Consider the following transformation for the einbein:

$$\tilde{\eta} = \eta \exp\left(\mp \frac{1}{2\pi} \int^{\xi} d\lambda \eta(\lambda)\right) \tag{2.2.16}$$

Using this re-defined einbein, let us construct a re-defined 'momentum', where $\tilde{p}_\mu$ is defined like p_μ but $\eta \to \tilde{\eta}$ (see [FG14]). One can re-write the equation of motion Eq. (2.2.15) in terms of $\tilde{p}_\mu$:

$$\begin{aligned} \dot{\tilde{p}}_\mu - \Gamma^{\tau}_{\mu\nu} \dot{\tilde{p}}_\tau \dot{X}^\nu &= 0 \\ \tilde{p}_\mu &= \frac{1}{\tilde{\eta}\alpha'} G_{\mu\nu} \frac{dX^\mu}{d\xi} \end{aligned} \tag{2.2.17}$$

It is easy to show that Eq. (2.2.17) is equivalent to Eq. (2.2.15), by substituting for $\tilde{\eta}$ using Eq. (2.2.16).

The backgrounds of interest all have space-time translation symmetry. It is well known that there exist quantities conserved along geodsics associated with isometries of the background. So one may question whether the momentum of the end point can really vary. This problem is resolved through the realisation that the conserved quantity, and the true momentum of the end point are not equivalent. The conserved quantity is defined with respect to $\tilde{\eta}$, where as the true energy of the end point is defined with respect to η.

An important feature of these string solutions is the event of snap back. Should the end point energy decay to 0, it is only consistent for the end point to instantly travel back along the path it came from. This snap-back can be seen in Fig. 2.1 plot, where the string reaches a point e.g. $x_0 = \frac{\pi}{2}$. One can see that the end points travel inwards until this point, and then travel outwards after this point. In the context

of the thermalisation of quarks, one can only consider those string whose end point decay to 0 in the black hole. The causal structure of the black hole prevents the end point from snapping back and leaving the black hole.

The previous computations of stopping distances faced some ambiguities. Firstly, the energy of the quark is extracted from an approximate solution to the string equations, that is only valid (up to corrections) in a window of time. This allows one to obtain a proposal for the energy and temperature dependencies of the distance. However to truly compute the proportionality, one must do numerical studies. Again, these numerical studies require one to extract the energy of the quark from the string energy in an ambiguous manner. The instantaneous energy loss rate computations also had some ambiguities e.g. where the flux is evaluated along the string.

The solutions to the new proposal are also solutions to the ordinary NG/Polyakov system. However, there is now a very physical picture. The end points of the string have momentum and can be identified with the quark momentum. The evolution of this energy is dictated strictly by the equations of motion of the system. The end points exactly follow geodesics and hence maximise the stopping distance; perturbations in the bulk of the string do not modify the boundary behaviour. The instantaneous rate of energy loss is again exactly determined by the equations of motion.

Let us consider solutions of these strings in the canonical AdS_5 planar black hole background, dual to the $\mathcal{N} = 4$ Super Yang-Mills plasma - (see [FG14]). The particular solutions of interest are strings whose end points are initially positioned near the boundary of the background, and fall into the black hole before snap back. As explained in [CJK09] and [CJKY09], the near boundary limit is shown to induce a localised charge density in the dual theory. This best represents a localised probe in the dual theory. The end point has initial velocity that does not contain components

in the AdS_5 radial direction. This is to maximise the initial speed of the end point in the directions parallel to the gauge theory directions, and hence maximise the initial velocity of the dual probe.

The metric for the five dimensional AdS_5 black hole background is given by:

$$\begin{aligned} ds^2_{AdS_5} &= \frac{L^2}{u^2}\left[-f(u)dt^2 + dx^2 + dy^2 + dz^2 + \frac{1}{f(u)}du^2\right] \\ f(u) &= 1 - \frac{u^4}{u_H^4} \end{aligned} \tag{2.2.18}$$

u_H defines the position of the horizon and L is the characteristic length scale of the space-time. The falling string initial conditions described above can be more precisely defined. At $\xi = 0$, the initial end point is given by $(t = 0, x = 0, y = 0, z = 0, u = u_0)$ and the initial tangent vector is given by:

$$\begin{aligned} \frac{dt}{d\xi} &= \sqrt{\alpha'} \\ \frac{dx}{d\xi} &= v_0 \\ \frac{dy}{d\xi} &= \frac{dz}{d\xi} = \frac{du}{d\xi} = 0 \end{aligned} \tag{2.2.19}$$

where v_0 is determined by using the null vector condition. Using these initial conditions, the end point trajectories can be solved numerically. This trajectory then provides the boundary conditions for the bulk string equations.

The same point-like conditions used in [FG14] will be used here. Initially, the

string world sheet is given by:

$$\begin{aligned} t(0,\sigma) &= 0 \\ x(0,\sigma) &= y(0,\sigma) = z(0,\sigma) = 0 \\ u(0,\sigma) &= u_0 \end{aligned} \tag{2.2.20}$$

As noted previously, the boundary conditions for the string are constrained to follow the null geodesics. This forces the following boundary conditions on the end points of the string:

$$\begin{aligned} \partial_\tau t(\tau,0) &= \partial_\tau t(\tau,\pi) = \sqrt{\alpha'} \\ \partial_\tau x(\tau,0) &= -\partial_\tau x(\tau,\pi) = \dot{x} \\ \partial_\tau y(\tau,0) &= -\partial_\tau y(\tau,\pi) = 0 \\ \partial_\tau z(\tau,0) &= -\partial_\tau z(\tau,\pi) = 0 \\ \partial_\tau u(\tau,0) &= -\partial_\tau u(\tau,\pi) = \dot{u} \end{aligned} \tag{2.2.21}$$

Finally, the initial string profile needs to be considered. It is important to note that this profile needs to obey the boundary conditions Eq. (2.2.21) at the end points. It also needs to obey the stress-energy constraints that the world sheet metric equation of motion imposes.

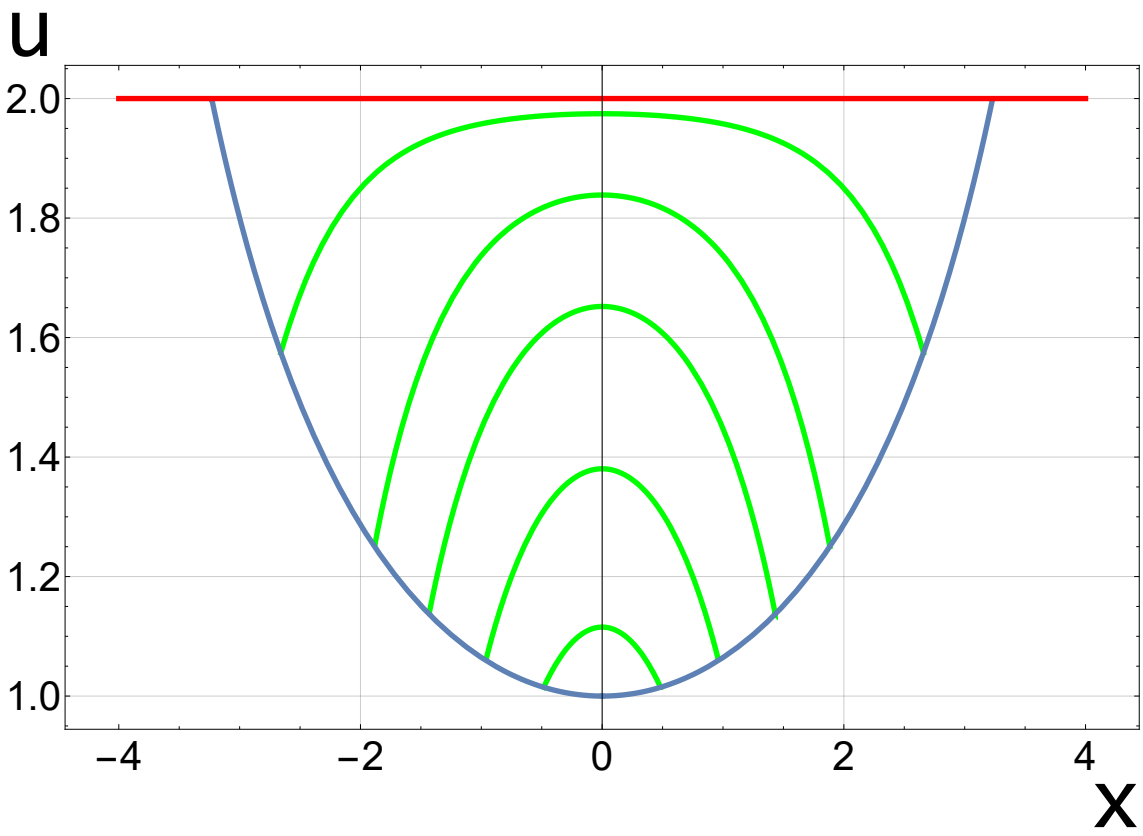

Figure 2.3: This is a plot of the falling string solution in the AdS_5 background. The starting radial co-ordinate is given by $u_0 = 1$ and the horizon radius is chosen to be $u_H = 2$ and denoted by the red line. The blue lines denote the end point null geodesic trajectory. The green lines show snapshots of the strings at five different times as it falls into the black hole.

Fig. 2.3 shows an example solution of the falling string with finite end point momentum. This shows the point-like initial state evolve into a stretched string that falls into the black hole. The end points follow the blue null geodesics as expected.

2.3 Stopping distance of light quarks in AdS_5 - Schwarzchild

In Sec. 2.2, the finite momentum endpoint strings were introduced. In this section, let us consider a particular finite momentum endpoint string that represents a dual

light quark traversing an $\mathcal{N} = 4$ Super Yang-Mills plasma.

In particular, it is the stopping distance of the light probe that is of interest to study. The stopping distance is found by computing the distance parallel to the boundary that the string endpoint travels before it falls into the black hole. The particular string solutions of interest are those found in 2.2. Since the end point motion decouples from the bulk string, the ambiguity in the initial conditions of the bulk string is not required. One can compute the string trajectory independently, without considering the full bulk string. The energy of probe can also be computed, by associating the end point energy of the string with the probe energy. Once more, the finite momentum end point equations of motion Eq. (2.2.3) can be used to determine the string end point energy independent of the bulk of the string.

In order to find the stopping distance for the light probe, the end point equation of motion 2.2.3 needs to be solved. As shown in Sec. 2.2, this involves solving for null geodesics in this background. It is possible to reduce the 2nd order geodesic equations to first order equations by considering conserved quantities. To be more specific, let us consider the conserved quantities associated to time translations and x translations:

$$\begin{aligned} E_{geo} &= -g_{0\nu}U^{\nu} \\ &= \frac{L^2}{u^2}\frac{(u_H^4 - u^4)}{u_H^4}\frac{dt}{d\lambda} \\ P_{geo} &= g_{x\nu}U^{\nu} \\ &= \frac{L^2}{u^2}\frac{dx}{d\lambda} \end{aligned} \tag{2.3.1}$$

$$\Rightarrow \frac{dx}{dt} = \frac{P_{geo}}{E_{geo}} \frac{(u_H^4 - u^4)}{u_H^4} \tag{2.3.2}$$

$U^\mu = \left(\frac{dt}{d\lambda}, \frac{dx}{d\lambda}, \frac{dy}{d\lambda}, \frac{dz}{d\lambda}, \frac{du}{d\lambda}\right)$ is the tangent vector along the geodesic.

Now the geodesics of interest are null, and using this constraint the 2nd order geodesic equations are reduced to a single 1st order equation.

$$\frac{du}{dt} = \frac{(u_H^4 - u^4)}{u_H^6} \frac{\sqrt{E_{geo}^2 u_H^4 + P_{geo}^2 (u^4 - u_H^4)}}{E_{geo}}$$

$$\Rightarrow \frac{dx}{du} = \frac{P_{geo} u_H^2}{\sqrt{E_{geo}^2 u_H^4 + P_{geo}^2 (u^4 - u_H^4)}} \tag{2.3.3}$$

Let us now implement initial conditions for the end point of the string, as described in Sec. 2.2. These describe light probes with dual charge densities that are local to the string end point and maximise the initial velocity. At $(t = 0, x = 0, y = 0, z = 0, u = u_0)$, the initial velocity of interest is $U^\mu = \left(1, \frac{dx_0}{d\lambda}, 0, 0, 0\right)$. This implies:

$$\frac{E_{geo}}{P_{geo}} = \frac{\sqrt{u_H^4 - u_0^4}}{u_H^2} \tag{2.3.4}$$

$$\Rightarrow \frac{dx}{du} = \frac{u_H^2}{\sqrt{u^4 - u_0^4}} \tag{2.3.5}$$

One cannot analytically integrate the equation above, however one can re-write the integral in terms of a hypergeometric function. The stopping distance trajectory, given the initial conditions stated above, can be written as:

$$x(u) = u_H^2 \left[\frac{\sqrt{\pi}\Gamma\left[\frac{5}{4}\right]}{\Gamma\left[\frac{3}{4}\right]} \frac{1}{u_0} - \frac{{}_2F_1\left[\frac{1}{4}, \frac{1}{2}; \frac{5}{4}; \frac{u_0^4}{u^4}\right]}{u} \right] \tag{2.3.6}$$

where ${}_2F_1[a,b,c,d]$ is the Gauss' hypergeometric function. The stopping distance is obtained by evaluating this at $u = u_H$.

$$\Delta x_{stop} = u_H^2 \left[\frac{\sqrt{\pi}\Gamma\left[\frac{5}{4}\right]}{\Gamma\left[\frac{3}{4}\right]} \frac{1}{u_0} - \frac{{}_2F_1\left[\frac{1}{4}, \frac{1}{2}; \frac{5}{4}; \frac{u_0^4}{u_H^4}\right]}{u_H} \right] \tag{2.3.7}$$

Having obtained an expression for the stopping distance, one would like to obtain its relation to the initial energy of the quark. The energy of the quark is defined by the endpoint momentum of the string, whose dynamics are determined by the boundary equation of motion [FG14]. The energy of the end point is defined as $E = -p_0$.

$$\dot{p}_\mu - \Gamma^\tau_{\mu\nu} p_\tau \dot{X}^\nu = -\frac{\eta}{2\pi} p_\mu \tag{2.3.8}$$

$$\Rightarrow \dot{E} + \Gamma^\tau_{t\nu} p_\tau \dot{X}^\nu = \frac{\eta}{2\pi} p_t \tag{2.3.9}$$

$$\dot{E} + \frac{1}{2\eta\alpha'} \partial_t G_{\nu\tau} \dot{X}^\nu \dot{X}^\tau = \frac{1}{2\pi\alpha'} G_{tt} \dot{t} \tag{2.3.10}$$

The last line is obtained by considering the definition $p_\mu = \frac{1}{\eta} G_{\mu\nu} \dot{X}^\nu$ and writing the connection out explicitly. Since the metric has no t dependence, this simplifies to:

$$\dot{E} = \frac{\sqrt{\lambda}}{2u^2\pi} f(u) \dot{t} \tag{2.3.11}$$

$$\Rightarrow \frac{dE}{du} = \frac{\sqrt{\lambda}}{2u^2\pi} f(u) \frac{dt}{du} \tag{2.3.12}$$

$$= \frac{\sqrt{\lambda}}{2\pi u^2} \frac{\sqrt{u_0^4 - u_H^4}}{\sqrt{u^4 - u_0^4}} \tag{2.3.13}$$

where $\sqrt{\lambda} = \frac{L^2}{\alpha'}$ is the t'Hooft coupling and Eq. (2.3.3) has been used.

The boundary conditions for the end point equations of motion will follow that of [FG14]. The energy of the end point must not reduce to zero before the end point of the horizon, as snap back occurs. The choice made in this discussion is the case where the end point energy reduces to zero at the horizon exactly. In other words, the end point loses all of its energy to the bulk of the string at the exact point it passes the horizon. Given these initial conditions, the initial energy is found by integrating Eq. (2.3.13) from $u = u_H$ to $u = u_0$.

$$E_{init} = \frac{\sqrt{\lambda}}{2\pi}\sqrt{u_H^4 - u_0^4}\left[\frac{\sqrt{\pi}\Gamma\left[\frac{3}{4}\right]}{\Gamma\left[\frac{1}{4}\right]}\frac{1}{u_0^3} - \frac{{}_2F_1\left[\frac{1}{2}, \frac{3}{4}; \frac{7}{4}; \frac{u_0^4}{u_H^4}\right]}{3u_H^3}\right] \tag{2.3.14}$$

Now let us combine the stopping distance expression in Eq. (2.3.7) with this expression by eliminating u_0. This is done in the so called near boundary limit. As explained in Sec. 2.2, the dual probe is more point like for $\frac{u_0}{u_H} \to 0$. Hence, let us perform the substitution after expanding and considering leading order terms in this near boundary expansion.

$$\begin{aligned} \Delta x_{stop} &= \frac{\sqrt{\pi}\Gamma[\frac{5}{4}]}{\Gamma[\frac{3}{4}]}\frac{u_H^2}{u_0} \\ E_{initial} &= \frac{\sqrt{\lambda}}{2\pi}\frac{\sqrt{\pi}\Gamma[\frac{3}{4}]}{\Gamma[\frac{1}{4}]}\frac{u_H^2}{u_0^3} \end{aligned} \tag{2.3.15}$$

Finally, the dependence on the horizon radius u_H is eliminated in favour of the plasma temperature. The temperature of the plasma is given by the black hole temperature, which is computed by removing the conical singularity at the Euclidean metric horizon. This is because the periodicity of the time co-ordinate, enforced by

the singularity, also affects the boundary time co-ordinate. Hence, the Euclidean time in the boundary theory also has the same periodicity as the black hole time co-ordinate periodicity. So the temperature of the black hole is dual to the temperature of the plasma.

$$\Delta x_{stop} = \frac{2^{\frac{1}{3}}\Gamma[\frac{1}{4}]^{\frac{1}{3}}\Gamma[\frac{5}{4}]}{\pi^{\frac{2}{3}}\lambda^{\frac{1}{6}}\Gamma[\frac{3}{4}]^{\frac{4}{3}}}\left[\frac{E_{init}}{T^4}\right]^{\frac{1}{3}} \tag{2.3.16}$$

This can be simplified using identities between gamma functions.

$$\Gamma[1+x] = x\Gamma[x] \tag{2.3.17}$$

$$\Gamma[x]\Gamma[1-x] = \frac{\pi}{sin(\pi x)} \tag{2.3.18}$$

$$\Rightarrow \Delta x_{stop} = \frac{\Gamma\left[\frac{1}{4}\right]^{\frac{8}{3}}}{2^{\frac{7}{3}}\pi^2\lambda^{\frac{1}{6}}}\left[\frac{E_{initial}}{T^4}\right]^{\frac{1}{3}} \tag{2.3.19}$$

An important point that has not been considered is the nature of the quark trajectory in the dual theory. Whilst the end point of the string is forced to follow null geodesics in the bulk, the trajectory in the boundary directions may not translate to a null curve. The norm of the tangent vector at any point along the trajectory is given by:

$$|V^\mu|^2_{AdS} = \eta_{\mu\nu}V^\mu V^\nu \tag{2.3.20}$$

$$= -1 + \frac{\left(u_H^4 - u^4\right)^2}{u_H^4\left(u_H^4 - u_0^4\right)} \tag{2.3.21}$$

where $V^\mu = (1, \frac{dx}{dt}, \frac{dy}{dt}, \frac{dz}{dt})$ and $\eta_{\mu\nu}$ is the field theory Minkowksi metric. The trajectory in the dual field theory is time-like for $u_0 \leq u \leq u_H$. Fig. 2.4 shows this for three different choices of u_H.

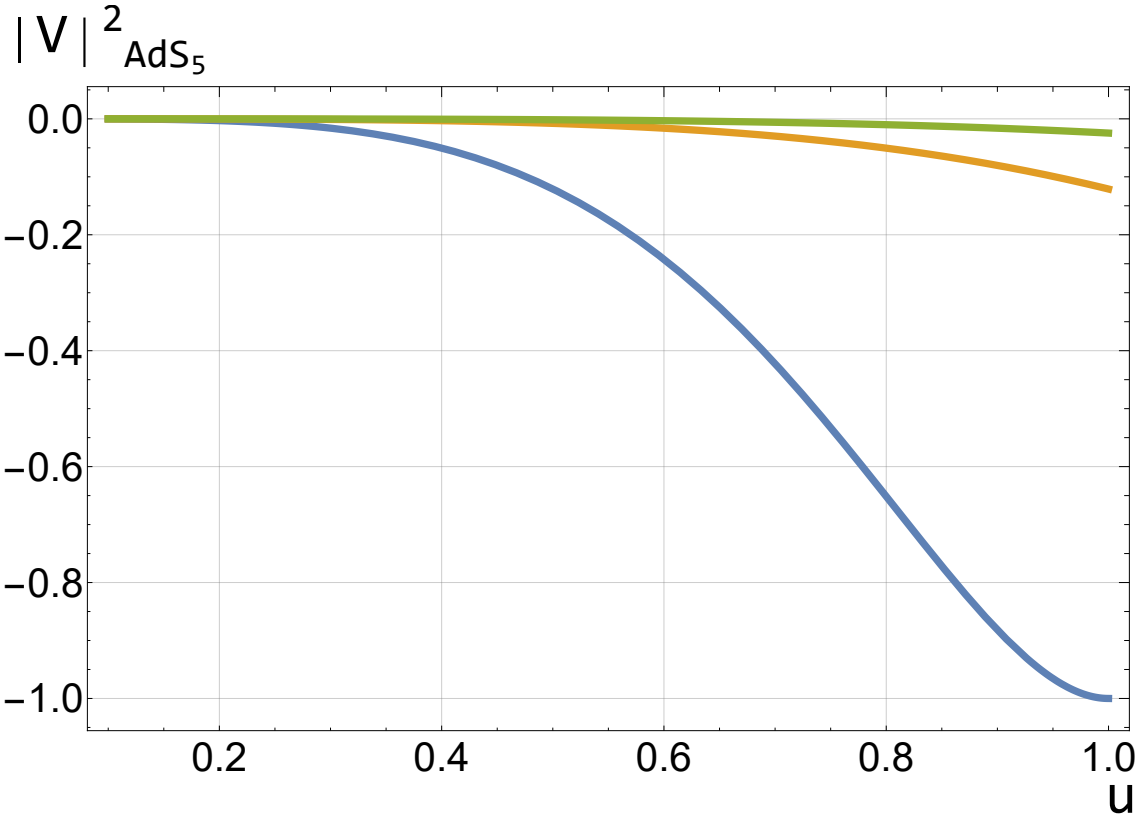

Figure 2.4: This is a plot of $|V^{\mu}|^2_{AdS}$ vs u for $u_h = 1$, $u_h = 2$ and $u_h = 3$.

It is important to note that whilst the probes are considered to be "light", they are not massless and hence do not follow null trajectories in the dual theory. The definition of light in this case is that $\frac{m}{T} \ll 1$.

2.4 Instantaneous rate of energy loss in the AdS_5 black hole

In the last section, the stopping distance for the falling strings with finite end point momentum was computed. This allows us to gain an insight into the quenching of light probes by the deconfining medium. As explained in Chapter 1, the stopping distance is not measured directly at the various heavy ion collision particle experiments. The jet nuclear modification R_{AA} is the observable measuring jet quenching within the medium. In order to compute R_{AA}, the rate at which the probe loses

energy is required.

In [FG14] and [FGG14], finite momentum strings are used to compute this rate of energy loss and thus calculate the jet nuclear modification factor. The falling strings are not used in this case and so called shooting strings are used. This is because the energy loss rates are phenomenologically more consistent to what is expected. The shooting strings are defined as strings that start near the black hole horizon, and have a large non-zero initial radial speed in the direction of the boundary. These are shown in more detail in Sec. 2.2.

Since the AdS_5 black hole has time reversal symmetry ($t \to -t$), one can use the solutions of the falling string Eq. (2.3.6) to find the shooting string solution. The starting radial co-ordinate of the end point is given by u_*, and thus u_0 becomes the nearest point to the boundary that it reaches before falling back down. Given these definitions, the end point trajectory for the shooting string is given by:

$$\begin{aligned} x_{\text{shoot}}(u) &= x(u_*) - x(u) \\ &= u_H^2 \left[\frac{{}_2F_1\left[\frac{1}{4}, \frac{1}{2}; \frac{5}{4}; \frac{u_0^4}{u^4}\right]}{u} - \frac{{}_2F_1\left[\frac{1}{4}, \frac{1}{2}; \frac{5}{4}; \frac{u_0^4}{u_*^4}\right]}{u_*} \right] \end{aligned} \tag{2.4.1}$$

As in the stopping distance case, a near boundary limit is taken on the solution. By taking $\frac{u_0}{u_H} \to 0$, one can invert this expression to eliminate u dependence on the final expression for the rate.

$$\begin{aligned} x_{\text{shoot}} &= u_H^2 \left[\frac{1}{u} - \frac{1}{u_*} \right] \\ \Rightarrow u &= \frac{u_H^2 u_*}{x u_* + u_H^2} \end{aligned} \tag{2.4.2}$$

Having obtained the shooting trajectory, let us focus on the rate itself. Looking at the end point equations of motion and using the falling distance equations Eq. (2.3.3), one can obtain the rate of energy loss.

$$\frac{dE}{dx} = -\frac{\sqrt{\lambda}}{2\pi L^2}\frac{\sqrt{f(u_0)}}{u^2} \tag{2.4.3}$$

In the near boundary limit, one can substitute for u using Eq. (2.4.2). The final expression, as obtained in [FG14] and [FGG14], is given by:

$$\frac{dE}{dx} = -\frac{\pi\sqrt{\lambda}T^2}{2}\left[\frac{1}{\hat{u}_*} + \pi T x\right]^2 \tag{2.4.4}$$

It is important to note a dimensionless parameter $\hat{u}_* = \frac{u_*}{\pi T}$ has been defined. For the shooting string, this should take a value close to 1 from below.

The form of this energy loss is interesting. In [FGG14], it is noted that for small x the rate goes as $\sim T^2$, which is of the form of pQCD elastic energy loss mechanisms. It also goes as $\sim T^3 x$ for intermediate x, which is of the form of pQCD radiative energy loss mechanisms. The large x contribution is the new strong coupling feature of the energy loss.

2.5 Light Probe Energy Loss in the Sakai-Sugimoto Model

The methods used in [FG14] and [FGG14] to compute the light probe stopping distance and rate of energy loss using finite end point momentum strings, has been explained in Sec. 2.3 and Sec. 2.4. In this section, let us consider the top down

model, describing the confinement/deconfinement transition, known as the Sakai-Sugimoto model [SS05b].

This model derives from a D_4/D_8 brane set up as described in Appendix A. The dual of this theory is a non-conformal gauge theory that is confining at low temperatures, but undergoes a phase transition at high temperatures into a deconfining phase. It is this deconfining phase that shall be the subject of interest in the context of light probe jet quenching. Both the stopping distance of falling strings and the rate of energy loss for shooting strings, shall be considered in the following subsections.

2.5.1 Stopping distance in the Sakai-Sugimoto Model

In this subsection, let us compute the stopping distance for falling strings in the the non-conformal Sakai-Sugimoto background. Since it is the deconfining phase that is of interest, it is the black hole high temperature solution that is studied below:

$$\begin{aligned} ds^2_{S-S} &= \left(\frac{r}{L}\right)^{\frac{3}{2}} \left[g(r)dt^2 + dx^2 + dy^2 + dz^2\right] + \left(\frac{L}{r}\right)^{\frac{3}{2}} \frac{1}{g(r)} dr^2 \\ g(r) &= 1 - \frac{r_H^3}{r^3} \end{aligned} \tag{2.5.1}$$

where L is the length scale of the background. In these co-ordinates, the boundary is approached when $r \to \infty$, rather than when approaching 0.

Let us apply the same procedure as in Sec 2.3. Since the background has both time and x translation symmetries, the following conserved quantities are found to be:

$$E_{geo} = \left(1 - \frac{r_H^3}{r^3}\right) \left[\frac{r}{L}\right]^{\frac{3}{2}} \frac{dt}{d\lambda}$$

$$P_{geo} = \left[\frac{r}{L}\right]^{\frac{3}{2}} \frac{dx}{d\lambda} \tag{2.5.2}$$

Using the null constraint and applying the falling string initial conditions, the end point trajectory is given by:

$$\begin{aligned} x(r) &= -\left[\frac{L}{r_H}\right]^{\frac{3}{2}} \int_{r_0}^{r} dr \frac{1}{\sqrt{1-\frac{r^3}{r_0^3}}} \\ &= \frac{1}{\Gamma\left[\frac{5}{6}\right]} \left[\frac{L}{r_H}\right]^{\frac{3}{2}} \left[(\sqrt{\pi} r_0 \Gamma\left[\frac{4}{3}\right] - r\Gamma\left[\frac{5}{6}\right] {}_2F_1\left[\frac{1}{3}, \frac{1}{2}; \frac{4}{3}; \frac{r^3}{r_0^3}\right]\right] \\ \Rightarrow \Delta x_{stop} &= \frac{1}{\Gamma\left[\frac{5}{6}\right]} \left(\frac{L}{r_H}\right)^{\frac{3}{2}} \left[\sqrt{\pi} r_0 \Gamma\left[\frac{4}{3}\right] - r_H \Gamma\left[\frac{5}{6}\right] {}_2F_1\left[\frac{1}{3}, \frac{1}{2}; \frac{4}{3}; \frac{r_H^3}{r_0^3}\right]\right] \end{aligned} \tag{2.5.3}$$

The near boundary limit is defined as $\frac{r_H}{r_0} \to 0$ in the case of these radial co-ordinates, and so one can write the stopping distance as:

$$\Delta x_{stop} = \left[\frac{L}{r_H}\right]^{\frac{3}{2}} \frac{r_0 \sqrt{\pi} \Gamma\left[\frac{4}{3}\right]}{\Gamma\left[\frac{5}{6}\right]} \tag{2.5.4}$$

The energy of the end point is computed in a similar manner. Again, there is no contribution from the affine connection term, as the metric has no time dependence.

$$\begin{aligned} E_{init} &= \frac{1}{2\pi\alpha'} \int_{r_H}^{r_0} dr \sqrt{\frac{r^3 \left(r_0^3 - r_H^3\right)}{r_H^3 \left(r_0^3 - r^3\right)}} \\ &= \frac{1}{10\pi\alpha'} \sqrt{\frac{r_0^3 - r_H^3}{r_0^3 r_H^3}} \frac{1}{\Gamma\left[\frac{1}{3}\right]} \left[5\sqrt{\pi} r_0^{\frac{5}{2}} \Gamma\left[\frac{5}{6}\right] - 2 r_H^{\frac{5}{2}} \Gamma\left[\frac{1}{3}\right] {}_2F_1\left[\frac{1}{2}, \frac{5}{6}; \frac{11}{6}; \frac{r_H^3}{r_0^3}\right]\right] \end{aligned}$$

(2.5.5)

By eliminating r_0 and r_H for temperature (see Appendix A), the final expression for the stopping distance is given by:

$$\Delta x_{stop} = \frac{3\sqrt{3}\Gamma\left[\frac{1}{3}\right]^{\frac{21}{5}} M_{KK}^{\frac{2}{5}}}{16 \times 2^{\frac{4}{15}}\pi^{\frac{16}{5}}\lambda^{\frac{2}{5}}}\left[\frac{E_{init}^2}{T^9}\right]^{\frac{1}{5}} \tag{2.5.6}$$

The Gamma function identities Eq. (2.3.17) and Eq. (2.3.18), and $\Gamma\left[\frac{1}{6}\right] = 2^{-\frac{1}{3}}3^{\frac{1}{2}}\pi^{-\frac{1}{2}}\Gamma\left[\frac{1}{3}\right]^2$ have been used to simplify the results. It is important to note that the string constant α' and the scale length L have been eliminated using Eq. (A.0.6) in favour of the mass scale M_{KK} and the coupling constant λ. It is important to note that λ has been defined using the perturbative QCD definition of the Yang-Mills constant, and not the definition used in most of the holographic literature - (see Appendix A).

As in Sec. 2.3, let us consider the norm of the quark trajectory as observed from the boundary field theory.

$$|V|_{S-S}^2 = \eta_{\mu\nu}V^\mu V^\nu \tag{2.5.7}$$

$$= -1 + \frac{r_0^3\left(r^3 - r_H^3\right)^2}{r^6\left(r_0^3 - r_H^3\right)} \tag{2.5.8}$$

Again, this is always negative implying a time-like nature for the trajectory. This can be seen clearly in Fig. 2.5.

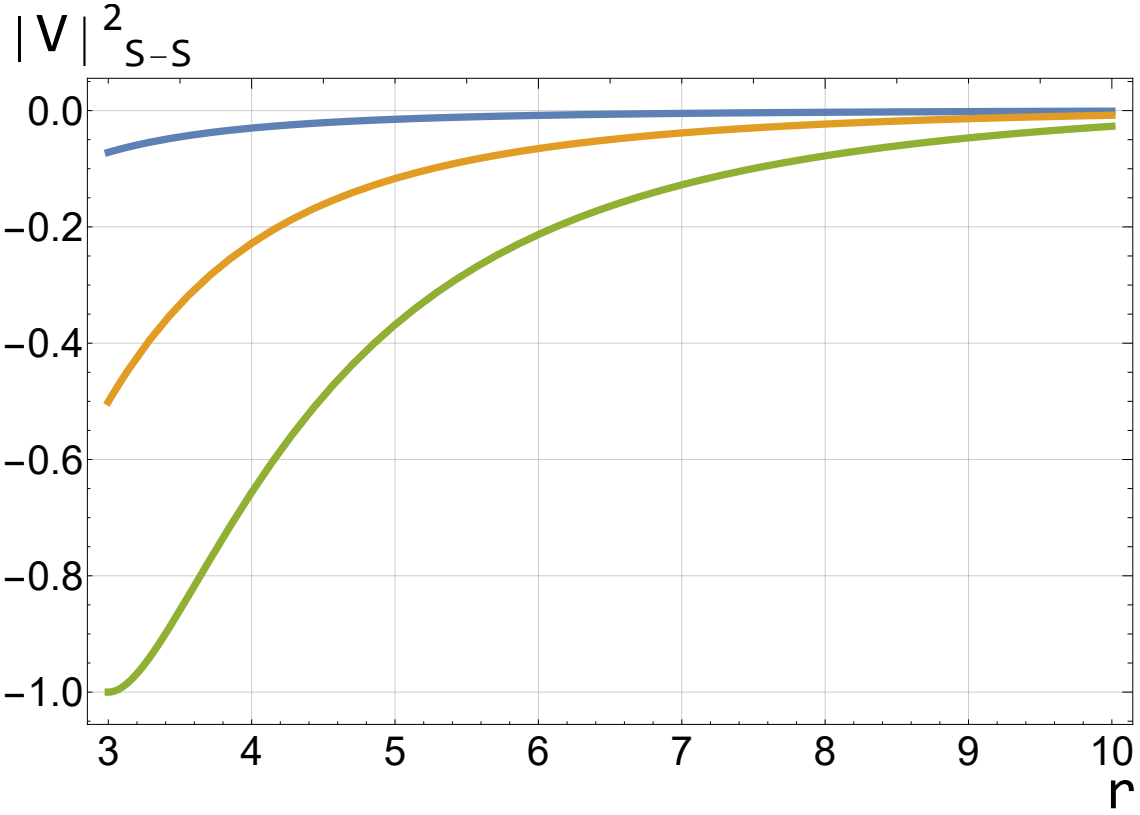

Figure 2.5: This is a plot of $|V^{\mu}|^2_{S-S}$ vs r for $r_h = 1$, $r_h = 2$ and $r_h = 3$.

2.5.2 Instantaneous rate of energy loss in the Sakai-Sugimoto model

Having computed the stopping distance for the falling strings in the Sakai-Sugimoto model, let us move on to the rate of energy loss for the shooting strings. Since the D_4 background still boasts the same t and x translation symmetries, the falling string trajectories can be used to find the shooting string trajectories, in the same fashion as the AdS_5 case.

Using Eq. (2.5.3), the shooting string trajectory is given by:

$$x_{shoot}(r) \quad = \quad x(r_*) - x(r)$$

$$= \frac{1}{\Gamma\left[\frac{5}{6}\right]}\left[\frac{L}{r_H}\right]^{\frac{3}{2}}\left[r\Gamma\left[\frac{5}{6}\right]\,{}_2F_1\left[\frac{1}{3},\frac{1}{2};\frac{4}{3};\frac{r^3}{r_0^3}\right]-r_*\Gamma\left[\frac{5}{6}\right]\,{}_2F_1\left[\frac{1}{3},\frac{1}{2};\frac{4}{3};\frac{r_*^3}{r_0^3}\right]\right]$$

$$\approx \left[\frac{L}{r_H}\right]^{\frac{3}{2}}(r-r_*) \tag{2.5.9}$$

The last line in Eq. (2.5.9) has been obtained by taking the near boundary limit.

Now let us focus on the rate of energy loss itself. Using the end point equation of motion and the stopping integrand in Eq. (2.5.3), the rate can be written as:

$$\frac{dE}{dx} = -\frac{8\pi^2\lambda T^3}{81\sqrt{3}M_{KK}}\left[3\hat{r_*}+4\pi Tx\right]^{\frac{3}{2}} \tag{2.5.10}$$

The temperature has been substituted, eliminating r_H and Eq. (A.0.10) has been used to eliminate α'. One can see the explicit dependence on M_{KK}, which is a direct consequence of the breaking of the conformal invariance.

The small and intermediate x behaviour is now very different $\sim T^3$ and $\sim T^4x$. The large x contribution is also very different $\sim T^{\frac{9}{2}}x^{\frac{3}{2}}$.

2.6 Analysis of the Sakai-Sugimoto light probe energy loss

Both the stopping distances of finite end point momentum falling string, and the rates of energy loss of finite end point momentum shooting strings have been computed. Before proceeding to analyse the jet quenching for the Sakai-Sugimoto model, let us re-iterate some features of the AdS_5 case as mentioned in [FG14].

Firstly, it is important to note that the energy and temperature dependence of Eq. (2.3.19) is the same obtained by considering normal strings without end point momentum - (see [CJKY09]). The stopping distance for these zero end point momentum strings is approximated, by assuming the string looks like a trailing string for large parts of the trajectory. Whilst the dependence on energy and temperature is the same, the overall constant of proportionality is larger, when finite momentum is included for the end points. This is a clear point of difference and could be due to the ambiguous definition of energy in the case with no end point momentum. There is no obvious way to clearly define how the total string energy divides into quark energy, and the energy lost by quark as explained in Sec. 2.2.

As noted in [CJKY09], the $\left[\frac{E}{T^4}\right]^{\frac{1}{3}}$ behaviour is substantially different to the weak coupling $\left[\frac{E}{T^2}\right]^{\frac{1}{2}}$ behaviour computed by considering gluon radiation of hard partons. It is also important to note that the holographic computation of the stopping distance of virtual gluons in [FGG14] also has an $E^{\frac{1}{3}}$ dependence. This is curious as the definition of the energy in the gluon case is quite ambiguous, and yet the same energy dependence is obtained.

Fig. 2.6 shows the rate of energy loss computed for the falling strings in the AdS_5 black hole background. One can see that the rate drops as x increases. As noted in [FGG14], the authors explain that this string state will be quenched quickly and hence is not observed. It is phenomenologically more consistent to consider strings that start nearer the horizon and shoot upwards. It is for this reason that the shooting strings are considered to describe the energy loss. It is also noted that the formation of the plasma, from the gravitational perspective, coincides with the formation of the event horizon. It is thus justified that the string end point should start near the horizon.

The shooting string rate of energy loss was used to compute the jet nuclear modific-

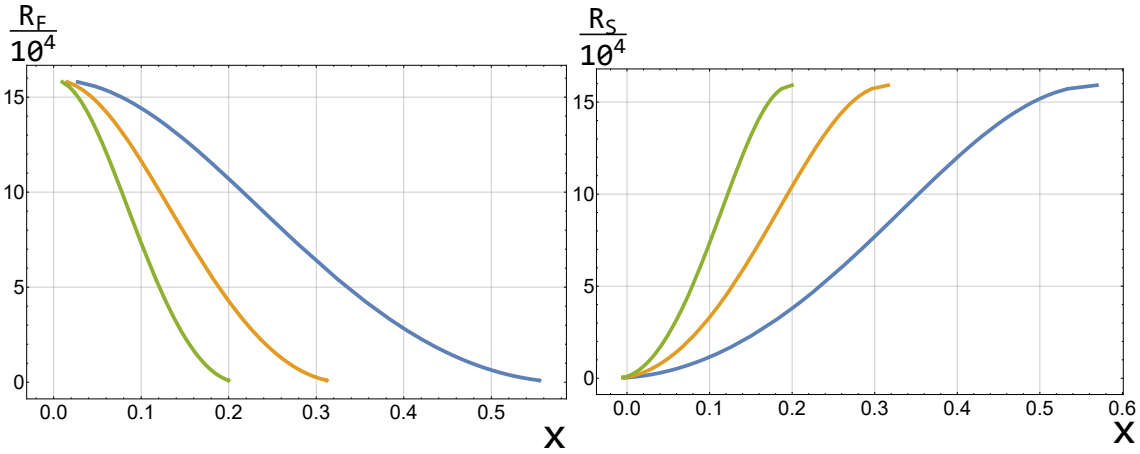

Figure 2.6: This is a plot showing $R = \frac{1}{\sqrt{\lambda}}\frac{dE}{dx}$ vs x for the falling string in the AdS_5 background for three different temperatures: $\hat{T} = 15$, $\hat{T} = 20$ and $\hat{T} = 25$. The temperature is measured in dimensionless units $\hat{T} = TL$. The left plot is for the falling string and the right plot is for the shooting string.

ation factor R_{AA} in [FGG14]. As noted in Chapter 1, this effectively measures the ratio of jets observed in heavy ion collisions to $p-p$ collisions, at a given momentum. It is this observable that is measurable at particle experiments such as the RHIC and the LHC. The authors found, that using the parameters that fit the computation of R_{AA} to experimental data to RHIC, does not match in the LHC case. One can see this sensitivity with the dependence of the rate on $\sqrt{\lambda}T^3$. This sensitivity could attest to the difference obtained in the fits for the two different experiments, which operate at different temperatures.

The key features of the AdS_5 black hole energy loss has been discussed. Let us consider the energy loss in the context of the Sakai-Sugimoto model. The first point of note is the energy and temperature dependence of the stopping distance. The $\left[\frac{E^2}{T^9}\right]^{\frac{1}{5}}$ dependence is clearly different to the AdS_5 black hole case. It is also important to note the dependence on the mass scale M_{KK}. This reflects the non-conformal nature of the Sakai-Sugimoto model. As explained in Appendix A, this scale is related to the confinement/deconfinement temperature, and also relates to the masses of glueballs and meson spectra found in the theory. By comparing to the masses of

such mesons, it was found that the choice $M_{KK} \approx 949MeV$ fits the data in [SS05b] and [SS05c]. The energy dependence matches the energy dependence of the virtual gluon stopping distance computed in [Pan08].

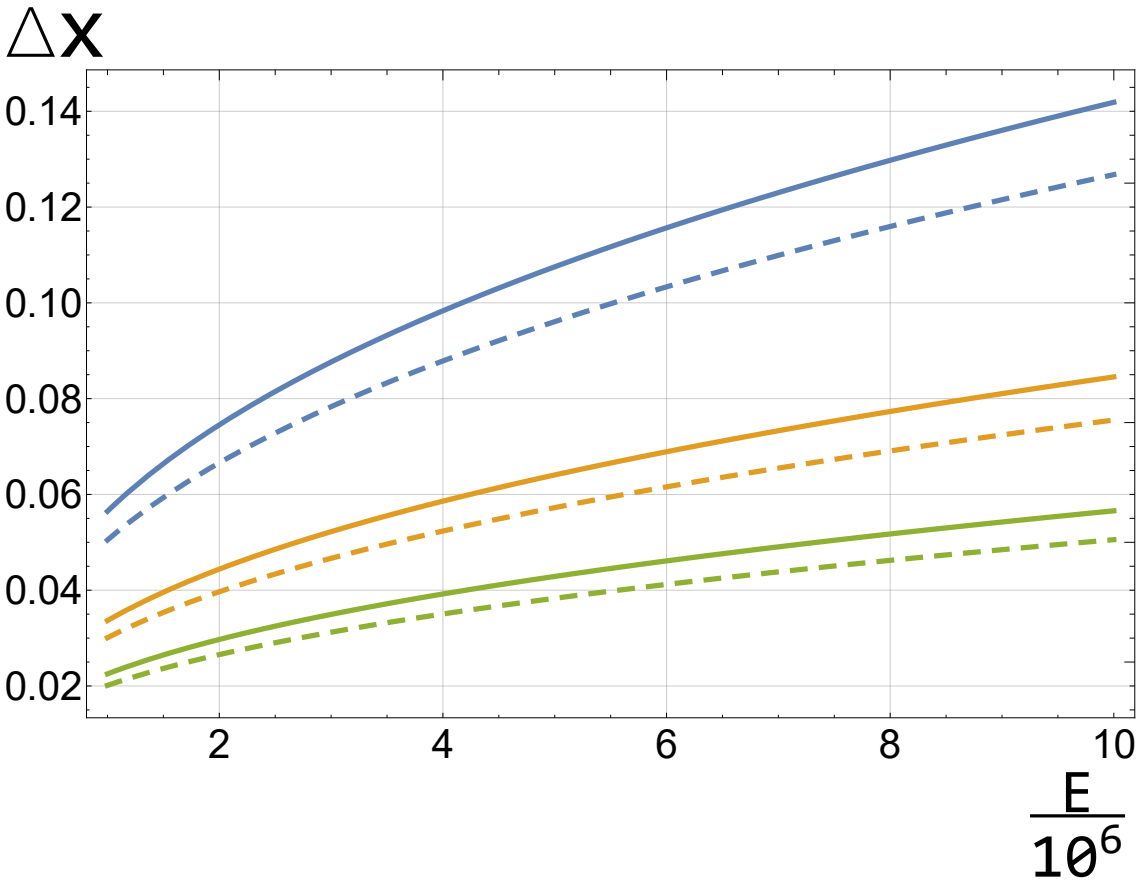

Figure 2.7: This is a plot of Δx vs E_{init} for three different temperatures in the Sakai-Sugimoto model. The temperatures are given by $T = 150MeV$, $T = 200MeV$ and $T = 250MeV$. The energy is measured in units of $L = (MeV)^{-1}$ and the distances are measured in units of $\frac{1}{L}$. The filled lines are for the small $\lambda = 25.1$ and the dashed lines are for large $\lambda = 33.26$.

In Fig. 2.7, one can see the lower and upper bounds of the stopping distance curves, by considering the two different possible values for λ. As explained in Appendix A, there are two ways of fixing the coupling λ. One involves fixing the coupling in order to match the pion decay constant f_π to experimental data. The other method involves matching the $\frac{m_\rho}{\sigma}$ to lattice QCD results, where m_ρ is the mass of the ρ vector meson and σ is the effective string tension of the string used to compute

the static Wilson loop. The former case results in a larger value of λ than in the latter. The plots show the maximum and minimum curves that bound the possible variation in stopping distance that occurs with varying λ. Since the Sakai-Sugimoto model is chiral, one expects a smaller value for f_π, and this is obtained using the smaller value of λ rather than the larger value. Thus, it is the smaller value obtained by fitting the ρ mass ratio that shall be used going forward. Also, the smaller value of λ gives a larger stopping distance, and it is more useful to work with the upper bound of the stopping distance.

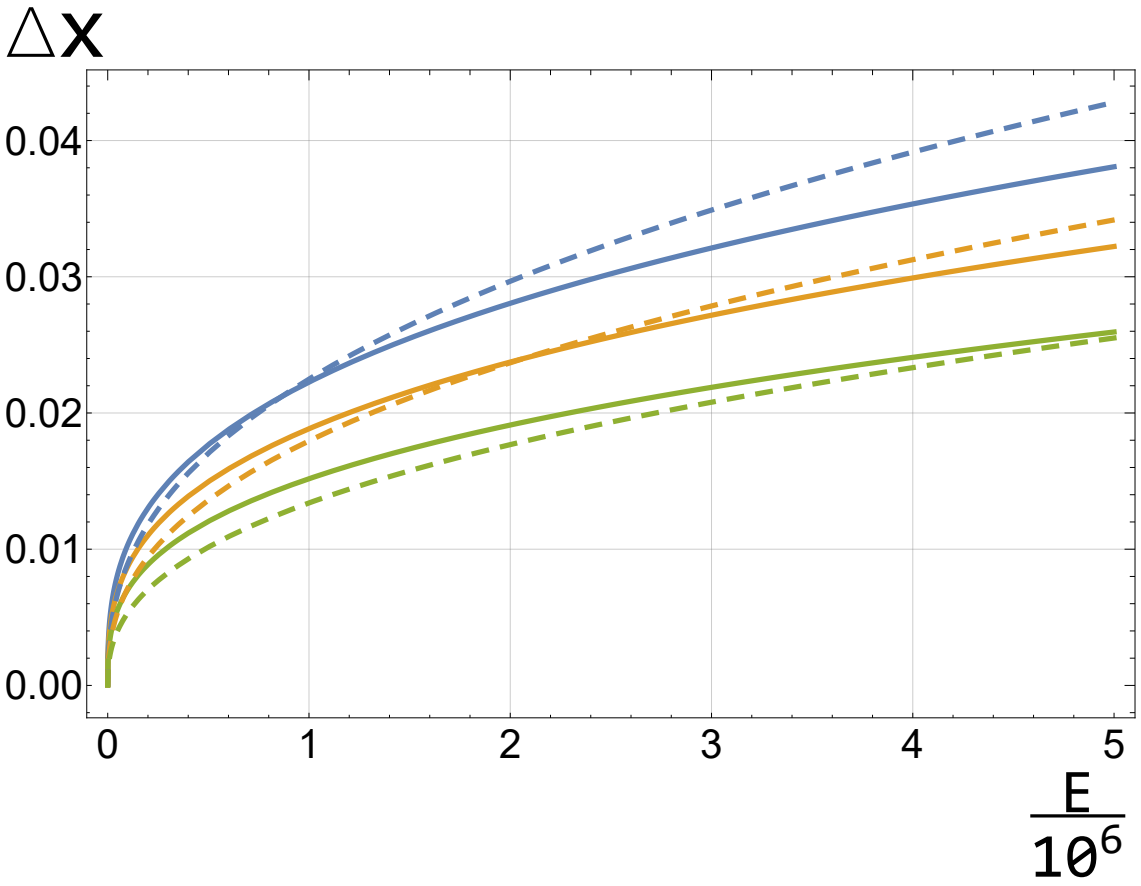

Figure 2.8: This is a plot of Δx vs E_{init} for three different temperatures in both the AdS_5 black hole and Sakai-Sugimoto models. The temperatures are given by $T = 150MeV$, $T = 170MeV$ and $T = 200MeV$. The energy is measured in units of $L = (MeV)^{-1}$ and the distances are measured in units of $\frac{1}{L}$. The filled lines are for the AdS_5 case and the dashed lines are for the Sakai-Sugimoto model.

Fig. 2.8 shows plots of the stopping distance against initial energy for both backgrounds. In the domain plotted, one can see that the AdS_5 background provides a higher stopping distance than the Sakai-Sugimoto model for small energies. As the energy increases, there is a crossover point, where the Sakai-Sugimoto stopping distance dominates. This cross over energy clearly increases with temperature; in fact the plot shows that the domain is not large enough to show the cross over point for the $T = 200MeV$ case. Using the near boundary expressions for the stopping distances Eq. (2.3.19) and Eq. (2.5.6), it is possible to find this cross over energy explicitly.

$$E_{Cross} = \frac{2^{29}\pi^{18}\Gamma\left[\frac{1}{4}\right]^{40}}{3^{\frac{45}{2}}\Gamma\left[\frac{1}{3}\right]^{63}}\frac{\lambda_S^6}{\lambda_A^{\frac{5}{2}}}T^7 \tag{2.6.1}$$

The coupling constants λ_A and λ_S are defined to be the constants for the AdS_5 black hole and Sakai-Sugimoto respectively. Since the energies of interest are large, it is the AdS_5 black hole that leads to larger jet quenching over the domain of study.

Having examined the stopping distance of the falling strings with finite end point momentum in the Sakai-Sugimoto model, let us move on to the rate of energy loss for shooting strings.

As noted in Sub. 2.5.2, the rate of energy loss has a cubic dependence on x rather than the quadratic dependence on x. This means the dependence differs quite a bit from pQCD behaviour for small and intermediate x. Fig. 2.9 shows that for the majority of the trajectory, the AdS_5 black hole energy loss is larger than that of the Sakai-Sugimoto case. However at smaller x, the Sakai-Sugimoto model incurs a more dominant energy loss. Since the temperature dependence is still large for intermediate and large x, it would seem that the same temperature scaling effects would still be in play for this model. This would indicate that the under prediction of R_{AA} at the LHC would still occur for this model. It was noted in [FGG14] that a

bottom up non-conformal model did not improve the situation, and it would seem that the top-down model is the same.

2.7 Jet quenching parameter for time-like light flavoured probes

In Chapter 1, one of the key observables used to study energy loss in the context of strongly coupled plasmas is the jet quenching parameter. It was noted that this parameter measures the transverse momentum broadening of jets travelling through the plasma. The two methods to compute such observables, using the gauge/gravity duality, are the light-like Wilson loop for light-like partons, and the falling doubled closed string method for time-like virtual gluons.

As shown by Fig. 2.4 and Fig. 2.5, the probes described by the finite end point momentum falling strings are light partons following time-like trajectories. It is thus instructive to use the stopping distances obtained from these strings to compute the jet quenching parameter. In order to do this, the operational definition of the parameter used for the virtual gluon in [FGG14] is applied to the finite end point momentum strings. This definition essentially takes the BDMPS method used to derive the Wilson loop method in [LRW06], and modifies it to consider time-like trajectories. The light-cone distance L^- used in the BDMPS formalism is effectively replaced, by the stopping distance of the gluon [GGPR08], [Pan08].

The final expression obtained for the jet quenching parameter $\hat{q}$ is given by the following:

$$\hat{q} = \frac{4E}{\alpha_S C_F (\Delta x)^2}$$

$$C_F = \frac{N_c^2 - 1}{2N_c} \tag{2.7.1}$$

where E is the energy lost by the parton, Δx is the stopping distance, α_S is the strong coupling, and C_F is the Casimir of the colour group $SU(N_c)$ in the fundamental representation.

As noted by Gubser in [GGPR08], there are caveats to using this effective description for $\hat{q}$. Firstly, there is the point already mentioned that the BDMPS method assumes the partons analysed obey light-like trajectories, rather than the time-like trajectories of the falling strings. Secondly, the BDMPS method involves a perturbative and radiative computation in order to find $\hat{q}$. In Chapter 1, it was explained that the classical gravity limit of gauge/gravity duality relates to the large colour ($N_c \to \infty$), t'Hooft limit ($\lambda \to \infty$) of the gauge theory. This is a sum of an infinite number of large N_c planar diagrams. The falling string contains the information of all these diagrams, and thus the detailed mechanics of the energy loss is not discernible from the string. Finally, the diffusion of the transverse momentum is excluded in the string computation, as string perturbations are not considered in our analysis.

Using Eq. (2.7.1) and the stopping distances computed in Eq. (2.3.19) and Eq. (2.5.3), the jet quenching parameter for the AdS and Sakai-Sugimoto models are found to be:

$$\begin{aligned} \hat{q}_A &= \frac{128\pi^4 N_c}{\alpha_S\left(N_c^2-1\right)}\left[\frac{4T^8\lambda E}{\Gamma\left[\frac{1}{4}\right]^{16}}\right]^{\frac{1}{3}} \\ \hat{q}_S &= \frac{2048 N_c}{27\alpha_S\left(N_c^2-1\right)}\left[\frac{2^{\frac{8}{3}}\pi^{32}T^{18}\lambda_S^4 E}{M_{KK}^4\Gamma\left[\frac{1}{3}\right]^{42}}\right]^{\frac{1}{5}} \end{aligned} \tag{2.7.2}$$

where $\hat{q}_A$ is the AdS_5 black hole case and $\hat{q}_S$ is the Sakai-Sugimoto model.

One can see the clear differences in energy and temperature dependencies of $\hat{q}$ for the two models. In order to clearly see the differences, let us plot the dimensionless parameter $\frac{\hat{q}}{T^3}$ vs T for both models. There are few issues that need to be clarified before doing so.

It is important to fix the parameters in Eq. (2.7.2) correctly. The choice of $N_c = 3$ is a clear choice for the colour number, as it matches that of QCD. In the following analysis, it will be useful to compare the behaviour of $\hat{q}$ in Eq. (2.7.2), and that found by phenomenological models. In [Ada+08], [CLQW18] and [Bur+14], a variety of models are used to compute both the jet nuclear modification factor and the jet quenching parameter. In order to compare with these models, we make the choice of $\alpha_S = 0.22 - 0.31$ for the strong coupling. Using these values of α_S, the couplings λ are defined through:

$$\lambda = 4\pi N_c \alpha_S \tag{2.7.3}$$

Whilst the choice of $\lambda_A = 6\pi$ and $\lambda_S = 25.1$ has been used in Sec. 2.6, these values of α_S will be used to define the λ in order to be consistent with the analysis.

Secondly, the choice of definition of the temperature needs to be considered when analysing $\hat{q}$. In [Gub07], [GGPR08] and [Pan08], the authors' choose to fix the energy density rather than fixed temperature. This is to take into account the fact that QCD has fundamentally different degrees of freedom than $\mathcal{N} = 4$ Super Yang-Mills, and the gauge theory dual to the Sakai-Sugimoto model. This choice of convention allows us to relate the temperatures in the gravitational theories T, and the QCD temperature T_{QCD}.

$$
\begin{aligned}
T_{\mathcal{N}=4} &= \frac{T_{QCD}}{3^{\frac{1}{4}}} \\
T_{S-S} &= \frac{T_{QCD}}{0.914\lambda_S^{\frac{1}{6}}}\left[\frac{T_d}{T_{QCD}}\right]^{\frac{1}{3}}
\end{aligned}
\tag{2.7.4}
$$

where $T_d = 170MeV$ is the deconfinement phase transition critical temperature.

Fig. 2.10 shows the plot of $\frac{\hat{q}}{T^3}$ for both AdS_5 and the Sakai-Sugimoto model cases. It is interesting to note that the strong coupling constant seems to have a significant impact on $\hat{q}$. For the smaller value of $\alpha_S = 0.22$, $\frac{\hat{q}}{T^3}$ is larger for all cases. In [XLG16], it was also noted that the influence of the coupling scheme on the jet quenching parameter was significant, and this seems also to be the case here. The Sakai-Sugimoto model case is shown to be smaller for both α_S and energies chosen in the plots. This is opposite to the virtual gluon case, where it is shown that the Sakai-Sugimoto model predicts larger values of the jet quenching parameter [Pan08].

The plots show that $\frac{\hat{q}}{T^3}$ qualitatively agrees with the behaviours computed, using the phenomenological models used in [CLQW18], [Bur+14] and [XLG16]. However, the magnitude of the parameter seems to be severely over predicted by the falling string model. In order to see this clearly, let us look at the absolute value of $\hat{q}$.

Tab. 2.1 shows the absolute value of $\hat{q}$ measured in $GeV^2\text{fm}^{-1}$ for both AdS_5 and Sakai-Sugimoto models, and varying temperature and coupling. The choice of $T = 280MeV/370MeV$ and $T = 470MeV$ were chosen to represent the RHIC and LHC plasmas respectively, and also allow us to compare $\hat{q}$ with the absolute values found by the models in [Bur+14], [Ada+08] and [CLQW18].

It is interesting to note that both the AdS_5 black hole and Sakai-Sugimoto cases

	$\frac{E}{GeV}$	α_S	$\frac{T}{GeV}$	$\frac{\hat{q}}{GeV^2\text{fm}^{-1}}$
AdS_5	10	0.22	0.370	26.28
			0.470	49.74
		0.31	0.370	20.91
			0.470	39.57
	20	0.22	0.280	15.75
		0.31		12.53
S-S	10	0.22	0.370	21.24
			0.470	37.72
		0.31	0.370	16.15
			0.470	28.67
	20	0.22	0.280	12.50
		0.31		9.50

Table 2.1: This table shows the absolute values for the falling string jet quenching parameter for the $E = 10GeV$ and $E = 20GeV$. The parameter is measured in units of $GeV^2\text{fm}^{-1}$.

fall within the range predicted in [Ada+08], for RHIC data for both values of the coupling - ($7GeV^2\text{fm}^{-1} < \hat{q} < 28GeV^2\text{fm}^{-1}$). However, the values are larger than those predicted by the phenomenological models obtained using RHIC and LHC data in [Bur+14] and [XLG16]. The absolute value of $\hat{q}$ using these models are found to be:

$$\begin{aligned} \hat{q} &= 1.2GeV^2\text{fm}^{-1} \qquad \text{at 370MeV} \\ \hat{q} &= 1.9GeV^2\text{fm}^{-1} \qquad \text{at 470MeV} \end{aligned} \tag{2.7.5}$$

It is important to note that these values are smaller than the range obtained in [Ada+08]. This is due to the fact that a larger parton energy ($E = 20GeV$) is used in [Ada+08], than in [Bur+14] ($E = 10GeV$). One can see from Tab. 2.1 that the falling string over predicts. The closest to the results shown in Eq.(2.7.5) is the Sakai-Sugimoto computation, using the larger strong coupling value of $\alpha_S = 0.31$.

Let us also compare the falling string $\hat{q}$ with the light-like Wilson loop compu-

tation. The expressions for $\hat{q}$ for both AdS_5 black hole and Sakai-Sugimoto model are given by ([LRW06] , [GXZ06]):

$$\begin{aligned} \hat{q}_A^W &= \frac{\pi^{\frac{3}{2}}\Gamma\left[\frac{3}{4}\right]}{\Gamma\left[\frac{5}{4}\right]}\sqrt{\lambda_A}T^3 \\ \hat{q}_S^W &= \frac{64\pi^{\frac{3}{2}}}{27}\frac{\Gamma\left[\frac{2}{3}\right]}{\Gamma\left[\frac{1}{6}\right]}\lambda_S\frac{T}{T_d} \end{aligned} \tag{2.7.6}$$

where $T_d = 170MeV$ is the deconfinement phase transition temperature.

It is interesting to note that there is no energy dependence in these expressions. This is significant when comparing to the phenomenological models. Both the AdS_5 and Sakai-Sugimoto model $\hat{q}^W$ under predict relative to the $E = 20GeV$ RHIC model used in [Ada+08]. On the other hand, $\hat{q}^W$ over predicts the $E = 10GeV$ case considered in [Bur+14], by a relatively small margin of error. In particular, the Sakai-Sugimoto model seems to be closer than the AdS_5 black hole case.

It is important to note that the error is reduced by including higher derivative corrections [ZHR13]. In Chapter 3, higher derivative corrections to the STU R-charged black hole is considered. The zero chemical potential case will tell us how higher derivative corrections affect $\hat{q}$.

In Fig. 2.11, the falling string $\hat{q}$ is compared to $\hat{q}^W$ against temperature for $E = 10GeV$. For both AdS_5 black holes and the Sakai-Sugimoto model, the falling string leads to a larger $\hat{q}$. The factor by which this is true is larger for the Sakai-Sugimoto model. This shows the over prediction of $\hat{q}$, as discussed above.

It is also important to note the virtual gluon computations performed in [GGPR08] and [Pan08]. These computations were performed before the LHC experiments were

started, and were thus computed for the RHIC case of [Ada+08]. The AdS_5 black hole virtual gluon $\hat{q}$ is found to lie within the range obtained using the RHIC data, by using the so-called alternative scheme ($\hat{q}^g_A = 21 GeV\,\mathrm{fm}^{-1}$). On the other hand, the same calculation performed in the Sakai-Sugimoto case over predicts this results ($\hat{q}^g_S > 89 GeV\,\mathrm{fm}^{-1}$). It is interesting to note that this is very different to our falling string computation, in which it seems both AdS_5 black holes and the Sakai-Sugimoto model lie within the RHIC data.

In [CLQW18], the authors' use the so called LBT model on experimental data from the RHIC and LHC in order to extract $\hat{q}$. However, this model distinguishes the parton involved, and so $\hat{q}$ is found for heavy quarks, light quarks and gluons. They find that the gluons have a $\frac{\hat{q}}{T^3}$ that is always greater than the quarks, both heavy and light. This is similarly observed using the falling string light probe case and the virtual gluon case for both AdS_5 black hole and Sakai-Sugimoto model cases.

2.8 Summary

In this Chapter, the overall method proposed by Ficnar and Gubser in [FG14] to analyse the energy loss of light quarks travelling through the deconfining phase of non-Abelian gauge theories, was reviewed. This included a brief discussion on strings that have longitudinal modes, through the inclusion of finite end point momentum. The momentum is added to the string by treating the end points as massless particles and thus, supplementing the Polyakov action with the einbein formulation of massless particles.

The use of this method is of interest, due to the fact that the string energy dual to the light probe, can be mapped to the probe energy in a more coherent manner. The simplification of the equations of motion, by the decoupling of the end point equations of motion to the bulk string motion, is also clearly convenient as it is

simpler to solve. In fact, the decoupling effect effectively reduces the string end point dynamics, to be analysed through the computation of null geodesics.

The example of the light probe stopping distance for the AdS_5 black hole was computed to show this method in practice, and the results of [FG14] were reproduced. Since the AdS_5 case is the gravitational dual of a conformal and supersymmetric theory, the Sakai-Sugimoto model was introduced. This model is dual to gauge theory with flavoured quarks, that does not contain these symmetries. It was concluded that the AdS_5 black hole seemed to have a stronger quenching effect than the Sakai-Sugimoto model.

These results were used to compute the effective jet quenching parameter $\hat{q}$ for time-like light flavoured probes. This was done by using the extension of the BDMPS method, following [GGPR08] and [Pan08]. It was found that the AdS_5 black hole value of $\hat{q}$ is larger than that of the Sakai-Sugimoto model, contrary to the observations made when using the doubled closed string method used for virtual gluons, but in agreement with the light probes using the Wilson Loop method.

When comparing the raw values to experimental data, it was found that the falling string $\hat{q}$ values were larger for the $E = 10GeV$, $T = 370MeV$ and $T = 470GeV$ cases. In particular, the over prediction from the Sakai-Sugimoto model is particularly erroneous. Yet for the $E = 20GeV$, $T = 280MeV$ case, both AdS_5 black holes and the Sakai-Sugimoto models seemed to lie within the acceptable range predicted by the phenomenological model.

Finally, the falling string method and virtual gluon method were compared, and it was found that the gluons produce a significantly larger value for $\hat{q}$, in both AdS_5 black holes and the Sakai-Sugimoto model. This is in agreement with phenomenological predictions made using the data from the RHIC and the LHC.

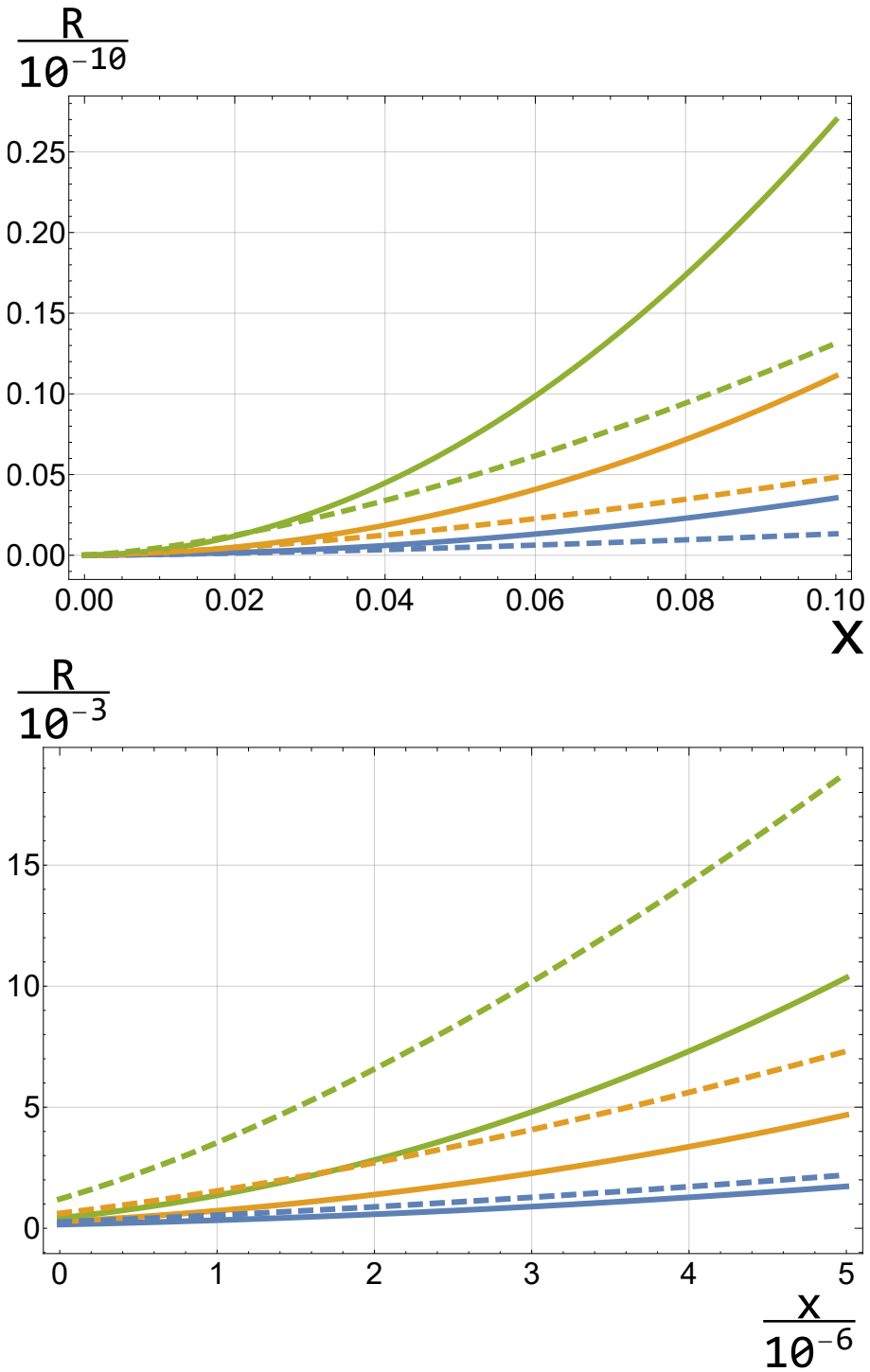

Figure 2.9: This shows plots of $R = -\frac{dE}{dx}$ vs x for the shooting strings, including both the AdS_5 black hole and the Sakai-Sugimoto model. The solid lines are for the AdS_5 black hole system and the dashed lines are for the Sakai-Sugimoto model. Three different temperatures are used in the plots: $T = 150MeV$, $T = 200MeV$ and $T = 250MeV$. The top plot is for a larger range of x but the bottom plot is for a much smaller, zoomed in domain of x.

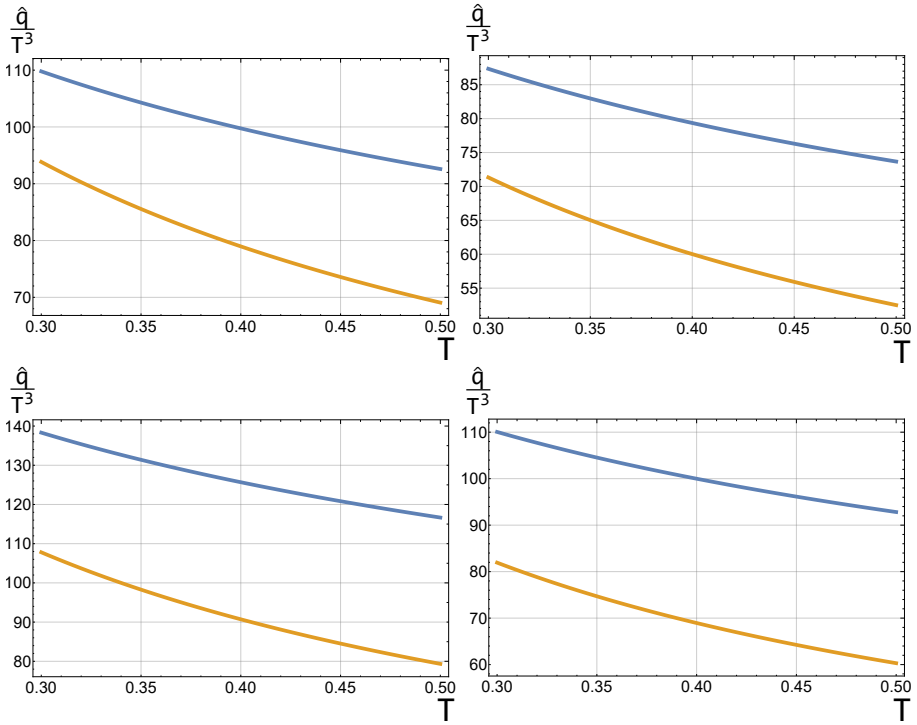

Figure 2.10: This is a plots of $\frac{\hat{q}}{T^3}$ vs T for both the AdS_5 and Sakai-Sugimoto model cases. The Blue colour is for the AdS_5 case and the Orange colour line represents the Sakai-Sugimoto model. The left plots are for the $\alpha_S = 0.22$ and the right plot are for the $\alpha_S = 0.31$ case. The top plots is for the $E = 10GeV$ jet and the bottom plots are for the $E = 20GeV$ jets.

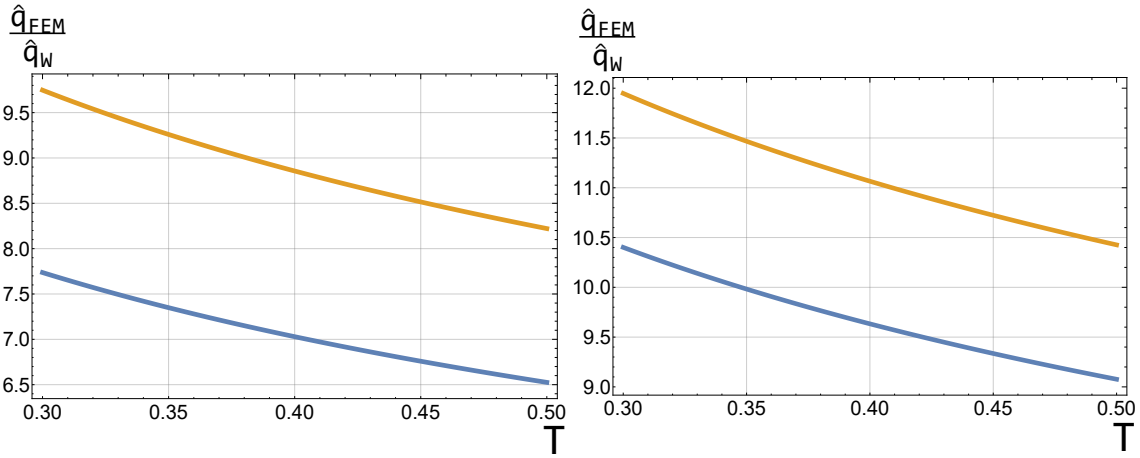

Figure 2.11: This is a plot of $\frac{\hat{q}_f}{\hat{q}_W}$ vs T for both the falling string and light-like Wilson loop cases. The left plot is for the $E = 10GeV$ case and the right plot is for the $E = 20GeV$. The colour of the lines are represented by Blue = AdS_5 and Orange = Sakai-Sugimoto. The plots are obtained using $\alpha_S = 0.31$.

Chapter 3

Light quark energy loss with chemical potential

In this Chapter, the effect that finite chemical potentials has on light probes traversing the QGP medium is studied. As explained in Chapter 1, the QGP medium reaches equilibrium after a short equilibration phase in which non-zero Baryon charges proliferate the medium. It is interesting to see how this affects the jet quenching of light probes through the medium.

There are two main cases of interest that is studied in this Chapter. First, the so called R-charged STU black hole is investigated. This is a solution to $5D$ $\mathcal{N} = 2$ supergravity, and is a top down approach to introducing chemical potential. The source of the gauge fields is from the compactification of the compact part of the full $10D$ system. The dual chemical potential is associated to the charges conserved due to R-symmetry. It is also possible to introduce higher derivative corrections to this system, and both the zero and non-zero chemical potential cases are studied in this Chapter. Whilst this system has been investigated in the context of heavy quark drag forces and light-like jet quenching parameter, it is interesting to see how the finite end point momentum strings are affected by the non-zero chemical potentials [CKY14], [LM06], [FPS11] and [AEM06].

The second case of interest is where the chemical potential is introduced via gauge fields on probe branes, introduced to include flavour multiplets into the dual theory. The introduction of the probes introduce matter multiplets with global flavour symmetry in the dual theory. The flavour symmetry is realised as a gauge symmetry on the probe branes, from the gravitational point of view. The chemical potentials, associated to the charges conserved due to this symmetry, can be turned on by looking at specific solutions to the gauge fields living on the probe branes ([MMT07], [MMT06], [Bha+14]). The trajectory of the probe strings is affected through the coupling of these gauge fields to the string end points. Thus, the non-zero chemical potential has an influence on the energy loss described by these strings. Using the finite end point momentum strings, the light probe energy loss is described for both the D_3/D_7 and Sakai-Sugimoto models, with finite flavour chemical potential.

3.1 Chemical potentials and the Grand Canonical ensemble in Holography

In this section, the introduction of chemical potentials in the context of holography shall be discussed. In particular, the chemical potentials are dual to two different global symmetries. The first case is the introduction of the chemical potential associated to R-charge in supersymmetric theories. The second case is the chemical potential associated to Baryon number. It is important to note that the behaviour of the finite momentum strings is very different in each of these cases. As it will be shown in this chapter, the end point equations of motion cannot be reduced to null geodesics in the flavour symmetry chemical potential case. This is because of the introduction of the gauge field coupling to the action, and subsequently the einbein transformation Eq. (2.2.16) no longer works. This means a numerical analysis must be performed on this system.

On the other hand, there are a few common features generic to the grand canonical ensemble which applies to both systems. Let us first review some basics about the nature of gauge fields in the context of the gauge/gravity correspondence.

The holographic dictionary states that global symmetry on the field theory side is realised as gauge symmetry in the bulk. In general, the holographic principle dictates that on-shell gravitational fields couple to the dual field operator $\mathcal{O}$ on the boundary, in the following manner:

$$\exp\left[-S_{grav}(\phi(x^\mu, r))\right] \leftrightarrow \left\langle \exp\left[-\int dx^4 \phi(x^\mu)\mathcal{O}\right]\right\rangle \tag{3.1.1}$$

$\phi(x^\mu, r)$ is an on-shell field in the gravity side that obeys $\phi(x^\mu, r \to \infty) \sim \phi(x) f(r)$[1].

In the gauge field case, the conformal factor $f(r) = 1$ and the asymptotic gauge field tends towards a constant. The dual operator $\mathcal{O}$ is the current j^μ, which is the conserved Noether current associated to the global symmetry on the boundary. This global symmetry is the global version of the gauge symmetry in the bulk. One can interpret large gauge transformations of the bulk, as global transformations in the boundary. Consider the following solution to the gauge field equations:

$$A_A = f(r, \vec{x})\delta^0_A \tag{3.1.2}$$

$$\lim_{r\to\infty} A_0 = \mu \tag{3.1.3}$$

where A_A is the gauge field and μ is the asymptotic constant. Turning on such a gauge field deforms the exponent in the field theory partition function by:

[1] $f(r)$ is a conformal factor.

$$\int dx^4 \hat{A}_\mu(r \to \infty) j^\mu = -\mu\beta Q \tag{3.1.4}$$

Q is the charge operator associated to j^μ and β is the inverse temperature. This is just like adding a chemical potential μ, and so this gauge field has induced the grand canonical ensemble thermal state.

As noted previously, there are two main cases of interest to investigate. For the R-charged case, the dual global symmetry is observed as the isometry of the compact part of the manifold. This is realised through gauge fields, when the gravitational theory is compactified over this compact manifold. The resulting $5D$ theory is now a gauge theory, where the local symmetry is the isometry group of the compact part of the $10D$ manifold. In the canonical case, this compact submanifold is the S^5.

Since the gauge fields for the R-charged chemical potential case are obtained through the compactification process, the gauge fields live in the bulk of the $5D$ theory. As we know, the deconfinement phase is represented by a black hole on the gravity side. The addition of the gauge fields mean it is the charged black hole that describes the deconfinement phase with chemical potential. Whilst the string doesn't couple to the gauge fields directly, the impact of the gauge fields on the metric affects the string trajectory. A particular solution of interest is the STU black hole solution [BCS99]. These black holes are solutions to a minimally truncated gauged supergravity (see Appendix B). The effect of the chemical potential on the light probe energy loss will be studied for this theory.

The second case of interest is the introduction of the chemical potential associated to flavour symmetry. In order to introduce quarks into the theory, it has already been discussed that probe branes are introduced into the bulk background. These probe branes support a gauge symmetry, which is dual to the global flavour

symmetry associated to these quarks. Since the probe limit is used, these gauge fields do not affect the background metric. Thus, one would naively think that the string describing the light probe, will be unaffected by the chemical potential. However, the open strings end on the probe branes by the definition of the boundary conditions, and the end points couple to the gauge fields living on the probe branes. So whilst the black hole is not charged in this case, the string couples to the gauge fields on the probe branes, which thus influence the trajectory of the string. Hence, the chemical potential has a non-trivial effect on the light probe.

3.2 Light probe energy loss in $\mathcal{N} = 2$ STU R-charged black holes

In this section, the light probe stopping distance and energy loss rate are computed for the R-charged case. As described in Sec. 3.1, the R-charged case is described by charged black holes. The gauge fields dual to the global symmetry live in the bulk of the theory and charge the black holes dual to the deconfining phase of the gauge theory.

In particular, the STU asymptotically AdS five dimensional solution to gauged $\mathcal{N} = 2$ SUGRA is considered [BCS99]. The details of this solution are described in Appendix B. The metric for the solution can be written by the following:

$$ds^2 = -(H_1H_2H_3)^{-\frac{2}{3}} f dt^2 + (H_1H_2H_3)^{\frac{1}{3}}(f^{-1}dr^2 + \frac{r^2}{L^2}d\vec{x}^2) \tag{3.2.1}$$

where

$$f = \frac{r^2}{L^2}H_1H_2H_3 - \frac{m}{r^2}, \quad H_i = 1 + \frac{q_i}{r^2}, \quad i = 1, 2, 3 \tag{3.2.2}$$

and the scalar fields X^i and three $U(1)$ fields A_t^i:

$$X^i = \frac{(H_1 H_2 H_3)^{\frac{1}{3}}}{H_i}, \qquad A_t^i = \bar{\mu}_i - \sqrt{\frac{m}{q_i}}(1 - H_i^{-1}) \tag{3.2.3}$$

Given this solution to the supergravity equations of motion, let us proceed to compute the stopping distance for the falling string, and the rate of energy loss for the shooting string. This follows the methods described in Chapter 2.

In order to solve the null geodesic equations of motion that describe the falling string, let us consider the conserved quantities associated to time translation invariance and spatial translation invariance.

$$\begin{aligned}
E_{geo} &= -G_{tt}\frac{dt}{d\lambda} \\
&= \frac{r_H^2\left(q_1+r^2\right)\left(q_2+r^2\right)\left(q_3+r^2\right) - r^2\left(q_1+r_H^2\right)\left(q_2+r_H^2\right)\left(q_3+r_H^2\right)}{r_H^2 L^2\left[\left(q_1+r^2\right)\left(q_2+r^2\right)\left(q_3+r^2\right)\right]^{\frac{2}{3}}}\frac{dt}{d\lambda} \\
P_{geo} &= G_{xx}\frac{dx}{d\lambda} \\
&= \frac{\left[\left(q_1+r^2\right)\left(q_2+r^2\right)\left(q_3+r^2\right)\right]^{\frac{1}{3}}}{L^2}\frac{dx}{d\lambda}
\end{aligned} \tag{3.2.4}$$

where Eq. (B.0.7) in Appendix B has been used to eliminate m. One can thus obtain:

$$\frac{dx}{dt} = \frac{P_{geo}(r-r_H)(r+r_H)\left(r^2 r_H^2\left(q_1+q_2+q_3+r^2\right) - q_1 q_2 q_3 + r^2 r_H^4\right)}{E_{geo} r_H^2\left(q_1+r^2\right)\left(q_2+r^2\right)\left(q_3+r^2\right)} \tag{3.2.5}$$

Using the null condition, one can obtain $\frac{dr}{dt}$ and use this to find an expression for $\frac{dx}{dr}$.

Now let us apply the initial conditions of interest. At $t=0$, $\vec{x}=0$, $r=r_0$ and $\frac{dt}{d\lambda}=1$, $\frac{dx}{d\lambda}=\frac{dx_0}{d\lambda}$ is the only other non-zero component of the initial tangent vector. The null condition can be used to fix this component of the initial tangent vector. Given these initial conditions, one can eliminate E_{geo} and P_{geo} and obtain the integrand $\frac{dx}{dr}$.:

The full form of $\frac{dx}{dr}$ is non-trivial and not particularly illuminating. In order to compute the stopping distance, one must integrate this between r_0 and the horizon. In Appendix C, it is shown that the near boundary leading order contribution to the integral is obtained by integrating the leading order contribution of the integrand. This is true if the integrand is non-singular as $r\to 0$, and is the case for $\frac{dx}{dr}$ obtained in our example. Thus, the leading order contribution is given by:

$$\begin{aligned}\Delta x_{stopping} &= -\int_0^1 \frac{L^2 r_H r_0}{\sqrt{(1-r^4)\left(q_1+r_H^2\right)\left(q_2+r_H^2\right)\left(q_3+r_H^2\right)}}dr \\ &= \frac{r_0 r_H \Gamma\left[\frac{1}{4}\right]^2 L^2}{4\sqrt{2\pi\left(q_1+r_H^2\right)\left(q_2+r_H^2\right)\left(q_3+r_H^2\right)}} \end{aligned} \tag{3.2.6}$$

where the integrand is the leading order contribution to $\frac{dx}{dr}$ in the near boundary expansion.

Now let us consider the energy of the end point, whose dynamics are defined from the end point equations of motion Eq. (2.2.3). The integral can again be computed by considering the leading order term of the integrand:

$$E_{init} = \frac{1}{2\pi\alpha'}\int_0^1 \frac{r^2 r_0^3 r_H}{\sqrt{-\left(r^4-1\right)\left(q_1+r_H^2\right)\left(q_2+r_H^2\right)\left(q_3+r_H^2\right)}}dr \tag{3.2.7}$$

$$= \frac{\pi^{\frac{1}{2}}}{2^{\frac{1}{2}}\alpha'}\frac{r_0^3 r_H}{\sqrt{\left(q_1+r_H^2\right)\left(q_2+r_H^2\right)\left(q_3+r_H^2\right)}}\Gamma\left[\frac{1}{4}\right]^{-2} \tag{3.2.8}$$

It is important to note that the string scale α' appears in both Eq. (3.2.6) and Eq. (3.2.8). It will be shown that α' is eliminated in favour of the 't Hooft coupling, when specific charge cases are considered below.

Let us now consider the shooting string model, in order to compute the instantaneous rate of energy loss. Let us once more use the near boundary limit, in order to evaluate the integral - see Appendix C.

$$\begin{aligned} x_{shoot}(r) &= -\int_{r}^{r_*} \frac{L^2 r_H}{\sqrt{(q_1+r_H^2)\,(q_2+r_H^2)\,(q_3+r_H^2)}} dr \qquad (3.2.9) \\ &= \frac{L^2 r_H (r-r_*)}{\sqrt{(q_1+r_H^2)\,(q_2+r_H^2)\,(q_3+r_H^2)}} \\ \Rightarrow r_{shoot}(x) &= \frac{x\sqrt{(q_1+r_H^2)\,(q_2+r_H^2)\,(q_3+r_H^2)}}{L^2 r_H} + r_* \qquad (3.2.10) \end{aligned}$$

Now let us consider the instantaneous rate of energy loss $\frac{dE}{dx}$, which is obtained from the end point equation of motion once more. By substituting Eq. (3.2.10) and taking the near boundary limit, one obtains:

$$\frac{dE_{ep}}{dx} = \frac{[g(q_1)g(q_2)g(q_3)]^{\frac{1}{3}}}{2\pi L^2 \alpha'} \qquad (3.2.11)$$

where

$$g(q) = \left[\frac{x\sqrt{(q_1+r_H^2)\,(q_2+r_H^2)\,(q_3+r_H^2)}}{L^2 r_H} + r_H \hat{r}_*\right]^2 + q \qquad (3.2.12)$$

In the expression for $g(q)$, the definition $\hat{r}_* = \frac{r_*}{r_H}$ has been used. Once more, the explicit dependence on α' will become a dependence on the t'Hooft coupling λ, when

specific cases are investigated in the next section.

As described in Sec. 1.3, it was noted that the large power temperature dependence for $\frac{dE}{dx}$ in the $\mu = 0$ case could account for the under prediction of the jet nuclear modification factor R_{AA} at the LHC, when using the RHIC parameters. The uncertainty in the Glauber model temperature potentially comes from the initial formation temperature τ_i.

It would be interesting to take note of the temperature dependence of the corrections term for finite chemical potential. If the temperature dependence of the correction term has a strong temperature dependence as well, the uncertainty in the temperature may exacerbate the scaling problem described in [HG11] and [FGG14].

3.2.1 Single Charge Black Hole

In Sec. 3.2, the general expressions for the falling string stopping distance and shooting string rate of energy loss have been found. Let us now consider three cases following the conventions of [PS13], in order to study the effect the non-zero chemical potential has on the energy loss of the light probes.

The single charge case, $q_1 = qL^2$ and $q_2 = q_3 = 0$, is the first to be considered. The parameter q is a dimensionless parameter chosen for ease of use. One can now obtain an expression for the stopping distance as a function of the initial energy and temperature, by eliminating r_0. It is important to note that we have rescaled the chemical potential to give it mass dimensions 1; this is done by rescaling the gauge field $A_\mu \to A_\mu L$. The expression obtained is highly non-trivial:

$$\Delta x_{stopping} = \left[\frac{g_1(T,\mu)}{h_1(T,\mu)}\right]^{\frac{1}{3}} \frac{\Gamma\left[\frac{1}{4}\right]^{\frac{8}{3}}}{2^{\frac{5}{3}}\pi^{\frac{2}{3}}\lambda^{\frac{1}{6}}} E^{\frac{1}{3}} \tag{3.2.13}$$

where

$$\begin{aligned} g_1(T,\mu) &= \mu^2 + \pi T\sqrt{\pi^2T^2 - 2\mu^2} + \pi^2T^2 \\ h_1(T,\mu) &= 4\pi^6T^6 + 4\pi^4\mu^2T^4 + 17\pi^2\mu^4T^2 - \mu^6 \\ &+ \sqrt{\pi^2T^2 - 2\mu^2}\left[4\pi^5T^5 - 5\pi\mu^4T + 8\pi^3\mu^2T^3\right] \end{aligned} \tag{3.2.14}$$

This is clearly still non-trivial. Since the QGP formed in both RHIC and LHC experiments have small charge densities, it is of interest to consider hot and low charge density plasmas. Therefore, it is useful to look at the first few terms in the expansion of the temperature and μ dependent function $\left[\frac{g_1(T,\mu)}{h_2(T,\mu)}\right]$, for $\frac{\mu}{T} \ll 1$:

$$\frac{g_1(T,\mu)}{h_1(T,\mu)} \approx \left[\frac{1}{2\pi^2T^2}\right]^{\frac{2}{3}}\left(1 - \frac{1}{3\pi^2}\left(\frac{\mu}{T}\right)^2 + \frac{1}{18\pi^4}\left(\frac{\mu}{T}\right)^4 - \frac{11}{324\pi^6}\left(\frac{\mu}{T}\right)^6 + \mathcal{O}\left[\left(\frac{\mu}{T}\right)^8\right]\right) \tag{3.2.15}$$

Having obtained the expression for the falling string stopping distance, let us consider the instantaneous rate of energy loss for the single charge shooting string. The full expression is highly non-trivial so let us focus on the small $\frac{\mu}{T}$ expansion. It is given by:

$$\begin{aligned} \frac{1}{\sqrt{\lambda}}\frac{dE}{dx} &\approx -\frac{\pi T^2}{2}(r_* + \pi Tx)^2 - \frac{T^2}{6\pi}\left[3\pi Tx(r_* + \pi Tx) + 1\right]\left(\frac{\mu}{T}\right)^2 \\ &+ \frac{T^2}{72\pi^3}\left[\frac{3\left(3r_*^2 - 6\pi^2T^2x^2 + 4\right)(r_* + \pi Tx)^2 - 4}{(r_* + \pi Tx)^2}\right]\left(\frac{\mu}{T}\right)^4 + \mathcal{O}\left[\left(\frac{\mu}{T}\right)^6\right] \end{aligned}$$

(3.2.16)

The correction terms have temperature dependence of the order of T^4 for large x. This indicates that the uncertainties in the temperature could be further exacerbated by the correction terms.

3.2.2 Two Charge Black Hole

Let us now consider the two charge black hole by setting $q_1 = q_2 = qL^2$ and $q_3 = 0$. the non-zero charges q_1 and q_2 are set to the same value, following the conventions of [SSPH09], [PS13] and [FPS11]. It is thus possible to compare results with these studies. This particular choice depends on a single parameter so let us define the gauge field through the following field re-definitions.

$$A'^{1}_{\mu} = \frac{1}{\sqrt{2}}\left(A^{1}_{\mu} + A^{2}_{\mu}\right)$$

$$A'^{2}_{\mu} = \frac{1}{\sqrt{2}}\left(A^{2}_{\mu} - A^{1}_{\mu}\right)$$

$$A'^{3}_{\mu} = A^{3}_{\mu} \tag{3.2.17}$$

This re-definition allows one to discard two gauge fields, because there is only one independent parameter q. This particular parameter choice picks a preferred direction in the $U(1)^3$ gauge group. In this case, it is clear that both A'^{2}_{μ} and A'^{3}_{μ} will vanish, leaving A'^{1}_{μ} as the only non-zero gauge field. The factor of $\frac{1}{\sqrt{2}}$ is required to leave a conventional normalisation in the action. So the chemical potential considered will be that associated to the asymptotic value of A'^{1}_{μ}.

The stopping distance is given by a simple expression.

$$\Delta x_{stopping} = g_2(T,\mu)\frac{\Gamma\left[\frac{1}{4}\right]^{\frac{8}{3}}}{2^{\frac{5}{3}}\pi^{\frac{2}{3}}\lambda^{\frac{1}{6}}}E^{\frac{1}{3}} \tag{3.2.18}$$

where

$$g_2(T,\mu) = \frac{1}{(\mu^2+2\pi^2T^2)^{\frac{2}{3}}} \tag{3.2.19}$$

One can expand for small $\frac{\mu}{T}$:

$$g_2(T,\mu) \approx \left[\frac{1}{2\pi^2T^2}\right]^{\frac{2}{3}}\left(1-\frac{1}{3\pi^2}\left(\frac{\mu}{T}\right)^2+\frac{5}{36\pi^4}\left(\frac{\mu}{T}\right)^4-\frac{5}{81\pi^6}\left(\frac{\mu}{T}\right)^6+\mathcal{O}\left[\left(\frac{\mu}{T}\right)^8\right]\right)$$

Now let us consider the instantaneous rate of energy loss for the shooting string. Again, we shall write the small $\frac{\mu}{T}$ expansion out explicitly, due to the non-trivial nature of the full expression.

$$\begin{aligned}\frac{1}{\sqrt{\lambda}}\frac{dE}{dx} &\approx -\frac{1}{2}\pi T^2(r_*+\pi Tx)^2-\frac{T^2}{6\pi}\left[3\pi Tx(r_*+\pi Tx)+1\right]\left(\frac{\mu}{T}\right)^2 \\ &- \frac{T^2}{72\pi^3}\left[\frac{9\pi^2T^2x^2\left(r_*+\pi Tx\right)^2-1}{(r_*+\pi Tx)^2}\right]\left(\frac{\mu}{T}\right)^4+\mathcal{O}\left[\left(\frac{\mu}{T}\right)^6\right]\end{aligned} \tag{3.2.20}$$

The first order correction term is the same as the one charge case, and thus the large temperature dependence is observed once more. This again could lead to an exacerbation of the temperature scaling effect, observed when using the parameters fitted to the RHIC data to predict LHC R_{AA}.

3.2.3 Three Charge Black Hole

Finally, let us consider the three charge case $q_1 = q_2 = q_3 = qL^2$. Once more, a field redefinition is performed in order to obtain a single independent chemical potential.

$$A'^1_\mu = \frac{1}{\sqrt{3}}\left(A^1_\mu + A^2_\mu + A^3_\mu\right)$$

$$A'^2_\mu = \frac{1}{\sqrt{2}}\left(A^2_\mu - A^3_\mu\right)$$

$$A'^3_\mu = \frac{1}{\sqrt{6}}\left(A^2_\mu + A^3_\mu - 2A^1_\mu\right) \tag{3.2.21}$$

Essentially, this is a basis change within the gauge field vector space. One can check that this new basis is orthonormal. The particular choice of gauge fields results in A'^2_μ and A'^3_μ vanishing. It is also important to note that the scalars $X^i = 1$. So the action reduces to the Einstein-Maxwell AdS_5 action, and the black hole solution is just the AdS_5 Reissner-Norstöm black hole. The chemical potential is now defined by the asymptotic value of A'^1_μ.

Again, the falling string stopping distance for the three charged black hole is highly non-trivial. The small $\frac{\mu}{T}$ expansion has a more trivial form given by:

$$\frac{\Delta x_{stopping}}{\Delta x\mid_{\mu=0}} = 1 - \frac{1}{3\pi^2}\left(\frac{\mu}{T}\right)^2 + \frac{1}{6\pi^4}\left(\frac{\mu}{T}\right)^4 - \frac{31}{324\pi^6}\left(\frac{\mu}{T}\right)^6 + \mathcal{O}\left[\left(\frac{\mu}{T}\right)^8\right] \tag{3.2.22}$$

Now, let us consider the instantaneous rate of energy loss for the shooting string. The small $\frac{\mu}{T}$ expansion is given by:

$$\frac{1}{\sqrt{\lambda}}\frac{dE}{dx} \approx -\frac{1}{2}\pi T^2(r_* + \pi T x)^2 - \frac{T^2\left(3\pi T x(r_* + \pi T x) + 1\right)}{6\pi}\left(\frac{\mu}{T}\right)^2$$

$$- \frac{T^2\left(3r_*^2+6\pi^2T^2x^2-4\right)}{72\pi^3}\left(\frac{\mu}{T}\right)^4+\mathcal{O}\left[\left(\frac{\mu}{T}\right)^6\right] \tag{3.2.23}$$

Again, the first order correction matches both the single and doubly charged black hole solutions, and the temperature scaling problem seems independent of the direction in the $U(1)^3$ gauge field space.

3.2.4 Analysis of the light probe energy loss in the STU black hole background

In Sub. 3.2, the light probe energy loss for probes travelling in a QGP with non-zero chemical potential dual to the STU black hole was computed. Both falling string stopping distances and shooting string rates of energy loss were considered.

The most obvious point of note is that the stopping distance is reduced by the introduction of the chemical potential; in fact increasing the chemical potential leads to a smaller and smaller stopping distance. This can be seen explicitly in all the small $\frac{\mu}{T}$ expansions in Eq. (3.2.15), Eq. (3.2.20) and Eq. (3.2.22) and also in Fig. 3.1.

In this plot, the ratio of stopping distance with chemical potenital μ vs. zero chemical potential is plotted against the dimensionless parameter $\hat{\mu}=\frac{\mu}{T}$. It is important to note that using $\hat{\mu}$ removes temperature dependence from the ratio R. This occurs for all three cases. It is also important to note that the way the energy factorises in Eq. (3.2.13), Eq. (3.2.18 and Eq. (3.2.22) means that R is also independent of energy.

This effect can be observed for all three cases considered. It is fairly non-trivial and expected from a physical stand point. As noted in [CKY14], the increase in chemical potential leads to an increase in entropy and hence a larger number of states. Thus, the probe is interacting with a more dense plasma.

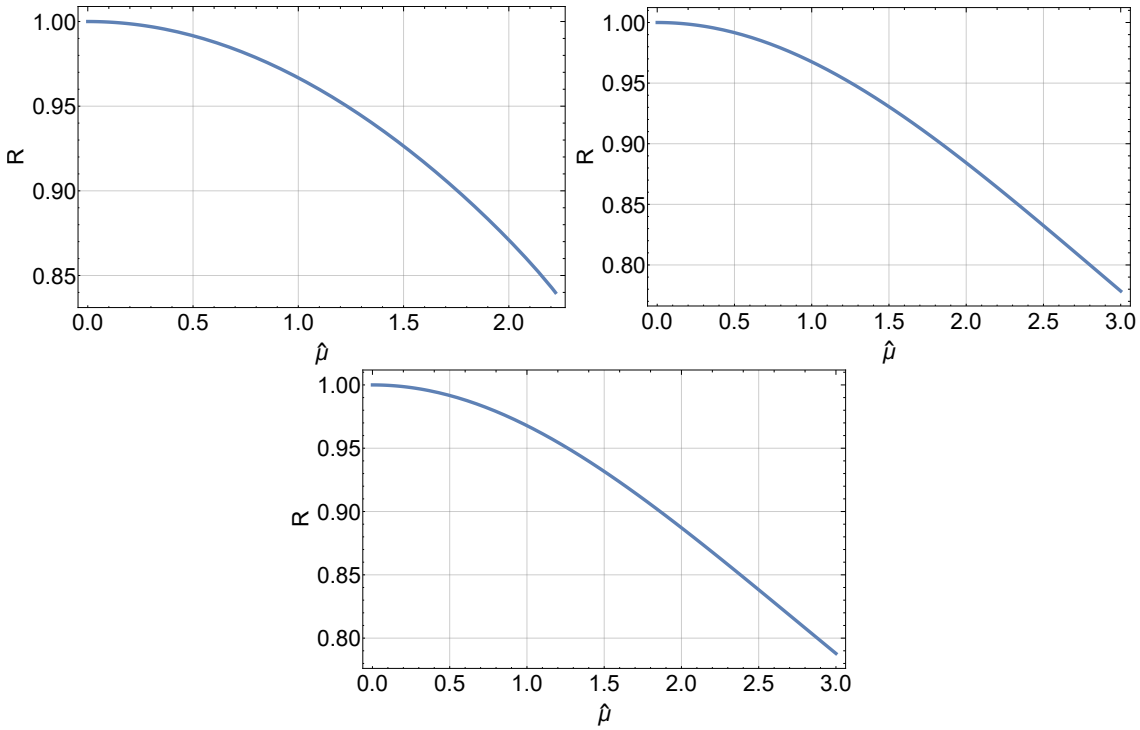

Figure 3.1: This shows the plot of $R = \frac{x(\hat{\mu})}{x(\hat{\mu}=0)}$ vs $\hat{\mu}$. The top left plot is for the single charged case, the top right plot is for the double charged case and the bottom plot is for the triple charged case.

Three separate plots have been shown in Fig. 3.1, because the differences between the three different charge cases are so small and it is hard to distinguish between the curves. This is seen more explicitly when considering the small $\hat{\mu}$ expansion for $\hat{q}$, shown later. There is one significant difference for the single charge case, where a cut off appears as $\hat{\mu}$ is increased to $\hat{\mu} = \frac{\pi}{\sqrt{2}}$. One can see this explicitly from Eq. (3.2.13), where the stopping distance gains a non-zero imaginary part for $\hat{\mu} > \frac{\pi}{\sqrt{2}}$. This is seen explicitly in Fig. 3.1.

This behaviour deviates from the computations performed for the drag force of heavy quarks performed in [PS13]. The three difference cases result in three different behaviours. However, the plots obtained in this paper are based on varying the charge parameter q, rather than the chemical potential directly. The non-trivial relationship between q and μ could result in the similar features seen in the light

probe stopping distance shown in Fig. 3.1.

Having obtained small chemical potential expressions for the stopping distance, let us use these to find how the jet quenching parameter $\hat{q}$ is effected. The method to use the jet quenching parameter is that used for the Sakai-Sugimoto model in Chapter 2.7. The first order corrections for the low density plasmas are considered for the following expressions:

$$\begin{aligned}
\hat{q} &= \frac{8N_c\Delta E}{\alpha_S(N_c^2-1)\left(\Delta x\right)^2} \\
\Rightarrow \hat{q}_1 &= \frac{128N_c}{9\alpha_S\left(N_c^2-1\right)}\left(\frac{4\lambda ET^8}{\Gamma\left[\frac{1}{4}\right]^{16}}\right)^{\frac{1}{3}}\left[9\pi^4+6\pi^2\hat{\mu}^2+2\hat{\mu}^4\right] \\
\hat{q}_2 &= \frac{128N_c}{9\alpha_S\left(N_c^2-1\right)}\left(\frac{4\lambda ET^8}{\Gamma\left[\frac{1}{4}\right]^{16}}\right)^{\frac{1}{3}}\left[9\pi^4+6\pi^2\hat{\mu}^2+\frac{1}{2}\hat{\mu}^4\right] \\
\hat{q}_3 &= \frac{128N_c}{9\alpha_S\left(N_c^2-1\right)}\left(\frac{4\lambda ET^8}{\Gamma\left[\frac{1}{4}\right]^{16}}\right)^{\frac{1}{3}}\left[9\pi^4+6\pi^2\hat{\mu}^2+\frac{1}{18\pi^2}\hat{\mu}^6\right] \qquad (3.2.24)
\end{aligned}$$

As noted in Sec. 2.7 , the non-trivial energy dependence has quite a different effect for the light flavoured quark vs. the virtual gluon described in [GGPR08]. The $T^{\frac{8}{3}}$ temperature dependence observed in 2.7 is apparent here as expected. This leads to the large discrepancy with the observed transport coefficient.

The first thing to notice from Eq. (3.2.24) is the fact that the 1st order corrections for all three cases is the same. This was mentioned in the context of the stopping distance. As expected, the chemical potential increases the jet quenching parameter. Since the corrections are so similar for small $\hat{\mu} = \frac{\mu}{T}$, the three charge case shall be considered for the next discussion.

Let us compare the falling string light probe $\hat{q}_f$ with the light-like Wilson loop method used to compute $\hat{q}_{LRW}$. In order to see the effect of the chemical potential on the parameter, let us define the following ratio:

$$R_\mu = \frac{\hat{q}(\hat{\mu})}{\hat{q}(\hat{\mu}=0)} \tag{3.2.25}$$

where $\hat{\mu} = \frac{\mu}{T}$. The Wilson loop calculation is performed using the methods described in [FPS11] and [PS13]. Fig. 3.2 shows the plot comparing R_q for both methods. One can see that the effect of the chemical potential on $\hat{q}$ is more pronounced for the falling string method. It is also important to note that this difference increases with chemical potential; the larger $\hat{\mu}$ is, the larger the difference between R_q^{LRW} and R_q^f is.

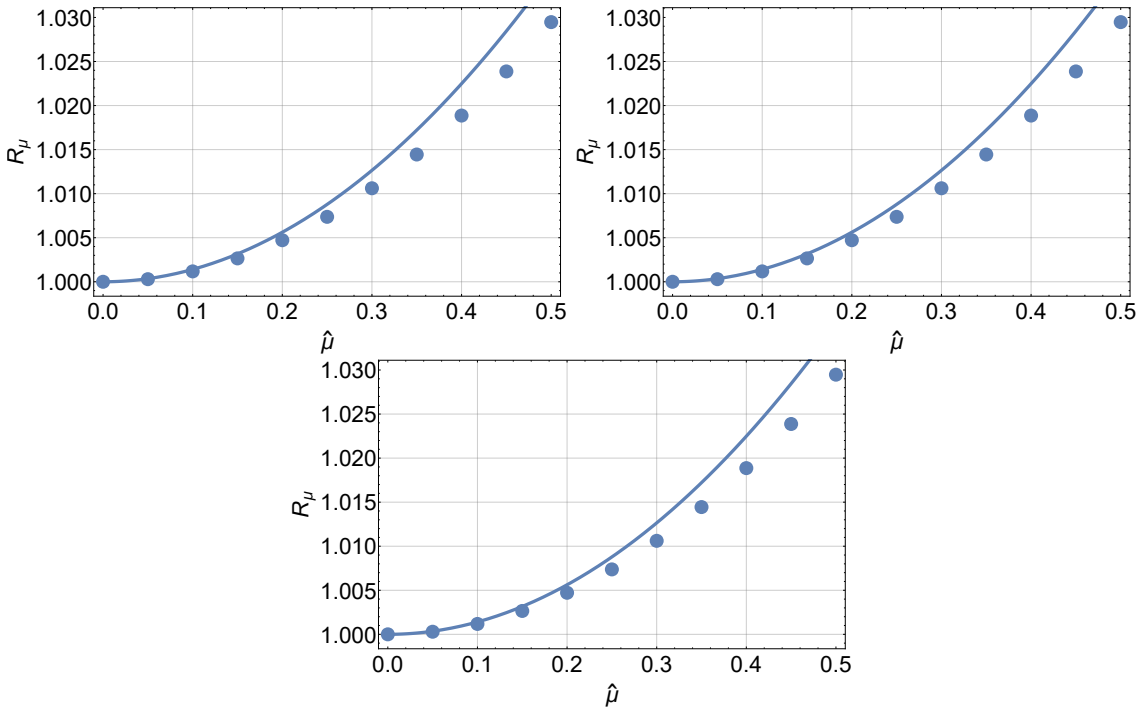

Figure 3.2: These are plots showing the ratio R_μ vs. $\hat{\mu}$ for the light-like Wilson loop and the falling string. The dots give the light-like Wilson loop computation and the lines give the falling string computation. The top left is for $T = 280MeV$, the top right is for $T = 370MeV$ and the bottom is for $T = 470MeV$.

In this analysis, the choice of $\alpha_S = 0.3$, $N_c = 3$ and $E = 10GeV$ has been used, following the analysis in Sec. 2.7.

It is also useful to consider $\hat{q}$ for fixed $\kappa = \frac{8\pi^2\rho^2}{s^2}$ for the single charged case, where ρ is the charge density and s is the entropy density. In [LM06], the authors note that a strange maximum for R_κ is found as κ is increased. It is interesting to see whether this feature, observed using the light-like Wilson loop method, is also seen using the falling string method.

In Fig. 3.3, it is shown that a similar maximum is also seen for the falling string method. It is important to note that system is thermodynamically unstable for $\kappa > 2$, as can be shown by the Hessian matrix positive definiteness condition (see Appendix B). Thus, this is the domain chosen for the plots.

3.2.5 Higher Derivative Corrections

In Sec. 3.2, the light probe energy loss in the STU black hole background has been studied. The full three charge solution was considered, and three specific cases were analysed. In [FGG14], the authors highlight the importance of higher derivative corrections, in the context of the jet nuclear modification factor. The Gauss-Bonnet term was required in order to match the modelled jet nuclear modification factor to the data, when using the finite end point momentum shooting strings.

As mentioned in Sec. 2.7, the jet quenching parameter for light-like probes over predict the parameter, when computed using RHIC and LHC data. This is corrected somewhat, by including higher derivative terms [ZHR13]. It is thus relevant to analyse the impact of the higher derivative terms.

Higher derivative corrections to supergravity are of much interest in the context

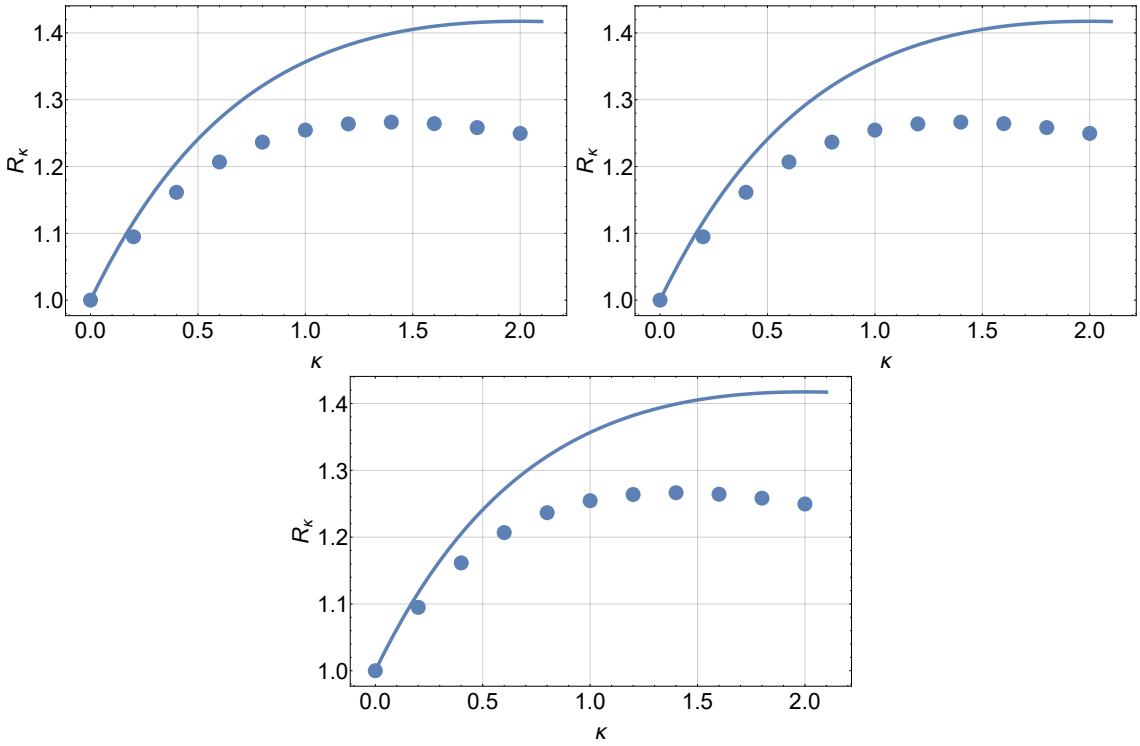

Figure 3.3: These are plots showing the ratio R_κ vs. $\hat{\mu}$ for the light-like Wilson loop and the falling string for the single charged fixed κ case. The dots give the light-like Wilson loop computation and the lines give the falling string computation. The top left is for $T = 280MeV$, the top right is for $T = 370MeV$ and the bottom is for $T = 470MeV$.

of holography, because the corrections give an insight into finite λ corrections to the dual theory. This is simple to see from the holographic parameter relations $\frac{1}{\sqrt{\lambda}} = \frac{\alpha'}{L^2}$.

Let us look at the higher derivative corrections to the R-charged black hole solution Eq. (3.2.1) obtained in [CHLS09] - see Appendix B. The solution to this system is given by[2]:

$$ds^2 = -H^{-2} f dt^2 + H(f^{-1}dr^2 + r^2 d\Omega_{3,k}) \tag{3.2.26}$$

where

[2]The flat $k = 0$ is the case of interest.

$$
\begin{aligned}
H &= H_0 - \frac{\lambda_D}{24}\left[\frac{qm}{3r^6 H_0^2}\right]\alpha' \\
f &= f_0 + \frac{\lambda_D}{24}\left[\frac{m^2}{4r^6 H_0} - \frac{8qm}{3r^2 L^2}\right]\alpha' \\
A &= A_0 + \frac{\lambda_D}{24}\frac{\sqrt{3qm}}{2r^8 H_0^4}\left[2mr^2 - mr^2 H_0\right]\alpha'
\end{aligned}
\tag{3.2.27}
$$

H_0, A_0 and f_0 are the uncorrected zeroth order solutions given by Eq. (3.2.1). The parameter λ_D is a dimensionless parameter that characterises the higher derivative terms in the action. It is important to note that the correction is for the three charge case described in Sub. 3.2.5.

It is of interest to re-parameterise this solution in terms of the chemical potential μ and the horizon radius r_H. The parameters m and μ can be written as:

$$
m = \frac{(q + r_H^2)^3}{L^2 r_H^2}\left[1 + \frac{\lambda_D}{288 L^4 r_H^6}\left(3q^2 - 26qr_H^2 + 3r_H^4\right)\alpha'\right] \tag{3.2.28}
$$

$$
\mu = \frac{\sqrt{q(q + r_H^2)}}{L r_H}\left[\sqrt{3} + \frac{\lambda_D}{192\sqrt{3} L^2 r_H^4}\left(3q^2 - 14qr_H^2 - 9r_H^4\right)\alpha'\right] \tag{3.2.29}
$$

Let us start by computing the stopping distance for the falling string. Following the method in Chapter 2, the null geodesics in the background given by Eq. (3.2.26) need to be found. Since the metric has both time and space translation symmetries, let us consider the associated conserved quantities:

$$
E_{geo} = \frac{1}{L^2(q + r^2)^2}\left[\left[\left(q + r^2\right)^3 - L^2 m r^2\right]\right.
$$

$$+ \quad \lambda_D \frac{L^2 m^2 \left(3q^2 - 2qr^2 + 3r^4\right) - 24qm\left(q+r^2\right)^3}{288\left(q+r^2\right)^3}\alpha' \Bigg] \frac{dt}{d\lambda}$$

$$P_{geo} = \frac{1}{L^2}\left[\left(q+r^2\right) - \lambda_D \frac{mq}{72\left(q+r^2\right)^2}\alpha'\right]\frac{dx}{d\lambda} \tag{3.2.30}$$

Using these expressions and the null constraint, one can obtain the following first order equation:

$$\frac{dx}{dr} = -\frac{L^2 P_{geo} r}{\sqrt{E_{geo}^2\left(q+r^2\right)^3 - P_{geo}^2\left[\left(q+r^2\right)^3 - L^2 m r^2\right]}}$$

$$- \quad \lambda_D \frac{L^2 m P_{geo} r\left[4q\left(3E_{geo}^2 - 8P_{geo}^2\right)\left(q+r^2\right) + 3L^2 m P_{geo}^2\right]}{576\left(q+r^2\right)\left[\left(E_{geo}^2\left(q+r^2\right)^3 - P_{geo}^2\left(\left(q+r^2\right)^3 - L^2 m r^2\right)\right)\right]^{\frac{3}{2}}}\alpha' \tag{3.2.31}$$

Now, let us apply the initial conditions of interest. At $t=0$, let us impose $\vec{x}=0$, $r=r_0$ and $\frac{dt}{d\lambda}=\sqrt{\alpha'}$. As explained in Chapter 2, the initial radial speed is turned off, and the initial speed in the x- direction is specified by the null condition. Given these initial conditions, one can eliminate E_{geo} and P_{geo} from Eq. (3.2.31).

Using these expressions, Eq. (3.2.31) can be integrated in order to find the quark stopping distance. This is done in the near boundary limit $\frac{r_H}{r_0} \ll 1$, by using the expansion shown in Appendix C.

$$\Delta x_{stopping} = \frac{r_0}{\left(q+r_H^2\right)^{\frac{3}{2}}}\int_1^0 dr \frac{1}{\sqrt{1-r^4}}\left[-L^2 r_H + \lambda_D \frac{\left(3q^2 - 26qr_H^2 + 3r_H^4\right)}{576 r_H^3}\alpha'\right]$$

$$= \frac{r_0 \Gamma\left[\frac{1}{4}\right]^2}{4\sqrt{2\pi}\left(q+r_H^2\right)^{\frac{3}{2}}}\left[L^2 r_H - \frac{\lambda_D}{576 r_H^3}\left(3q^2 - 26qr_H^2 + 3r_H^4\right)\alpha'\right]$$

(3.2.32)

Now let us consider the energy of the system. Using the end point equation of motion and the geodesic equations of motion, one can obtain an expression for $\frac{dE}{dr}$. Integrating this to leading order in $\frac{r_H}{r_0} \ll 1$, the initial energy of the probe is found to be:

$$\begin{aligned} E &= \frac{r_0^3}{2\pi\alpha' \left(q + r_H^2\right)^{\frac{3}{2}}} \int_0^1 dr \frac{r^2}{\sqrt{1-r^4}} \left[r_H - \lambda_D \frac{(3q^2 - 26qr_H^2 + 3r_H^4)}{576L^2 r_H^3} \alpha' \right] \\ &= \frac{r_0^3}{\Gamma\left[\frac{1}{4}\right]^2 \alpha' \left(q + r_H^2\right)^{\frac{3}{2}}} \sqrt{\frac{\pi}{2}} \left[r_H - \lambda_D \frac{(3q^2 - 26qr_H^2 + 3r_H^4)}{576L^2 r_H^3} \alpha' \right] \end{aligned} \tag{3.2.33}$$

One can now eliminate r_0 and obtain an expression for the stopping distance as a function of the energy. It is also important to consider the temperature of the black hole in order to eliminate dependence on r_H.

$$T = \frac{\sqrt{q + r_H^2}}{2\pi L^2 r_H^2} \left[\left(2r_H^2 - q \right) + \lambda_D \frac{(14q^2 r_H^2 + 29qr_H^4 - 6r_H^6 - 3q^3)}{288L^2 r_H^4} \alpha' \right] \tag{3.2.34}$$

The final expression for $\Delta x_{stopping}$ in terms of E, T and μ is given by the following:

$$\Delta x_{stopping} = \Gamma\left[\frac{1}{4}\right]^{\frac{8}{3}} \frac{E^{\frac{1}{3}}}{2^{\frac{7}{3}} \pi^2 T^{\frac{4}{3}} \lambda^{\frac{1}{6}}} \left[h_0(T,\mu) + \frac{\lambda_D}{\sqrt{\lambda}} h_1(T,\mu) \right] \tag{3.2.35}$$

The functions h_0 and h_1 are non-trivial, but can be expanded for small chemical potential $\frac{\mu}{T} \ll 1$.

$$h_0^L(T,\mu) = 1 - \frac{1}{3\pi^2}\left(\frac{\mu}{T}\right)^2 + \frac{1}{6\pi^4}\left(\frac{\mu}{T}\right)^4 - \frac{31}{324\pi^6}\left(\frac{\mu}{T}\right)^6 + \mathcal{O}\left[\left(\frac{\mu}{T}\right)^8\right] \tag{3.2.36}$$

$$h_1^L(T,\mu) = -\frac{5}{288}+\frac{7}{216\pi^2}\left(\frac{\mu}{T}\right)^2-\frac{49}{1728\pi^4}\left(\frac{\mu}{T}\right)^4+\frac{1075}{46656\pi^6}\left(\frac{\mu}{T}\right)^6+\mathcal{O}\left[\left(\frac{\mu}{T}\right)^8\right] \tag{3.2.37}$$

The h_0^L function matches Eq. (3.2.22) as expected.

Having obtained expressions for the stopping distance in the higher derivative theory, let us consider the shooting string energy loss. In order to compute the string trajectory, one can simplify the complex integrals, as explained in Appendix C. The shooting string trajectory is given by:

$$x(r)=\frac{r-r_H r_*}{(q+r_H^2)^{\frac{3}{2}}}\left[L^2 r_H-\frac{\lambda_D}{576 r_H^3}\left(3q^2-26qr_H^2+3r_H^4\right)\alpha'\right] \tag{3.2.38}$$

Using the end point equation of motion and this trajectory, the final expression for the rate of energy loss for the shooting string is written as:

$$\frac{1}{\sqrt{\lambda}}\frac{dE}{dx}=g_0(x)+\frac{\lambda_D}{\sqrt{\lambda}}g_1(x) \tag{3.2.39}$$

Let us expand $g_0(x)$ and $g_1(x)$ for the low density $\frac{\mu}{T}\ll 1$ plasma:

$$\begin{aligned} g_0^L(x) &= -\frac{1}{2}\pi\sqrt{\lambda}T^2(r_*+\pi Tx)^2-\frac{\sqrt{\lambda}T^2(3\pi Tx(r_*+\pi Tx)+1)}{6\pi}\left(\frac{\mu}{T}\right)^2 \\ &- \frac{\sqrt{\lambda}T^2\left(3r_*^2+6\pi^2T^2x^2-4\right)}{72\pi^3}\left(\frac{\mu}{T}\right)^4+\mathcal{O}\left[\left(\frac{\mu}{T}\right)^6\right] \end{aligned} \tag{3.2.40}$$

$$g_1^L(x) = -\frac{\pi T^2(r_*+\pi Tx)(2r_*+5\pi Tx)}{192}$$

$$+ \quad T^2 \frac{(52r_*^2 + 127\pi r_* Tx + 48\pi^2 T^2 x^2 - 18)\,(r_* + \pi Tx)^4 + 8}{3456\pi (r_* + \pi Tx)^4} \left(\frac{\mu}{T}\right)^2$$

$$+ \quad \mathcal{O}\left[\left(\frac{\mu}{T}\right)^4\right] \tag{3.2.41}$$

One can see that $g_0^L(x)$ correctly matches the uncorrected solution of the three charged black hole as expected Eq. (3.2.23).

In order to see the impact of the higher derivative term, let us plot the correction to the stopping distance, as a fraction of the $\mu = 0$ case. This is given by:

$$\begin{aligned} \delta_{HD} &= \frac{h_1(T,\mu)}{h_1(T,0)} \\ &= \frac{h_1(\hat{\mu})}{h_1(0)} \end{aligned} \tag{3.2.42}$$

It is important to note that the scaled energy $\bar{E} = \frac{E}{\sqrt{\lambda}}$ has been used in this expression. Since the energy dependence is an overall factor in Eq. (3.2.35), the ratio has no energy dependence. It is also important to note that, using the dimensionless chemical potential $\hat{\mu} = \frac{\mu}{T}$, removes the temperature dependence in comparison to the case when μ is used.

Fig. 3.4 shows the plots of δ_{HD} vs. $\hat{\mu}$. The plot shows that as the chemical potential is increased, the effect of the correction decreases. In other words, the higher derivative correction reduces the stopping distance by a smaller amount for larger chemical potentials. This can be seen clearly in the low density expansions shown in Eq. (3.2.37). The first order term in the low density expansion of $h_1(T,\mu)$ is the opposite

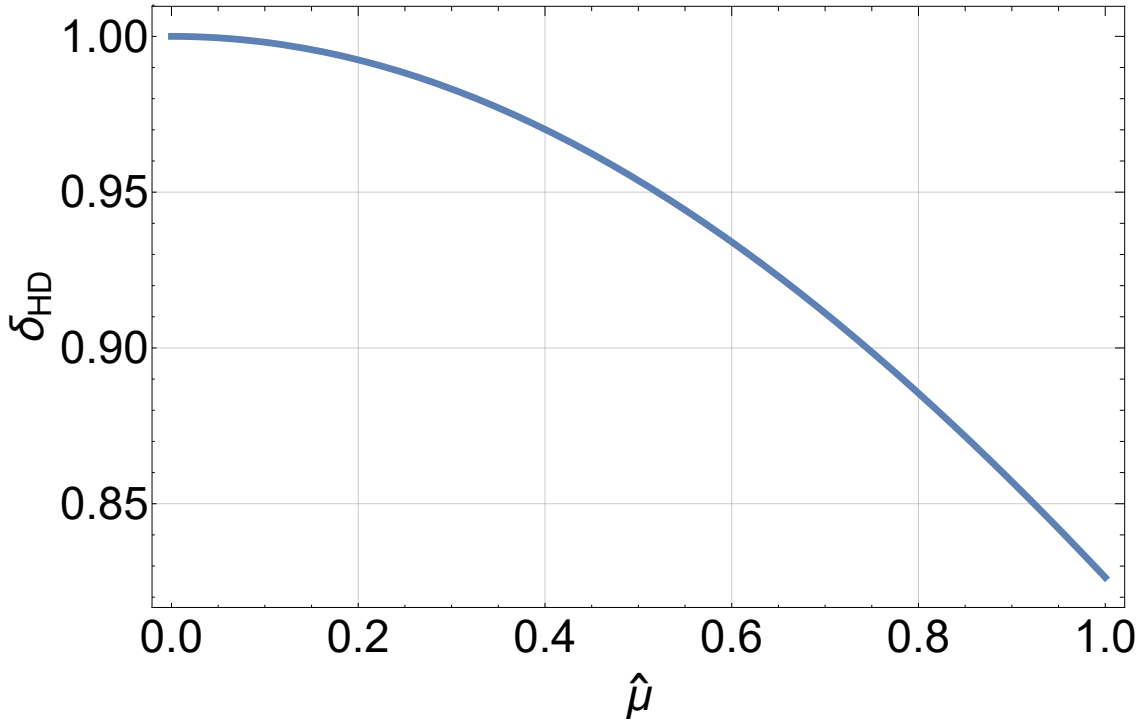

Figure 3.4: This is a plot showing the ratio δ_{HD} vs. $\hat{\mu}$ for the R-charged higher derivative case. It is important to note that plotting against $\hat{\mu}$ removes all temperature dependence and thus only one curve is plotted.

sign of the $\mu = 0$ term.

Higher derivative correction to the Jet Quenching parameter for the R-charged case

Having obtained the higher derivative correction to the falling string stopping distance in Sub. 3.2.5, let us use this results to find the jet quenching parameter $\hat{q}$. Using Eq. (2.7.1) in Sec. 2.7 and Eq. (3.2.35), the jet quenching parameter is computed.

$$\hat{q} = \frac{2^{\frac{2}{3}} N_c \left[T^8 \lambda E\right]^{\frac{1}{3}}}{(N_c^2-1)\alpha_S \Gamma\left[\frac{1}{4}\right]^{\frac{16}{3}}} \left[K_0(T,\mu) + \frac{\lambda_D}{\sqrt{\lambda}} K_1(T,\mu)\right] \tag{3.2.43}$$

The forms of K_0 and K_1 are non-trivial, but can be expanded for small $\frac{\mu}{T} \ll 1$.

$$K_0(T,\mu) = 128\pi^4 + \frac{256\pi^2}{3}\left[\frac{\mu}{T}\right]^2 + \frac{64}{81\pi^2}\left[\frac{\mu}{T}\right]^6 + ...$$

$$K_1(T,\mu) = \frac{40\pi^4}{9} - \frac{104\pi^2}{27}\left[\frac{\mu}{T}\right]^2 - \frac{8}{27}\left[\frac{\mu}{T}\right]^4 - \frac{46}{729\pi^2}\left[\frac{\mu}{T}\right]^6 + ... \quad (3.2.44)$$

The first thing to notice is the the $(\mu = 0, \lambda_D = 0)$ case reduces to the AdS_5 black hole expression found in Eq. (2.7.2). In Fig. 3.5, the jet correction parameter for $\hat{\mu} = 0$ has been plotted against the higher derivative parameter $|\lambda_D|$. In this case, λ_D is treated as free parameter, in a similar manner to the Gauss-Bonnet parameter in [FGG14] and the c_1 parameter in [PS13].

It is important to note that a negative λ_D has been chosen, because we want to reduce $\hat{q}$ with the inclusion of this parameter. Eq. (3.2.44) shows this explicitly. One can see from this figure the decrease in $\hat{q}$ with λ_D and the increase in $\hat{q}$ with temperature. The choices $\alpha_S = 0.31$ and $N_c = 3$ are made and the fixed energy density temperature has been used, following the method used in Sec. 2.7.

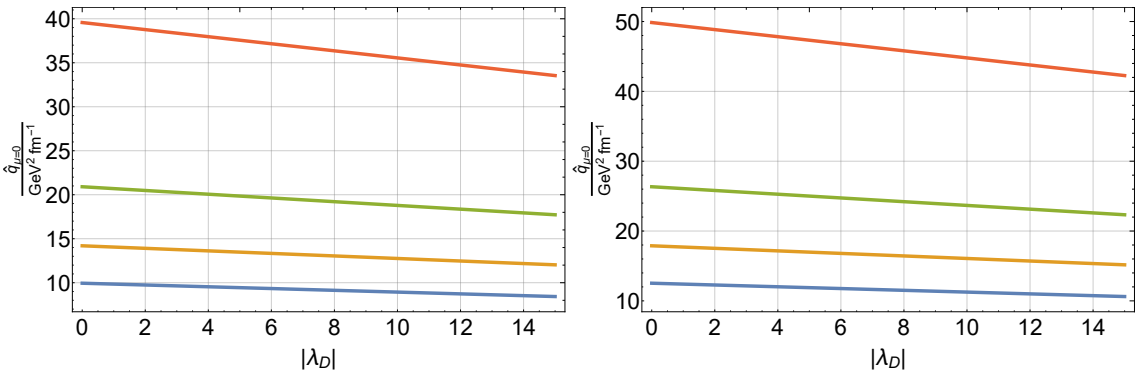

Figure 3.5: This is a plot showing $\hat{q}$ vs $|\lambda_D|$ for the $\hat{\mu} = 0$ case. The left plot it for $E = 10GeV$ and right plot is for $E = 20GeV$. The colour of the lines if given by $T = 280MeV$, $T = 320MeV$, $T = 370MeV$ and $T = 470MeV$. It is important to note that λ_D is negative so the absolute value has been plotted. The choices $\alpha_S = 0.31$ and $N_c = 3$ has been made.

In Sec. 2.7, a few phenomenological models were compared to the falling string $\hat{q}$ for the AdS_5 black hole and Sakai-Sugimoto models. It was found that the falling string over predicts $\hat{q}$ for the $E = 10GeV$ and $T = 370MeV/470MeV$ LHC cases computed in [Bur+14] ($\hat{q} = 1.2/1.9\ GeV^2\text{fm}^{-1}$), but fell into the range found in [Ada+08] for the $E = 20GeV$ and $T = 280MeV$ ($7\ GeV^2\text{fm}^{-1} < \hat{q} < 28GeV^2\ \text{fm}^{-1}$) RHIC case.

Let us perform a naive analysis to see if is possible to choose λ_D in order to reduce $\hat{q}$ for the LHC cases, without modifying $\hat{q}$ outside of the range $7\ GeV^2\text{fm}^{-1} < \hat{q} < 28GeV^2\ \text{fm}^{-1}$ in the RHIC case. In order to do this, one solves for λ_D, by setting $\hat{q} = 7\ GeV^2\text{fm}^{-1}$ for the $E = 20GeV$ and $T = 280MeV$ RHIC case. The lower bound is chosen so it maximises the reduction in $\hat{q}$ that is obtained when considering the LHC $E = 10GeV$ cases. The value of $\lambda_D = -43.44$ is obtained. It is important to note that $\sqrt{\lambda} = 4\pi N_c \alpha_S \sim 3.42$. In order for the higher derivative expansion to be valid, $|\lambda_D| < \sqrt{\lambda}$ must be true, because the first order correction to $\hat{q}$ goes as $\frac{\lambda_D}{\sqrt{\lambda}}$ - see Eq. (3.2.43). Clearly, this is not the case for $\lambda_D = -43.44$.

This means the correction to $\hat{q}$, obtained using a valid λ_D, does not reduce $\hat{q}$ substantially to match the LHC predictions in [Bur+14]. To get a rough idea of this, one can choose a valid λ_D i.e. $|\lambda_D| < \sqrt{\lambda} \sim 3.42$, and see how this hardly affects $\hat{q}$ for all three cases. Since $\sqrt{\lambda} \sim 3.42$, let us use an example of $\lambda_D = -3$.

In Tab. 3.1, the values of $\hat{q}$ are shown for the LHC and RHIC cases. One can see that the difference to the $\lambda_D = 0$ is small, and hence $\hat{q}$ is still much larger than the values of $\hat{q}(E = 10GeV, T = 370/480MeV) = 1.2/1.9\ GeV^2\text{fm}^{-1}$, obtained in the phenomenological model [Bur+14]. This means that the higher derivative correction cannot account for the over prediction of $\hat{q}$ at the LHC. The correction in the $E = 20GeV$, $T = 280MeV$ RHIC case is also small, and so still lies in the $7\ GeV^2\text{fm}^{-1} < \hat{q} < 28GeV^2\ \text{fm}^{-1}$ range.

$\frac{E}{GeV}$	$\frac{T}{GeV}$	$\left[\frac{\hat{q}}{GeV^2\text{fm}^{-1}}\right]_{\lambda_D=0}$	$\left[\frac{\hat{q}}{GeV^2\text{fm}^{-1}}\right]_{\lambda_D=-3}$
10	0.370	20.91	20.27
	0.470	39.57	38.37
20	0.280	12.53	12.15

Table 3.1: This table shows the absolute values for the falling string jet quenching parameter, for both $\lambda_D = 0$ and $\lambda_D = -3$. Both the $E = 10GeV$ and $E = 20GeV$ cases are chosen. The parameter is measured in units of $GeV^2\text{fm}^{-1}$.

Let us now turn the chemical potential on and see how the correction is affected by the chemical potential. Fig. 3.6 shows the plot of $\frac{\hat{q}}{\hat{q}_{\mu=0}}$ for both the cases with and without the higher derivative corrections. One can see that the effect of the chemical potential is increased by the higher derivative corrections.

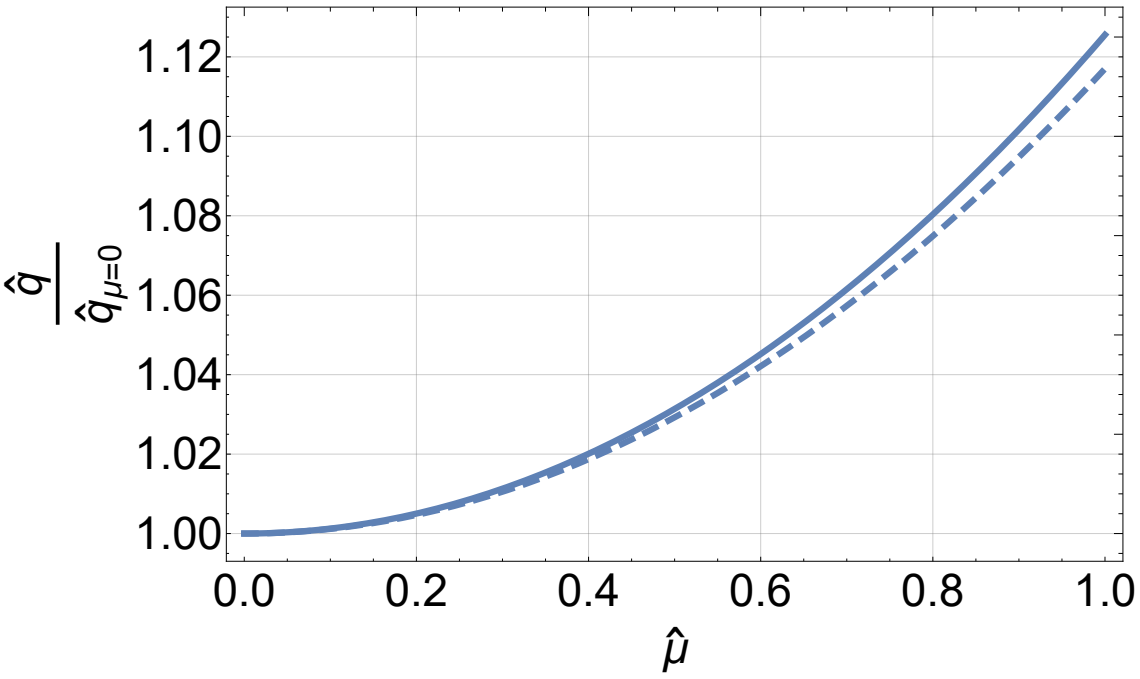

Figure 3.6: This is a plot showing $\frac{\hat{q}}{\hat{q}_{\mu=0}}$ vs $\hat{\mu}$. This fraction is both temperature and energy independent when plotted as a function of the dimensionless parameter $\hat{\mu} = \frac{\mu}{T}$. The choices $\alpha_S = 0.31$ and $N_c = 3$ have been made. The solid line includes higher derivative corrections ($\lambda_D = -3$) and the dashed line is for $\lambda_D = 0$.

3.3 Light Quark energy loss with flavour chemical potential

In Sec. 3.3, a chemical potential was introduced by considering particular black hole solutions; that is the black holes are charged under gauge fields living in the bulk geometry. These gauge fields are dual to R - symmetry currents for particular supersymmetric theories. For example, the gauge fields in the $\mathcal{N} = 2$ theory of Sec. 3.2 are obtained by compactifying over the S^5. The isometries of the S^5 are associated with the $SU(4)$ R-symmetry of the dual theory. QCD is of course non-supersymmetic, and thus does not contain R-symmetry. However, there are other global symmetries that exist in QCD, whose charges allow for non-zero chemical potentials. The global symmetries of particular consideration are the flavour and chiral symmetries of the quarks in QCD. In this section, let us consider the effect that the chemical potentials associated with these symmetries have on the light probe energy loss.

Flavour symmetry is associated to matter hypermultiplets that are introduced to the system via probe branes. Whilst QCD contains both left and right handed quarks, the explicit mass terms break chiral symmetry from $U(N_f)_L \times U(N_f)_R$ to $U(N_f)$. If the quarks are massless, the chiral symmetry exists at the level of the classical action, but undergoes spontaneous symmetry breaking. The $U(N_f)_L \times U(N_f)_R$ symmetry can be written as $SU(N_f)_L \times SU(N_f)_R \times U(1)_V \times U(1)_A$ by suitable basis choices. The non-Abelian part of the symmetry $SU(N_f)_L \times SU(N_f)_R$ breaks to the group $SU(N_f)_V$, through the development of a non-zero quark condensate $\langle \bar{\psi}\psi \rangle \neq 0$. It is important to note that this symmetry is restored at large enough temperatures. In other words, there exists a phase transition at large temperatures at which the spontaneous symmetry breaking no longer occurs, and this is known as the chiral restoration phase. One can understand this intuitively through the realisation that the quark masses are negligible relative to the large temperature $\frac{m}{T} \to 0$. It is this chiral restoration phase that will be the subject of interest in the following discussion.

The first system of consideration is the D_3/D_7 system. In this case, the background stack of N_c colour D_3 branes are probed by a stack of N_f flavour D_7 branes. The full probe brane embeddings are given in Appendix D. The $SO(6)$ R-symmetry of the $\mathcal{N} = 4$ Yang-Mills theory is broken to $SO(4)$ and $SO(2) \approx U(1)_R$ symmetries. These are apparent from the embedding form Eq. (D.1.1). For non-zero mass, the $U(1)_R$ symmetry is explicitly broken. The flavour symmetry is apparent as a gauge symmetry on the probe branes. In this case, both left and right handed fermions are added as part of the multiplet. The fluctuations of the trivial embeddings in this background give rise to a discrete spectrum of mesons.

Above the Hawking-Page phase transition there exist two possible solutions; the so called Minkowski phase and the black hole phase. The Minkowski solutions are embeddings where the probe branes end outside of the black hole. Once more, the fluctuations of the branes admit a discrete spectrum of mesons. However at large enough temperature, a phase transition occurs. The gravitational pull of the black hole is large enough to overcome the tension of the branes, and pull them to the horizon. The fluctuations no longer give a real spectrum of masses. Instead one obtains complex eigenvalues, and hence the modes are quasi-normal. These quasi-normal modes describe the so called melting of the mesons.

The second system of interest is the Sakai-Sugimoto model. In this case, N_f probe D_8 and $\bar{N}_f$ $\bar{D}_8$ branes are embedded in a background of N_c D_4 branes. The probe brane/anti-brane dynamics are once more encapsulated in the DBI action (see Appendix D for details on the brane embeddings). The branes/anti-branes connect in a U-shape in the τ - u plane of the black branes, representing the breaking of the $U(N_f)_L \times U(N_f)_R$ symmetry [SS05b]. One can see this explicitly by expanding the DBI actions for the probe branes/anti-branes, and writing the gauge fields as sums of radial modes. The resulting action contains massless modes representing

the Goldstone bosons of the broken symmetry and retains the $U(N_f)$ little group symmetry. These Goldstone bosons are massless pions π_0.

Above the Hawking-Page phase transition temperature, there are two distinct embedding phases once more. The Minkowski phase is similar to the zero temperature case, and the branes connect in the similar U shape outside the black hole. Chiral symmetry is spontaneously broken in this phase. The high temperature black hole phase is where the probe/anti-branes do not connect to form a U shape, and fall into the horizon of the black hole. This represents the chiral symmetry restoration phase. It is important to note that the phase transition exists when the electric field on the brane is turned on for fixed chemical potential i.e. the grand canonical ensemble[3].

Since light quarks are the subject of interest, let us focus on the high temperature black hole embeddings. In particular, the solutions considered will be the $\frac{m}{T} = 0$ case. The branes themselves have trivial profiles, but the gauge field on the branes are not. Branes with a single $U(1)$ gauge field are considered. For the D_7 branes, this is just the gauge field associated to a $U(1)$ subgroup of the $U(N_f)$ flavour symmetry. In the Sakai-Sugimoto case, the chiral restoration phase exhibits the $U(N_f)_L \times U(N_f)_R$ symmetry, and the $U(1)$ is just a subgroup of either $U(N_f)$ group.

In the R-charged case, the chemical potential was introduced via the bulk equations of motion. The non-zero bulk gauge fields couple to the metric, and hence affect the background metric solution. The string trajectory is therefore affected through change in the background geometry.

In the case of the flavour charge case, the probe brane gauge field does not af-

[3]The Minkowski phase does not exist for the canonical ensemble, where the number density is fixed. This is because the field lines have no where to end.

fect the bulk geometry so long as the large N_c, t'Hooft limit is taken[4]. Hence, the non-trivial effect on the string is not due to the background geometry, as this is unaffected by the probe brane gauge fields. Instead, the trajectory is affected by the direct coupling of the gauge field on the probe brane with the string end point. The finite end point momentum string action, as described by Eq. (2.2.1), is supplemented with the gauge field coupling term:

$$S_{int} = -\frac{1}{\alpha'}\int A_\mu(X)\frac{dX^\mu}{d\xi}d\xi \tag{3.3.1}$$

It is important to note that the gauge field has been defined with length dimension one. This choice is made to simplify the equations of motion, through the cancellation of α' factors. The interaction term adds the usual force term to the end point equation of motion.

$$\dot{p}_\mu - \Gamma^\lambda_{\mu\nu}\dot{X}^\nu p_\lambda + \frac{1}{\alpha'}F_{\mu\nu}\dot{X}^\nu = \mp\frac{1}{2\pi\alpha'}G_{\mu\nu}\dot{X}^\nu \tag{3.3.2}$$

Since the force term is independent of the einbein, the re-definition of η affects the end point equation of motion differently. In the case with no gauge field, the einbein re-definition Eq. (2.2.16) casts the equations of motion into the form of that of a null geodesic. This is not the case when the gauge field is introduced. After the transformation, the equation reduces to:

$$\dot{\tilde{p}}_\mu - \Gamma^\lambda_{\mu\nu}\dot{X}^\nu\tilde{p}_\lambda = -\frac{1}{\alpha'}\frac{\eta}{\tilde{\eta}}F_{\mu\nu}\dot{X}^\nu \tag{3.3.3}$$

One can see there is explicit dependence on the einbein here. If the gauge field is turned off, the transformation of the einbein allows us to define two conserved quant-

[4]At finite coupling and N_c, the probe limit fails and one must include the effect of back reaction.

ities. These are usually interpreted as momentum and energy of the null geodesic[5]. The two conserved quantities, in combination with the null constraint, allow the equations of motion to be reduced to first order equations that can be analytically solved. The explicit einbein dependence in the gauge field term of Eq. (3.3.3) means that there is only one conserved quantity. Thus, the transformation does not lead to a simple first order reduction, and analytic solutions are non-trivial.

Using Eq. (3.3.2), one can now compute the stopping distances and rate of instantaneous energy loss for the finite endpoint momentum strings coupled to the probe gauge fields. The dependence on the einbein means the appropriate conservation laws do not exist, and hence analytic approaches are non-trivial. A perturbative method was also attempted, in order to find first order flavour chemical potential corrections. The full analytic solution to the non-charged equations of motion are known - see Eq. (2.3.6). By perturbing by a linear term in the constant d (see Appendix D), one can linearise the 2nd order equations of motion. This was attempted and yet the equations were still analytically unsolvable for the perturbation.

Since the system is not solvable analytically, both the D_3/D_7 and Sakai-Sugimoto D_4/D_8 systems are numerically analysed in Subsections 3.3.2 and 3.3.3.

3.3.1 Boundary Conditions and Errors

In Subsection 3.3, it was concluded that the only way to solve the high temperature flavour chemical potential system is numerically. In order to do this, the appropriate boundary conditions must be chosen. To remain consistent with prior calculations, the zero radial velocity boundary condition is considered. This boundary condition, along with the null curve constraint, specifies the initial velocity vector up to an overall scale. The scale determines the initial energy of the quark, as one can clearly

[5]The true endpoint momenta are defined using the original einbein and are not conserved due to the boundary term.

see by its definition:

$$E_{init} = -\frac{1}{\eta} G_{tt} \frac{dt_0}{d\lambda} + \frac{1}{\alpha'} A_0 \tag{3.3.4}$$

It is important to note that the energy of the quark is defined as the energy observed by the asymptotic observer in the co-ordinate time t. It is clear that by scaling $\frac{dt_0}{d\lambda}$, the first term in the energy is scaled by the same factor. The A_0 term tends towards the length dimension chemical potential $\mu\alpha'$. This chemical potential takes values much smaller than the first term contribution in the near boundary limit. Since the gauge field term in the energy is negligible for the near boundary limit, it is not necessary to count the scaling of the gauge field term. Hence, the energy is scaled by the same factor as the velocity vector for the near boundary case of interest.

The second boundary condition of interest is the condition that the energy of the quark is zero at the horizon; all the energy of the quark is lost to the plasma. Whilst this condition was trivial to impose in the analytically solvable cases, it proposes a problem in the numerical context. The zero energy condition is a boundary condition at the end of the trajectory, but the zero initial radial velocity is an initial condition. In other words, the first derivative condition involves both information at $t = 0$ and $u = u_H$.

In order to solve the system, the NDSolve method in Mathematica has been used. This method requires either boundary conditions or initial conditions. To obtain the solutions of interest, an iterative procedure is used. An arbitrary scale is initially chosen and the system is solved. The energy at the horizon is computed and compared with a tolerance ($E_{final} < 10^{-3}$). If the energy violates this tolerance, the initial velocity vector is re-scaled by solving for k in the following equation:

$$kE_{init} - E_{final} = 0 \tag{3.3.5}$$

The initial vector is re-scaled by $k + c$, where c is a small constant e.g. $c = 10^{-30}$. This constant is required to avoid some errors that may occur if k is used as the raw scaling factor. In order to explain why this small c addition is needed, one must consider solutions where all the energy at the end point goes to zero at some $u > u_H$. For these solutions, the string shrinks to a point at this value of u. The string then undergoes a "snapback" - see Sec. 2.2. These solutions are unobtainable through numerical means. This means the scale one multiplies the initial vector must be large enough, such that final energy is greater than zero. Scaling by the factor k from Eq. (3.3.5), one often obtains an initial vector that leads to one of the forbidden solutions. This leads to errors on attempting to solve numerically, and so the small constant is added to k to prevent this from occurring. The re-scaled vector is used to solve the equations of motion, and the process is repeated until the final energy falls below the chosen tolerance.

An important thing to note about the final energy boundary condition is the effect that the limitations of working precision has on the numerics. For a given starting radial co-ordinate $u = u_0$, there is a limit to the value of E_{final} that can be obtained. The change in the initial vector required to lower E_{final} further requires a factor that is significant to a number larger than the precision of k that is returned by the numerics.

Consider a particular initial vector V, whose solution leads to a final energy of the order of 10^{-2}. In order to reduce this final energy, one must multiply V by some factor $k < 1$. However, the k required has a such a large number of significant figures, one requires to solve the system to a very high precision. There is a limit where it is no longer possible to solve the system, due to the precision required to solve the system. Since the required precision is not possible, the scale k converges to 1, and thus the same initial conditions are solved for repeatedly. The working

precision used in this thesis is accurate up to 60 significant figures, above which it was not possible to solve the system. This is concretely analysed in both Subsections 3.3.2 and 3.3.3.

The final consideration for the boundary conditions is the value of the initial radial co-ordinate u_0. As considered in previous cases, it is of interest to study the near boundary limit $u_0 \to 0$. Of course, the numerical nature of the solution limits exactly how small u_0 can be. As stated previously, there is a limit to how small E_{final} can be for a given u_0. As u_0 is decreased, the minimum value for E_{final} increases, and so the zero final energy boundary tolerance condition must be more lax. There is competition between taking the near boundary limit, and maintaining this zero final energy boundary condition. The specifics are detailed for both the D_3/D_7 system and the Sakai-Sugimoto model in Subsections 3.3.2 and 3.3.3. It is by considering this tension that appropriate choice of u_0 are chosen for the stopping distance and energy loss analysis.

Finally, the manner in which errors are accounted for must be discussed. Mathematica has an in-built method by which it checks errors. It involves computing the solution at the next time step, using both the grid size used in the full computation and a grid with less points as well. The scaled difference between the two values must be greater than a given tolerance [Her+06]. Should the solution violate this process, Mathematica outputs a suitable error message. This in-built error check is used as a first port of call, when evaluating the accuracy of the solution.

The secondary method of consideration will be the residual of the system[6]. A residual of the order of 10^{-6} at maximum is demanded from the solution.

[6]The residual is defined as the absolute value of the subtraction of the LHS from the RHS of the differential equation.

$$r^{\mu} = \text{Abs}\left[\dot{p}_{\mu} - \Gamma^{\lambda}_{\mu\nu}\dot{X}^{\nu}p_{\lambda} + \frac{1}{\alpha'}F_{\mu\nu}\dot{X}^{\nu} + \frac{1}{2\pi\alpha'}G_{\mu\nu}\dot{X}^{\nu}\right] \tag{3.3.6}$$

The focus will be on the v, x, and u components of r^{μ}, and these will be denoted with the superscript i. It is important to note v is the Eddington-Finkelstein time co-ordinate used in the numerical calculations. This shall be explained in detail in Sections 3.3.2 and 3.3.3.

Also, the null condition is used to check errors. To be more specific, the absolute value of the end point trajectory tangent vector norm is used. The tolerance for the maximum of this error is again 10^{-6}.

$$n = \text{Abs}\left[\text{Numerator}\left(G_{\mu\nu}\frac{dX^{\mu}}{d\lambda}\frac{dX^{\nu}}{d\lambda}\right)\right] \tag{3.3.7}$$

For r^{μ} and n, it is important to qualify what is meant by maximum error. The global maxima of these functions are numerically computed using Mathematica routines. However, this may not give the true maximum over the domain. One must also consider the value of r^{μ} and n at the end of the trajectory. The global maximum routines look for points along the trajectory with zero derivative. These error functions may not have zero derivative at the end of the trajectory, yet the value of the functions may be larger at this point than at the global maximum. Thus it is important to consider the error at both the global maximum and the end point of the trajectory. Whichever of these is the largest, is the true maximum over the domain.

3.3.2 Stopping distance of light probes in the D_3/D_7 system

Let us consider the canonical D_3/D_7 system first. In Appendix D, the solution to the probe brane embedding is found for the case $\frac{m}{T} = 0$. The embedding profile is

the trivial solution ($\chi = 0, \phi = 0$), but the gauge field is non-trivial. It is given by:

$$A_0'(u) = -\frac{dr_H u}{\sqrt{1+4\pi^2 d^2 u^6}} \tag{3.3.8}$$

$$\Rightarrow A_0(u) = \frac{1}{2} dr_H \left[{}_2F_1\left[\frac{1}{3}, \frac{1}{2}; \frac{4}{3}; -4d^2\pi^2\right] - {}_2F_1\left[\frac{1}{3}, \frac{1}{2}; \frac{4}{3}; -4d^2\pi^2 u^6\right] u^2 \right] \tag{3.3.9}$$

The dimensionless constant d is related to the number density and the radial coordinate $u = \frac{r_H}{r}$ has been defined. One can relate the constant d to the chemical potential, by taking the limit of the gauge field to the boundary $\mu = \frac{1}{\alpha'} \lim_{u\to 0} A_0(u)$. It is also important to remember the choice of dimensions used for the gauge field. As explained previously, a choice of length dimensions has been chosen for the gauge field. This choice simplifies the end point equations of motion. In order to define the chemical potential, one must take this into account and divide by a factor of α'.

$$\begin{aligned}
\mu &= \frac{dr_H}{2\alpha'} {}_2F_1\left[\frac{1}{3}, \frac{1}{2}; \frac{4}{3}; -4d^2\pi^2\right] \\
\Rightarrow \hat{\mu} &= \frac{\mu}{T\sqrt{\lambda}} \\
&= \frac{d\pi}{2} {}_2F_1\left[\frac{1}{3}, \frac{1}{2}; \frac{4}{3}; -4d^2\pi^2\right] \\
&\approx \frac{d\pi}{2} - \frac{1}{4}\pi^3 d^3 + \frac{3}{7}\pi^5 d^5 + \mathcal{O}(d^7)
\end{aligned} \tag{3.3.10}$$

The fact that the t'Hooft coupling λ can be written as $\frac{L^4}{\alpha'^2}$ has been used to eliminate α'.

In order to solve Eq. (3.3.2), it is convenient to use in-going Eddington-Finkelstein co-ordinates.

$$dt = dv + \sqrt{\frac{G_{uu}}{-G_{tt}}}du \tag{3.3.11}$$

The resulting metric is given by:

$$\begin{aligned} ds^2 &= \left(\frac{r_H}{uL}\right)^2\left[-\left(1-u^4\right)dt^2+dx^2+dy^2+dz^2\right]+\frac{L^2}{u^2(1-u^4)}du^2+L^2d\Omega_5^2 \\ &= \frac{\hat{r}_H^2}{u}\left(-\left(1-u^4\right)dv^2+dx^2+dy^2+dz^2\right)-\frac{\hat{r}_H}{u^2}Ldvdu+L^2d\Omega_5^2 \end{aligned} \tag{3.3.12}$$

It is important to note that the horizon radius r_H has been rescaled to a dimensionless constant $\hat{r}_H = \frac{r_H}{L}$. In order to perform the numerical computations, a number of dimensionless variables need to be defined. The dimensionless chemical potential $\hat{\mu}$ has already been defined in Eq. (3.3.10). Observables such as energies and stopping distances are re-defined in terms of the following dimensionless variables

$$\begin{aligned} \hat{\mu} &= \frac{1}{\sqrt{\lambda}}\frac{\mu}{T} \\ \hat{x}^i &= \frac{x^i}{L} \\ \hat{E} &= \frac{L}{\sqrt{\lambda}}E \\ \hat{T} &= TL \end{aligned} \tag{3.3.13}$$

where $x^i = (v, x, y, z)$. Based on these newly defined variables, let us explicitly write

out the energy, instantaneous rate of energy loss and the numerator of the norm n.

$$\frac{d\hat{E}}{d\lambda} = \frac{\hat{r}_H}{2\pi u^2(\lambda)}\left[\hat{r}_H\left[u^4(\lambda)-1\right]\hat{v}'(\lambda)-u'(\lambda)\right] \tag{3.3.14}$$

$$\hat{E} = \frac{\hat{r}_H^2}{\eta(\lambda)u^2(\lambda)}\left[u'(\lambda)-\left(u(\lambda)^4-1\right)\hat{v}'(\lambda)\right] \tag{3.3.15}$$

$$+ \frac{1}{2}d\hat{r}_H\left[{}_2F_1\left[\frac{1}{3},\frac{1}{2};\frac{4}{3};-4d^2\pi^2\right]-{}_2F_1\left[\frac{1}{3},\frac{1}{2};\frac{4}{3};-4d^2\pi^2u^6\left(\lambda\right)\right]u^2\left(\lambda\right)\right]$$

$$n = \hat{r}_H\left[\hat{r}_H\left[\left(u^4(\lambda)-1\right)\left[\hat{v}'(\lambda)\right]^2+\left[\hat{x}'(\lambda)\right]^2\right]-2u'(\lambda)\hat{v}'(\lambda)\right] \tag{3.3.16}$$

Boundary Conditions and Errors for D_3/D_7

As mentioned previously, the end point equations of motion are solved numerically using the NDSolve method in Mathematica. Before analysing the stopping distances directly, let us first consider some of the issues regarding the boundary conditions and error checking.

First, let us demonstrate the sensitivity of the final energy at the horizon E_{final}, to the initial energy E_{init}. In order to do this, the equations of the end points are solved using particular choices of gauge, initial conditions and the first initial velocity vector[7]. The gauge used for the following analysis is given by:

$$\eta\left(\lambda\right) = 1 \tag{3.3.17}$$

$$\frac{d\hat{v_0}}{d\lambda} = 155 \tag{3.3.18}$$

[7]Remember the initial conditions are at $t=0$, $x=y=z=0$, $u=u_0$.

It is important to remember that specifying $\frac{d\hat{v}}{d\lambda}$ and the zero initial radial velocity completely specifies $\frac{d\hat{x}}{d\lambda}$[8].

Fig. 3.7 and Fig. 3.8 show plots describing the sensitivity of E_{final} to the initial velocity conditions. In Fig. 3.7, the plots show how E_{final} varies with the scale factor k for three different chemical potentials. One can see that k tends towards 1, as E_{final} tends towards a lower bound. This lower bound exists because a very large precision is required to specify a k that will re-scale the initial velocity vector in order to reduce E_{final} further. The working precision of the numerics specifies how precise this value will be, as it tends towards 1.

This feature is seen directly in Fig. 3.8, which shows plots of E_{final} vs E_{init}. Again, one can see that E_{init} approaches a fixed value, as one tries to adjust the initial velocity conditions to lower E_{final} as much as possible.

An important feature to note about this lower bound is how it relates to u_0. We want to keep E_{final} to be as small as possible, in order to satisfy the boundary condition. However, the near boundary limit $u_0 \to 0$ is also important in our analysis of the stopping distance. Fig. 3.9 shows that the lower bound of E_{final} increases as u_0 decreases. This means there is a tension between the boundary condition $E_{final} = 0$, and taking the near boundary limit. One must take this into account, when considering what values of u_0 to vary for the full investigation. A domain of u_0 is chosen such that E_{final} is kept relatively low whilst simultaneously keeping u_0 relatively small.

Another factor that needs to be considered is how E_{final} relates to the accuracy of the numerical solution. A curious feature of the numerics is that the errors seem to

[8] $\frac{d\hat{y}}{d\lambda} = \frac{d\hat{z}}{d\lambda} = 0$ at $t = 0$ are specified as initial conditions.

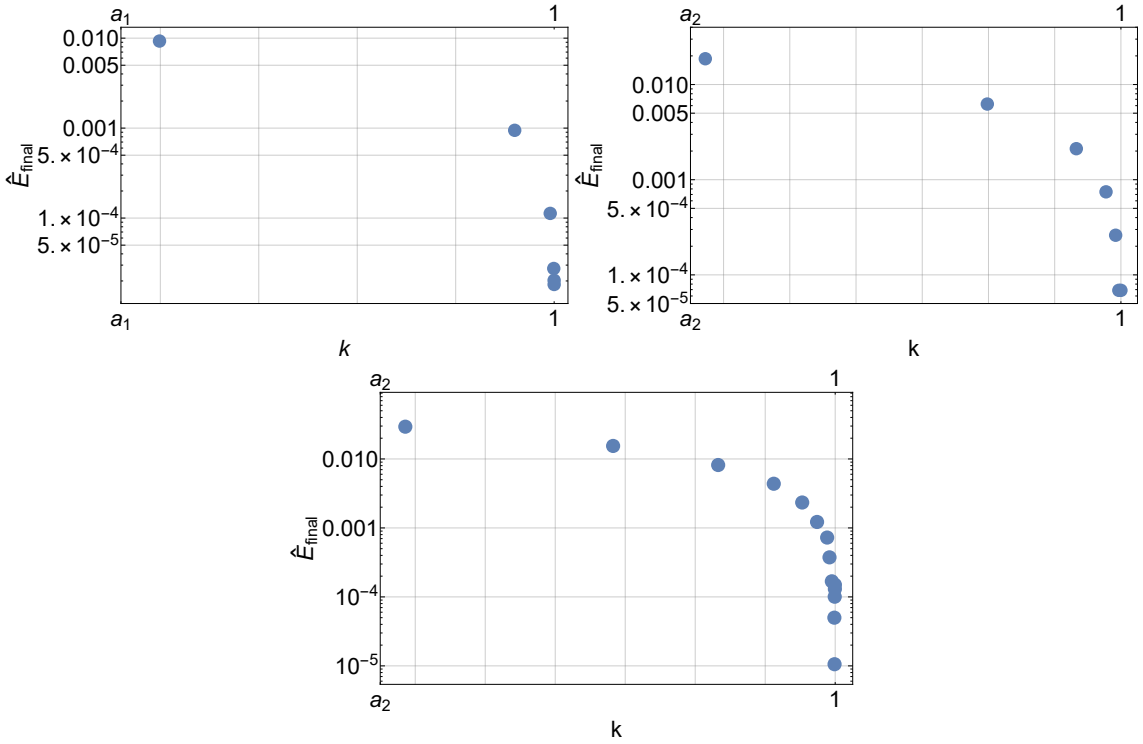

Figure 3.7: These are plots of the energy at the horizon E_{final} vs the re-scaling factor k. The horizon radius is fixed at $\hat{T} = 1$ and the initial radial co-ordinate u_0 is set to $\frac{1}{1700}$ for all plots. The constants determining the scale on the k axes are given by $a_1 = 0.999999999978$ and $a_2 = 0.999999999987$. The three plots considered vary in the dimensionless chemical potential $\hat{\mu}$. The top left plot is for $\hat{\mu} = 0$, the top right plot is for $\hat{\mu} = 0.0769$ and the bottom plot $\hat{\mu} = 0.154$.

increase with E_{final}. In Fig. 3.10 and Fig. 3.11, the errors are explicitly shown to increase with E_{final}. These plots are obtained with fixed $u_0 = \frac{1}{2100}$ and by lowering the tolerance. There is no current explanation as to why this occurs, yet the plots clearly indicate this. This provides another point of consideration when choosing the initial conditions of the system.

It is important to note that r^i is evaluated at the horizon, rather than the global maximum of r^i. This is because $r^i_H > r^i_{global}$, and hence is the true maximum of r^i over the domain. It has been found that there are a number of competing factors that must be considered, when dealing with the initial and boundary conditions of the system. On the one hand, the near boundary limit $u_0 \to 0$ is the initial condition

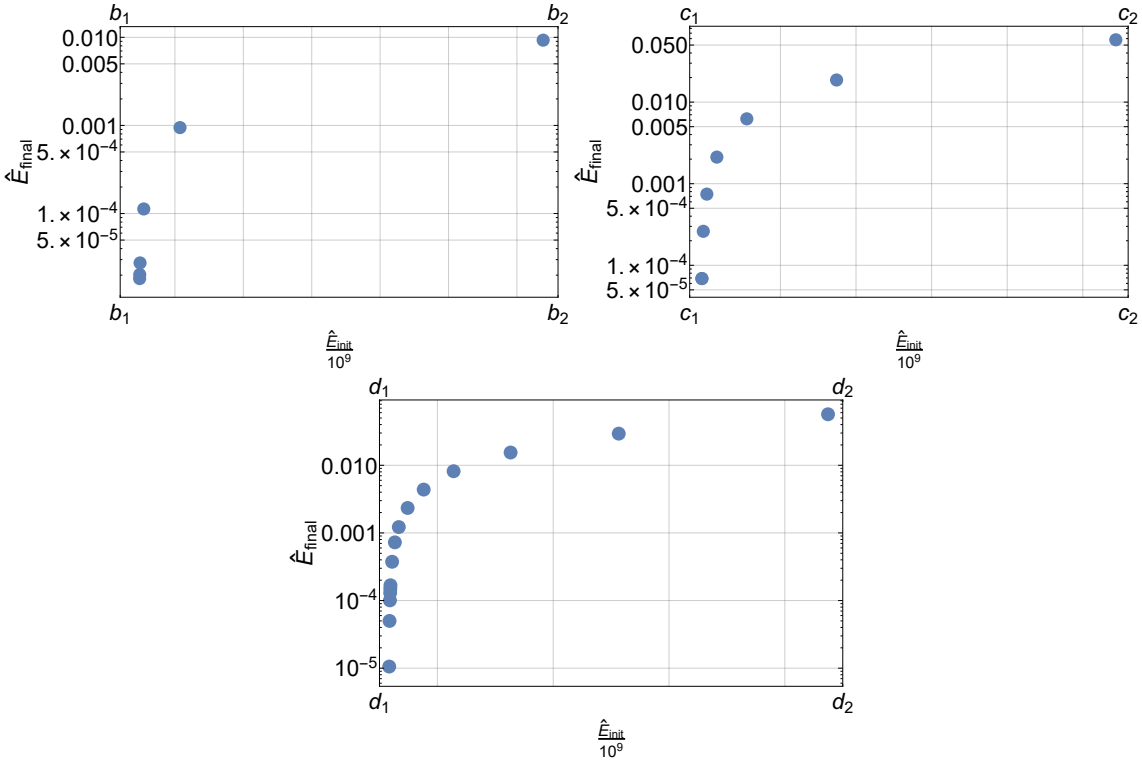

Figure 3.8: These are plots of the energy at the horizon E_{final} vs the initial $E_{initial}$. The horizon radius is fixed at $\hat{T} = 1$ and the initial radial co-ordinate u_0 is set to $\frac{1}{1700}$ for all plots. The constants determining the scale on the E_{init} axes are given by $b_1 = 1.4716157431471$, $b_2 = 1.4716157431503$, $c_1 = 1.471424907394$, $c_2 = 1.471424907423$, $d_1 = 1.471221010155$ and $d_2 = 1.471221010195$. The three plots considered vary in the dimensionless chemical potential $\hat{\mu}$. The top left plot is for $\hat{\mu} = 0$, the top right plot is for $\hat{\mu} = 0.0769$ and the bottom plot is for $\hat{\mu} = 0.154$.

of interest. On the other hand, it is required that the energy of the string end point at the horizon is 0. As noted above, the working precision forces a lower bound on E_{final} for a given u_0. The fact that this lower bound increases as $u_0 \to 0$, implies a competition between taking the near boundary limit and the $E_{final} = 0$ boundary condition. In addition to this, it was shown that the accuracy of the solution increases with a smaller E_{final}. This further adds a competition to the $u_0 \to 0$ limit. In the full analysis of the system, these important factors are considered when selecting the initial condition u_0. It is chosen such that u_0 is suitably “near boundary", whilst minimising E_{final} and hence the numerical errors to suitable tolerances. A final

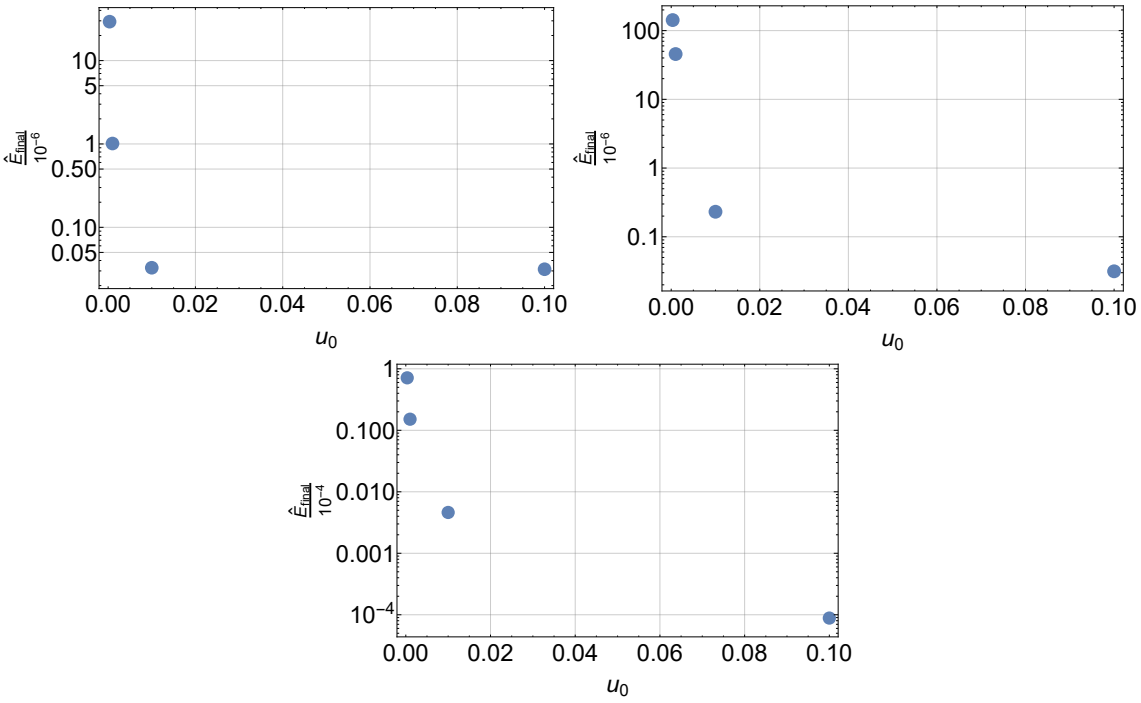

Figure 3.9: These are plot of the lowest E_{final} vs u_0 for three different chemical potentials. The top left plot is for $\hat{\mu} = 0$, the top right is for $\hat{\mu} = 0.308$ and $\hat{\mu} = 0.462$. Note that $\eta = 1$, $\hat{T} = 1$, $u_0 = \frac{1}{1700}$ and $\frac{d\hat{v}_0}{d\lambda} = 155$ were used for these plots.

consideration required when choosing the u_0 range, is the computation time. The smaller u_0 is, the larger the computation time and this is needed to be considered as well.

By considering the factors above, the range of u_0 is chosen to be $[0.000196, 0.000286]$. The E_{final} tolerance obtained for this range of u_0 is $E_{final} < 10^{-3}$. The errors n and r^i are tolerated if $n < 10^{-6}$ and $r^i < 10^{-6}$. Both these conditions are satisfied for the range of u_0 chosen above. The range of u_0 is suitably near boundary in the sense that fitting the analytic near boundary stopping distance to the $\hat{\mu} = 0$ case is a good fit - see Eq. (3.3.21). Also, a numerical study of stopping distances without the end point boundary terms is studied in [CJKY09]. The range of u_0 used in this investigation is $[0.00867, 0.019]$. The u_0 range is smaller in our investigation than used here, and provides a reference when deciding whether u_0 is small enough from the near boundary point of view.

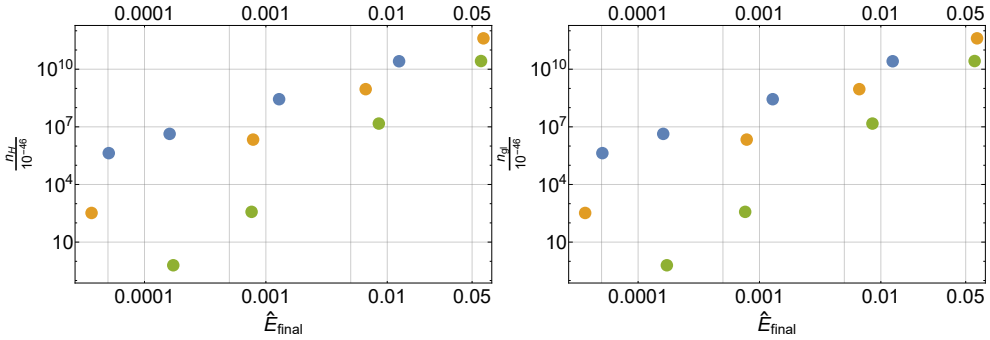

Figure 3.10: This shows the plot of n against E_{final}. The plot is obtained by setting $u_0 = \frac{1}{2100}$ and $\hat{T} = 1$. The plots are given for $\hat{\mu} = 0$, $\hat{\mu} = 0.0769$ and $\hat{\mu} = 0.154$. **Left:** In this plot, n is evaluated at the horizon. **Right:** In this plot, the global maximum of n is plotted against E_{final}. The gauge $\eta = 1$ and $\frac{d\hat{v}_0}{d\lambda} = 155$ is used for these plots.

The final point of consideration is how the $\hat{E}_{final}$ tolerance chosen affects the stopping distances itself. In other words, how does increasing the energy tolerance change the stopping distance. One expects the stopping distance to start to converge as one decreases the tolerance to 0.

Fig. 3.12 shows how the stopping distance changes with varying final energy tolerance. Since a numerical approximation to the $\hat{E}_{final} = 0$ boundary conditions is being used, $\Delta\hat{x}_{stop}$ converges towards the $\hat{E}_{final} = 0$ stopping distance when the final energy tolerance is lowered. By comparing the $\Delta\hat{x}_{stop}$ evaluated using a particular $\hat{E}_{final}$ tolerance with $\Delta\hat{x}_{stop}$ at a higher tolerance, one can see how accurate $\Delta\hat{x}_{stop}$ is to the "true" $\hat{E}_{final} = 0$ value. It is key that we check that the change in $\Delta\hat{x}_{stop}$ that occurs due to varying the chemical potential, is more significant than the accuracy of $\Delta\hat{x}_{stop}$ with respect to the energy tolerance. In order to do this, let us define a variable to measure the significance of the energy tolerance.

First, it is noted that $\Delta\hat{x}_{stop}$ converges to a large number of significant figures for the $\hat{\mu} = 0$ case. This is found by comparing $\Delta\hat{x}_{stop}$ for $\hat{E}_{final} < 10^{-1}$, $\hat{E}_{final} < 10^{-2}$

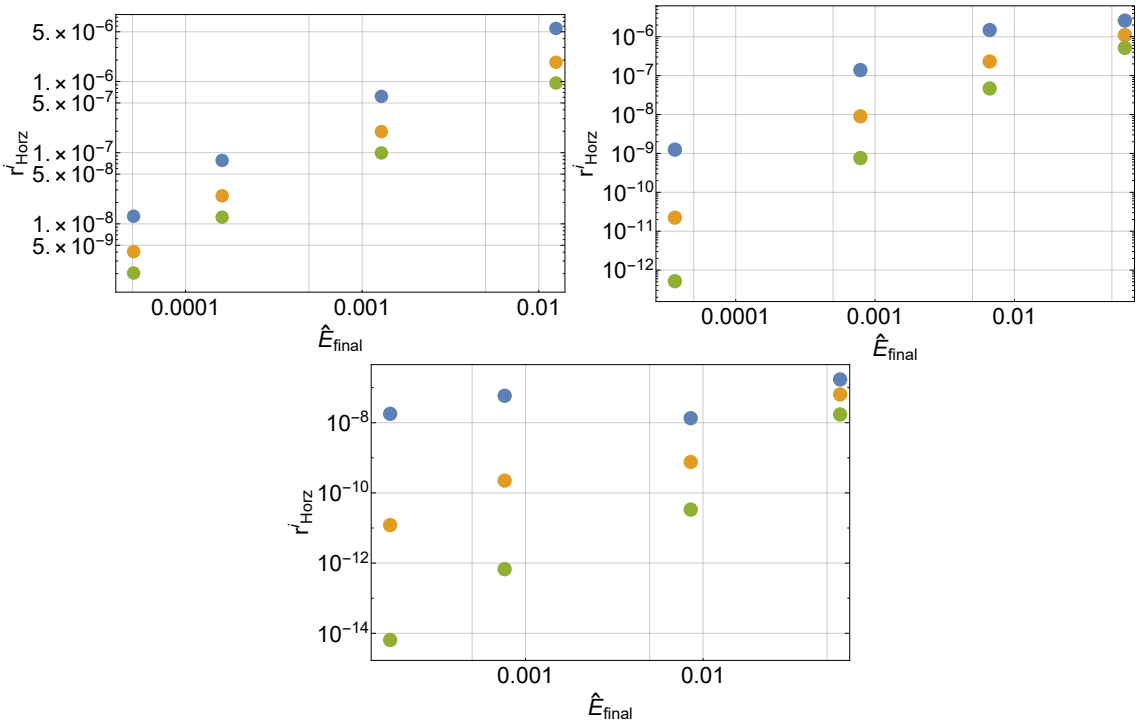

Figure 3.11: This shows the plot of r^i_{Horz} against E_{final}. The plot is obtained by setting $u_0 = \frac{1}{2100}$ and $\hat{T} = 1$. It is important to note that the value of r_i at the horizon is chosen over the global maximum because it is the true maximum over the domain $r^i_{\text{Horz}} > r^i_{gl}$. The colour legend is given by v, x and u. The top left plot is for $\hat{\mu} = 0$, the top right plot is for $\hat{\mu} = 0.0769$, and the bottom plot is for $\hat{\mu} = 0.1538$. The gauge $\eta = 1$ and $\frac{d\hat{v}_0}{d\lambda} = 155$ is used for these plots.

and $\hat{E}_{final} < 10^{-3}$. It is found that $\Delta\hat{x}_{stop}$ converges to the same value up to 20 decimal places.

The stopping distance is now evaluated whilst varying the energy tolerance. To be more precise, $\Delta\hat{x}_{stop}$ is computed for $\hat{E}_{final} < \frac{1}{10^p}$ and $p \in \{-1, 0, 1, 2, 3\}$. In order to measure the convergence as $\hat{E}_{final}$ is reduced, let us define the following:

$$c = \frac{\Delta\hat{x}|_{p+1} - \Delta\hat{x}|_p}{\Delta\hat{x}\,(\hat{\mu} = 0) - \Delta\hat{x}|_{p+1}} \tag{3.3.19}$$

The numerator takes the difference between the stopping distance for the tolerance $\hat{E}_{final} < \frac{1}{10^{p+1}}$ from that of $\hat{E}_{final} < \frac{1}{10^p}$. This is a measure of how the stopping

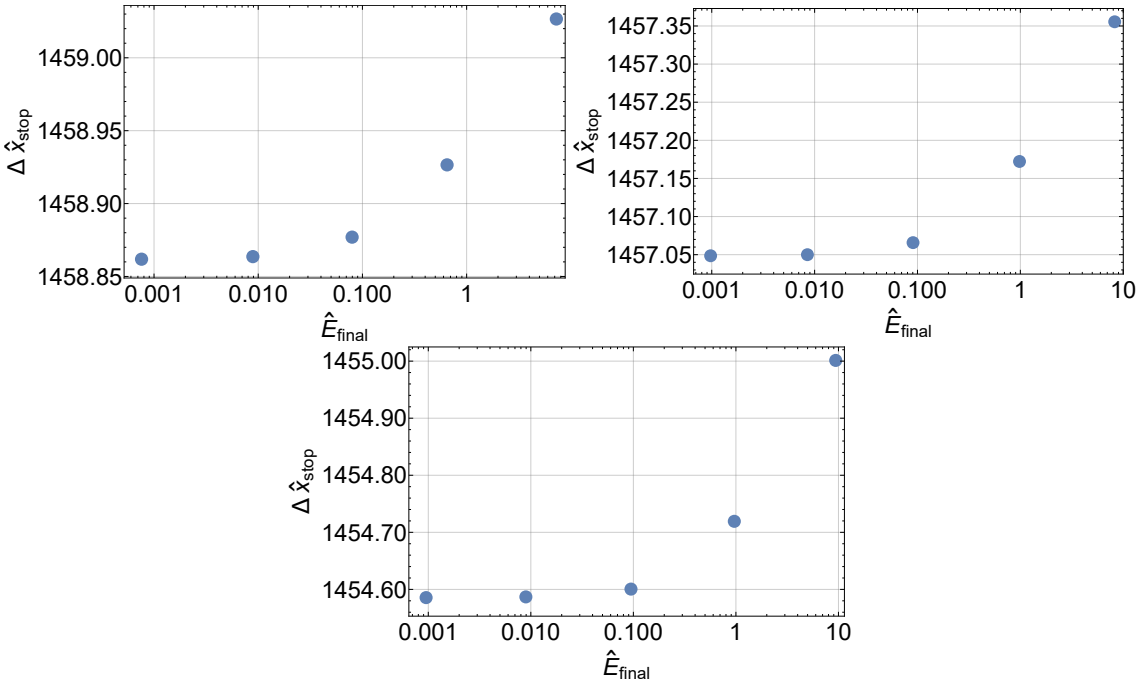

Figure 3.12: This plot shows the stopping distance vs E_{final} for fixed $u_0 = \frac{1}{3500}$, $\eta = 1$, $\hat{\mu} = 0.6$ and $\hat{T} = 1$. The stopping distance converges to the true $E_{final} = 0$ value, as E_{final} decreases. The tolerance of $E_{final} < 10^{-3}$ is shown to be a good choice because the convergence in the stopping distance is strong.

distance is converging towards the $\hat{E}_{final} = 0$ solution. The main variable of interest in this investigation is the chemical potential. It is important that the accuracy of the solution is smaller than the change in $\Delta\hat{x}_{stop}$ obtained by varying the chemical potential. The denominator takes this into account, and thus c gives an indication of whether a small enough energy tolerance has been chosen.

One can see in Fig. 3.13 that c decreases as E_{final} decreases. In other words for a lower tolerance, the change in the stopping distance due to the lowering of the tolerance relative to the change incurred by the chemical potential decreases. One can see that the chosen tolerance of $E_{final} < 10^{-3}$ is a good choice because $c \ll 1$. This indicates that any discrepancy in being unable to obtain the absolute $E_{final} = 0$ solution occurs at a smaller order of magnitude, compared to the change in the stopping distance that occurs due to the chemical potential. Thus, the con-

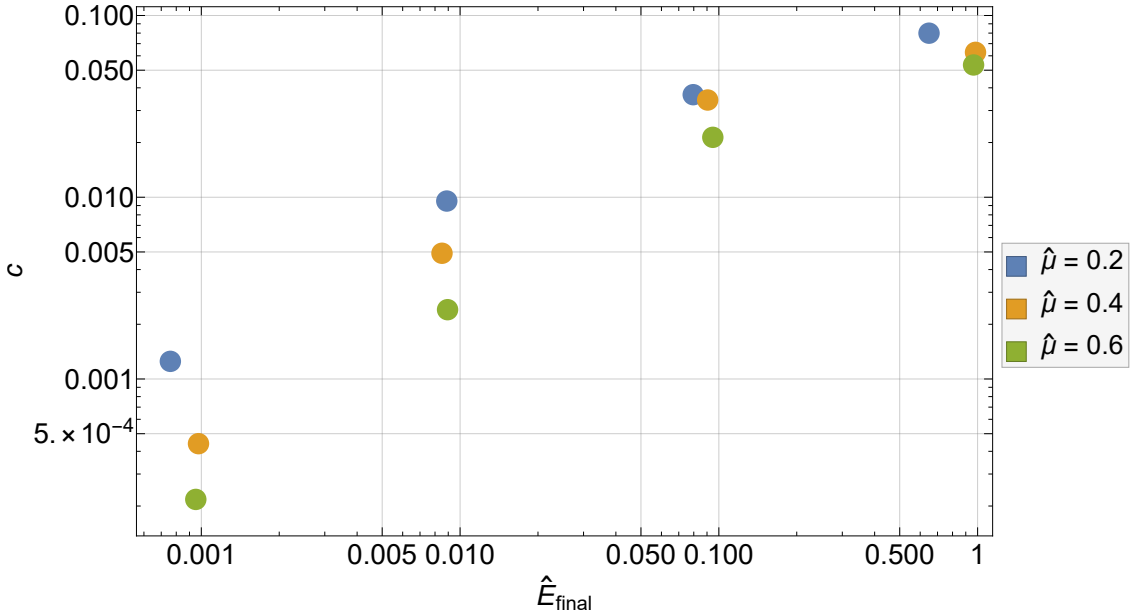

Figure 3.13: This shows the plot of c vs E_{final} for three different chemical potentials: $\hat{\mu} = 0.2$, $\hat{\mu} = 0.4$ and $\hat{\mu} = 0.6$. The plots are obtained by fixing $u_0 = \frac{1}{3500}$, $\eta = 1$ and $\hat{T} = 1$.

clusions drawn from the analysis is physical and not due to the numerical inability to obtain the true $E_{final} = 0$ solution.

Stopping Distance Analysis and Polynomial Fit

In the Sub. 3.3.2, the initial conditions, boundary conditions, errors and energy tolerances have all been analysed in order to obtain appropriate parameters to use in the investigation. In this subsection, the stopping distance for the D_3/D_7 system is investigated. In particular, the effect of the chemical potential arising from charges associated to flavour symmetry are compared to those arising from R-symmetry. This is both done qualitatively and also by obtaining an approximate small $\hat{\mu}$ expansion, which can be compared directly with small $\hat{\mu}$ expansion in the R-symmetry case.

Firstly, the general effect of the flavour symmetry chemical potential is observed. Fig. 3.14 shows direct plots of the stopping distance against $\hat{\mu}$. One can see the

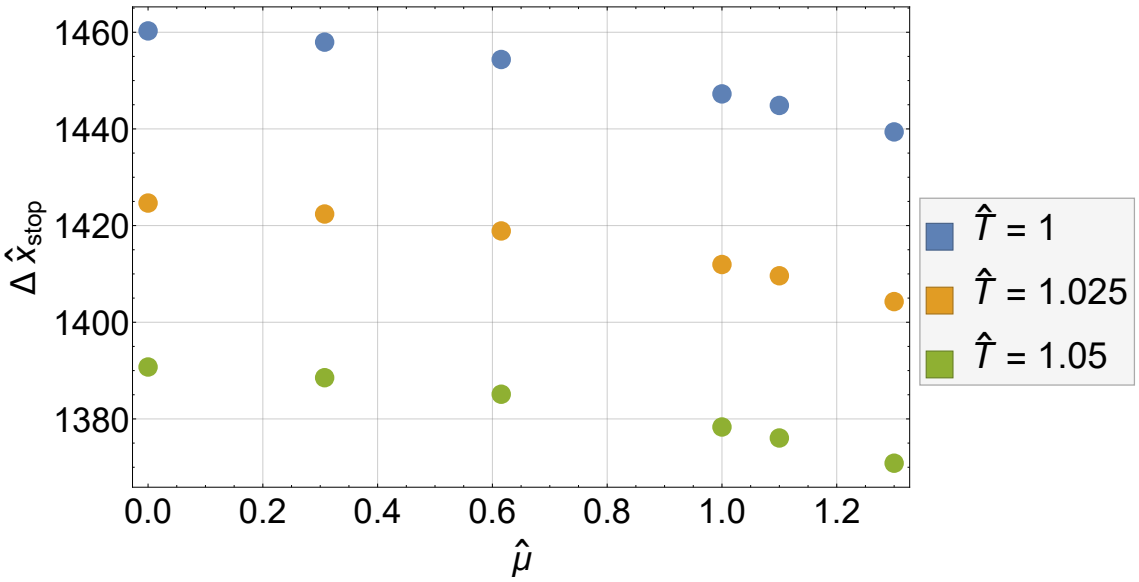

Figure 3.14: The plot shows how Δx_{stop} varies with $\hat{\mu}$ for three different temperatures. The plots are obtained by fixing $u_0 = \frac{1}{3500}$. As expected, the stopping distance decrease with chemical potential and temperature.

expected behaviour that the stopping distance decreases with chemical potential and temperature. It is important to note that these plots are obtained by fixing $u_0 = \frac{1}{3500}$ and not E_{init}. This is because the energy is a function of $\hat{\mu}$, as shown in Eq. (3.3.4). However, the near boundary initial conditions that are chosen, mean the effect the gauge field term has on the energy is relatively small. To quantify this, consider the following:

$$\frac{E_{init}\left(\hat{\mu}_1\right) - E_{init}\left(\hat{\mu}_2\right)}{E_{init}\left(\hat{\mu}_{1/2}\right)} \sim 10^{-4} \tag{3.3.20}$$

Having obtained a check that the behaviour of the stopping distance is consistent with basic expectations, it is useful to consider extracting a functional form for Δx_{stop}. In order to obtain such a form, Δx_{stop} is computed over a suitable range of u_0, $\hat{T}$ and $\hat{\mu}$. The range of u_0 has been discussed extensively in the last section, and it is this chosen range of $[0.000196, 0.000286]$ that is used.

Before the temperature range is discussed, it is important to note that the metric

length scale L is used to define the physical temperature. In other words, one can choose any value for $\hat{T}$ and use L to tune this to the physical temperature one requires. Keeping this in mind, the range chosen for $\hat{T}$ is $[1 : 1.1]$. The system is both in the deconfinement phase, but also in the chiral restoration phase for $T > 200MeV$[Bha+14]. It is useful to consider measured temperatures of the fire-ball produced at the LHC in order to choose a suitable value for L. The maximum temperature measured at the LHC is given by $T \approx 500MeV$ [And14], and so the choice of $L^{-1} = 450MeV$ will be used in the following analysis.

Finally, the range for the chemical potential must be considered. Before defining the range, it is important to discuss a particular non-trivial feature of the chemical potential in the charged end point string. The chemical potential scales with the t'Hooft coupling λ and this provides a complication when attempting to define a range for μ. This scaling is the same as the scaling that the energy of the end point undergoes - see Eq. (2.3.14). The dimensionless parameter used to set the chemical potential $\hat{\mu}$ is defined by absorbing the t'Hooft coupling factor - see Eq. (3.3.10).

In order to compare with different systems e.g. the R-charged case, one needs to specify μ in order to compare the stopping distances over the same parameter ranges. This means the t'Hooft coupling needs to be specified. The simple choice used in this case is obtained by comparing the QCD coupling to the $\mathcal{N} = 4$ gauge theory for tree level computations. It is assumed that gluon scattering amplitudes at tree level are the same in both theories, and hence the choice $\lambda = 6\pi$ is made [Gub06]. This now gives us a well defined notion of the chemical potential, given $\hat{\mu}$ and T. The range of $\hat{\mu}$ used in the following analysis will be $[0 : 0.6923]$.

Using the NonLinearFit function in Mathematica, the following polynomial fit is obtained for the stopping distance:

$$\Delta x_{stop} = \sum_{n=0}^{9} a_n \hat{E}^{b_n} \hat{T}^{-c_n} \hat{\mu}^n \tag{3.3.21}$$

The coefficients a_n, b_n and c_n are given in Tab. 3.2. Before proceeding, let us

n	a_n	b_n	c_n
0	0.6227674853776879	0.3333888209755	1.3333888209754996
1	−1.6216120126362104	0.05754102478894711	1.066713691203862
2	−317.10173465879944	−0.1821702553836234	0.7903349640357311
3	$2.518058795219925 \times 10^{-6}$	0.7086133065127947	1.8330033183454557
4	$-4.036030380069361 \times 10^{-10}$	1.1625476628732898	2.3241976242841074
5	$5.249765160328638 \times 10^{-14}$	1.593564813194463	2.783837610564587
6	$-1.3232714935622939 \times 10^{-17}$	1.9739904023524355	3.1795929974528137
7	$5.95476915792492 \times 10^{-21}$	2.307758294256115	3.5181049687055532
8	$-3.788212998653256 \times 10^{-24}$	2.601541449919216	3.809143935686847
9	$2.2875304848362594 \times 10^{-27}$	2.8612322619511885	4.061155414689042

Table 3.2: This table shows the parameters for the polynomial fit of the stopping distance data, as shown in Eq. (3.3.21).

confirm the accuracy of the polynomial fit Eq. (3.3.21). In order to do this, the fractional error δ is defined:

$$\delta_{\hat{\mu}} = \text{Abs}\left[\frac{\Delta x_{dat}\left(\hat{\mu}, \hat{T}, \hat{E}\right) - \Delta x_{fit}\left(\hat{\mu}, \hat{T}, \hat{E}\right)}{\Delta x_{dat}\left(\hat{\mu}, \hat{T}, \hat{E}\right)}\right] \tag{3.3.22}$$

$\Delta x_{dat}\left(\hat{\mu}, \hat{T}, \hat{E}\right)$ is the actual stopping distance computed using the numerical methods described previously, and $\Delta x_{fit}\left(\hat{\mu}, \hat{T}, \hat{E}\right)$ is the stopping distance obtained using the polynomial fit Eq. (3.3.21).

Fig. 3.15 shows plots of δ against $\hat{E}_{init}$ and $\hat{T}$ for a variety of chemical potentials. The most important thing to note is that the fractional error remains relatively small $\delta < 10^{-5}$ across the domain of investigation. In order to have context for this upper bound, let us consider the fractional variation of the stopping distance caused by a non-zero chemical potential. Let us define the fractional variation due to the chemical potential as Δ_μ:

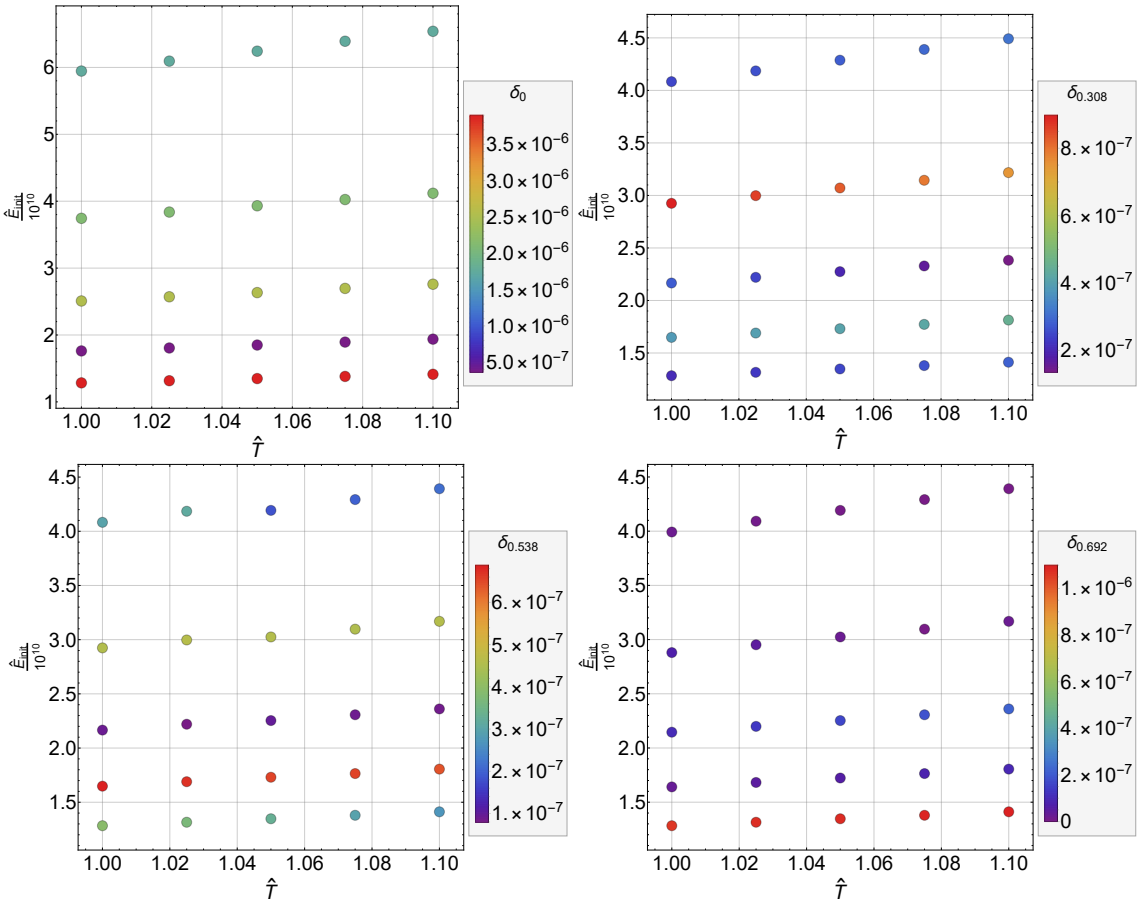

Figure 3.15: The plot shows $\delta_{\hat{\mu}}$ plotted against $\hat{E}_{init}$ and $\hat{T}$ for different chemical potentials: $\hat{\mu} = 0$, $\hat{\mu} = 0.307692$, $\hat{\mu} = 0.538462$ and $\hat{\mu} = 0.692308$. The colour of the points indicate the value of δ, as the legend describes for each plot. The plots show that the fit leads to very small fraction errors, $\delta < 10^{-5}$.

$$\Delta_\mu = \text{Abs}\left[\frac{\Delta x\left(\hat{\mu}, \hat{T}, \hat{E}\right) - \Delta x\left(\hat{\mu} = 0, \hat{T}, \hat{E}\right)}{\Delta x\left(\hat{\mu} = 0, \hat{T}, \hat{E}\right)}\right] \tag{3.3.23}$$

The smallest non-zero chemical potential used when calculating the stopping distance is $\hat{\mu} = 0.076923$. Using the numerical data, it can be shown that $\Delta_\mu \sim 10^{-4}$ for $\hat{\mu} = 0.076923$. If one compares this to the fractional error δ obtained from the polynomial fit Eq. (3.3.22), one can see that the physical variation due to the chemical potential occurs at a higher order of magnitude. In other words, the change in the stopping distance, due to turning the chemical potential on, is larger than the error of the polynomial fit. This means the fit is a good approximation for the

stopping distance in the context of non-zero flavour symmetry chemical potential. For $\hat{\mu} > 0.076923$, the fractional variation Δ_μ will be larger, and hence the fractional error of the fit is even less consequential.

The first thing of note with regards to the polynomial fit is the $n = 0$ term in Tab. 3.2. The near boundary analytic computation for the stopping distance is described in 2.3 and the final expression is shown in Eq. (2.3.19). The coefficient described by the Gamma functions is approximately given by :

$$\frac{2^{\frac{1}{3}}\Gamma[\frac{1}{4}]^{\frac{1}{3}}\Gamma[\frac{5}{4}]}{\pi^{\frac{2}{3}}\Gamma[\frac{3}{4}]^{\frac{4}{3}}} \approx 0.62370582224979 \tag{3.3.24}$$

It is clear that the numerically obtained $n = 0$ term does not quite match the expected analytic result. This is because it is impossible to achieve the true near boundary limit. Having noted this, it is important to note that the values of a_0, b_0 and c_0 approximate the near boundary values to a fairly good degree of accuracy. As explained previously, the choice of u_0 was limited by various factors, such as attempting to obtain the boundary condition $E_{final} = 0$ and also numerical errors. If it were possible to choose smaller values of u_0, it is expected the $n = 0$ term would match Eq. (2.3.19) more accurately.

Comparison with the non-zero R-charge chemical potential

Having obtained the fit for the stopping distance, let us now compare the stopping distance with non-zero flavour chemical potential μ_f, and non-zero R-charged chemical potential μ_R from Sec. 3.2. In order to compare these systems, the domain in the $\left(\hat{\mu}_{f|R}, \hat{T}, \hat{E}_{init}\right)$ space must be chosen carefully.

As noted previously, the dimensionless chemical potential $\hat{\mu}$ (see Eq. (3.3.13)) depends on the t'Hooft coupling λ. In Sec. 3.2, the gauge fields are canonically defined as dimensionless, and the physical chemical potential is obtained by scaling

with the AdS_5 length scale L. Thus, one is left with a natural dimensionless chemical potential that is independent of the t'Hooft coupling. It is of interest to compare the stopping distance by varying the physical chemical potential, rather than the λ scaled chemical potential.

Let us denote the physical dimensionless chemical potential as :

$$\bar{\mu}_{f|R} = \frac{\mu_{f|R}}{T} \tag{3.3.25}$$

Eq. (3.3.13) shows us that multiplying $\hat{\mu}$ by $\sqrt{\lambda}$ gives us $\bar{\mu}_f$. One can then use the values of $\bar{\mu}_f$ to compute the stopping distances for the R-charged case, and obtain a comparison over the same domain of the physical $\bar{\mu}$. As discussed previously, the value of $\lambda = 6\pi$ is chosen by considering the QCD Yang-Mills coupling.

Finally, it is important to note that the definitions of $\hat{T}$ and $\hat{E}$ are consistent across both systems. So the domain of $\bar{\mu}_R$ and $\hat{T}$ can be obtained from the domain used in the flavour charge case, and a similar domain of u_0 can be used to calculate for the stopping distance and energy in the R-charged case. $\hat{T}$ and $\bar{\mu}_R$ are inverted using their definitions as shown in Eq. (B.0.13) and Eq. (B.0.15). The methods discussed in Sec. 3.2 can be used to find expressions for $\frac{d\hat{x}}{du}$ and $\frac{d\hat{E}_{init}}{du}$, and integrating these expressions gives the required stopping distance and energy.

Fig. 3.16 shows plots of the stopping distance against $\hat{E}_{init}$, varying both $\hat{T}$ and $\bar{\mu}_{f|R}$. The $\bar{\mu}_{f|R} = 0$ provides a check on the computation method, and shows no discrepancy between both types of chemical potential. As the chemical potential is turned on, the stopping distance is affected more by $\bar{\mu}_R$ than $\bar{\mu}_f$ at the same point in $\left(\bar{\mu}_{f|R}, \hat{T}, \hat{E}_{init}\right)$ space.

In order to gain a better understanding into the differences between the two systems,

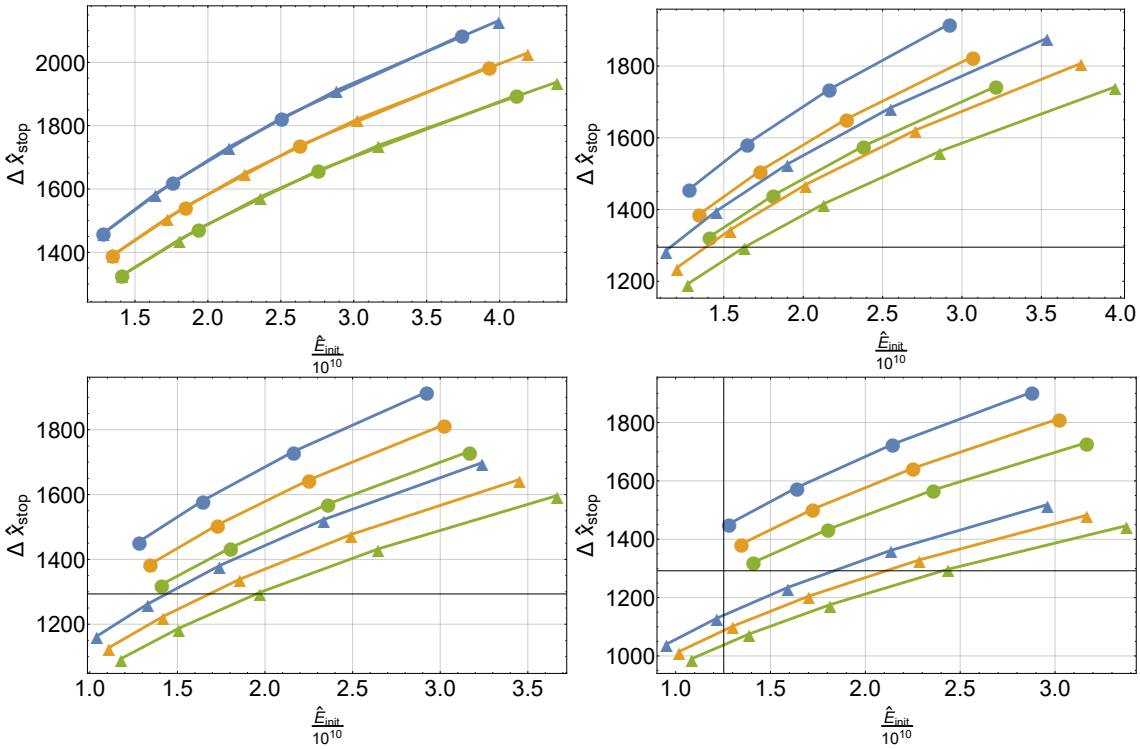

Figure 3.16: This plot shows how the stopping distance varies with E_{init} for a variety of of $\bar{\mu}$ and $\hat{T}$. This is done for the R-charged chemical potential $\bar{\mu}_R$ and the flavour charged chemical potential $\bar{\mu}_f$. The ● represent the flavour charged case and the ▲ represent the R-charged case. Three different temperatures: ● $\hat{T} = 1$, ● $\hat{T} = 1.05$ and ● $\hat{T} = 1.1$ are considered. Each of the four plots are obtained by selecting four different chemical potentials: top left is for $\bar{\mu}_{f/R} = 0$, top right is for $\bar{\mu}_{f/R} = 1.67$, bottom left is for $\bar{\mu}_{f/R} = 2.34$, and $\bar{\mu}_{f/R} = 3.01$.

the polynomial fit Eq. (3.3.21) and the small $\bar{\mu}_R$ expansion Eq. (3.2.22) are considered. An obvious difference between the two expressions is the fact that there are odd powers of $\bar{\mu}_f$ in Eq. (3.3.21), whilst there are only even powers in Eq. (3.2.22). One can see this directly from the R-charged black hole, because the solution is symmetric under the transformation $q \to -q$. In order to see the origins of the linear term in the flavour charge case, let us consider the energy loss rate:

$$\frac{dE}{d\xi} = \frac{1}{2\pi\alpha'} G_{0\nu} \frac{dX^\nu}{d\xi} - \frac{1}{\alpha'} F_{0\nu} \frac{dX^\nu}{d\xi} \tag{3.3.26}$$

The transformation $d \to -d$ leads to a change in sign for $F_{\mu\nu}$.

It is explicit that the energy loss occurs at a smaller rate. The expansion requires odd powers of $\bar{\mu}_f$ in order for this to be reflected in the stopping distance. The odd terms leads to a curious physical picture. It would seem that introducing a negative chemical potential leads to an increase in the stopping distance, rather than a reduction in the stopping distance.

Another feature is that each term in the series has a different dependence on $\hat{E}_{init}$ and $\hat{T}$ for the flavour charged case - see Eq. (3.3.21). This is not the case for Eq. (3.2.22), where each term has the same dependence on these parameters. Let us restrict the analysis to the first order terms:

$$\Delta x_f^{(1)} = -1.622 \hat{E}^{0.05754} \hat{T}^{-1.0667} \left[\frac{\mu}{T}\right] \tag{3.3.27}$$

$$\Delta x_R^{(2)} = -\frac{2^{\frac{1}{3}}\Gamma\left[\frac{1}{4}\right]^{\frac{1}{3}}\Gamma\left[\frac{5}{4}\right]}{\pi^{\frac{2}{3}}\lambda^{\frac{1}{6}}\Gamma\left[\frac{3}{4}\right]^{\frac{4}{3}}}\left(\frac{E_{initial}}{T^4}\right)^{\frac{1}{3}}\frac{1}{3\pi^2}\left[\frac{\mu}{T}\right]^2 \tag{3.3.28}$$

One can see clearly that the energy and temperature dependence of the correction is the same as the zeroth order term for the R-charged case. The non-trivial dependence on energy and temperature for the correction in the flavour case is something to keep in mind when looking at the jet quenching parameter.

3.3.3 Stopping distance of light probes in the Sakai-Sugimoto Model

In Subsection 3.3.2, the stopping distance for the non-zero D_3/D_7 flavour chemical potential was computed. This was done in the meson melting phase. In this subsec-

tion, the computation is repeated for the the non-zero flavour chemical potential, in the Sakai-Sugimoto model. In this case, the high temperature chiral restoration phase is considered.

The probe brane embedding for this phase is given in Appendix D. As in the D_3/D_7 case, this phase is represented by trivial $D_8/\bar{D}_8$ embeddings ($\tau'(u) = 0$). On the other hand, the gauge fields have non-trivial profiles on these embeddings.

$$\begin{aligned} A'(u) &= -\frac{d^2 r_H \sqrt{u}}{\sqrt{1+4\pi^2 d^4 u^5}} \\ \Rightarrow A(u) &= \frac{2}{3} d^2 r_H \left[{}_2F_1\left[\frac{3}{10}, \frac{1}{2}; \frac{13}{10}; -4d^4\pi^2\right] - u^{\frac{3}{2}}\, {}_2F_1\left[\frac{3}{10}, \frac{1}{2}; \frac{13}{10}; -4d^4\pi^2 u^5\right]\right] \end{aligned} \tag{3.3.29}$$

The radial co-ordinate is defined as $u = \frac{r_H}{r}$ and the constant d is dimensionless. The chemical potential is obtained by taking the $u \to 0$ limit:

$$\begin{aligned} \mu &= \frac{2}{3} d^2 r_H\, {}_2F_1\left[\frac{3}{10}, \frac{1}{2}; \frac{13}{10}; -4d^4\pi^2\right] \\ \hat{\mu} &= \frac{\mu}{\lambda_S}\frac{M_{KK}}{T^2} \\ &= \frac{8}{27} d^2 \pi_2^2 F_1\left[\frac{3}{10}, \frac{1}{2}; \frac{13}{10}; -4d^4\pi^2\right] \end{aligned} \tag{3.3.30}$$

where $M_{KK} = 949MeV$ is the mass scale defining the mass of the meson spectrum of the theory, and λ_S is the dimensionless gauge field coupling - see Appendix A.

As in the D_3/D_7 case, ingoing Eddington-Finkelstein co-ordinates are used to help

with the numerics. Using Eq. (3.3.11), one obtains the following form for the metric:

$$ds^2 = \left(\frac{\hat{r}_H}{u}\right)^{\frac{3}{2}} \left[-\left(1-u^3\right)dv^2 + dx^2 + dy^2 + dz^2\right] - 2\frac{L\hat{r}_H}{u^2}dvdu + L^2 d\Omega_5 \quad (3.3.31)$$

The horizon has been scaled to form a dimensionless form given by $\hat{r}_H = \frac{r_H}{L}$. The dimensionless variables for x^i and the temperature are the same as the D_3/D_7 case - see Eq. (3.3.16). However, the chemical potential and the energy variables are given by:

$$\begin{aligned} \hat{\mu} &= \frac{\mu}{\lambda_S}\frac{M_{KK}}{T^2} \\ \hat{E} &= \frac{4M_{KK}L^2}{\lambda_S}E \end{aligned} \quad (3.3.32)$$

where $x^i = (v, x, y, z)$.

Boundary Conditions and Errors in the Sakai-Sugimoto Model

Following from Subsection 3.3.1, the boundary conditions and errors in the Sakai-Sugimoto model case are analysed. Similar boundary conditions are used in this case as in the D_3/D_7 case. The choice of $\eta = 1$ is consistently chosen as the gauge for the computations detailed below.

Fig. 3.17 shows the existence of the lower bound for E_{final}. It is important to note that the plot shown uses $1-k$ rather than k like in Fig. 3.7. This is done to simplify the presentation. However, the same result is seen. The scale converges to 1 as one tries to reduce E_{final}. This again is due to the limit of the working precision. In order to scale the initial velocity to reduce E_{final}, one needs to tune k to a precision higher than the working precision allows. This leads to the lower

bound on E_{final}.

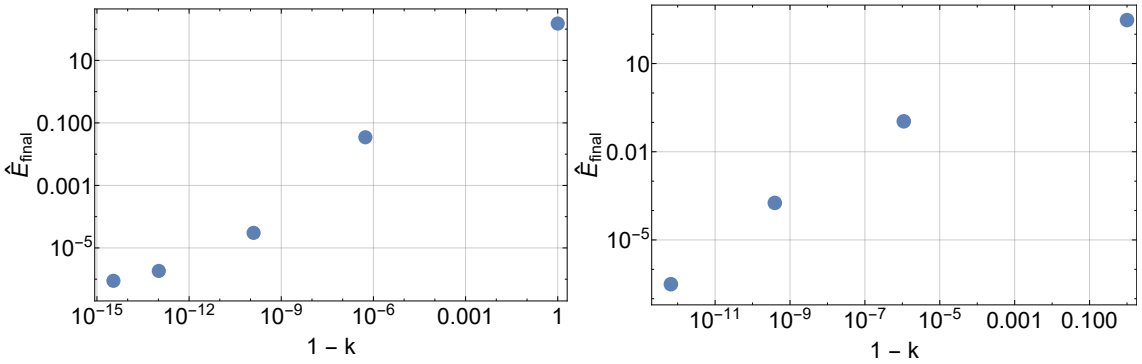

Figure 3.17: These are plots of the energy at the horizon E_{final} vs the re-scaling factor $1-k$. The horizon radius is fixed at $\hat{T}=1$ and the initial radial co-ordinate u_0 is set to $\frac{1}{1000}$ for all plots. The two plots considered vary in the dimensionless chemical potential $\hat{\mu}$. The left plot is for $\hat{\mu}=0.000316$ and the right plot is for $\hat{\mu}=0.000631$. Note that $\eta=1$ and $\frac{dv_0}{d\lambda}=10^4$.

Similarly, Fig. 3.18 shows a similar relationship between u_0 and the lower bound. The smaller u_0 is, the larger the lower bound of E_{final}. Once again the tension between the near boundary limit and the $E_{final}=0$ boundary condition can be seen. Also, Fig. 3.19 and Fig. 3.20 shows that the errors decrease as E_{final} decreases. This is the same effect observed in the D_3/D_7 case - see Sub. 3.3.2.

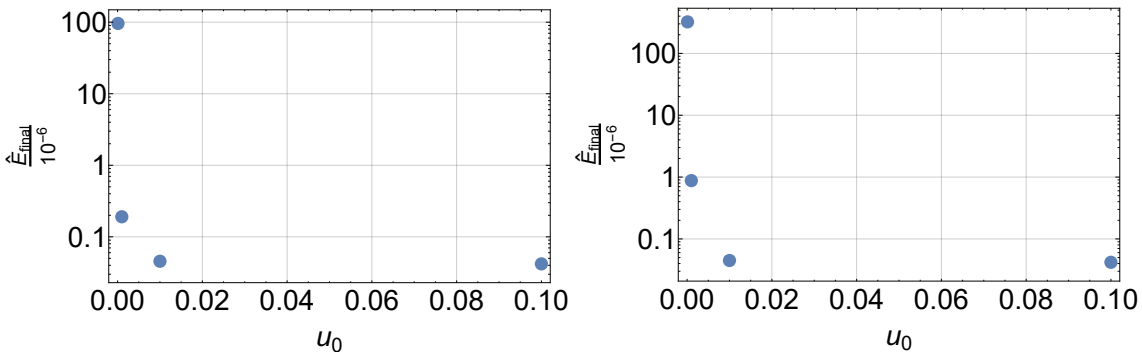

Figure 3.18: These are plots of the energy at the horizon E_{final} vs u_0. This is done for two chemical potentials. The horizon radius is fixed by choosing $\hat{T}=1$. The left plot is given by $\hat{\mu}=0$ and the right plot is given by $\hat{\mu}=0.000316$. Note that $\eta=1$ and $\frac{dv_0}{d\lambda}=10^4$.

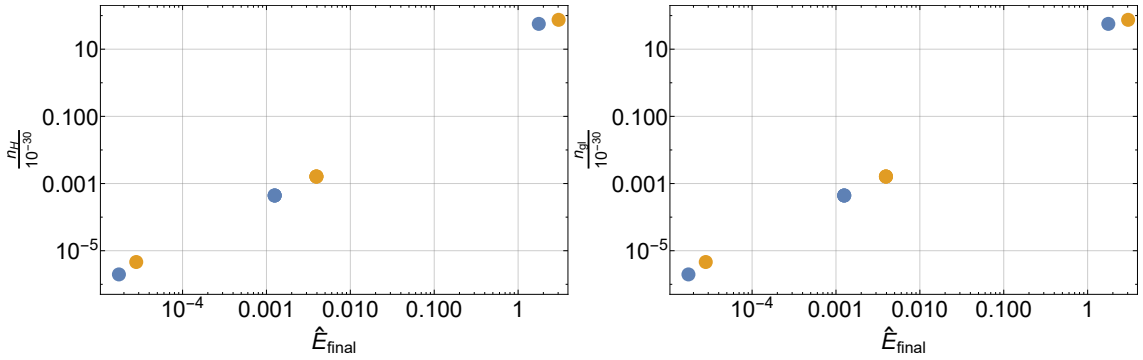

Figure 3.19: These are plots of the norm vs. E_{final} for two chemical potentials. The colors in the plots are given by $\hat{\mu} = 0.000316$ and $\hat{\mu} = 0.000631$ The left plot is the norm evaluated at the horizon and the right plot is the global maximum of the norm.

The same tension between the near boundary limit and the accuracy of the solution is found for the Sakai-Sugimoto model as in the D_3/D_7 case. There is also another point of consideration, when it comes to choosing the range of u_0 for the numerical study. In order to compare the Sakai-Sugimoto system with that of the D_3/D_7 system, the appropriate parameters must be chosen. The range of u_0 and $\hat{\mu}$, chosen for the D_3/D_7, leads to a particular range of initial energies. Using the definitions of the dimensionless energies given by Eq. (3.3.13) and Eq. (3.3.32), one finds that:

$$\hat{E}_S = 4\frac{\sqrt{\lambda_A}}{\lambda_S} M_{KK} L \hat{E}_A \tag{3.3.33}$$

Using this expression, it is found that choosing a range of $u_0 = [0.0000667 : 0.0000933]$ replicates the energy range used in the D_3/D_7 case. The choice of $\lambda_A = 6\pi$ and $\lambda_S = 25.1$ has been used, as described in Appendix A. It is also important to note that the following range is chosen for the dimensionless horizon radius $\hat{r}_H = [17.55 : 20.80]$, along with $M_{KK} = 949MeV$ and a suitable choice of $L^{-1} = 450MeV$. The choice of L is made in order to define the correct temperature range. As noted previously, the temperature range of the plasma fireball created at the RHIC and LHC is found to be $200 - 500MeV$ - see [And14]. The choice of

L and the range of $\hat{r}_H$ gives us a range of temperature between $(450 - 500)MeV$. Using these initial conditions, it is possible to retain errors no larger than 10^{-5} for an energy tolerance of $E_{final} < 10^{-3}$.

It is also important to consider the chemical potential. The relation between the D_3/D_7 dimensionless chemical potential and the Sakai-Sugimoto chemical potential is:

$$\hat{\mu}_S = \frac{M_{KK}\sqrt{\lambda_A}\hat{\mu}_A}{\lambda_S T} \tag{3.3.34}$$

The range of $\hat{\mu}_A$ used in Sec. 3.3.2 is $\hat{\mu}_A = [0 : 0.7]$. Using Eq. (3.3.34), the associated range for $\hat{\mu}_S$ is given by $\hat{\mu}_S = [0 : 0.23]$. This allows a correct comparison over the same physical range.

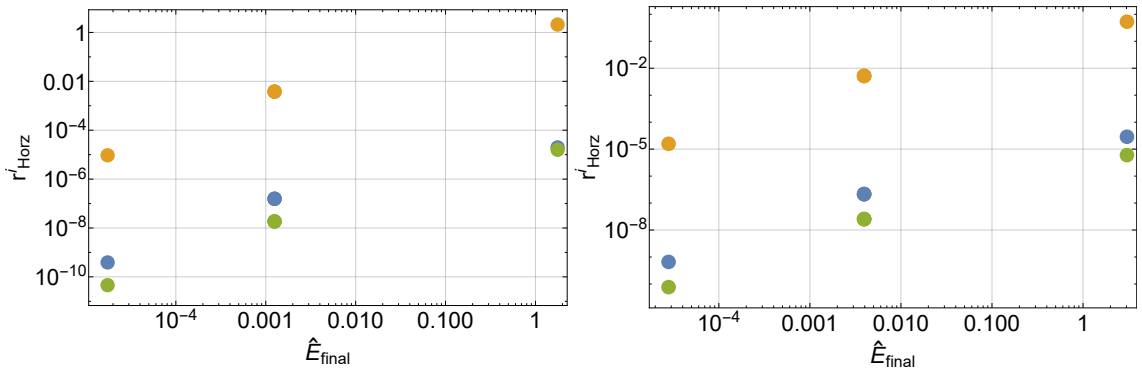

Figure 3.20: These are plots of the r^i vs. E_{final} evaluated at the horizon. The colors in the plots determine which equation of motion is used: $\hat{v}$ and $\hat{x}$ and $\hat{u}$ The left plot is evaluated for $\hat{\mu} = 0.000316$ and the right plot is evaluated for $\hat{\mu} = 0.000631$.

The final point to consider is how the choice of E_{final} tolerance affects the stopping distance itself. The parameter c, as defined in Eq. (3.3.19), is used to measure the variation of the stopping distance due to varying the tolerance vs. the variation caused by the non-zero chemical potential. As explained in Sub. 3.3.2, the error obtained from the tolerance variation should be much smaller than the physical variation due to the chemical potential. Fig. 3.21 shows the plot of c vs E_{final}. The plot once more shows the fact that lowering the tolerance decreases the error due

to the non-zero E_{final} value relative to the effect of the chemical potential. The small values of c for small E_{final} show that $E_{final} < 10^{-3}$ is an acceptable choice of tolerance.

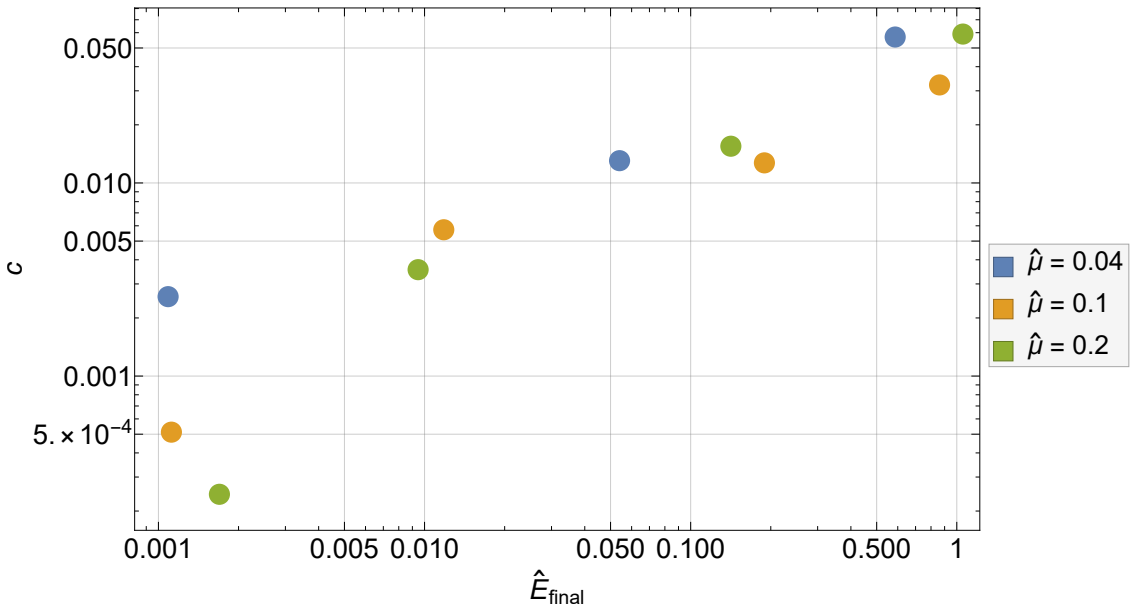

Figure 3.21: This shows the plot of c vs E_{final} for three different chemical potentials: $\hat{\mu} = 0.04$, $\hat{\mu} = 0.1$ and $\hat{\mu} = 0.2$. The plots are obtained by fixing $u_0 = \frac{1}{15000}$, $\eta = 1$ and $\hat{T} = 1$.

Stopping Distance Analysis and Polynomial Fit

Having considered the numerical limitations and errors in Sub. 3.3.3, a suitable domain for the parameters in the stopping distance calculation have been obtained. Using this domain, the stopping distance is computed and the effect of the flavour chemical potential in the Sakai-Sugimoto case is analysed. Both a qualitative and small $\hat{\mu}$ polynomial fit analysis are performed on the data, obtained from the numerical computation.

Fig. 3.22 shows the raw stopping distance vs. $\hat{\mu}$ for three different temperatures. The expected effect, that the stopping distance is reduced by the non-zero chemical

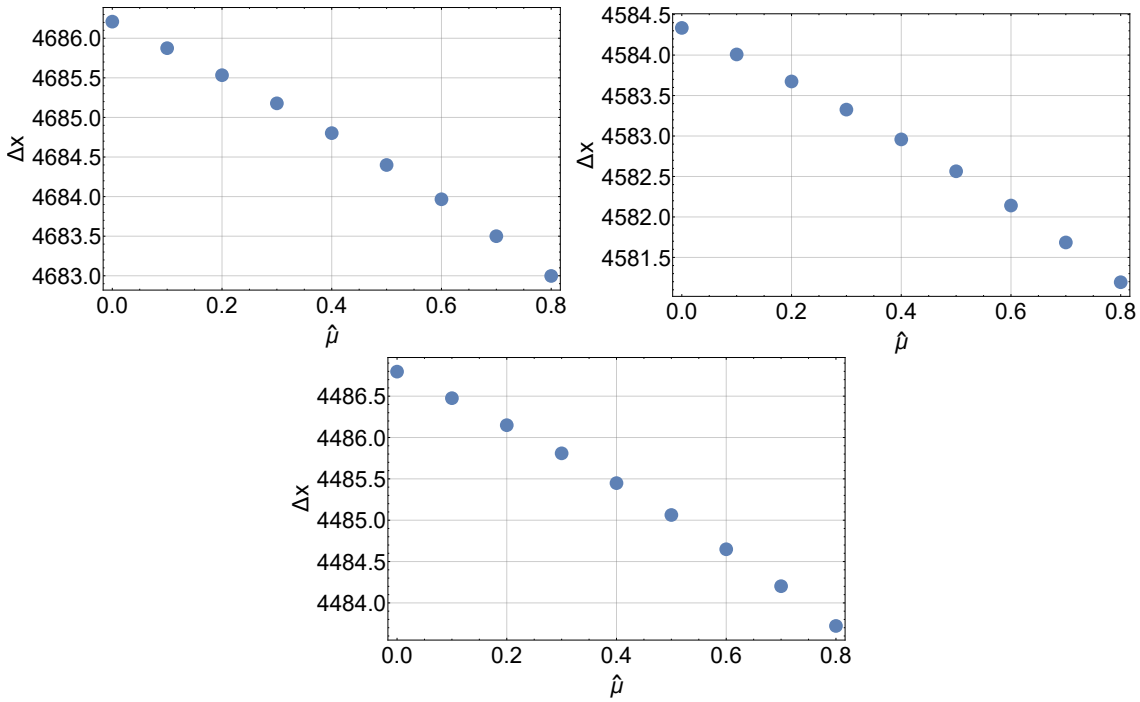

Figure 3.22: This shows the plots for the stopping distance $\Delta\hat{x}$ vs $\hat{\mu}$ for three different temperatures. The top left plot is for $\hat{T} = 1$, the top right plot is for $\hat{T} = 1.02$ and the bottom plot is for $\hat{T} = 1.04$. All plots were obtained by setting $u_0 = \frac{1}{14000}$, $\eta = 1$ and $L^{-1} = 450MeV$.

potential, is observed in the plot. Much like the D_3/D_7 case, the fixed u_0 condition does not fix the initial energy. However, the near boundary condition means that the chemical potential has little effect on the energy, and one can show that:

$$\frac{E_{init}\left(\hat{\mu}_1\right) - E_{init}\left(\hat{\mu}_2\right)}{E_{init}\left(\hat{\mu}_{1/2}\right)} \sim 10^{-4} \tag{3.3.35}$$

So one can assume that the fixed u_0 condition is effectively a fixed E_{init} condition.

Following Sub. 3.3.2, let us extract a functional form for Δx_{stop}. The range and domain of the three parameters u_0, $\hat{T}$ and $\hat{\mu}$ were discussed in Sub. 3.3.3 and using the NonLinearFit function in Mathematica, the following polynomial fit is obtained for the stopping distance:

$$\Delta x_{stop} = \sum_{n=0}^{7} a_n \hat{E}^{b_n} \hat{T}^{-c_n} \hat{\mu}^n \tag{3.3.36}$$

The coefficients a_n, b_n and c_n are given in Tab. 3.3. To confirm the accuracy of the

n	a_n	b_n	c_n
0	0.24932452183602946	0.40002246375204875	1.8000446249669027
1	-3.177387643	-0.0014739748648616503	0.9917747521268921
2	-28.530209659709012	-0.6307351109727402	55.975792865426281
3	$1.5300971874362376 \times 10^{-18}$	1.7663214571055033	4.379645632831567
4	$-2.8116945464551947 \times 10^{-35}$	3.467191393500518	7.911482913171373
5	$3.213679273650739 \times 10^{-46}$	4.568362243560916	10.164215033300993
6	$-2.4186768354306914 \times 10^{-57}$	5.6380242360553074	12.34244169
7	-0.7517573646187425	0.2406197411571071	1.305650226807804

Table 3.3: This table shows the parameters for the polynomial fit of the stopping distance data, as shown in Eq. (3.3.36)

polynomial fit Eq. (3.3.36), the fractional error δ is considered - see Eq. (3.3.22).

Fig. 3.23 shows plots of δ against $\hat{E}_{init}$ and $\hat{T}$ for a variety of chemical potentials. The fractional error remains relatively small $\delta < 10^{-6}$, as shown by the plots. This is much smaller than the fractional difference caused by the physical effect of the chemical potential, as measured by the variable Δ_μ - see Eq. (3.3.23). Once more, this indicates the plot is a good fit, when it comes to describing the physical effect of the chemical potential.

The first thing of note with regards to the polynomial fit is the $n = 0$ term in Tab. 3.3. It is easy to see the fitted parameters match the analytic form of the stopping distance for the Sakai-Sugimoto model computed in Sub. 2.5.1.

Comparison with the non-zero R-charge case and D_3/D_7 flavour case

Having obtained the fit for the stopping distance in the Sakai-Sugimoto case, let us now compare the stopping distance with non-zero flavour chemical potential μ_f and non-zero R-charged chemical potential μ_R from Sec. 3.2. The domains in the

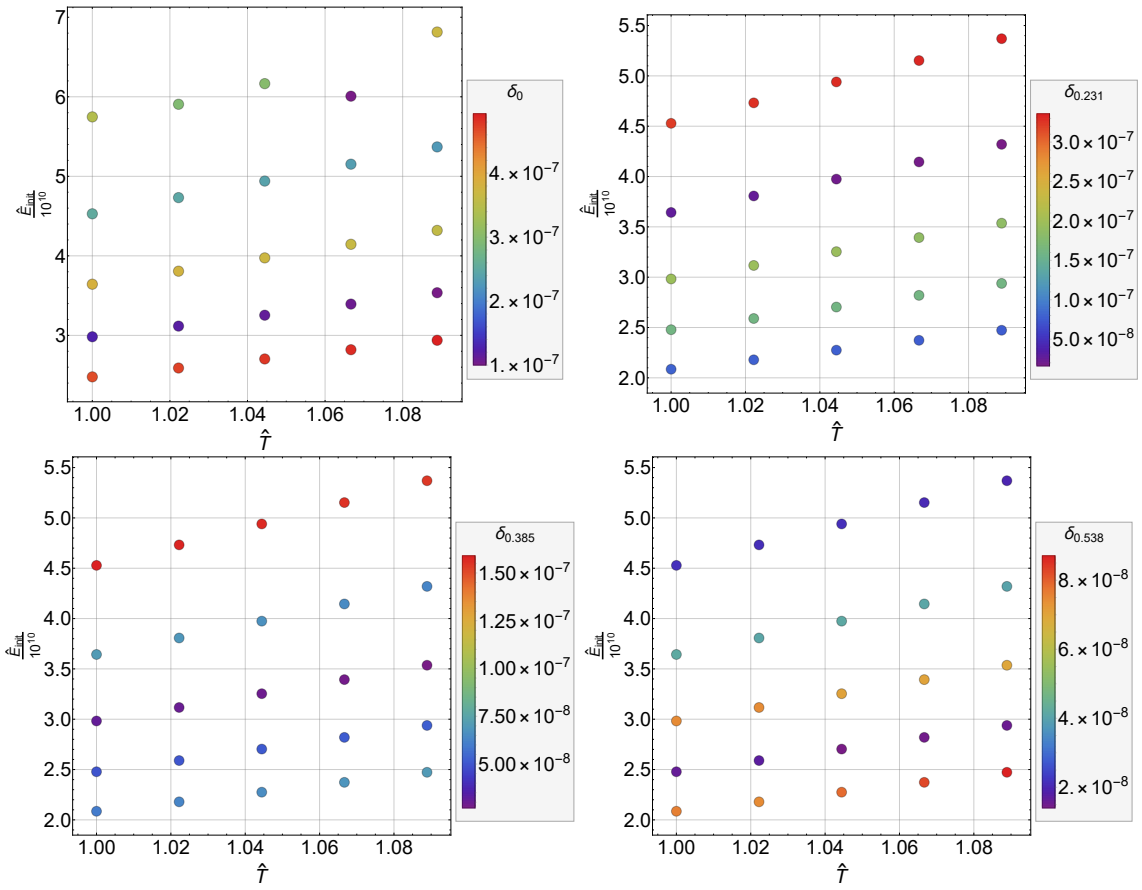

Figure 3.23: The plot shows $\delta_{\hat{\mu}}$ plotted against $\hat{E}_{init}$ and $\hat{T}$ for different chemical potentials: $\hat{\mu} = 0$, $\hat{\mu} = 0.084$, $\hat{\mu} = 0.14$ and $\hat{\mu} = 0.22$. The colour of the points indicate the value of δ, as the legend describes for each plot.

$\left(\hat{\mu}_{f|R}, \hat{T}, \hat{E}_{init}\right)$ space must be chosen appropriately in order to perform this comparison.

Eq. (3.3.32) is used in order to obtain the physical dimensionless chemical potential and physical dimensionless energy:

$$\begin{aligned} \bar{\mu}_f &= \frac{\mu_f}{T} \\ &= \lambda_S \frac{T}{M_{KK}} \hat{\mu}_f \end{aligned} \tag{3.3.37}$$

$$\begin{aligned} \bar{E}_f &= E_f L \\ &= \frac{\lambda_S}{4M_{KK}L}\hat{E}_f \end{aligned} \tag{3.3.38}$$

Using Eq. (3.3.38), one can convert the dimensionless parameters used in the numerical investigation $(\hat{\mu}_f, \hat{E}_f)$ to the physical parameters, and use this domain for these parameters to compute the stopping distance in the R-charged case. The values $M_{KK} = 949MeV$, $L^{-1} = 450MeV$ and $\lambda_S = 25.1$ are used in order to achieve this.

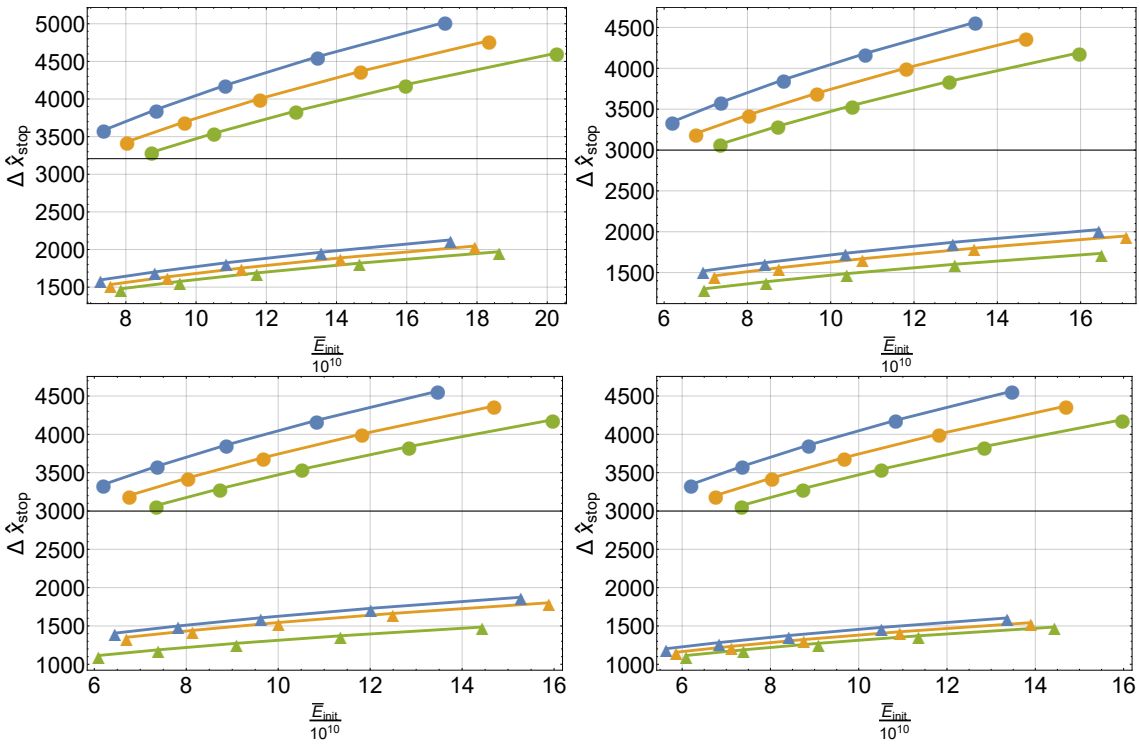

Figure 3.24: This plot shows how the stopping distance varies with $\bar{E}_{init}$ for a variety of of $\bar{\mu}$ and $\hat{T}$. This is done for the R-charged chemical potential $\bar{\mu}_R$ and the flavour charged chemical potential $\bar{\mu}_f$. The ● represent the flavour charged case and the ▲ represent the R-charged case. Three different temperatures: ● $\hat{T} = 1$, ● $\hat{T} = 1.04$ and ● $\hat{T} = 1.08$ are considered. Each of the four plots are obtained by selecting four different chemical potentials: top left is for $\bar{\mu}_{f/R} = 0$, top right is for $\bar{\mu}_{f/R} = 1$, bottom left is for $\bar{\mu}_{f/R} = 1.67$, and $\bar{\mu}_{f/R} = 2.67$.

Fig. 3.24 shows plots of the stopping distance against $\bar{E}_{init}$, varying both $\hat{T}$ and $\bar{\mu}_{f|R}$. The $\bar{\mu}_{f|R} = 0$ shows the AdS_5 and Sakai-Sugimoto comparison performed in Chapter 2. As the chemical potential is turned on, the stopping distance is affected more by $\bar{\mu}_R$ than $\bar{\mu}_f$, following the pattern observed in the D_3/D_7 case - see Sub. 3.3.2. As explained in Sub. 3.3.2, this seems to be due to the very nature of using the gauge field on the brane vs. the effect of the gauge fields on the background metric. The fact the correction is linear for the flavour cases seems to directly come from coupling the gauge field to the end point. The quadratic nature of the correction for the R-charged case seems to arrive from the fact that the black hole metric is symmetric under $q \to -q$ transformations that leads to q^2 dependence in the metric.

The non-trivial energy and temperature dependence of the correction is also a feature that is consistent with both flavour charge cases. This is clear from the polynomial fit Eq. (3.3.36).

Having compared the finite chemical potential Sakai-Sugimoto case with the R-charged case, let us compare the two flavour charge cases. Fig. 3.25 shows the plots comparing the stopping distance for these systems for different temperatures and chemical potentials. It is important to note that the plots are obtained by fixing the physical chemical potential $\bar{\mu}_f$ and $\bar{E}_f$, given by the definitions in Eq. (3.3.25) and Eq. (3.3.38). For all chemical potentials and temperatures, the Sakai-Sugimoto case shows that the effect of the chemical potential is much smaller than in the D_3/D_7 case. This difference seems to increase as the chemical potential increases. It can be clearly seen by the coefficient of the first order correction obtained from the polynomial fit.

$$\Delta x_A^{(1)} = -\frac{1.765\bar{E}^{0.05754}}{\hat{T}^{1.0667}}\bar{\mu}_f \tag{3.3.39}$$

$$\Delta x_S^{(2)} = -\frac{3.172}{\bar{E}^{0.00147}\hat{T}^{0.992}}\bar{\mu}_f \tag{3.3.40}$$

The A subscript denotes the D_3/D_7 case and the S subscript denotes the Sakai-Sugimoto case. It is important to note that $\hat{E}$ have been converted to $\bar{E}$ and this leads to the different coefficients shown here compared to those shown in Tab. 3.2 and Tab. 3.3. Whilst the coefficient of the correction term is larger for the Sakai-Sugimoto case, the negative power for the energy reduces the effect of the chemical potential. On the other hand, the D_3/D_7 case has a positive power and so the effect of the chemical potential is exacerbated in the D_3/D_7 case.

3.4 Comparison of the Jet Quenching Parameter for the flavour and R-charged cases

In Sec. 3.3, the stopping distance for light probes with non-zero flavour charge chemical potential was numerically computed. Using the numerics, polynomial fits were obtained for the data. In this section, the fits are used to find expressions for the jet quenching parameter $\hat{q}$.

Using Eq. (2.7.1) in Sec. 2.7 and Eq. (3.3.21) and Eq. (3.3.36), the jet quenching parameter is computed. The fixed energy density condition is used to define temperature and the physical dimensionless parameters are considered, in order to match the domains of both the D_3/D_7 and Sakai-Sugimoto cases - see Eq. (3.3.25) and Eq. (3.3.38).

Fig. 3.26 shows the plots of the jet quenching parameter as a function of the zero chemical potential case $\left(\frac{\hat{q}}{\hat{q}(\mu=0)}\right)$ vs. $\bar{\mu}$. The first thing to note is that the effect of the chemical potential is so small for the Sakai-Sugimoto model, and so the following parameter has been used for this model:

$$\tau = \frac{\hat{q}}{\hat{q}(\mu = 0)} - 1 \tag{3.4.1}$$

This agrees with the behaviour of the stopping distance, as seen in Fig. 3.25.

The second point of interest is the fact that the D_3/D_7 flavour chemical potential increases the jet quenching parameter less significantly than the R-charged case. The fact that the effect seems so small for the flavour case indicates that the non-zero chemical potentials in the plasma at experiments such as the RHIC and LHC experiments has an incredibly small effect.

In [RFFN16] , the authors construct a bottom up holographic model for the QGP. This involved a Einstein-Maxwell-Dilaton theory that was numerically solved to model the plasma. The non-zero chemical potential, described as the Baryon chemical potential, is related to the gauge fields living in the bulk. Using this model, a variety of observables including probe energy loss is investigated. The Wilson loop method is used to compute $\hat{q}$, and it is found that the chemical potential does indeed increase $\hat{q}$ as expected.

The increase in the $\hat{q}$ found in this paper seems to be larger than the observed effect in the falling string case computed above. This seems to be a feature of introducing the chemical potential through bulk gauge fields, rather than probe gauge fields living on the brane. Whilst the gauge fields studied in the R-charged case come strictly from top-down supergravity theories rather than a bottom up approach, the gauge fields couple to the metric in both cases. The string is affected through the coupling to the metric, rather than a direct coupling to the gauge field itself. This is significantly different to the direct end point coupling of the gauge field on the probe brane, described in the flavour chemical potential case.

3.5 Summary

In this chapter, the finite end point momentum strings, described in Chapter 2, were used to analyse the energy loss of light probes traversing a medium with non-zero chemical potential. The two cases of interest were the R-charged chemical potential and the flavour symmetry chemical potential.

The R-charge case is where the gauge fields, required to introduce chemical potentials, arise from the compactification of the compact part of the gravitational manifold. The particular $5D$ charged black hole solution is a solution of $\mathcal{N} = 2$ supergravity. First, the stopping distance for the finite end point momentum falling string was computed in this background and whilst the full analytic expressions were found to be non-trivial, small chemical potential expansions could be extracted for three separate cases. Secondly, analytic expressions for the shooting string rate of energy loss were also obtained. Once more small chemical potential expansions were written and these can be used to compute the jet nuclear modification factor R_{AA} in further work.

The three cases for the charge were particular choices within the three dimensional parameter space of the Cartan subalgebra for the R-symmetry. It was found that the stopping distance seemed to be independent to the direction within this parameter space for small chemical potential.

The stopping distance expressions could be used to compute the time-like light flavour jet quenching parameter - see Sec. 2.7. It was curious to note that the energy and temperature dependence factors out of the small chemical potential expansion, and thus scales the overall stopping distance rather than having an effect term by term. Finally, the parameter was compared to the light-like probe method and it was found that the effect of the chemical potential is greater in the falling string

case, than the Wilson loop case. It was also found that the existence of a global maximum is a universal feature for both methods, when fixing the ratio $\kappa = \frac{8\pi^2\rho^2}{s^2}$ rather than the chemical potential.

Finally, the impact of higher derivative corrections were analysed in the context of the R-charge black holes. The magnitude of the correction for the stopping distance decreased with chemical potential, such that a large chemical potential could negate the effect of the higher derivative correction. The jet quenching parameter was also computed and it was found that a negative λ_D is required to reduce the jet quenching parameter, as is desirable in the context of matching the values obtained in particular phenomenological models.

It was shown that it is not possible to choose a suitable λ_D, such that $\hat{q}$ for the LHC cases are lowered significantly towards the values obtained in phenomenological models in [Bur+14] and [CLQW18], whilst keeping $\hat{q}$ for the RHIC case within the range obtained in the model used in [Ada+08]. The value that reduces $\hat{q}_{LHC}$ the most is $\lambda_D = -43.44$, however this is not valid as it is required that $\lambda_D < \sqrt{\lambda} \sim 3.42$. In other words, the higher derivative correction does not account for the over prediction that one obtains using the falling string method for $\hat{q}_{LHC}$.

The next case of interest was the chemical potential associated to flavour symmetry, rather than R-charge symmetry. In this case, the gauge fields live on the probe branes introduced to include flavour multiplets in the dual gauge theory. These gauge fields couple to string end points and affect the string trajectory, and hence the light probes in a significantly different manner.

The inclusion of the boundary gauge coupling was shown to prevent the einbein transformation used in Chapter 2. The simplification to a null geodesic or even a charged null particle is not possible. The conserved quantities, required to simplify

the end point equations of motion to first order equations, do not exist and one requires to solve the full second order equations numerically.

Both the D_3/D_7 and Sakai-Sugimoto models with finite chemical potential were considered. The numerical system provided a few challenges, including the competition between the $E_{final} = 0$ boundary condition and the near boundary initial conditions we wanted to solve for. Also, the increase in numerical error with increasing E_{final} also provided some difficulties. Through some preliminary investigations, the final domain of investigation could be chosen in a way to balance these two issues.

For both systems, the stopping distance was numerically solved for and polynomials were fitted to the data. In both cases, the flavour chemical potential seemed to affect the stopping distances less than the R-charged black hole; the stopping distances were decreased more substantially by the R-charged chemical potential. In particular, the Sakai-Sugimoto model seemed particularly robust to changes in chemical potential. This could be clearly seen when directly comparing to the D_3/D_7 model.

Finally, the polynomial fits for both cases were used to compute the jet quenching parameter. As the analysis of the stopping distance alluded to, the parameter is much less affected by the flavour symmetry chemical potential. In fact, the Sakai-Sugimoto model is essentially unchanged for $\bar{\mu} < 1$. In the flavour charge cases, the polynomial fit shows non-trivial temperature dependence term by term in the expansion, and so cannot be factored out like in the R-charged case. This means the ratio $\frac{\hat{q}}{\hat{q}(\mu=0)}$ has significant temperature dependence for the flavour case, however the R-charge case does not.

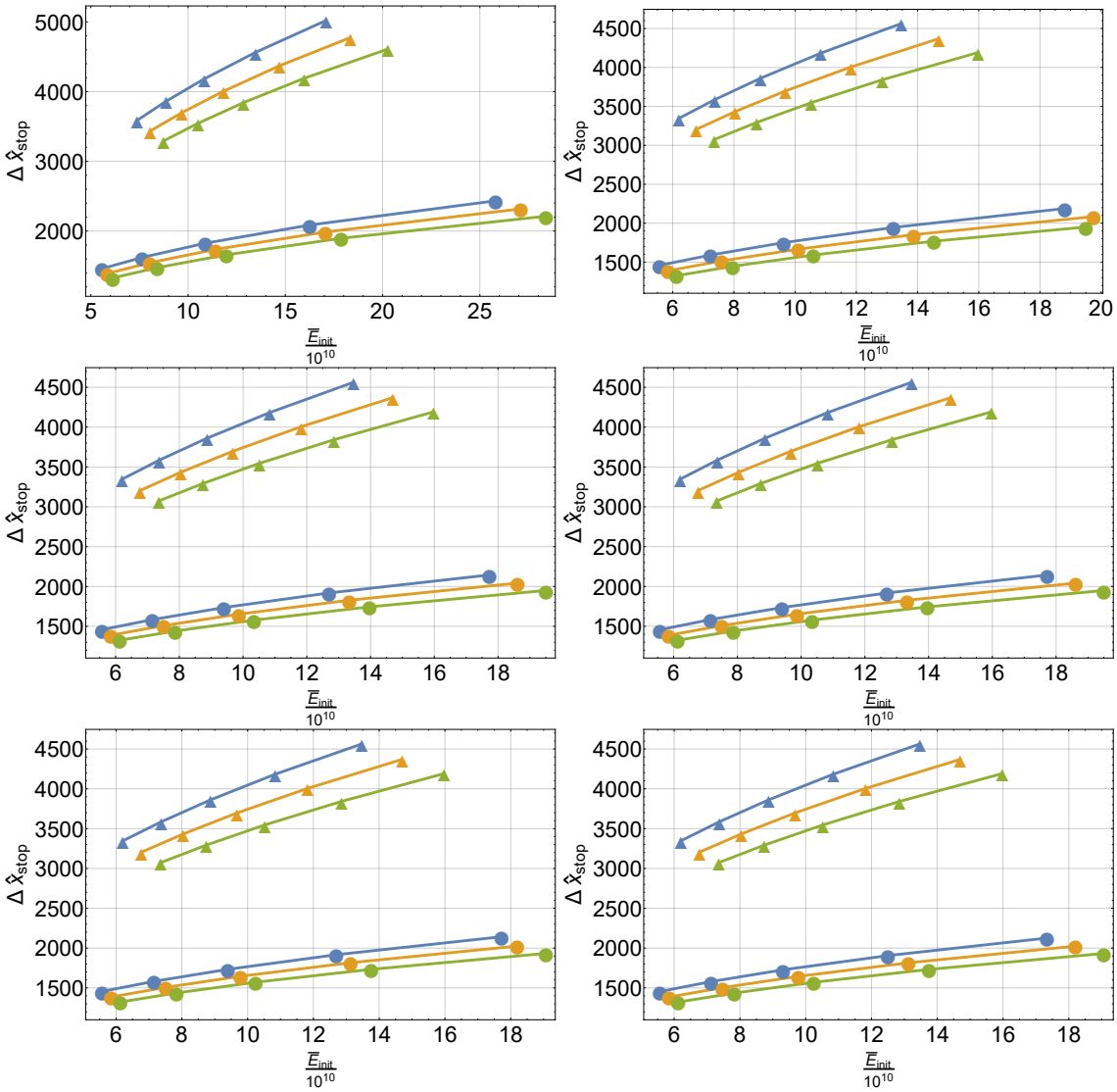

Figure 3.25: This plot shows how the stopping distance varies with $\bar{E}_{init}$ for a variety of of $\bar{\mu}$ and $\hat{T}$. This is done for the D_3/D_7 chemical potential $\bar{\mu}_A$ and the Sakai-Sugimoto flavour charged chemical potential $\bar{\mu}_S$. The ● represent the D_3/D_7 case and the ▲ represent the Sakai-Sugimoto case. Three different temperatures: ● $\hat{T} = 1$, ● $\hat{T} = 1.04$ and ● $\hat{T} = 1.1$ are considered. Each of the six plots are obtained by selecting four different chemical potentials: top left is for $\bar{\mu}_f = 0$, top right is for $\bar{\mu}_f = 1$, middle left is for $\bar{\mu}_f = 1.34$, middle right is for $\bar{\mu}_f = 1.67$, bottom left is for $\bar{\mu}_f = 2.34$, and the bottom right is for $\bar{\mu}_f = 2.67$.

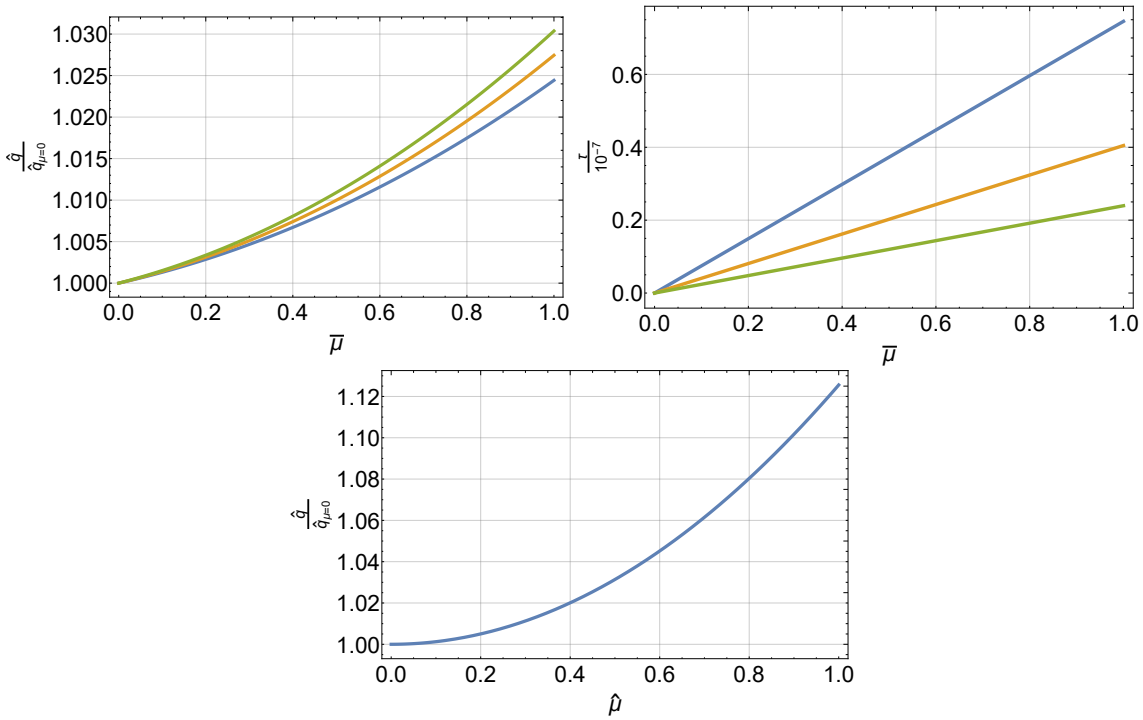

Figure 3.26: This plot shows three plots for the jet quenching parameter with chemical potential vs $\bar{\mu} = \frac{\mu}{T}$. The top left plot shows $\frac{\hat{q}}{\hat{q}(\mu=0)}$ vs $\bar{\mu}$ for the D_3/D_7 case. The top right plot shows $\tau = \frac{\hat{q}}{\hat{q}(\mu=0)} - 1$ vs $\bar{\mu}$ for the Sakai-Sugimoto model. The colour of the lines represent $T = 280MeV$, $T = 370MeV$ and $T = 470MeV$. The bottom plot shows the plot for $\frac{\hat{q}}{\hat{q}(\mu=0)}$ for the R-charged case. As noted previously, this is temperature independent.

Chapter 4

Light Quark energy loss in the Anisotropic Plasma

In Chapter 3, the light probe jet quenching with finite chemical potential was investigated. It was noted in Sec. 1.1.1 that after a quick equilibration time, the QGP produced in heavy ion collisions reaches an anisotropic state. This is caused by peripheral collisions in particular. In this chapter, the finite end point momentum strings are used to probe a field theory in an anisotropic strongly coupled plasma state, dual to a gravitational system found by [MT11].

In Sec. 4.2, the stopping distance is calculated for all three types of motion ($x-y$ plane, z-direction and the $x-z$ plane) of the falling string. In Sec. 4.4, the shooting string energy loss rate is computed for all the above directions. Finally, the stopping distances are used to compute the jet quenching parameter $\hat{q}$, by using the method described in Sec. 2.7. This is done in Sec. 4.6.

4.1 Review of the Anisotropic gravitational dual

In [MT11], the authors generalise a Type IIB SUGRA solution found in [ALT09] to the finite temperature case. The resulting solution describes a gravitational dual

to a strongly coupled anisotropic non-Abelian plasma. Whilst the plasmas created at the heavy ion collisions at the LHC and RHIC are known to reach a locally isotropic state, they initially carry a small local anisotropy. It is with this in mind that the stopping distance and energy loss rates of light probes are investigated. It is interesting to note how small anisotropies in the initial stages of the plasma formation may influence energy losses of the probes.

In Appendix E, the gravitational dual to the anisotropic plasma, found by Mateos and Trancanelli in [MT11], is described. The field theory viewpoint is that the canonical $\mathcal{N} = 4$ Super Yang-Mills theory is deformed by a space-time dependent θ term. To be more specific, the θ term is dependent on the z direction; this is the direction in which the anisotropy is introduced. These space-time dependent θ terms have been used to introduce so called 'bubbles" into the plasma [KZ07]. The bubbles are consequences of the CP-violation introduced due to the non-trivial vacuum structure of QCD.

The full deformed action is given by:

$$S_{Aniso.} = S_{\mathcal{N}=4} + \frac{1}{8\pi}\int \theta(z)\mathrm{Tr}F \wedge F \tag{4.1.1}$$

This is a marginally relevant deformation of the conformal $\mathcal{N} = 4$ theory, and hence introduces the notion of a renormalisation scale into the system. This is explicitly seen in [MT11], when the authors compute the stress-energy tensor.

The gravitational dual is given by a solution to the Einstein-Dilaton-Axion theory, as shown in Appendix E. To be more specific, the full gravitational dual is given by $ds^2_{Aniso.} \times S^5$, where $ds^2_{Aniso.}$ is the solution to the Einstein-Dilaton-Axion theory. The solution described in Appendix E is in the Einstein frame. In order to compute the string endpoint trajectories for the light probes, this solution needs to

be transformed into the string frame. The string frame metric is given by:

$$ds^2_{string} = e^{\frac{1}{2}\phi(r)} ds^2_{Einstein} \tag{4.1.2}$$

It is also useful to change co-ordinates from the inverted radial co-ordinate u into $r = \frac{L^2}{u}$. This helps when performing the integrals required to compute the light probe trajectories.

4.2 Stopping Distance

In this section, the stopping distance for the light probes traversing the anisotropic plasma is computed. As noted in Appendix E, the anisotropy is introduced in the z-direction, but rotational symmetry still remains in the $x-y$ plane. The stopping distance is first computed in the the x and z directions independently, taking into account this rotational invariance. The stopping distance is then computed for motion within the $x-z$ plane itself.

4.2.1 Motion in the $x-y$ plane

Let us compute the stopping distance for motion in the $x-y$ plane. The rotational symmetry in this plane means the stopping distance in the x-direction captures all motion in this plane. Consider the conserved quantities associated to both time and x translation symmetry:

$$\begin{aligned} E_{geo} &= \frac{(r^4 - r_H^4)}{r^2 L^2} \frac{dt}{d\xi} \\ &+ \frac{a^2 L^2}{r_H^2} \left[\frac{(r^4 + 4r_H^4) \log\left[1 + \frac{r_H^2}{r^2}\right] - r_H^4(5\log 2 - 1) - r^2 r_H^2}{12 r^2} \right] \frac{dt}{d\xi} \end{aligned} \tag{4.2.1}$$

$$P^x_{geo} = \frac{r^2}{L^2}\frac{dx}{d\xi} \tag{4.2.2}$$

The initial conditions are the canonical conditions used for the stopping distance throughout the investigations. At $t = 0$, $r = r_0$ and $x = y = z = 0$ and $\frac{dr}{d\xi} = 0$. Since the focus is on the x-direction, $\frac{dy}{d\xi} = \frac{dz}{d\xi} = 0$ at $t = 0$. These conditions and Eq. (4.2.2) allow us to obtain an expression for $\frac{dx}{dt}$. This can then be used in conjunction with the null condition to find $\frac{dx}{dr}$, in the canonical method used throughout. The form of this is non-trivial and impossible to integrate. Since the near boundary limit $\frac{r_H}{r_0} \to 0$ is the initial condition of interest, one can use the near boundary expansion method explained in Appendix C.

Before expanding in powers of $\omega = \frac{r_H}{r_0}$, one first retains the expansion in a^2. In other words, the near boundary expansion is performed order by order in the expansion in a^2. The integrand of each coefficient of the a^2 expansion in $\frac{dx}{dr}$ is analytic at $r = 0$. The reasoning in Appendix C shows us that the leading order term in the stopping distance can be obtained by integrating the leading order term in the $\frac{dx}{dr}$ expansion. The stopping distance is thus given by:

$$\Delta x_{stop} = -\frac{L^2 r_0}{r_H^2}\int_1^0 d\hat{r}\left[\frac{1}{\sqrt{1-\hat{r}^4}}\right] + \frac{a^2 L^6 r_0}{r_H^4}\int_1^0 d\hat{r}\left[\frac{\log 1024 - 1}{48\sqrt{1-\hat{r}^4}}\right] \tag{4.2.3}$$

$$= \frac{\Gamma\left[\frac{1}{4}\right]^2}{4\sqrt{2\pi}}\frac{L^2 r_0}{r_H^2} - a^2\left[\frac{\Gamma\left[\frac{1}{4}\right]^2(\log 1024 - 1)}{192\sqrt{2\pi}}\right]\frac{L^6 r_0}{r_H^4} \tag{4.2.4}$$

In order to perform the expansion, the radial co-ordinate is measured in units of r_0 i.e. the co-ordinate transformation $r = \hat{r} r_0$.

Having acquired this expression for the stopping distance, let us analyse the energetics of the system. The endpoint equation of motion for the time component gives an

expression for the energy loss rate. Each coefficient in the a^2 expansion is analytic at $r = 0$ once more, and thus one can expand each coefficient to leading order in $\omega = \frac{r_H}{r_0}$. The boundary condition for the energy is that all endpoint energy is lost at the horizon. The initial energy can thus be written as :

$$\begin{aligned} E_{init} &= \frac{r_0^3}{r_H^2 \alpha'} \int_0^1 d\hat{r} \left[\frac{\hat{r}^2}{2\pi\sqrt{1-\hat{r}^4}} \right] \\ &- \frac{a^2 L^4 r_0^3}{r_H^4 \alpha'} \int_0^1 d\hat{r} \left[\frac{\hat{r}^2 \left(\log 1024 - 1\right)}{96\pi\sqrt{1-\hat{r}^4}} \right] \qquad (4.2.5) \\ &= \frac{\pi^{\frac{1}{2}}}{2^{\frac{1}{2}} \Gamma\left[\frac{1}{4}\right]^2} \frac{r_0^3}{r_H^2 \alpha'} \\ &- a^2 \left[\frac{(\log 1024 - 1)\left[E(-1) - K(-1)\right]}{96\pi} \right] \frac{L^4 r_0^3}{r_H^4 \alpha'} \qquad (4.2.6) \end{aligned}$$

Let us invert this expression in order to write r_0 as a function of E_{init} and r_H.

$$\begin{aligned} r_0 &= \left(\frac{2}{\pi}\right)^{\frac{1}{6}} \left[\Gamma\left[\frac{1}{4}\right]^2 E_{init} r_H^2 \alpha' \right]^{\frac{1}{3}} \\ &+ a^2 L^4 \left[\frac{\log 1024 - 1}{72 \times 2^{\frac{5}{6}} \pi^{\frac{1}{6}}} \right] \left[\frac{\Gamma\left[\frac{1}{4}\right]^2 E_{init} \alpha'}{r_H^4} \right]^{\frac{1}{3}} \qquad (4.2.7) \end{aligned}$$

Using the inversion in Eq. (4.2.7) and the stopping distance expression Eq. (4.2.4), one can write the stopping distance in terms of the energy:

$$\Delta x_{stop} = \frac{L^2 \Gamma\left[\frac{1}{4}\right]^{\frac{8}{3}}}{4 \times 2^{\frac{1}{3}} \pi^{\frac{2}{3}}} \left[\frac{E_{init} \alpha'}{r_H^4} \right]^{\frac{1}{3}} - a^2 L^6 \left[\frac{\log 1024 - 1}{288} \right] \left[\frac{\Gamma\left[\frac{1}{4}\right]^8 E_{init} \alpha'}{2\pi^2 r_H^{10}} \right]^{\frac{1}{3}} \qquad (4.2.8)$$

The three cases of fixed temperature, energy density and entropy density for the

plasma are the systems of interest. Thus, the horizon radius r_H needs to be eliminated in favour of these physical parameters. First, let us consider the temperature of the black hole in order to eliminate the horizon radius r_H. The temperature of the black hole is found in the canonical manner and is given by Eq. (E.0.11) in Appendix E. In terms of r_H (rather than the inverse horizon radius u_H), the temperature is given by:

$$T = \frac{r_H}{\pi L^2} + a^2 \frac{L^2}{48\pi r_H} [\log 32 - 2] \tag{4.2.9}$$

$$\Rightarrow r_H = \pi L^2 T - a^2 \frac{L^2}{48\pi T} [\log 32 - 2] \tag{4.2.10}$$

In the second line, the temperature expression has been inverted in order to obtain the expansion for r_H. By substituting this into Eq. (4.2.8), the stopping distance can be written as:

$$\Delta x^T_{stop} = \frac{\Gamma\left[\frac{1}{4}\right]^{\frac{8}{3}}}{2^{\frac{7}{3}}\pi^2\lambda^{\frac{1}{6}}}\left[\frac{E_{init}}{T^4}\right]^{\frac{1}{3}} - \hat{a}_T^2 \frac{\Gamma\left[\frac{1}{4}\right]^{\frac{8}{3}}}{96\times 2^{\frac{1}{3}}\pi^4\lambda^{\frac{1}{6}}}\left[\frac{E_{init}}{T^4}\right]^{\frac{1}{3}} \tag{4.2.11}$$

The dimensionless parameter $\hat{a}_T$ has been defined as $\hat{a}_T = \frac{a}{T}$. The choice of scale is a natural choice that validates the small a expansion for the series. This is the main requirement for the small a expansion solution for the action Eq. (E.0.3). It is important to note that the energy dependence of the correction term is the same as the isotropic term, and thus for $\hat{a} \ll 1$, the series expansion is valid.

The string length α' has been eliminated using the holographic relationship $L^4 = \lambda\alpha'$. It is interesting to note that the first order correction reduces the stopping distance.

The t'Hooft coupling plays an interesting role, as it scales with the energy. In

fact, one can define a scaled energy $\bar{E}_{init} = \frac{E_{init}}{\sqrt{\lambda}}$ and the series can be re-written as :

$$\Delta x^{T}_{stop} = \frac{\Gamma\left[\frac{1}{4}\right]^{\frac{8}{3}}}{2^{\frac{7}{3}}\pi^{2}}\left[\frac{\bar{E}_{init}}{T^{4}}\right]^{\frac{1}{3}} - \hat{a}_{T}^{2}\frac{\Gamma\left[\frac{1}{4}\right]^{\frac{8}{3}}}{96\times 2^{\frac{1}{3}}\pi^{4}}\left[\frac{\bar{E}_{init}}{T^{4}}\right]^{\frac{1}{3}} \tag{4.2.12}$$

Let us now consider the system at fixed entropy. The entropy density s is given by Eq. (E.0.12) as a function of T. Using Eq. (4.2.10), the entropy is written as a function of the horizon radius r_H.

$$\begin{aligned} \hat{s} &= \frac{r_H^3}{2\pi L^6} + \frac{5a^2 r_H \log 2}{32\pi L^2} \\ \Rightarrow r_H &= L^2\left(2\pi\hat{s}\right)^{\frac{1}{3}} - \frac{5a^2L^2\log 2}{48\left(2\pi\hat{s}\right)^{\frac{1}{3}}} \end{aligned} \tag{4.2.13}$$

It is important to note that a scaled entropy density $\hat{s} = N_c^{-2}s$ has been defined, in order to remove the colour number dependence of the stopping distance.

Using the inversion in Eq. (4.2.13) and Eq. (4.2.8), the final stopping distance for fixed $\hat{s}$ is given by:

$$\Delta x^{\hat{s}}_{stop} = \frac{\Gamma\left[\frac{1}{4}\right]^{\frac{8}{3}}}{4\times 2^{\frac{7}{9}}\pi^{\frac{10}{9}}}\left[\frac{\bar{E}^3_{init}}{\hat{s}^4}\right]^{\frac{1}{9}} + \hat{a}_{\hat{s}}^{2}\frac{\Gamma\left[\frac{1}{4}\right]^{\frac{8}{3}}}{576\times 2^{\frac{4}{9}}\pi^{\frac{16}{9}}}\left[\frac{\bar{E}^3_{init}}{\hat{s}^4}\right]^{\frac{1}{9}} \tag{4.2.14}$$

The dimensionless parameter $\hat{a}_{\hat{s}}$ is defined by $\hat{a}_{\hat{s}} = \frac{a}{\hat{s}^{\frac{1}{3}}}$ for the fixed entropy density case.

Finally, the fixed energy density case is considered. Using the energy density in Eq. (E.0.12) and Eq. (4.2.10), the energy density is expressed as a function of r_H:

$$\begin{aligned}\hat{\epsilon} &= \frac{3\pi^2 T^4}{8} + \frac{a^2 T^2}{32} \\ \Rightarrow r_H &= \frac{2^{\frac{3}{4}}\sqrt{\pi} L^2 \hat{\epsilon}^{\frac{1}{4}}}{3^{\frac{1}{4}}} + \frac{a^2 L^2 (1 - 5\log 2)}{16 \times 6^{\frac{3}{4}}\sqrt{\pi}\hat{\epsilon}^{\frac{1}{4}}} \end{aligned} \tag{4.2.15}$$

Once more the colour number dependence is scaled into the redefinition $\hat{\epsilon} = N_c^{-2}\epsilon$. So the final stopping distance for fixed energy density is given by:

$$\Delta x^{\hat{\epsilon}}_{stop} = \left(\frac{3}{2}\right)^{\frac{1}{3}} \frac{\Gamma\left[\frac{1}{4}\right]^{\frac{8}{3}}}{8\pi^{\frac{4}{3}}} \left[\frac{\bar{E}_{init}}{\hat{\epsilon}}\right]^{\frac{1}{3}} - \hat{a}^2_{\hat{\epsilon}} \frac{\Gamma\left[\frac{1}{4}\right]^{\frac{8}{3}}}{384 \times 96^{\frac{1}{6}}\pi^{\frac{7}{3}}} \left[\frac{\bar{E}_{init}}{\hat{\epsilon}}\right]^{\frac{1}{3}} \tag{4.2.16}$$

where $\hat{a}_{\hat{\epsilon}} = \frac{a}{\hat{\epsilon}^{\frac{1}{4}}}$.

4.2.2 Motion in the z-direction

In this section, the stopping distance in the z-direction is computed. The anisotropy requires a different result to the motion in the $x - y$ plane. As noted in Appendix E, the field theory action is indeed z-translation invariant, even though the θ term seems to break the symmetry at first glance. However, one can integrate this term by parts and show that this is not the case. The Einstein-Dilaton-Axion action dual to the field theory is more self-evidently z-translation invariant.

Consider the conserved quantities associated with time and z translations.

$$\begin{aligned} E_{geo} &= \frac{(r^4 - r_H^4)}{r^2 L^2}\frac{dt}{d\xi} \\ &+ \frac{a^2 L^2}{r_H^2}\left[\frac{(r^4 + 4r_H^4)\log\left[1 + \frac{r_H^2}{r^2}\right] - r_H^4(5\log 2 - 1) - r^2 r_H^2}{12 r^2 r_H^2}\right]\frac{dt}{d\xi} \end{aligned} \tag{4.2.17}$$

$$P^z_{geo} = \left[\frac{r^2}{L^2} + a^2\frac{r^2L^2}{4r_H^2}\log\left[1+\frac{r_H^2}{r^2}\right]\right]\frac{dz}{d\xi} \tag{4.2.18}$$

Using these conserved quantities and the null constraint, one can obtain the integrand $\frac{dz}{dr}$. For the z-direction motion, the initial conditions are slightly different. At $t=0$, $r=r_0$ and $x=y=z=0$ and $\frac{dr}{d\xi}=0$. Now the focus is on the z-direction, so $\frac{dx}{d\xi}=\frac{dy}{d\xi}=0$ at $t=0$. Once more, the explicit expression for $\frac{dz}{dr}$ is non-trivial, and its integral is also complicated. The stopping distance is found by integrating this in the near boundary limit as in Appendix C. The stopping distance is given by:

$$\begin{aligned}\Delta z_{stop} &= -\frac{L^2r_0}{r_H^2}\int_1^0 d\hat{r}\left[\frac{1}{\sqrt{1-\hat{r}^4}}\right] + \frac{a^2L^6r_0^3}{r_H^6}\int_1^0 d\hat{r}\left[\frac{\hat{r}^2}{8\left(1+\hat{r}^2\right)\sqrt{1-\hat{r}^4}}\right] \\ &= \frac{\Gamma\left[\frac{1}{4}\right]^2}{4\sqrt{2\pi}}\frac{L^2r_0}{r_H^2} - \frac{a^2L^6r_0^3}{r_H^6}\frac{\left[\Gamma\left[\frac{1}{4}\right]^4-8\pi^2\right]}{64\sqrt{2\pi}\Gamma\left[\frac{1}{4}\right]^2}\end{aligned} \tag{4.2.19}$$

Now let us consider the energetics of the system. Once more, the energy is found by considering the time component of the endpoint equations of motion. The coefficients of the a^2 expansion are analytic at $r=0$, so one can take the integral of the leading term in the near boundary expansion. This integral is again taken with the boundary condition that all the probe energy is lost just as the probe enters the black hole. The initial energy can be written as:

$$\begin{aligned}E_{init} &= \frac{r_0^3}{r_H^2\alpha'}\int_0^1 d\hat{r}\left[\frac{\hat{r}^2}{2\pi\sqrt{1-\hat{r}^4}}\right] - \frac{a^2L^4r_0^5}{16\pi r_H^6\alpha'}\int_0^1 d\hat{r}\left[\frac{\hat{r}^4}{\left(1+\hat{r}^2\right)\sqrt{1-\hat{r}^4}}\right] \\ &= \frac{\pi^{\frac{1}{2}}}{2^{\frac{1}{2}}\Gamma\left[\frac{1}{4}\right]^2}\frac{r_0^3}{r_H^2\alpha'} - \frac{a^2L^4r_0^5}{r_H^6\alpha'}\left[\frac{24\pi^2-\Gamma\left[\frac{1}{4}\right]^4}{128\sqrt{2}\pi^{\frac{3}{2}}\Gamma\left[\frac{1}{4}\right]^2}\right]\end{aligned} \tag{4.2.20}$$

Having obtained this expression for the energy, let us now invert this to write r_0 as a

function of E_{init}. The fifth order polynomial is non-trivial to solve, so the inversion is performed order by order in a^2.

$$\begin{aligned} r_0 &= k_0 + a^2 k_1 \\ \Rightarrow k_0 &= \left(\frac{2}{\pi}\right)^{\frac{1}{6}} \left[\Gamma\left[\frac{1}{4}\right]^2 E_{init} r_H^2 \alpha'\right]^{\frac{1}{3}} \\ k_1 &= \left[\frac{\Gamma\left[\frac{1}{4}\right]^2 \left(24\pi^2 - \Gamma\left[\frac{1}{4}\right]^4\right)}{192\sqrt{2}\pi^{\frac{5}{2}}}\right] \frac{L^4 E_{init}\alpha'}{r_H^2} \end{aligned} \tag{4.2.21}$$

Using Eq. (4.2.21) and Eq. (4.2.19), the stopping distance in the z-direction is written as:

$$\Delta z_{stop} = \frac{L^2 \Gamma\left[\frac{1}{4}\right]^{\frac{8}{3}}}{4 \times 2^{\frac{1}{3}} \pi^{\frac{2}{3}}} \left[\frac{E_{init}\alpha'}{r_H^4}\right]^{\frac{1}{3}} - a^2 \left[\frac{\Gamma\left[\frac{1}{4}\right]^8 - 192\pi^4}{1536\pi^3}\right] \frac{L^6 E_{init}\alpha'}{r_H^4} \tag{4.2.22}$$

The stopping distance is now expressed in term of the three physical cases of interest; fixed temperature, entropy density and energy density. For fixed temperature, r_H is eliminated using Eq. (4.2.10).

$$\begin{aligned} \Delta z_{stop}^T &= \frac{\Gamma\left[\frac{1}{4}\right]^{\frac{8}{3}}}{2^{\frac{7}{3}} \pi^2 \lambda^{\frac{1}{6}}} \left[\frac{E_{init}}{T^4}\right]^{\frac{1}{3}} \\ &+ \frac{\hat{a}_T^2}{4608\pi^7 T} \left[16 \times 2^{\frac{2}{3}} \pi^3 (\log 32 - 2) \Gamma\left[\frac{1}{4}\right]^{\frac{8}{3}} \left[\frac{E_{init}}{\sqrt{\lambda} T}\right]^{\frac{1}{3}}\right. \\ &+ \left.\left(576\pi^4 - 3\Gamma\left[\frac{1}{4}\right]^8\right) \left[\frac{E_{init}}{\sqrt{\lambda} T}\right]\right] \end{aligned} \tag{4.2.23}$$

It is important to note that there are terms in the $\hat{a}^2$ coefficient that are lower order

in E_{init}. Consider the fixed temperature case and let us write $\frac{r_0}{r_H}$ as a function of E_{init} and T:

$$\begin{aligned}\frac{r_0}{r_H} &= \frac{2^{\frac{1}{6}}\Gamma\left[\frac{1}{4}\right]^{\frac{2}{3}}}{\pi^{\frac{1}{2}}}\left[\frac{E_{init}}{\sqrt{\lambda}T}\right]^{\frac{1}{3}} \\ &+ a^2\frac{(\log(32)-2)\Gamma\left[\frac{1}{4}\right]^{\frac{2}{3}}}{72\times 2^{\frac{5}{6}}\pi^{\frac{5}{2}}}\left[\frac{E_{init}}{\sqrt{\lambda}T}\right]^{\frac{1}{3}} \\ &- a^2\frac{\Gamma\left[\frac{1}{4}\right]^2\left(\Gamma\left[\frac{1}{4}\right]^4-24\pi^2\right)}{192\sqrt{2}\pi^{\frac{11}{2}}}\left[\frac{E_{init}}{\sqrt{\lambda}T}\right] \end{aligned} \tag{4.2.24}$$

From Eq. (4.2.24), it is clear that the near boundary limit $\frac{r_0}{r_H}\to\infty$ is equivalent to the limit $\left[\frac{E_{init}}{\sqrt{\lambda}T}\right]\to\infty$.

So the final expression, written in terms of the scaled energy $\bar{E}_{init}$, is given by:

$$\Delta z^T_{stop} = \frac{\Gamma\left[\frac{1}{4}\right]^{\frac{8}{3}}}{2^{\frac{7}{3}}\pi^2}\left[\frac{\bar{E}_{init}}{T^4}\right]^{\frac{1}{3}} - \hat{a}_T^2\left[\frac{\Gamma\left[\frac{1}{4}\right]^8-192\pi^4}{1536\pi^7}\right]\frac{\bar{E}_{init}}{T^2} \tag{4.2.25}$$

Using both Eq. (4.2.13) and Eq. (4.2.15), the stopping distance for the fixed entropy and fixed energy densities are given by:

$$\begin{aligned}\Delta z^{\hat{s}}_{stop} &= \frac{\Gamma\left[\frac{1}{4}\right]^{\frac{8}{3}}}{4\times 2^{\frac{7}{9}}\pi^{\frac{10}{9}}}\left[\frac{\bar{E}^3_{init}}{\hat{s}^4}\right]^{\frac{1}{9}} - \hat{a}_{\hat{s}}^2\left[\frac{\Gamma\left[\frac{1}{4}\right]^8-192\pi^4}{3072\times 2^{\frac{1}{3}}\pi^{\frac{13}{3}}}\right]\frac{\bar{E}_{init}}{\hat{s}^{\frac{2}{3}}} \\ \Delta z^{\hat{\epsilon}}_{stop} &= \left(\frac{3}{2}\right)^{\frac{1}{3}}\frac{\Gamma\left[\frac{1}{4}\right]^{\frac{8}{3}}}{8\pi^{\frac{4}{3}}}\left[\frac{\bar{E}_{init}}{\hat{\epsilon}}\right]^{\frac{1}{3}} - \hat{a}_{\hat{\epsilon}}^2\left[\frac{\Gamma\left[\frac{1}{4}\right]^8-192\pi^4}{4096\pi^5}\right]\frac{\bar{E}_{init}}{\hat{\epsilon}^{\frac{1}{2}}}\end{aligned} \tag{4.2.26}$$

A similar argument is used to neglect the extra term in the $\hat{a}^2$ coefficient for the fixed entropy and energy density cases. Once more, the stopping distance is decreased

by the introduction of the anisotropy parameter $\hat{a}$. It is important to note that the energy dependence of the correction term is larger than the $\hat{a} = 0$ term. This means that $\hat{a}$ must obey some constraints in order for the series to be valid as an approximation to the stopping distance. At a minimum, one requires the correction term to be smaller than the zeroth order term. This forces the following constraints for the various cases of interest:

$$\begin{aligned} \hat{a}_T &\ll \left(\frac{T}{\bar{E}_{init}}\right)^{\frac{1}{3}} \\ \hat{a}_{\hat{s}} &\ll \left(\frac{\hat{s}}{\bar{E}^3_{init}}\right)^{\frac{1}{9}} \\ \hat{a}_{\hat{\epsilon}} &\ll \left(\frac{\hat{\epsilon}}{\bar{E}^4_{init}}\right)^{\frac{1}{12}} \end{aligned} \tag{4.2.27}$$

These constraints do not violate the requirement $\hat{a}_T \ll 1$ for the small a expansion to be valid. This is because the expressions obtained are only valid in the near boundary limit.

4.2.3 Motion in the $x - z$ plane

In the last section, the stopping distance for motion in both the $x - y$ plane and the z-direction independently was studied. Let us now look at the general case motion in the $x - z$ plane. There will now be explicit dependence on a parameter characterising the angle in the $x - z$ plane that the string endpoint moves in.

As usual, let us consider the conserved quantities associated to translation symmetry. In particular, the introduction of movement in both the x and z directions means an additional conserved quantity for z translations must be considered. The expressions for these quantities are found in Eq. (4.2.2) and Eq. (4.2.18).

The initial conditions are the canonical conditions used for the stopping distance throughout the investigations. At $t = 0$, $r = r_0$ and $x = y = z = 0$ and $\frac{dr}{d\xi} = 0$. Since the focus is on the $x - z$ plane, $\frac{dy}{d\xi} = 0$ at $t = 0$. Given the conserved quantities and the null conditions, one can find expressions for both $\frac{dx}{dr}$ and $\frac{dz}{dr}$. In order to do this let us fully establish the initial conditions. Using the null conditions, one can establish a relationship between $\frac{dx_0}{d\xi}$ and $\frac{dz_0}{d\xi}$[1]. This relationship is re-written in terms of the momenta[2].

$$\begin{aligned} P_x &= \frac{\sqrt{r_0^4 - r_H^4 - P_z^2 L^4}}{L^2} \\ &- \frac{a^2 L^2}{24 r_H^2}\left[\frac{r_0^2 r_H^2 + r_H^4(\log 32 - 1) - (r_0^4 + 3P_z^2 L^4 + 4r_H^4)\log\left[1 + \frac{r_H^2}{r_0^2}\right]}{\sqrt{r_0^4 - P_z^2 L^4 - r_H^4}}\right] \end{aligned} \tag{4.2.28}$$

Given these initial conditions, the near boundary limit expansion of the stopping distance in both x and z directions are given by:

$$\begin{aligned} \frac{dx}{d\hat{r}} &= -\frac{L^2 r_0}{r_H^2}\frac{\sin\phi}{\sqrt{1-\hat{r}^4}} \\ &+ \frac{a^2 \sin\phi L^6}{\sqrt{1-\hat{r}^4}}\left[\frac{\hat{r}^2\cos^2\phi}{8\left(1+\hat{r}^2\right) r_H^3}\frac{1}{\omega^3} - \frac{5 + 3\cos(2\phi) - 20\log 2}{96 r_H^3}\frac{1}{\omega}\right] \\ \frac{dz}{d\hat{r}} &= -\frac{L^2}{\sqrt{1-\hat{r}^4} r_H}\frac{\cos\phi}{\omega} + \frac{a^2}{r_H^3}\frac{\hat{r}^2\cos^3\phi}{8\left(1+\hat{r}^2\right)\sqrt{1-\hat{r}^4}}\frac{L^6}{\omega^3} \end{aligned} \tag{4.2.29}$$

[1] E_{geo} is determined by the initial conditions and $\frac{dt_0}{d\xi} = 1$.

[2] The notation $P_{x/z}$ is used instead of $P_{geo}^{x/z}$.

where $\omega = \frac{r_H}{r_0}$ and $\hat{r} = \frac{r}{r_0}$. The momentum in the x-direction P_x is eliminated using Eq. (4.2.28). P_z is eliminated in favour of the angle ϕ, which is the angle the probe moves in the $x-z$ plane with the z-axis.

Before proceeding further, it is important to note that the next to leading order contribution to the near boundary expansion has been included for the a^2 coefficient of $\frac{dx}{d\hat{r}}$. This was included to note that the leading order term is proportional to $\cos\phi$, and hence vanishes when $\phi = \frac{\pi}{2}$. This means that the leading order a^2 contribution comes at a lower order in ω for the x-direction only case ($\phi = \frac{\pi}{2}$). The case $\phi < \frac{\pi}{2}$ is of interest in this section, so the leading order contribution in the ω expansion will be taken into account.

Integrating Eq. (4.2.29), one obtains:

$$\begin{aligned}
\Delta x_{stop} &= \sin\phi \frac{\Gamma\left[\frac{1}{4}\right]^2}{4\sqrt{2\pi}} \frac{L^2 r_0}{r_H^2} \\
&- a^2 \cos^2\phi \left[\frac{\Gamma\left[\frac{1}{4}\right]^4 - 8\pi^2}{64\sqrt{2\pi}\Gamma\left[\frac{1}{4}\right]^2}\right] \frac{L^6 r_0^3}{r_H^6} \qquad (4.2.30) \\
\Delta z_{stop} &= \frac{\Gamma\left[\frac{1}{4}\right]^2 \cos\phi}{4\sqrt{2\pi}} \frac{L^2 r_0}{r_H^2} - a^2 \cos^3\phi \left[\frac{\Gamma\left[\frac{1}{4}\right]^4 - 8\pi^2}{64\sqrt{2\pi}\Gamma\left[\frac{1}{4}\right]^2}\right] \frac{L^6 r_0^3}{r_H^6} \qquad (4.2.31)
\end{aligned}$$

The energy of the system is computed using the endpoint equations of motion and the initial conditions described by Eq. (4.2.28). The near boundary expansion of the energy is given by:

$$E_{init} = \frac{r_0^3}{r_H^2 \alpha'} \int_0^1 d\hat{r} \left[\frac{\hat{r}^2}{2\pi\sqrt{1-\hat{r}^4}}\right] - a^2 \frac{L^4 r_0^5 \cos^2\phi}{16\pi r_H^6 \alpha'} \int_0^1 d\hat{r} \left[\frac{\hat{r}^4}{(1+\hat{r}^2)\sqrt{1-\hat{r}^4}}\right]$$

$$= \frac{\pi^{\frac{1}{2}}}{2^{\frac{1}{2}}\Gamma\left[\frac{1}{4}\right]^2}\frac{r_0^3}{r_H^2\alpha'} - \frac{a^2}{128\sqrt{2}\pi^{\frac{3}{2}}}\left[\frac{24\pi^2 - \Gamma\left[\frac{1}{4}\right]^4}{\Gamma\left[\frac{1}{4}\right]^2}\right]\frac{L^4 r_0^5 \cos^2\phi}{r_H^6\alpha'} \tag{4.2.32}$$

Eq. (4.2.32) shows that the a^2 correction is proportional to $\cos\phi$. This means the $\phi < \frac{\pi}{2}$ correction occurs at a lower order in the $\omega = \frac{r_H}{r_0}$ expansion than the $\phi = \frac{\pi}{2}$ case, in a similar fashion to the stopping distance in Eq. (4.2.29). In order to invert this expression, one must work order by order in the a^2 expansion:

$$\begin{aligned} r_0 &= k_0 + a^2 k_1 \\ \Rightarrow k_0 &= \left(\frac{2}{\pi}\right)^{\frac{1}{6}}\left[\Gamma\left[\frac{1}{4}\right]^2 E_{init} r_H^2\alpha'\right]^{\frac{1}{3}} \\ k_1 &= \frac{\Gamma\left[\frac{1}{4}\right]^2\left(24\pi^2 - \Gamma\left[\frac{1}{4}\right]^4\right)\cos^2\phi}{192\sqrt{2}\pi^{\frac{5}{2}}}\left[\frac{L^4 E_{init}\alpha'}{r_H^2}\right] \end{aligned} \tag{4.2.33}$$

Using the inversion in Eq. (4.2.33) and Eq. (4.2.31), the final expression for the stopping distance is given by:

$$\begin{aligned} \Delta x_{stop} &= \frac{L^2\Gamma\left[\frac{1}{4}\right]^{\frac{8}{3}}\sin\phi}{4\times 2^{\frac{1}{3}}\pi^{\frac{2}{3}}}\left[\frac{E_{init}\alpha'}{r_H^4}\right]^{\frac{1}{3}} \\ &- a^2\sin\phi\cos^2\phi\left[\frac{\Gamma\left[\frac{1}{4}\right]^8 - 192\pi^4}{1536\pi^3}\right]\left[\frac{L^6 E_{init}\alpha'}{r_H^4}\right] \end{aligned} \tag{4.2.34}$$

$$\begin{aligned} \Delta z_{stop} &= \frac{L^2\Gamma\left[\frac{1}{4}\right]^{\frac{8}{3}}\cos\phi}{2^{\frac{7}{3}}\pi^{\frac{2}{3}}}\left[\frac{E_{init}\alpha'}{r_H^4}\right]^{\frac{1}{3}} \\ &- a^2\cos^3\phi\left[\frac{\Gamma\left[\frac{1}{4}\right]^8 - 192\pi^4}{1536\pi^3}\right]\left[\frac{L^6 E_{init}\alpha'}{r_H^4}\right] \end{aligned} \tag{4.2.35}$$

As expected, Δz_{stop} agrees with Eq. (4.2.22) for $\phi \to 0$.

The total stopping distance is computed using the Euclidean distance:

$$\begin{aligned}
\Delta s_{stop} &= \Delta x_{stop}\sin\phi + \Delta z_{stop}\cos\phi \\
&= \frac{L^2\Gamma\left[\frac{1}{4}\right]^{\frac{8}{3}}}{2^{\frac{7}{3}}\pi^{\frac{2}{3}}}\left[\frac{E_{init}\alpha'}{r_H^4}\right]^{\frac{1}{3}} \\
&- a^2\cos^2\phi\left[\frac{\Gamma\left[\frac{1}{4}\right]^8 - 192\pi^4}{1536\pi^3}\right]\left[\frac{L^6 E_{init}\alpha'}{r_H^4}\right]
\end{aligned} \tag{4.2.36}$$

Let us now consider the three cases of interest; fixed temperature, entropy density and energy density plasmas. Using Eq. (4.2.10), Eq. (4.2.13) and Eq. (4.2.15), the final stopping distances are given by:

$$\begin{aligned}
\Delta s^T_{stop} &= \frac{\Gamma\left[\frac{1}{4}\right]^{\frac{8}{3}}}{2^{\frac{7}{3}}\pi^2}\left[\frac{\bar{E}_{init}}{T^4}\right]^{\frac{1}{3}} - \hat{a}_T^2\cos^2\phi\left[\frac{\Gamma\left[\frac{1}{4}\right]^8 - 192\pi^4}{1536\pi^7}\right]\left[\frac{\bar{E}_{init}}{T^2}\right] \\
\Delta s^{\hat{s}}_{stop} &= \frac{\Gamma\left[\frac{1}{4}\right]^{\frac{8}{3}}}{4\times 2^{\frac{7}{9}}\pi^{\frac{10}{9}}}\left[\frac{\bar{E}^3_{init}}{\hat{s}^4}\right]^{\frac{1}{9}} - \hat{a}_{\hat{s}}^2\cos^2\phi\left[\frac{\Gamma\left[\frac{1}{4}\right]^8 - 192\pi^4}{3072\times 2^{\frac{1}{3}}\pi^{\frac{13}{3}}}\right]\left[\frac{\bar{E}_{init}}{\hat{s}^{\frac{2}{3}}}\right] \\
\Delta s^{\hat{\epsilon}}_{stop} &= \left(\frac{3}{2}\right)^{\frac{1}{3}}\frac{\Gamma\left[\frac{1}{4}\right]^{\frac{8}{3}}}{8\pi^{\frac{4}{3}}}\left[\frac{\bar{E}_{init}}{\hat{\epsilon}}\right]^{\frac{1}{3}} - \hat{a}_{\hat{\epsilon}}^2\cos^2\phi\left[\frac{\Gamma\left[\frac{1}{4}\right]^8 - 192\pi^4}{4096\pi^5}\right]\left[\frac{\bar{E}_{init}}{\hat{\epsilon}^{\frac{1}{2}}}\right]
\end{aligned} \tag{4.2.37}$$

It is important to note that a term in the $\hat{a}^2$ coefficient is neglected in a similar way to the z-direction stopping distance. This is again a manifestation of the near boundary limit, and can be seen explicitly by writing $\frac{r_0}{r_H}$ as a function of E_{init} and

T - see Subsection 4.2.2.

As in the z-direction case, the correction term has an energy dependence that is greater than the zeroth order term. This forces the same constraints on the $\hat{a}$ parameters as in Eq. (4.2.27).

4.3 Analysis of the light probe Stopping Distance

In the last section, the stopping distance of the light probe in the anisotropic plasma has been analytically computed for motion in the $x-y$ plane, and the longitudinal z-direction. Finally, motion within the $x-z$ plane is considered.

A feature consistent for most of the cases analysed is that the anisotropy increases the quenching of the light probe. The exception to this is when the probe is moving in the $x-y$ plane for fixed entropy density - see Eq. (4.2.14). This increase in the stopping distance is in agreement with the analysis performed in [MY13]. In this paper, the authors computed the stopping distance using the methods of [AV10] and [AV11]. This involves considering the probe as an R-charged current that is produced through a gauge field. The probe follows a null geodesic and the stopping distance is computed using this geodesic.

It is important to note that the anisotropy induces an increase in the jet quenching for longitudinal motion and fixed entropy density. This is a clear physical manifestation of the anisotropy of the system. It is also qualitatively different to the heavy probe case discussed in [CFMT12a]. In this case, the anisotropic drag force is stronger than the isotropic drag force in the longitudinal direction for both fixed temperature and entropy. The opposite is true in the transverse direction. This contradicts the results of the stopping distances computed in this thesis. The fixed

entropy density longitudinal jet quenching is weaker in the anisotropic case, but it is stronger in the case of fixed temperature as shown in Fig. 4.1.

There are also qualitative differences observed to the results obtained in [FM18]. In this paper, the stopping distance is computed considering full falling string solutions without the boundary terms, following the method in [CJKY09]. In this case, the jet quenching is enhanced by the anisotropy for motion in both directions, for fixed temperature and entropy density. The reduction in transverse jet quenching, obtained for fixed entropy, is not observed for any cases of the transverse string solutions computed in this paper.

Let us first compare the energy dependence of the transverse $x-y$ plane motion and the longitudinal z-directional motion. In [FM18], the authors use a range of initial conditions in order to fit the stopping distance to the fit:

$$\Delta x_{stop} = \frac{C}{T}\left(\frac{\bar{E}_{init}}{T}\right)^{n_{eff}} \tag{4.3.1}$$

For a variety of chosen values for a, the effective power n_{eff} is found to increase as the anisotropy is increased. This is expected due to the increased quenching effect introduced by the anisotropy. However, the direction in which the probe is moving is not considered. The longitudinal string computations in this thesis, clearly shows the motion direction affects the energy dependence of the stopping distance. For transverse motion, the energy dependence is not affected by the anisotropy, but the overall constant scaling the function is reduced.

For all three physical cases, the energy dependence of the correction term is exactly the same as the zeroth order term in the transverse direction. In fact, the ratio of anisotropic to isotropic stopping distances $\left(R = \frac{x_{aniso}}{x_{iso}}\right)$ are a function of $\hat{a}$ only.

$$
\begin{aligned}
R^T &= 1 - \frac{\hat{a}_T^2}{24\pi^2} \\
R^{\hat{s}} &= 1 + \frac{\hat{a}_{\hat{s}}^2}{72(2\pi)^{\frac{1}{3}}} \\
R^{\hat{\epsilon}} &= 1 - \frac{\hat{a}_{\epsilon}^2}{48\sqrt{6}\pi}
\end{aligned}
\tag{4.3.2}
$$

In the longitudinal case, the correction term has a different energy and temperature dependence. Since this dependence is larger than the isotropic term, the anisotropy has a more significant influence in the longitudinal direction. As noted in Subsec. (4.2.2), this has an effect on the domain of validity of the small a expansion.

In order to see the difference in the orthogonal directions clearly, consider the coefficient to the correction terms of both the stopping distances for the $x-y$ plane and the z-direction. These correction terms are shown in Table 4.1.

Fig. 4.1 shows plots for both δ^x and δ^z vs. $\bar{E}_{init}$ for all three cases of fixed temperature, entropy and energy densities. One can clearly see that the correction term is more significant for the z-direction. The enhancement of the stopping distance for fixed entropy in the $x-y$ plane is also clear to see. For transverse motion, δ is clearly more significant for fixed temperature, and smallest for fixed energy density. The converse is true in the longitudinal case.

$$
\begin{aligned}
\bar{E}_{Cross}^{T} &= \frac{32\sqrt{2}\pi^{\frac{9}{2}}\Gamma\left[\frac{1}{4}\right]^4 T}{\left[\Gamma\left[\frac{1}{4}\right]^8 - 192\pi^4\right]^{\frac{3}{2}}} \\
\bar{E}_{Cross}^{\hat{\epsilon}} &= \frac{642^{\frac{1}{4}}\pi^4\Gamma\left[\frac{1}{4}\right]^4 \hat{\epsilon}^{\frac{1}{4}}}{3^{\frac{7}{4}}\left(\Gamma\left[\frac{1}{4}\right]^8 - 192\pi^4\right)^{\frac{3}{2}}}
\end{aligned}
\tag{4.3.3}
$$

	$x-y$	z
δ_T	$-\frac{\Gamma\left[\frac{1}{4}\right]^{\frac{8}{3}}}{96\times 2^{\frac{1}{3}}\pi^4}\left[\frac{\bar{E}_{init}}{T^4}\right]^{\frac{1}{3}}$	$-\left[\frac{\Gamma\left[\frac{1}{4}\right]^8-192\pi^4}{1536\pi^7}\right]\frac{\bar{E}_{init}}{T^2}$
$\delta_{\hat{s}}$	$\frac{\Gamma\left[\frac{1}{4}\right]^{\frac{8}{3}}}{576\times 2^{\frac{4}{9}}\pi^{\frac{16}{9}}}\left[\frac{\bar{E}^3_{init}}{\hat{s}^4}\right]^{\frac{1}{9}}$	$-\left[\frac{\Gamma\left[\frac{1}{4}\right]^8-192\pi^4}{3072\times 2^{\frac{1}{3}}\pi^{\frac{13}{3}}}\right]\frac{\bar{E}_{init}}{\hat{s}^{\frac{2}{3}}}$
$\delta_{\hat{\epsilon}}$	$-\frac{\Gamma\left[\frac{1}{4}\right]^{\frac{8}{3}}}{384\times 96^{\frac{1}{6}}\pi^{\frac{7}{3}}}\left[\frac{\bar{E}_{init}}{\hat{\epsilon}}\right]^{\frac{1}{3}}$	$-\left[\frac{\Gamma\left[\frac{1}{4}\right]^8-192\pi^4}{4096\pi^5}\right]\frac{\bar{E}_{init}}{\hat{\epsilon}^{\frac{1}{2}}}$

Table 4.1: This table shows the corrections the stopping distance for motion in the $x-y$ plane and the z directions independently. All three cases of fixed temperature, entropy and energy densities are considered.

For energies $\bar{E} < \bar{E}_{Cross}$, the transverse corrections are larger than the longitudinal corrections, and hence the transverse probes are quenched more. However, it is important to note that $\frac{\bar{E}_{Cross}}{T} = 1.15$ and thus for these energies, one may require high order terms in the near boundary expansion to get a better picture of this. Having noted this, it provides an indication that there exist energies for which the effect of the anisotropy on the transverse stopping distance is greater than that of the longitudinal motion. These energies are so small that it is unlikely to obtain the required resolution to measure this effect. Hence, it is justified to assume the anisotropic effect dominates in the longitudinal direction for energies of interest.

Having studied how the anisotropy affects the stopping distance for transverse and longitudinal motion, let us consider motion in the $x-z$ plane. As briefly discussed in Subsection 4.2.3, the leading order term in the near boundary expansion of the correction term for Δx_{stop} is proportional to $\hat{P}_z$. This means that the leading order contribution to the correction for transverse motion occurs as a smaller order in $\frac{\bar{E}_{init}}{T}$.

This is clear indication of the dominant effect the anisotropy has on longitudinal motion.

Fig. 4.2 shows the ratio of anisotropic stopping distance to isotropic stopping distance $R = \frac{\Delta s_{stop}(\hat{a})}{\Delta s_{stop}(\hat{a}=0)}$ against the angle ϕ the probe is travelling in the $x-z$ plane. The first thing to notice is that for $\phi = \frac{\pi}{2}$ (the transverse direction), $R = 1$ for all cases. This is not correct as there are non-zero correction terms that affect the ratio at a lower order in $\frac{r_H}{r_0}$. By definition this correction is small relative to corrections that occur when there is longitudinal motion.

The plot shows the increase in the effect that the anisotropy has on the $x-z$-plane stopping distance at larger energies. This is a similar effect shown in [CFMT12a] for the heavy probe drag force. In this paper, it is shown that the faster the heavy probe is moving at, the larger the effect the anisotropy has on the stopping distance. A clear difference, between the drag force case and the light probes, is the fact that the isotropic drag force is larger than the anisotropic case for a $\phi > \phi_c$, where ϕ_c is a particular critical angle. There is no such region in the light probe case, where the anisotropic quenching is greater than the isotropic case for $\phi < \frac{\pi}{2}$. This may be due to the fact that the authors in [CFMT12a] consider mid to large anisotropy in their analysis.

It is also important to note that the anisotropic jet quenching is stronger for all ϕ as $\hat{a}_{\hat{s}}$ is increased - (see Eq. (4.2.37)). In [FM18], the authors find that the fixed entropy anisotropic jet quenching at smaller $\hat{a}_{\hat{s}}$ is a larger effect above a certain angle ϕ.

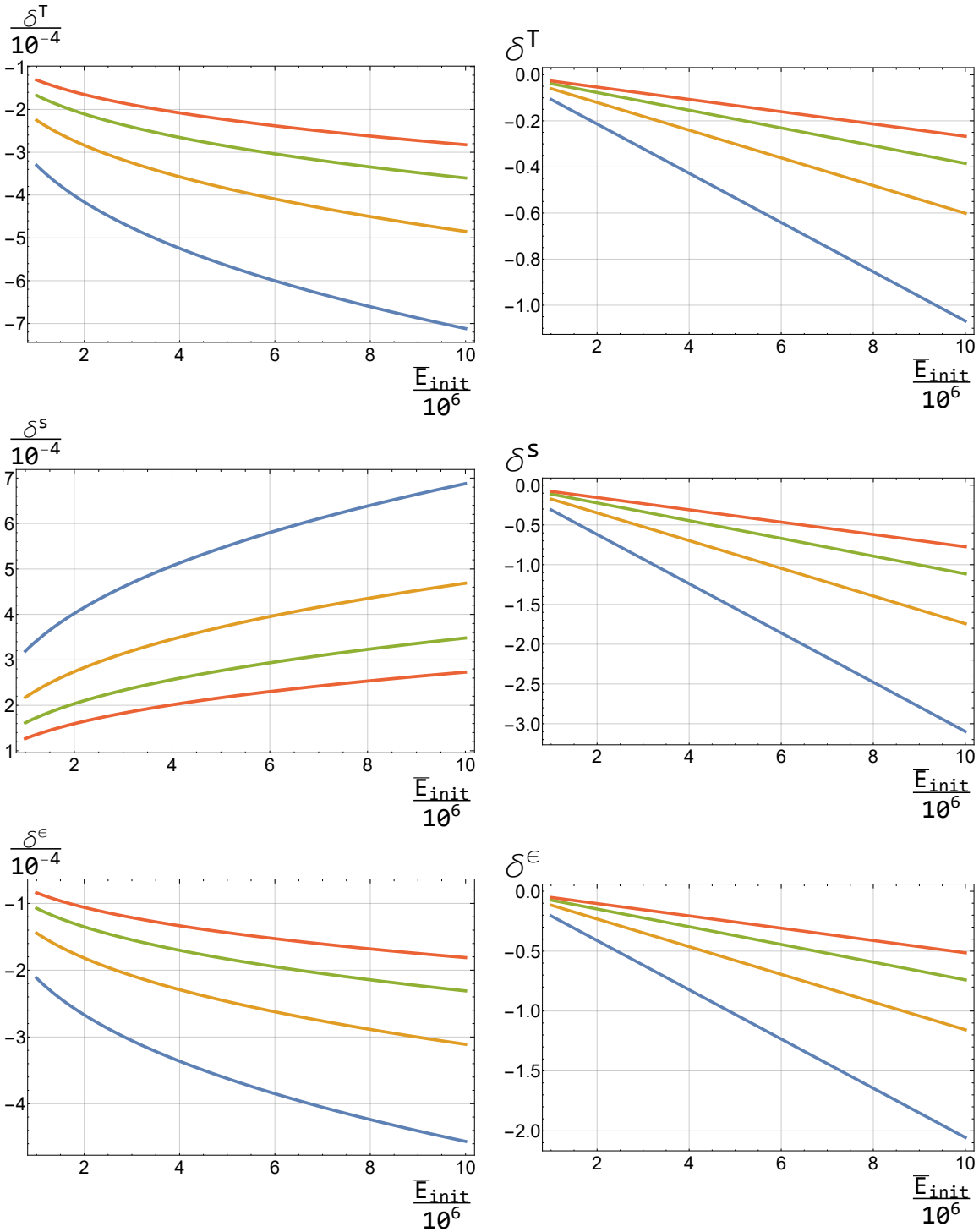

Figure 4.1: This shows the plots of the $\hat{a}^2$ correction term δ vs. $\bar{E}_{init}$ for fixed temperature, entropy density and energy density. The four different temperatures that are shown are $\hat{T} = 150$, $\hat{T} = 200$, $\hat{T} = 250$ and $\hat{T} = 350$ for the Blue, Orange, Green and Red curves respectively.. The entropy and energy densities are computed using these temperatures and Eq. (E.0.12). The left plots show the correction for motion in the $x - y$ plane and the right plots show the correction for motion in the z-direction.

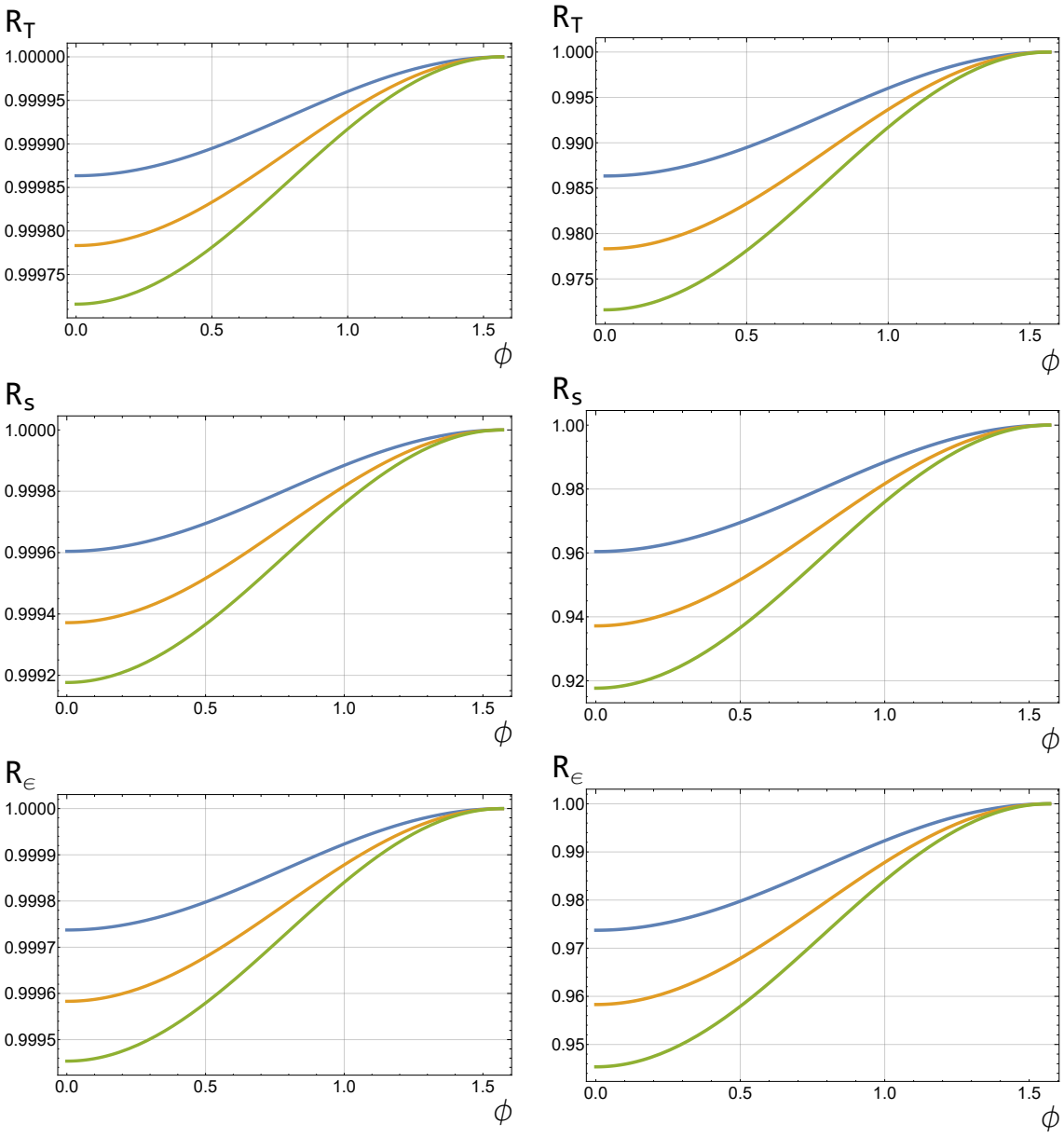

Figure 4.2: This shows the plots of $R = \frac{\Delta x(a)}{\Delta x(a=0)}$ vs. ϕ for three different energies; $\bar{E}_{init} = (10^6, 2 \times 10^6, 3 \times 10^6)$ for the Blue, Orange and Green curves respectively. The left plots are for $a = 0.01$ and $\hat{T} = 150$, $\hat{s} = \frac{150^3 \pi^2}{2}$ and $\hat{\epsilon} = \frac{3}{8}(150^4 \pi^2)$ from top to bottom. The right plots are for $a = 0.1$.

4.4 Instantaneous rate of Energy loss

In the last section, the stopping distance of the falling string was analysed. Let us now consider the shooting string and instantaneous rate of energy loss. In

order to compute the shooting string trajectory, the method described in Appendix C.2 is used. It is important to note that this method relies on both translation and reflection $x^i \to -x^i$ symmetries, and it has already been established that the anisotropic holographic model is symmetric with respect to these transformations. As in the stopping distance case, motion in the x and z directions are first analysed independently. The motion in the $x-z$ plane is also investigated after this. Once more, any motion in the y-direction may be obtained through rotations in the $x-y$ plane.

4.4.1 Motion in the $x-y$ plane

The first string to consider is where the endpoint moves in the $x-y$ plane alone. Once more, the rotation symmetry in the $x-y$ plane will be used and the x motion determines all motion in this plane. In order to compute the shooting string trajectory, let us refer to the method described in Appendix C.2.

Eq. (4.2.4) shows us the leading order contributions to the near boundary expansion of $\frac{dx}{d\hat{r}}$.

$$\frac{dx}{d\hat{r}} = -\frac{L^2 r_0}{r_H^2}\int_1^0 d\hat{r}\left[\frac{1}{\sqrt{1-\hat{r}^4}}\right] + \frac{a^2L^6 r_0}{r_H^4}\left[\frac{\log 1024 - 1}{48\sqrt{1-\hat{r}^4}}\right] \tag{4.4.1}$$

This expansion determines $f_0(\hat{r}, r_H)$ in Eq. (C.2.4), for each term in the a^2 expansion. Using Eq. (C.2.6), the final string trajectory is given by:

$$x(r) = \frac{R^2}{r_H^2}(r-r_*) - \frac{a^2L^6}{r_H^4}\left[\frac{\log 1024 - 1}{48}\right](r-r_*) \tag{4.4.2}$$

$$\Rightarrow r = r_* + \frac{r_H^2 x}{L^2} + a^2L^2 x\left[\frac{\log 1024 - 1}{48}\right] \tag{4.4.3}$$

The instantaneous rate of energy loss is given by the time component of the endpoint equation of motion, and $\frac{dx}{dr}$ is obtained from solving the geodesic equtions.

$$\frac{dE}{dx} = -\frac{r^2}{2\pi\alpha' L^2} + a^2 \frac{r^2 L^2}{96\pi\alpha' r_H^2} \left[\log 1024 - 1\right] \tag{4.4.4}$$

The near boundary limit has been taken in Eq. (4.4.4). Substituting Eq. (4.4.3) in order to eliminate r, one obtains a function of x:

$$\frac{dE}{dx} = -\frac{\left(L^2 r_* + r_H^2 x\right)^2}{2\pi L^6 \alpha'} - a^2 \left[\log 1024 - 1\right] \left[\frac{L^2 r_* x + r_H^2 x^2}{48\pi\alpha' L^2}\right] \tag{4.4.5}$$

Let us now eliminate the horizon radius r_H for the three cases of interest. Using Eq. (4.2.10), Eq. (4.2.13) and Eq. (4.2.15), the rate of energy loss is given by:

$$\begin{aligned}
\left.\frac{d\bar{E}}{dx}\right|_T &= -\frac{\pi T^2}{2}\left[\frac{1}{\hat{u}_T} + \pi T x\right]^2 - \hat{a}_T^2 \frac{T^3}{16}\left[\frac{1}{\hat{u}_T} + \pi T x\right] x \\
\left.\frac{d\bar{E}}{dx}\right|_{\hat{s}} &= -\frac{\hat{s}^{\frac{2}{3}}}{2\pi}\left[\frac{\pi}{\hat{u}_{\hat{s}}} + \left(4\pi^2 \hat{s}\right)^{\frac{1}{3}} x\right]^2 + \hat{a}_{\hat{s}}^2 \frac{\hat{s}}{48\pi}\left[\frac{\pi}{\hat{u}_{\hat{s}}} + \left(4\pi^2 \hat{s}\right)^{\frac{1}{3}} x\right] x \\
\left.\frac{d\bar{E}}{dx}\right|_{\hat{\epsilon}} &= -\frac{\pi}{6}\left[\frac{3\epsilon^{\frac{1}{2}}}{\left[\hat{u}_{\hat{\epsilon}}\right]^2} + \frac{96^{\frac{1}{2}}\hat{\epsilon}^{\frac{3}{4}} x}{\hat{u}_{\hat{\epsilon}}} + 8\hat{\epsilon} x^2\right] - \hat{a}_{\hat{\epsilon}}^2 \frac{\hat{\epsilon}^{\frac{3}{4}}}{144}\left[\frac{3}{\hat{u}_{\hat{\epsilon}}} + 2\sqrt{6}\hat{\epsilon}^{\frac{1}{4}} x\right] x
\end{aligned} \tag{4.4.6}$$

In accordance with the shooting string solutions described in [FG14] and [FGG14], let us re-define r_*.

$$\begin{aligned}
r_* &= \frac{\pi L^2 T}{\hat{u}_T} \\
&= \frac{\pi L^2 s^{\frac{1}{3}}}{\hat{u}_{\hat{s}}}
\end{aligned}$$

$$= \frac{\pi L^2 \hat{\epsilon}^{\frac{1}{4}}}{\hat{u}_{\hat{\epsilon}}} \tag{4.4.7}$$

The scaled energy $\bar{E} = \frac{E}{\sqrt{\lambda}}$ is also used.

4.4.2 Motion in the z-direction

Having computed the rate of energy loss for motion in the $x-y$ plane, let us look in the longitudinal z direction. The near boundary expansion of $\frac{dz}{dr}$, as shown by Eq. (4.2.19), is given by:

$$\frac{dz}{d\hat{r}} = f_0(\hat{r}, r_H)\omega^{l_0} + a^2\left(f_0^a(\hat{r}, r_H)\omega^{l_0^a} + f_1^a(\hat{r}, r_H)\omega^{l_1^a}\right) \tag{4.4.8}$$

$$= -\frac{L^2}{r_H}\left[\frac{1}{\sqrt{1-\hat{r}^4}}\right]\frac{1}{\omega} + a^2\left[\frac{\hat{r}^2}{8\left(1+\hat{r}^2\right)\sqrt{1-\hat{r}^4}}\frac{L^6}{r_H^3\omega^3}\right.$$

$$\left. + \frac{\log 32 - 2}{24\sqrt{1-\hat{r}^4}}\frac{L^6}{r_H^3\omega}\right] \tag{4.4.9}$$

It is important to note that the next to leading order of the near boundary expansion has been included for the a^2 coefficient. This is because $f_0^a(0, r_H) = 0$, and hence the next terms in the near boundary expansion must be considered. First, let us expand the integral of $f_0^a(\hat{r}, r_H)$.

$$\int_1^{\frac{r\omega}{r_H}} d\hat{r} f_0^a(\hat{r}, r_H)\omega^{l_0^a} = \int_1^0 d\hat{r}\left[f_0^a(\hat{r}, r_H)\omega^{l_0^a}\right] + f_0^a(0, r_H)\frac{r}{r_H}\omega^{l_0^a+1}$$

$$+ \frac{1}{2}f_0^{a\prime}(0, r_H)\left(\frac{r}{r_H}\right)^2\omega^{l_0^a+2} + \frac{1}{6}f_0^{a\prime\prime}(0, r_H)\left(\frac{r}{r_H}\right)^3\omega^{l_0^a+3} + ...$$

$$= C_0^a \frac{1}{\omega^3} + \frac{1}{24}\frac{L^6}{r_H^3}\left(\frac{r}{r_H}\right)^3 + ... \tag{4.4.10}$$

The constant C_0^a is independent of r, and thus will not contribute to the trajectory when the subtraction in Eq. (C.2.2) is applied. It is important to note that both $f_0^a(0, r_H)$ and $f_0^{a\prime}(0, r_H)$ are zero, and hence the first contribution occurs at the $\omega^{l_0^a+3} = \omega^0$ order.

Now, let us consider the integral of the $f_1^a(\hat{r}, r_H)$ term:

$$\int_1^{\frac{r\omega}{r_H}} d\hat{r} f_1^a(\hat{r}, r_H)\omega^{l_1^a} = \int_1^0 d\hat{r} f_1^a(\hat{r}, r_H)\omega^{l_1^a} + f_1^a(0, r_H)\frac{r}{r_H}\omega^{l_1^a+1} + ... \tag{4.4.11}$$

$$= C_1^a + \frac{\log 32 - 2}{24}\frac{L^6}{r_H^4}\frac{r}{r_H} \tag{4.4.12}$$

The constant C_1^a is once again not important, as it cancels in the final trajectory. It is important to note that the power of the contribution here is also ω^0. The total contribution can be summed up as:

$$z_t^a(r) = C^a + \frac{1}{24}\frac{L^6}{r_H^3}\left(\frac{r}{r_H}\right)^3 + \frac{\log 32 - 2}{24}\frac{L^6}{r_H^3}\frac{r}{r_H} \tag{4.4.13}$$

Having integrated Eq. (4.4.9) in the near boundary limit, the shooting string trajectory is written as:

$$z(r) = -\frac{L^2(r_* - r)}{r_H^2} + \frac{a^2 L^6}{24 r_H^4}\left[\frac{r_*^3 - r^3}{r_H^2} + [\log 32 - 2]\,(r_* - r)\right] \tag{4.4.14}$$

This expression is non-trivial to invert due to the r^3 term in Eq. (4.4.14). However, one can obtain an inversion by working order by order in the a^2 expansion.

$$r = k_0 + a^2 k_1 \tag{4.4.15}$$

$$k_0 = \frac{L^2 r_* + r_H^2 z}{L^2} \tag{4.4.16}$$

$$k_1 = \frac{L^4 r_H^2 z \log 32 + 3L^4 r_*^2 z + 3L^2 r_H^2 r_* z^2 + r_H^4 z^3 - 2L^4 r_H^2 z}{24 L^2 r_H^2} \tag{4.4.17}$$

The rate is computed using the end point equations of motion and the inversion obtained in Eq. (4.4.17). The final form of the rate is found for the three physical cases of interest, by eliminating the horizon radus r_H.

$$\begin{aligned}
\left.\frac{d\bar{E}}{dz}\right|_T &= -\frac{\pi T^2}{2}\left[\frac{1}{\hat{u}_T} + \pi T z\right]^2 - \frac{\hat{a}_T^2}{[\hat{u}_T]^3}\frac{T^2}{24\pi} G_T(z) \\
\left.\frac{d\bar{E}}{dz}\right|_{\hat{s}} &= -\frac{\hat{s}^{\frac{2}{3}}}{2\pi}\left[\frac{\pi}{\hat{u}_{\hat{s}}} + \left(4\pi^2 \hat{s}\right)^{\frac{1}{3}} z\right]^2 - \frac{\hat{a}_{\hat{s}}^2}{[\hat{u}_{\hat{s}}]^3}\frac{\hat{s}^{\frac{2}{3}}}{48\pi} G_{\hat{s}}(z) \\
\left.\frac{d\bar{E}}{dz}\right|_{\hat{\epsilon}} &= -\frac{\pi}{6}\left[\frac{3\epsilon^{\frac{1}{2}}}{[\hat{u}_{\hat{\epsilon}}]^2} + \frac{96^{\frac{1}{2}}\epsilon^{\frac{3}{4}} z}{\hat{u}_{\hat{\epsilon}}} + 8\epsilon z^2\right] - \frac{\hat{a}_\epsilon^2}{[\hat{u}_{\hat{\epsilon}}]^3}\frac{\hat{\epsilon}^{\frac{1}{2}}}{288\pi} G_{\hat{\epsilon}}(z)
\end{aligned} \tag{4.4.18}$$

where

$$G_T(z) = \pi^4 T^4 [\hat{u}_T]^3 z^4 + 4\pi^3 T^3 [\hat{u}_T]^2 z^3 + 6\pi^2 T^2 \hat{u}_T z^2 + 3\pi T z + 3[\hat{u}_T]^3$$

$$\begin{aligned}
G_{\hat{s}}(z) &= 4 \times 2^{\frac{1}{3}} \pi^{\frac{4}{3}} \hat{s}^{\frac{4}{3}} [\hat{u}_{\hat{s}}]^3 z^4 - 4(2\pi)^{\frac{2}{3}} \hat{s}^{\frac{2}{3}} [\hat{u}_{\hat{s}}]^3 z^2 + 12\pi^2 \hat{s}^{\frac{2}{3}} \hat{u}_{\hat{s}} z^2 \\
&+ 8 \times 2^{\frac{2}{3}} \pi^{\frac{5}{3}} \hat{s} [\hat{u}_{\hat{s}}]^2 z^3 - 4\pi \hat{s}^{\frac{1}{3}} [\hat{u}_{\hat{s}}]^2 z + 3 \times 2^{\frac{1}{3}} \pi^{\frac{7}{3}} \hat{s}^{\frac{1}{3}} z + 6[\hat{u}_{\hat{s}}]^3
\end{aligned}$$

$$G_{\hat{\epsilon}}(z) = 32\pi^2 \left[\hat{u}_{\hat{\epsilon}}\right]^3 z^4 \hat{\epsilon} - 8\sqrt{6}\pi \left[\hat{u}_{\hat{\epsilon}}\right]^3 z^2 \sqrt{\hat{\epsilon}} + 36 \left[\hat{u}_{\hat{\epsilon}}\right]^3 + 32\pi^2\sqrt{6} \left[\hat{u}_{\hat{\epsilon}}\right]^2 z^3 \hat{\epsilon}^{\frac{3}{4}}$$

$$- 12\pi \left[\hat{u}_{\hat{\epsilon}}\right]^2 z\hat{\epsilon}^{\frac{1}{4}} + 72\pi^2 \hat{u}_{\hat{\epsilon}} z^2 \sqrt{\hat{\epsilon}} + 9\pi^2\sqrt{6} z \hat{\epsilon}^{\frac{1}{4}} \tag{4.4.19}$$

The definitions of u_* and $\hat{a}$ are given in Subsections 4.4.1 and 4.2.1. It is also important to note that the re-scaled energy $\bar{E} = \frac{E}{\sqrt{\lambda}}$ is used for the rate of energy loss.

4.4.3 Motion in the $x - z$ plane

Having computed the rates of energy loss in both independent directions, let us consider the motion in the $x - z$ plane. In order to find the rate of energy loss, the shooting string trajectory needs to be found. Rather than considering the trajectory in terms of these x and z directions, let us rotate the $x - z$ frame to a $x' - z'$ frame. This frame is defined such that $z' = 0$ along the trajectory.

Let us first consider the $\frac{dx}{d\hat{r}}$ integrand given by Eq. (4.2.29).

$$\frac{dx}{d\hat{r}} = f_0(\hat{r}, r_H)\omega^{l_0} + a^2 \left(f_0^a(\hat{r}, r_H)\omega^{l_0^a} + f_1^a(\hat{r}, r_H)\omega^{l_1^a} \right) \tag{4.4.20}$$

$$= -\frac{L^2}{r_H} \frac{\sin\phi}{\sqrt{1-\hat{r}^4}} \frac{1}{\omega} + a^2 \sin\phi \left[\frac{\hat{r}^2 \cos^2\phi}{8\left(1+\hat{r}^2\right)\sqrt{1-\hat{r}^4}} \frac{L^6}{r_H^3 \omega^3} \right.$$

$$\left. - \frac{(5 + 3\cos(2\phi) - 20\log 2)}{96\sqrt{1-\hat{r}^4}} \frac{L^6}{r_H^3 \omega} \right] \tag{4.4.21}$$

The $\frac{1}{\omega^3}$ term in the a^2 coefficient vanishes as $\hat{r} \to 0$. So, one cannot use Eq. (C.2.6) and a full expansion needs to be considered.

Let us consider the expansion of the integral of this term:

$$\begin{aligned}\int_1^{\frac{r\omega}{r_H}} d\hat{r} f_0^a(\hat{r},r_H)\omega^{l_0^a} &= \int_1^0 d\hat{r}\left[f_0^a(\hat{r},r_H)\omega^{l_0^a}\right] + f_0^a(0,r_H)\frac{r}{r_H}\omega^{l_0^a+1} \\ &+ \frac{1}{2}f_0^{a\prime}(0,r_H)\left(\frac{r}{r_H}\right)^2\omega^{l_0^a+2} + \frac{1}{6}f_0^{a\prime\prime}(0,r_H)\left(\frac{r}{r_H}\right)^3\omega^{l_0^a+3} + ... \\ &= C_0^a\frac{1}{\omega^3} + \frac{\cos^2\phi\sin\phi}{24}\frac{L^6}{r_H^3}\left(\frac{r}{r_H}\right)^3 + ... \end{aligned} \tag{4.4.22}$$

As in Eq. (4.4.10), the $\hat{r}$ dependent contribution occurs for the $f_0^{a\prime\prime}(\hat{r},r_H)$ term. The constant C_0^a is unimportant for the trajectory, as it will cancel out for the final trajectory. Performing the same expansion for $f_1^a(\hat{r},r_H)$, one obtains the following contribution:

$$\begin{aligned}\int_1^{\frac{r\omega}{r_H}} d\hat{r} f_1^a(\hat{r},r_H)\omega^{l_1^a} &= \int_1^0 d\hat{r} f_1^a(0,r_H)\omega^{l_1^a} + f_1^a(0,r_H)\frac{r}{r_H}\omega^{l_1^a+1}... \\ &= C_1^a - \sin\phi\left[\frac{5+3\cos(2\phi)-20\log 2}{48}\frac{L^6}{r_H^3}\right]\frac{r}{r_H} \end{aligned} \tag{4.4.23}$$

Having obtained the leading order near boundary contribution for the correction term, the trajectory in the x-direction can be written as:

$$\begin{aligned}x(r) &= \frac{L^2(r-r_*)\sin\phi}{r_H^2} \\ &+ \frac{a^2L^6\sin\phi}{r_H^4}\left[\frac{\cos^2\phi}{24}\frac{r_*^3-r^3}{r_H^2} - \frac{5+3\cos(2\phi)-20\log 2}{96}(r_*-r)\right] \end{aligned} \tag{4.4.24}$$

Having obtained the x-direction trajectory, let us compute the z-direction trajectory

in a similar fashion. Using Eq. (4.2.29), the stopping integrand in the z-direction is given by:

$$\begin{aligned}\frac{dz}{d\hat{r}} &= -\frac{L^2\cos\phi}{\sqrt{1-\hat{r}^4}r_H}\frac{1}{\omega} \\ &+ \frac{a^2L^6\cos\phi}{r_H^3}\left[\frac{\hat{r}^2\cos^2\phi}{8\left(1+\hat{r}^2\right)\sqrt{1-\hat{r}^4}}\frac{1}{\omega^3} - \frac{5+3\cos(2\phi)-20\log 2}{96\sqrt{1-\hat{r}^4}}\frac{1}{\omega}\right]\end{aligned} \tag{4.4.25}$$

Once more, the extended expansion is required to compute the trajectory rather than the simple formula expressed in Eq. (C.2.6). The final expression for the trajectory is given by:

$$\begin{aligned}z(r) &= \frac{L^2\cos\phi}{r_H^2}\left(r-r_*\right) \\ &+ \frac{a^2L^6\cos\phi}{r_H^3}\left[\frac{\cos^2\phi}{24}\frac{r_*^3-r^3}{r_H^3} - \frac{5+3\cos(2\phi)-20\log 2}{96}\frac{r_*-r}{r_H}\right]\end{aligned} \tag{4.4.26}$$

Now that the trajectory in both directions has been obtained, let us perform the following co-ordinate transformation:

$$X(r) = x(r)\sin\phi + z(r)\cos\phi \tag{4.4.27}$$

$$\begin{aligned}&= \frac{L^2(r-r_*)}{r_H^2} - \frac{a^2R^6(r-r_*)}{96r_H^6}\Bigg[\cos(2\phi)\left[2\left(r^2+rr_*+r_*^2\right)-3r_H^2\right] \\ &+ 2\left(r^2+rr_*+r_*^2\right)+5r_H^2(\log 16-1)\Bigg]\end{aligned}$$

$$\begin{aligned} Z(r) &= z(r)\sin\phi - x(r)\cos\phi \\ &= 0 \end{aligned} \tag{4.4.28}$$

One can invert this order by order in the a^2 expansion to obtain:

$$r = k_0 + \frac{a^2}{96L^2r_H^2}k_1 \tag{4.4.29}$$

$$k_0 = \frac{L^2r_* + r_H^2X}{L^2} \tag{4.4.30}$$

$$\begin{aligned} k_1 &= 2X^3r_H^4\cos(2\phi) + 2X^3r_H^4 + 6X^2L^2r_H^2r_*\cos(2\phi) + 6X^2L^2r_H^2r_* \\ &- 3XL^4r_H^2\cos(2\phi) - 5XL^4r_H^2 + 5XL^4r_H^2\log 16 + 6XL^4r_*^2\cos(2\phi) \\ &+ 6XL^4r_*^2 \end{aligned} \tag{4.4.31}$$

Having obtained the shooting trajectory in terms of the distance travelled, let us compute the rate of energy loss. Using the shooting string trajectory and the end-point equation of motion, the final rate of energy loss is given by:

$$\begin{aligned} \left.\frac{d\bar{E}}{dX}\right|_T &= -\frac{\pi T^2}{2}\left[\frac{1}{\hat{u}_T} + \pi TX\right]^2 - \frac{\hat{a}_T^2}{[\hat{u}_T]^3}\frac{T^2}{96\pi}H_T(X) \\ \left.\frac{d\bar{E}}{dX}\right|_{\hat{s}} &= -\frac{\hat{s}^{\frac{2}{3}}}{2\pi}\left[\frac{\pi}{\hat{u}_{\hat{s}}} + \left(4\pi^2\hat{s}\right)^{\frac{1}{3}}X\right]^2 - \frac{\hat{a}_{\hat{s}}^2}{[\hat{u}_{\hat{s}}]^3}\frac{\hat{s}^{\frac{2}{3}}}{96\pi}H_{\hat{s}}(X) \\ \left.\frac{d\bar{E}}{dX}\right|_{\hat{\epsilon}} &= -\frac{\pi}{6}\left[\frac{3\epsilon^{\frac{1}{2}}}{[\hat{u}_{\hat{\epsilon}}]^2} + \frac{96^{\frac{1}{2}}\epsilon^{\frac{3}{4}}X}{\hat{u}_{\hat{\epsilon}}} + 8\epsilon z^2\right] - \frac{\hat{a}_\epsilon^2}{[\hat{u}_{\hat{\epsilon}}]^3}\frac{\hat{\epsilon}^{\frac{1}{2}}}{288\pi}H_{\hat{\epsilon}}(X) \end{aligned} \tag{4.4.32}$$

where:

$$
\begin{aligned}
H_T(X) &= 3\pi XT\left[\hat{u}_T\right]^2\cos(2\phi) - 2\pi^4X^4T^4\left[\hat{u}_T\right]^3\cos(2\phi) - 2\pi^4X^4T^4\left[\hat{u}_T\right]^3 \\
&- 8\pi^3X^3T^3\hat{u}_T^2\cos(2\phi) - 8\pi^3X^3T^3\hat{u}_T^2 - 3\pi^2X^2T^2\left[\hat{u}_T\right]^3 - 12\pi^2X^2T^2\hat{u}_T \\
&+ 3\pi^2X^2T^2\hat{u}_T^3\cos(2\phi) - 12\pi^2X^2T^2\hat{u}_T\cos(2\phi) - 3\pi XT\left[\hat{u}_T\right]^2 - 6\pi XT \\
&- 12\left[\hat{u}_T\right]^3\cos^2(\phi) - 6\pi XT\cos(2\phi) \\
H_{\hat{s}}(X) &= 5(2\pi)^{\frac{2}{3}}\hat{s}^{\frac{2}{3}}\left[\hat{u}_{\hat{s}}\right]^3X^2 - 8\times 2^{\frac{1}{3}}\pi^{\frac{4}{3}}\hat{s}^{\frac{4}{3}}\left[\hat{u}_{\hat{s}}\right]^3X^4\cos^2(\phi) + 5\pi\hat{s}^{\frac{1}{3}}\left[\hat{u}_{\hat{s}}\right]^2X \\
&- 24\pi^2\hat{s}^{\frac{2}{3}}\hat{u}_{\hat{s}}X^2\cos^2(\phi) - 16\times 2^{\frac{2}{3}}\pi^{\frac{5}{3}}\hat{s}\left[\hat{u}_{\hat{s}}\right]^2X^3\cos^2(\phi) + 3\pi\hat{s}^{\frac{1}{3}}\left[\hat{u}_{\hat{s}}\right]^2X\cos(2\phi) \\
&- 6\times 2^{\frac{1}{3}}\pi^{\frac{7}{3}}\hat{s}^{\frac{1}{3}}X\cos^2(\phi) - 12\left[\hat{u}_{\hat{s}}\right]^3\cos^2(\phi) + 3(2\pi)^{\frac{2}{3}}\hat{s}^{\frac{2}{3}}\left[\hat{u}_{\hat{s}}\right]^3X^2\cos(2\phi) \\
H_{\hat{\epsilon}}(X) &= 6\pi\sqrt{6}\left[\hat{u}_{\hat{\epsilon}}\right]^3X^2\hat{\epsilon}^{\frac{1}{2}}\cos(2\phi) - 32\pi^2\left[\hat{u}_{\hat{\epsilon}}\right]^3X^4\hat{\epsilon}\cos^2(\phi) + 2\pi\sqrt{6}\left[\hat{u}_{\hat{\epsilon}}\right]^3X^2\hat{\epsilon}^{\frac{1}{2}} \\
&- 36\left[\hat{u}_{\hat{\epsilon}}\right]^3\cos^2(\phi) - 32\sqrt{6}\pi^2\left[\hat{u}_{\hat{\epsilon}}\right]^2X^3\hat{\epsilon}^{\frac{3}{4}}\cos^2(\phi) + 9\pi\left[\hat{u}_{\hat{\epsilon}}\right]^2X\hat{\epsilon}^{\frac{1}{4}}\cos(2\phi) \\
&+ 3\pi\left[\hat{u}_{\hat{\epsilon}}\right]^2X\hat{\epsilon}^{\frac{1}{4}} - 72\pi^2\hat{u}_{\hat{\epsilon}}X^2\hat{\epsilon}^{\frac{1}{2}}\cos^2(\phi) - 9\sqrt{6}\pi^2X\hat{\epsilon}^{\frac{1}{4}}\cos^2(\phi) \qquad (4.4.33)
\end{aligned}
$$

4.5 Analysis of the shooting string rate of energy loss

In Sec. 4.4, the rate of energy loss of the light probes dual to the shooting string was computed. This was done for motions in the $x-y$ plane and z directions independently, and motion in the $x-z$ plane as well.

When considering the anisotropic rates of energy losses, it is firstly important to note that the correction terms for motion in any direction do not depend on energy. Most phenomenological models of the jet quenching of probes in plasmas have non-trivial energy dependence. This is not the case for the isotropic case, as shown in [FG14] and [FGG14], and it is clear there is no energy dependence for the anisotropic case, as shown in Eq. (4.4.6), Eq. (4.4.18) and Eq. (4.4.32). It is also important to note that the non-trivial polynomials in $x/z/X$ mean the temperature dependence is also non-trivial. This could be important when considering anisotropic effects on the jet nuclear modification factor.

In order to compare the rates of energy loss for motions in the $x-y$ plane and the z-directions, consider the fractional correction as defined by:

$$\begin{aligned} K_x &= \frac{\frac{d\bar{E}}{dx} - \frac{d\bar{E}}{dx}\Big|_{a=0}}{\frac{d\bar{E}}{dx}\Big|_{a=0}} \\ K_x &= \frac{\frac{d\bar{E}}{dx} - \frac{d\bar{E}}{dx}\Big|_{a=0}}{\frac{d\bar{E}}{dx}\Big|_{a=0}} \end{aligned} \tag{4.5.1}$$

Let us consider the energy loss rate for motion in the $x-y$ plane only. Fig. 4.3 shows plots of K_x vs. x for a variety of fixed temperatures, entropy densities and energy densities. One can see from the plot that as x increases, K_x tends towards a constant. By expanding Eq. (4.4.6), one finds that this constant is given by:

$$\begin{aligned}
\lim_{x\to\infty} K_x^T &= \frac{\hat{a}_T^2}{8\pi^2} \\
\lim_{x\to\infty} K_x^{\hat{s}} &= -\frac{\hat{a}_{\hat{s}}^2}{24(2\pi)^{\frac{2}{3}}} \\
\lim_{x\to\infty} K_x^{\hat{\epsilon}} &= \frac{\hat{a}_\epsilon^2}{16\sqrt{6}x\pi}
\end{aligned} \tag{4.5.2}$$

This reflects the fact that the correction term is a polynomial in x of order 2, which is the same as the isotropic term. Thus, the fractional correction must tend to a constant.

For fixed temperature and energy density, the anisotropy is shown to increase the rate at which energy is lost and hence describes an increasing jet quenching effect. However, the fixed entropy case shows the opposite effect. The negative fractional correction indicates a smaller jet quenching effect. This is in agreement with the stopping distance analysis described in Sec. 4.3.

Let us consider motion in the independent z-direction. Fig. 4.4 shows that for all cases, the rate of energy loss is larger for the anisotropic case. This once more agrees with the observations when computing the stopping distances in Sec. 4.3. Also, the fractional change does not tend to a constant and increases with z. This points to the higher order polynomial of the correction term coefficient in Eq. (4.4.18). It is also important to note the large increase in the magnitude of the rate of energy loss in the z-direction relative to the x-direction. This is also reflected in the stopping distances in Sec. 4.3.

Fig. 4.5 shows plots of K vs X for a variety of angles ϕ and fixed temperature, entropy and energy. One can see that the fractional correction decreases as the

angle increases. Once more, the effect of any motion in the z-direction significantly boosts the rate of energy loss, and motion in this direction leads to such a large energy loss.

Finally, it is worth noting that the temperature dependence for the corrected terms is strong. This again exacerbates any uncertainties in the Glauber temperature due to the initial formation time - see Sec. 1.3.

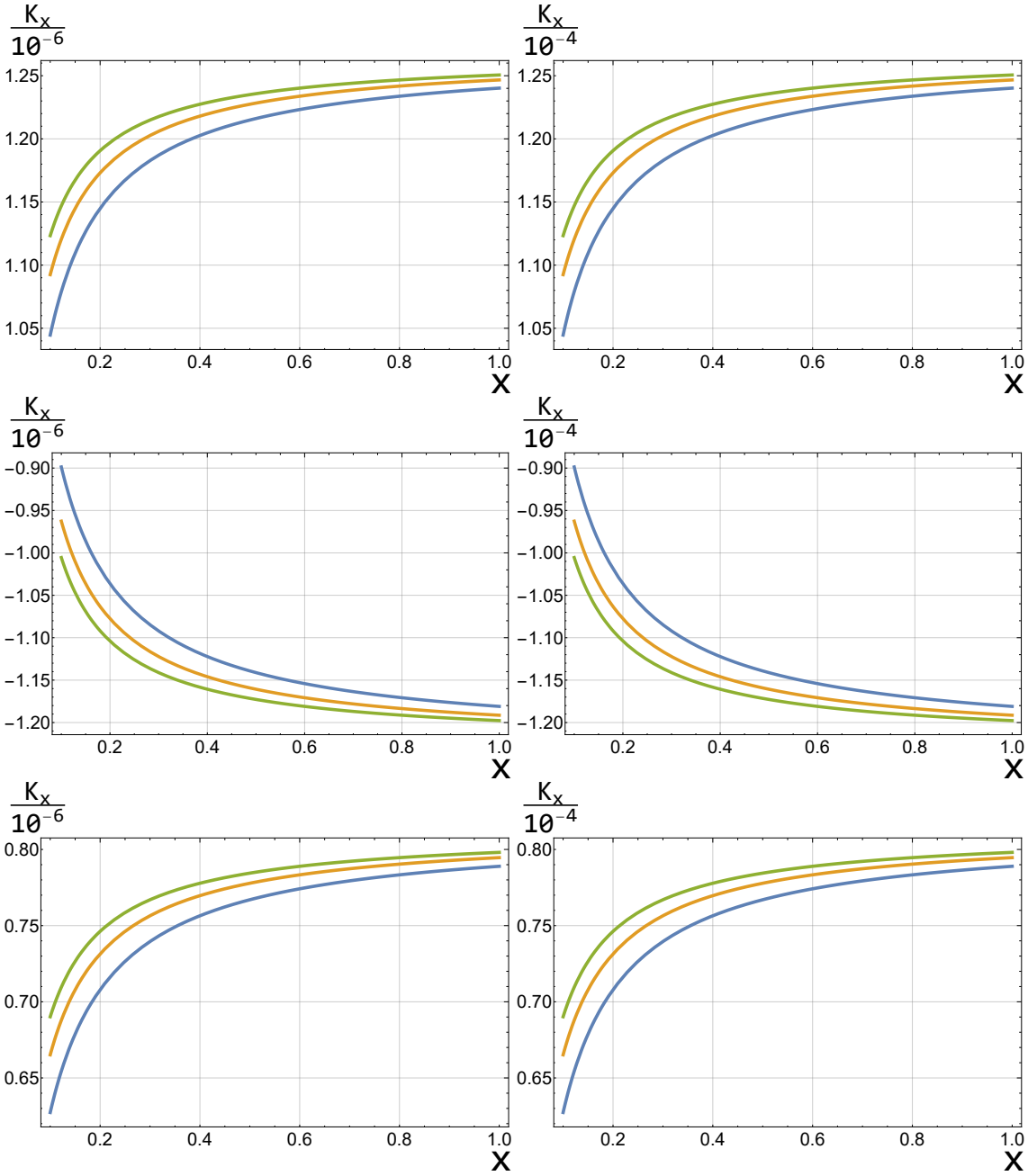

Figure 4.3: This shows the plots of K_x vs x for fixed temperature, entropy and energy densities, going from top to bottom. For the fixed temperature plots, $\hat{T} = (15, 20, 25)$ and these temperatures are used to fix the entropy and energy densities in the middle and bottom plots. The left plots are obtained by fixing $\hat{a} = 0.01$ and the right is obtained by fixing $\hat{a} = 0.1$.

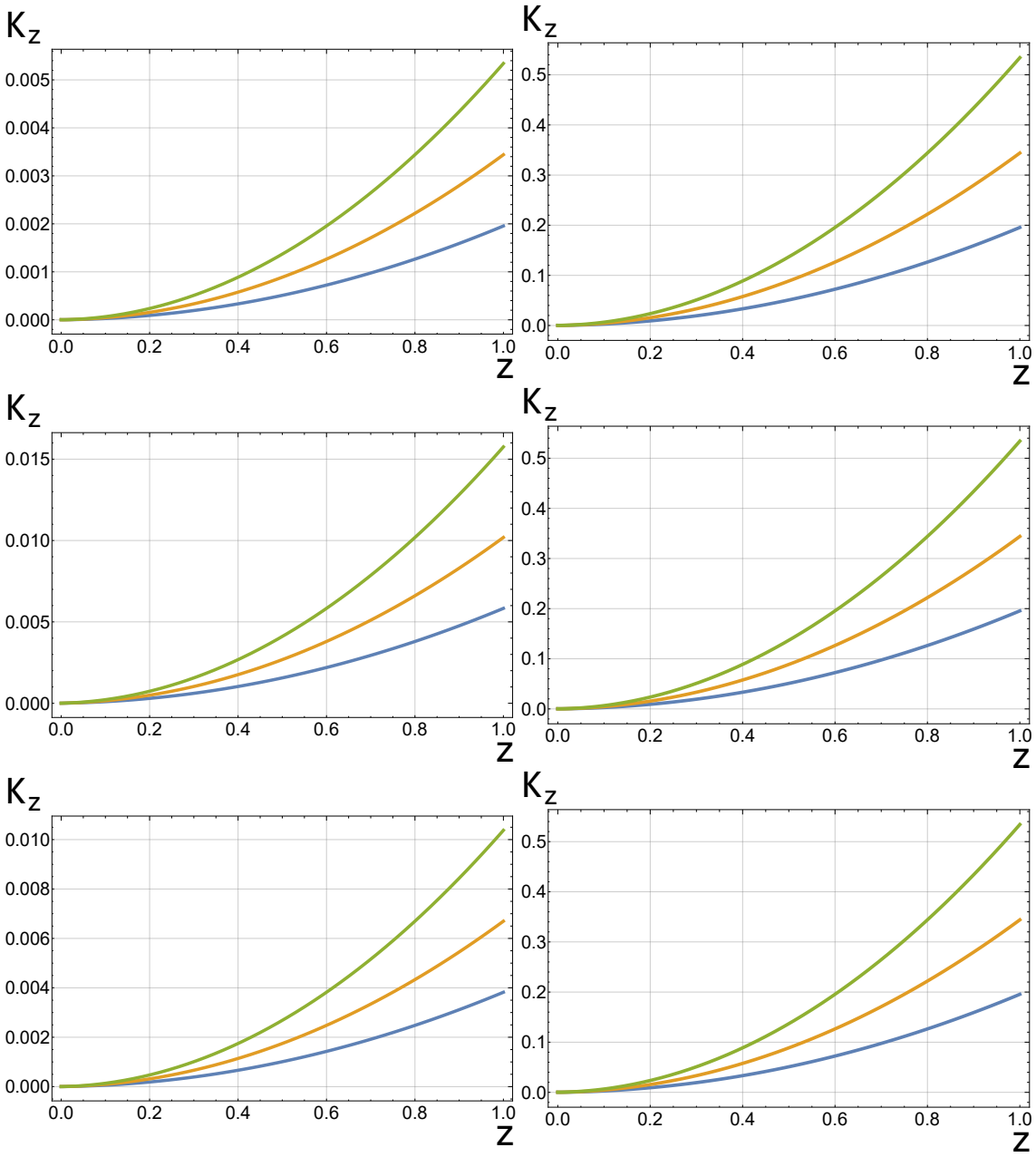

Figure 4.4: This shows the plots of K_z vs z for fixed temperature, entropy and energy densities, going from top to bottom. For the fixed temperature plots, $\hat{T} = (15, 20, 25)$ and these temperatures are used to fix the entropy and energy densities in the middle and bottom plots. The left plots are obtained by fixing $\hat{a} = 0.01$ and the right is obtained by fixing $\hat{a} = 0.1$.

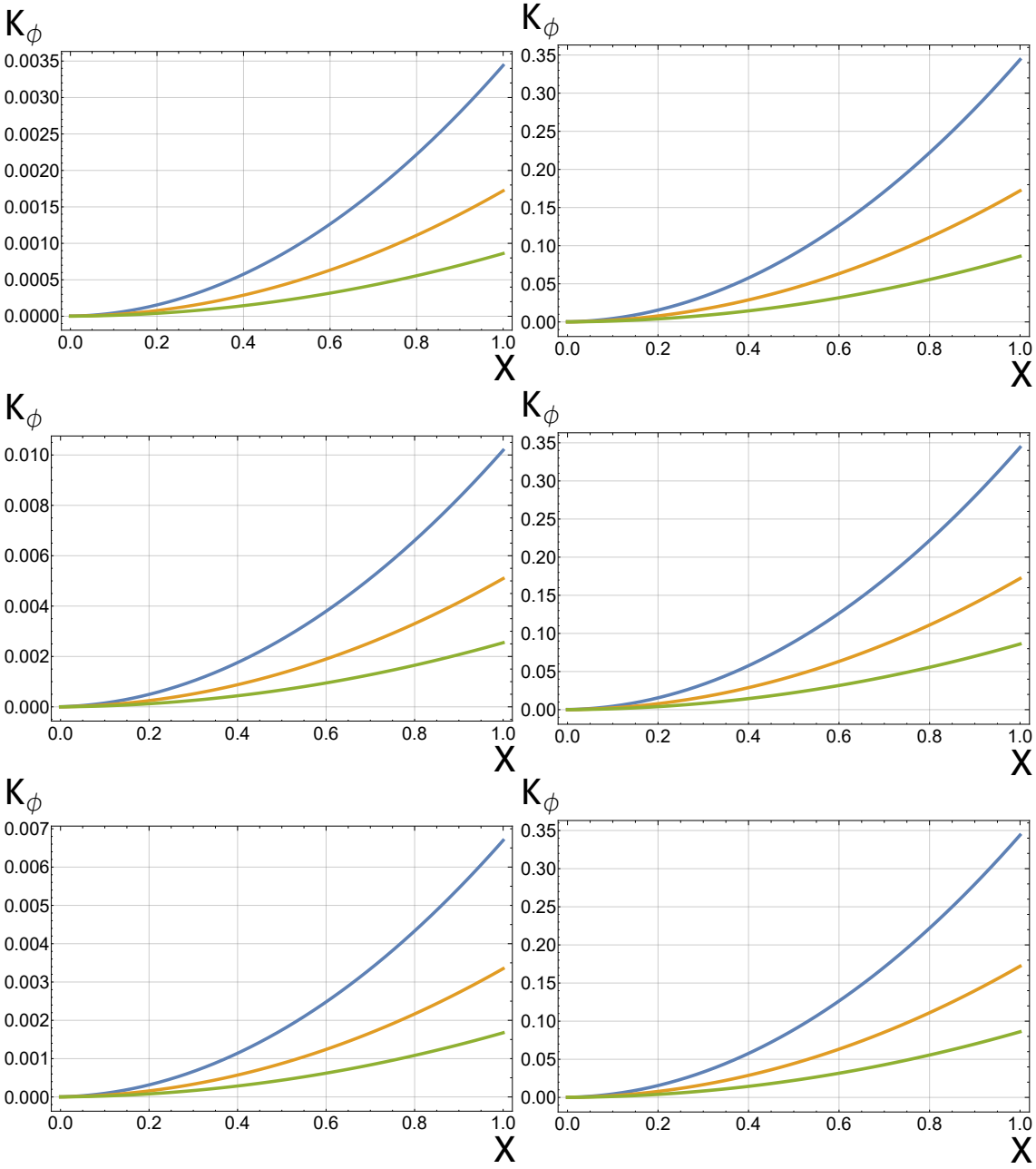

Figure 4.5: This shows the plots of K_ϕ vs X for fixed temperature, entropy and energy densities, going from top to bottom. The plots are obtained for a variety of angles $\hat{\phi} = (0, \frac{\pi}{4}, \frac{\pi}{3})$. The temperature is fixed to $\hat{T} = 15$ for the top plot and this temperatures is used to fix the entropy and energy densities in the middle and bottom plots. The left plots are obtained by fixing $\hat{a} = 0.01$ and the right is obtained by fixing $\hat{a} = 0.1$.

4.6 Jet quenching parameter

Having computed the stopping distance for the falling string in Sec. 4.2, and the rate of energy loss for the shooting string for both the $x-y$ plane, z-direction and $x-z$ plane, let us now use the methods described in Sec. 2.7 to compute the correction to $\hat{q}$ due to anisotropy.

Using Eq. (2.7.1) and the stopping distances computed in Sec. 4.2, one obtains the following expressions for $\hat{q}$:

$$\begin{aligned}
\hat{q}^T_{x/y} &= \left[\frac{2^{\frac{2}{3}}\lambda^{\frac{1}{3}}N_c T^4}{\alpha_S\left(N_c^2-1\right)\Gamma\left[\frac{1}{4}\right]^{\frac{16}{3}}}\right]\left[128\pi^4+\hat{a}_T^2\frac{32\pi^2}{3}\right]\left[\frac{E}{T^4}\right]^{\frac{1}{3}} \\
\hat{q}^T_{z} &= \left[\frac{\lambda^{\frac{1}{3}}N_c T^2}{\alpha_S\left(N_c^2-1\right)}\right]\left[\frac{128\times 2^{\frac{1}{3}}\pi^4 T^2}{\Gamma\left[\frac{1}{4}\right]^{\frac{16}{3}}}\left[\frac{E}{T^4}\right]^{\frac{1}{3}}+\hat{a}_T^2\frac{4\left(\Gamma\left[\frac{1}{4}\right]^8-192\pi^4\right)}{3\pi\Gamma\left[\frac{1}{4}\right]^8}E\right] \\
\hat{q}^T_{x/z} &= \left[\frac{\lambda^{\frac{1}{3}}N_c T^2}{\alpha_S\left(N_c^2-1\right)}\right]\left[\frac{128\times 2^{\frac{1}{3}}\pi^4 T^2}{\Gamma\left[\frac{1}{4}\right]^{\frac{16}{3}}}\left[\frac{E}{T^4}\right]^{\frac{1}{3}}+\hat{a}_T^2\cos^2\phi\frac{4\left(\Gamma\left[\frac{1}{4}\right]^8-192\pi^4\right)}{3\pi\Gamma\left[\frac{1}{4}\right]^8}E\right]
\end{aligned} \tag{4.6.1}$$

The trivial thing to notice first is that the jet quenching parameter is enhanced by the correction term for all three cases of motion. One would expect this since the stopping distance is reduced in all three cases - see Sec. 4.3.

In order to see the effect of the anisotropy on the jet quenching parameter, let us plot the ratio of $\frac{\hat{q}(a)}{\hat{q}(a=0)}$. The choice of parameters is the same as in Sec. 2.7; $N_c=3$, $\lambda=12\pi\alpha_S$, $\alpha_S=0.3$, and the fixed energy density temperature is used $\left(T^4\to\frac{T^4}{3}\right)$. The choice of energy $E=10GeV$ and $E=20GeV$, is a reflection of the phenomenological models used in [Ada+08], [Bur+14] and [CLQW18].

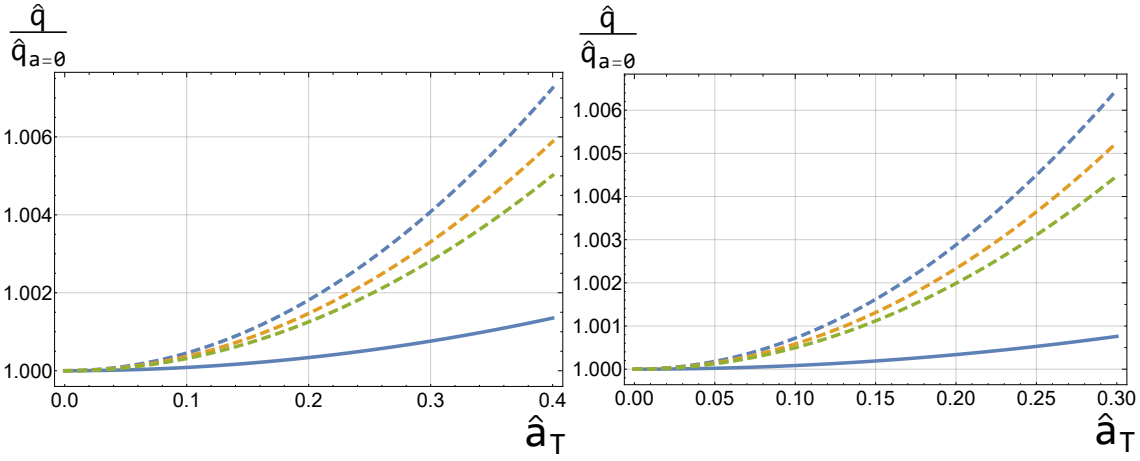

Figure 4.6: This shows the plot of $\frac{\hat{q}}{\hat{q}_{a=0}}$ vs $\hat{a}_T$ for motion in the $x-y$ plane and the z-direction. The solid blue line is for the $x-y$ direction for all temperatures. The dashed lines are for the z-direction. The Blue is for $T = 280MeV$, Orange is for $T = 370MeV$ and Green is for $T = 470MeV$. The left plot is for $E = 10GeV$ and the right plot is for $E = 20GeV$.

It is also important to remember that the small $\hat{a}$ expansion is only valid for the $x-z$ plane and z-direction for the condition given in Eq. (4.2.27). This is taken into account in the plots, and an appropriate domain for $\hat{a}_T$ is chosen.

Fig. 4.6 shows the plot of the ratio $\frac{\hat{q}}{\hat{q}_{a=0}}$ vs $\hat{a}_T$ for both the $x-y$ plane and z-direction motion. The ratio is independent of temperature, for the $x-y$ plane motion. This reflects the behaviour observed for the stopping distance, as shown by Eq. (4.3.2). This is not the case of the z-direction. It is also clear that the z-direction $\hat{q}$ is affected more by the anisotropy than in the x-direction. This follows from the stopping distance results shown in Sec. 4.3. It is directly caused by the fact that the first order correction occurs at different orders in the near boundary expansion. It is also interesting to note that the ratio decreases as the temperature increases for the z-direction case.

Fig. 4.7 shows the plots of $\frac{\hat{q}}{\hat{q}_{a=0}}$ vs ϕ for the $x-z$ plane direction. As the motion rotates from parallel to the anisotropy to perpendicular, the jet quenching

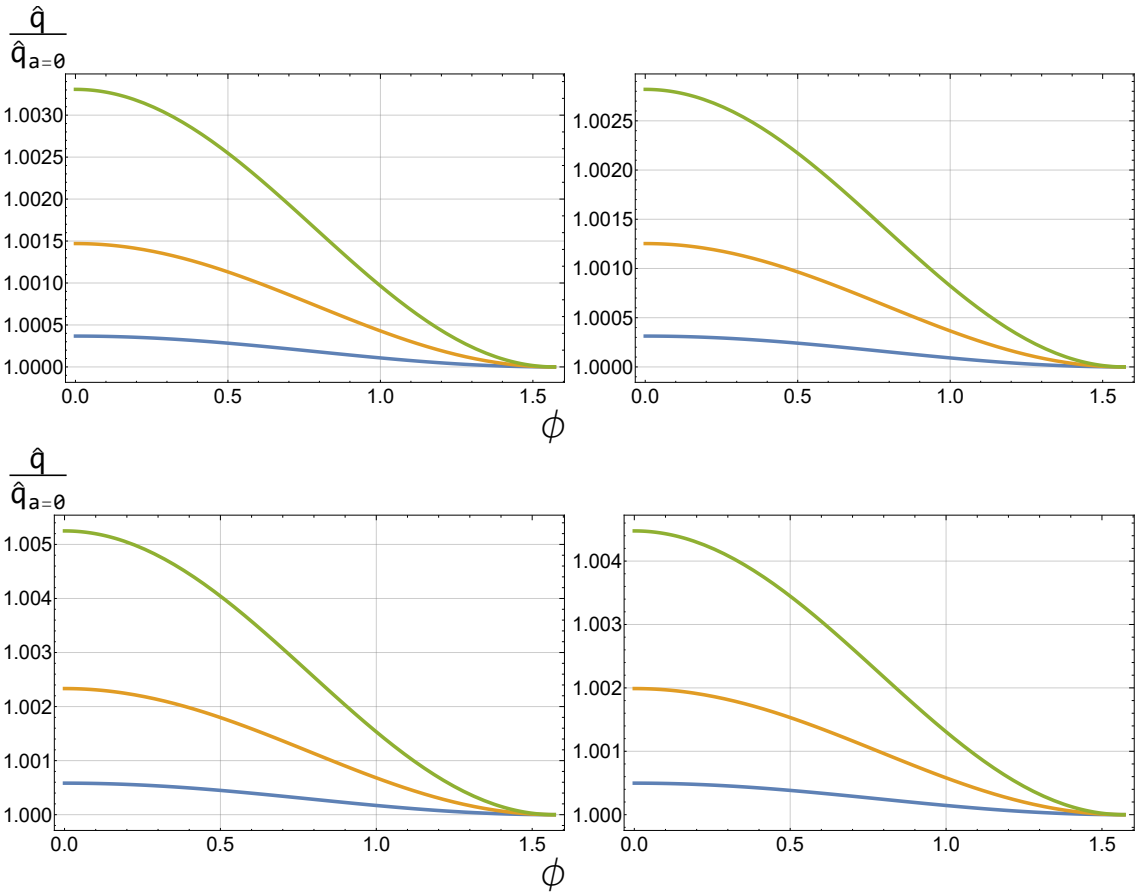

Figure 4.7: This shows the plot of $\frac{\hat{q}}{\hat{q}_{a=0}}$ vs ϕ for motion in the x/z plane. The left plot is for $E = 10GeV$ and the right plot is for $E = 20GeV$. The left plots are for $T = 370MeV$ and the right plot is for $T = 470MeV$. The coloured lines for each plot are given by Blue is for $\hat{a} = 0.1$, Orange is for $\hat{a} = 0.2$ and Green is for $\hat{a} = 0.3$.

parameter decreases. It is again important to note that whilst the plot shows that the ratio tends to 1 for $\phi = \frac{\pi}{2}$, this does not include the next order term in the near boundary expansion and there is in fact a small non-zero correction. Fig. 4.6 shows the plot for the transvere $\phi = \frac{\pi}{2}$ case, and one can see this non-zero contribution in this plot.

So far, we have presented the case for fixed temperature. Let us now study the jet quenching parameter for fixed entropy.

$$\hat{q}^s_{x/y} = \frac{32\times 2^{\frac{5}{9}}\pi^{\frac{14}{9}}N_c s^{\frac{8}{9}}}{9\alpha_S(N_c^2-1)\Gamma\left[\frac{1}{4}\right]^{\frac{16}{3}}}\left[72\pi^{\frac{2}{3}}-2^{\frac{1}{3}}\hat{a}_s^2\right]E^{\frac{1}{3}}\lambda^{\frac{1}{3}}$$

$$\hat{q}^s_z = \frac{4N_c s^{\frac{2}{3}}}{3\pi\alpha_S(N_c^2-1)\Gamma\left[\frac{1}{4}\right]^8}\left[192\times 2^{\frac{5}{9}}\pi^{\frac{29}{9}}\lambda^{\frac{1}{3}}s^{\frac{2}{9}}\Gamma\left[\frac{1}{4}\right]^{\frac{8}{3}}+\hat{a}_s^2\left(\Gamma\left[\frac{1}{4}\right]^8-192\pi^4\right)E^{\frac{2}{3}}\right] \tag{4.6.2}$$

An interesting point to note here is that the fixed entropy $\hat{q}$ seems to decrease for the $x-y$ plane, but increase for the z-direction. One can see that Fig. 4.8 also shows this. Once more, the $x-y$ plane motion is independent of the entropy, but $\hat{q}$ decreases for this case. The opposite is true for the z-direction case.

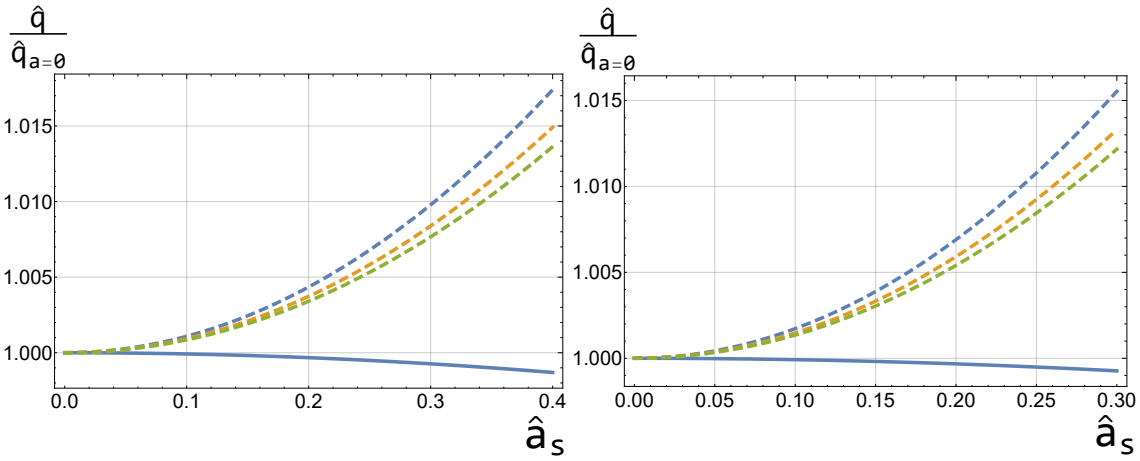

Figure 4.8: This shows the plot of $\frac{\hat{q}}{\hat{q}_{a=0}}$ vs $\hat{a}_s$ for motion in the $x-y$ plane and the z-direction. The solid blue line is for the $x-y$ direction for all entropies. The dashed lines are for the z-direction. The Blue is for $s=0.1GeV^3$, Orange is for $s=0.2GeV^3$ and Green is for $s=0.3GeV^3$. The left plot is for $E=10GeV$ and the right plot is for $E=20GeV$.

In [CFMT12b], the jet quenching parameter is computed using the light-like Wilson loop method described in Sec. 1.2. It is interesting to note that very similar qualitative behaviour is observed for the Wilson loop computation. For fixed temperature, the z-direction case dominates, and the parameter increases as $\hat{a}_T$ increases for all

directions. It is also found in this paper that for fixed entropy and small $\hat{a}_s$, that $\hat{q}$ is smaller than the isotropic case for the $x-y$ plane motion. However, the opposite is true of the z-direction motion.

The authors of [CFMT12b] note that the light-like Wilson loop computation behaves qualitativeley similar to phenomenological models [Rom07], [DNSS08] and [SDNS08] for small $\hat{a}$. The finite momentum falling string $\hat{q}$ also behaves in a similar manner to these models. In the small a limit, the anisotropy increases $\hat{q}$ for fixed temperature and for all directions. The direction parallel to the anisotropy (z-direction) has a larger increase in $\hat{q}$. However, the models state that for larger $\hat{a}$, the transverse $\hat{q}$ is smaller than that of the isotropic case, i.e. $\hat{q}_z > \hat{q}_{a=0} > \hat{q}_{x-y}$. It would be interesting to see if this was the case at larger anisotropies for the falling string model.

4.7 Summary

In this chapter, the finite end point momentum strings have been used to probe and study anisotropy of the strongly coupled plasma, dual to the gauge/gravity model found by Mateos and Trancanelli in [MT11]. First, the gauge/gravity model was briefly reviewed. This model adds anisotropy in the z-direction, through the introduction of an axion field. One can think of the beam direction as the z-direction, and the $x-y$ plane as the transverse plane in which most of the broadening will take place. In particular, the small anisotropy expansion was used, because the plasma isotropises after some time τ_{iso}.

Firstly, the stopping distance of finite end point momentum falling strings was computed for three cases; motion in the $x-y$ plane, z-direction and the $x-z$ plane. The first interesting thing to note is that the leading order correction to the stopping distance, for the $x-y$ motion, occurs at a higher order in the near boundary expansion. This means the effect of the anisotropy on the stopping distance is significantly

less for the transverse direction than the longitudinal direction.

For fixed temperature, the stopping distance decreases when a is increased. This is true for all three trajectories. However, this is not the case for fixed entropy. The transverse stopping distance is increased by the anisotropy in the fixed entropy density case. As the azimuthal angle in increased from 0 to $\frac{\pi}{2}$, the stopping distance is found to decrease.

The finite end point momentum strings allow us to obtain analytic expressions for the corrections due to anisotropy. This means one can get explicit energy and temperature dependencies for the stopping distance corrections. It is found that there could well be a cross-over point, where transverse motion jet quenching dominates. However, this energy seems to be extremely small, and thus is not of concern for our purposes.

In Sec. 4.4, the rate of energy loss of the shooting string was computed. The analytic correction terms were highly non-trivial, but agreed qualitatively with the picture the stopping distances gave. These expressions can be used to compute the jet nuclear modification factor, using the methods used in [FGG14].

Finally, the falling string stopping distances were used to compute the jet quenching parameter in Sec. 4.6. Analytic expressions for the correction terms can be obtained, due to the finite momentum end point strings.

For fixed temperature, the anisotropy increases the jet quenching for motion in all directions. However, this is not the case for the fixed entropy. In this case, the transverse direction $\hat{q}$ decreases. This agrees with the light-like Wilson loop computation performed in [CFMT12b]. It is also important to note that the increase in the transverse momentum broadening for longitudinal and transverse motion agrees

with real QGP computations, for small $\hat{a}$.

Chapter 5

Conclusions and Discussion

In this thesis, the gauge/gravity duality has been applied to the system of strongly coupled non-Abelian plasmas. These plasmas are of interest to study for many reasons, including the fact that the early Universe is believed to have been in such a state. In order to study such a medium, the most clear first step is to observe how probes interact with said medium. The gauge/gravity duality has provided us with a method to study these processes that cannot be computed with lattice techniques, and are by definition non-perturbative.

Whilst a number of different probes have been described using the duality, the finite end point momentum strings, describing light probes, is an elucidating method to study the plasmas. In this thesis, the use of such strings has been used to study features of the plasma.

In this chapter, the key points that are discussed in this thesis are summarised. We will then move on to comment on further work that is of interest to pursue, and a few preliminary computations in the context of this further work will be presented.

5.1 Summary and Conclusions

Let us first briefly review the reasons as to why the finite end point momentum strings are considered to be useful, in the context of light probe jet quenching. The gauge/gravity duality dictionary states that the thermalisation of light quarks is described by Nambu-Goto strings, falling into the dual black hole describing the strongly coupled non-Abelian plasma.

However, it is typical that the energy of the dual light probes is difficult to define from the perspective of the Nambu-Goto string. Other probes such as heavy quarks and virtual gluons, dual to trailing strings and falling doubled closed strings, suffer similar problems. On the other hand, the finite end point momentum strings have a clear and well defined method of distinguishing the quark energy from the flux energy from the string.

These strings also undergo a decoupling transformation, such that the end points are curiously independent from the bulk of the string. It also turns out a transformation of the einbein allows us to write the end point trajectories as simple null geodesics. The decoupling means that the string end point, quark trajectories and energetics are more easily solved. It is even possible to extract analytic information, rather than relying on numerics.

In this thesis, analytic results for the falling string stopping distance for the Sakai-Sugimoto model, chemical potential with R-charge and anisotropic plasma has been computed. The methods used previously required fits to be prescribed to numerical solutions in order to extract functional fits. For example in [FM18], the authors use an effective power to try and extract energy dependence on the stopping distance of light probes in the anisotropic plasma. The finite momentum end point strings allow us to exactly calculate this dependence, for the first order correction in anisotropy.

In the context of the study of the QGP and heavy ion collisions, the jet nuclear modification factor is a useful experimental observable, that can be measured clearly in experiments such as those at the RHIC and the LHC. The energy loss rate of partons that provide the key ingredient in the theoretical computation of R_{AA} has been modelled using so-called shooting finite end point momentum strings. These strings have energy loss rates that have physical Bragg-like behaviours. The motivation for these strings starting near the horizon is that the QGP formation is dual to the formation of the black hole event horizon. It is suggested in [FGG14] that the partons involved in the jet quenching should be produced near the horizon in the gravitational side of the duality.

In this thesis, the energy loss rates for the Sakai-Sugimoto model, finite R-charge chemical potential, and all three motions of the anisotropic plasma has been computed. Whilst the conversion to R_{AA} has been left to further work, these preliminary steps have given us a few hints that the so-called temperature scaling problem exists even for top-down non-conformal theories, such as the Sakai-Sugimoto model.

Whilst holographic methods to compute the transverse momentum broadening are well established, the partons involved are assumed to follow light-like trajectories. This was extended to include time-like vitual gluons in [GGPR08], and since the trajectories of the falling finite end point momentum strings follow time-like trajectories on the boundary, it was natural to extend this to these light probes. Using this method it was possible to obtain analytic expressions for the jet quenching parameter for the Sakai-Sugimoto model, finite R-charged chemical potential, finite baryon chemical potential and anisotropic plasma cases.

Having established some of the applications of the finite end point momentum strings, let us review some of the conclusions made from applying these strings to

the models described above. The first main application was to the non-conformal confining/deconfining Sakai-Sugimoto model. The Sakai-Sugimoto model has a smaller jet quenching effect than the conformal supersymmetric $\mathcal{N} = 4$ super Yang-Mills plasma, which is dual to the canonical AdS_5 black hole.

It was also found that the jet quenching parameter, computed using the falling strings, is smaller for the Sakai-Sugimoto model than the AdS_5 model. This agrees with the canonical Wilson-loop light-like trajectory. Both the AdS_5 black hole and the Sakai-Sugimoto model falling string $\hat{q}$ is over predicted relative to phenomenological studies, but the Sakai-Sugimoto model is closer to the values predicted by these models.

The non-trivial energy dependence of $\hat{q}$ is significant as the value of $\hat{q}$ for the larger energy $E = 20GeV$ matches the phenomenological studies for both models. This is not seen for the light-like Wilson loop method simply because there is no energy dependence. In fact, this method will not extract an energy dependence for $\hat{q}$, and hence why the finite end point momentum strings provides an interesting tool for computing $\hat{q}$.

It was also shown that it is not possible to substantially reduce $\hat{q}$ closer to the values obtained from the experimental data, by including Weyl term higher derivatives to the AdS_5 case. In order to reduce $\hat{q}$ closer to the values predicted in [Bur+14] for the LHC $E = 10GeV$, whilst keeping $\hat{q}$ in the range for the RHIC case, a value of $\lambda_D = -43.44$ is required. Since $\lambda_D > \sqrt{\lambda}$, this violates the validity of the higher derivative expansion. In other words, the corrections, obtained from valid values of λ_D, are not substantial enough to match $\hat{q}$ with phenomenological models.

In Chapter 3, finite chemical potentials were added to the plasma. Both R-charged and finite baryon chemical potential cases were considered. From the gravity side,

the computations are very distinct. For the R-charged case, the gauge fields interact with the metric and it is through the metric that the string trajectories are affected. On the other hand, the gauge fields associated to the baryon chemical potential lives on the probe branes. This means they interact with the string through the coupling at the end points. This non-trivial coupling means the simple geodesic interpretation is no longer valid and requires a numerical solution.

This was done for the falling string case in both the D_3/D_7 case and the Sakai-Sugimoto model with chemical potential. Flavour or baryon chemical potential seems to affect jet quenching far less than the R-charged case. The Sakai-Sugimoto model was particular resistant to affecting the stopping distance, and hence the jet quenching parameter.

Finally, the anisotropic plasma was analysed. For fixed temperature, anisotropy increases the jet quenching effects in the plasma, but it is the longitudinal direction in particular that is more affected. This agrees with phenomenological studies for small $\hat{a}$, which predict an increase in jet quenching in the longitudinal and transverse directions, where the longitudinal effect is larger. However for fixed entropy, the transverse direction stopping distance increases due to the anisotropy. This again is reflected in the jet quenching parameter.

The nature of the finite end point momentum allowed us to find the explicit energy dependence of the correction terms for the anisotropic stopping distance. It is shown that the energy dependence of the longitudinal direction is larger $\sim E$ than the isotropic term. On the other hand, the transverse correction has the same energy scaling as the isotropic case. It is important to note that the correction term for longitudinal motion is constrained. For the expansion to be valid at fixed temperature:

$$\begin{aligned}
\hat{a}_T &\ll \left(\frac{T}{\bar{E}_{init}}\right)^{\frac{1}{3}} \\
\hat{a}_{\hat{s}} &\ll \left(\frac{\hat{s}}{\bar{E}^3_{init}}\right)^{\frac{1}{9}} \\
\hat{a}_{\hat{\epsilon}} &\ll \left(\frac{\hat{\epsilon}}{\bar{E}^4_{init}}\right)^{\frac{1}{12}}
\end{aligned} \tag{5.1.1}$$

5.2 Further Work and preliminary results

Having summarised the core of the thesis, let us discuss further study that could be done, in the context of finite end point momentum string and light quark jet quenching. There are cases of extending the computations performed in this thesis, and others where the finite end point momentum strings are used to probe other strongly coupled plasmas. In the latter case, a few preliminary computations have been performed. We will outline these results, along with a few conclusion before discussing how to proceed.

The first point to note is the conversion of the energy loss rates to the jet nuclear modification factor. Whilst the computations performed in this thesis give the parton energy loss rate, this is not observable in the laboratory. It is thus instructive to follow the method outlined in [FGG14].

The second extension to the computations performed in this thesis is the energy loss rate of shooting strings, traversing the plasma with finite flavour chemical potential. It is natural to ask how the shooting strings are affected when they are coupled to the non-zero gauge fields living on the probe D_7 probe branes (for the D_3 case) and the D_8 probe branes (for the Sakai-Sugimoto case). Whilst the stopping distance gives an indication that the effect will be negligible, it would be instructive to see

this explicitly.

The next two cases are two different models that were not considered in this thesis. It has already been discussed that the peripheral collisions in the heavy ion experiments lead to anisotropies in the plasma. It is useful to see how effects, such as rotation and shearing, could effect the jet quenching in the plasma.

When two heavy ions collide, they do not collide head on i.e. the collision occurs off centre. This leads to a net angular momentum for the plasma created by such collisions. In order to investigate how this rotation affects the light probe quarks, one must consider asymptotically AdS Kerr black holes. It was shown in [BLLM08] that these black holes are dual to a rotating plasma on a 3-sphere.

In this paper, a rotating conformal fluid on the 3-sphere is analysed, by considering a hydrodynamic description of the system; it is assumed that observables vary over length scales much larger than microscopic quantum and thermal fluctuations. The fluid is described as a continuum, where infinitesimal elements are prescribed a local velocity. Each fluid element may be considered in local thermal equilibrium i.e. each element is considered as a box of thermal conformal gas in thermodynamic equilibrium [AC07]. By considering the standard hydrodynamic expansion, applying the conservation of the stress tensor and using conformal symmetry, one can find a generic form of the stress tensor in terms of the angular speeds and temperature.

It was found in [BLLM08] that this system is described by the AdS-Kerr system on the gravity side. The stress tensor of the asymptotically AdS background may be computed by considering metric perturbations. The form of the dual tensor (after taking away the Casimir energy) is the same as the rotating conformal fluid, after identifying the Hawking temperature with the fluid temperature (as usual), and the so called Kerr parameters a_i with the angular speeds ω_i.

It is important to note that the identification of these systems is only valid in the hydrodynamic limit. This can be expressed as $l_{mfp} \ll L$, where l_{mfp} is the mean free path of particle collisions and L is the characteristic length scale of the background. This effectively translates to a large temperature limit i.e. $l_{mfp} \sim \frac{1}{T}$. Thus, one must work in the $T \gg \frac{1}{L}$ limit.

The dual system is in a thermal state in thermodynamic equilibrium, with a non-zero chemical potential associated to angular momentum. The large black hole limit coincides with the hydrodynamic limit in the dual theory. The system is now dual to a rotating conformal fluid on $\mathbb{R} \times S^3$. There are two independent directions the plasma can rotate, however one of these directions shall be switched off in our analysis. We have computed the stopping angle in the frame co-rotating with the plasma for equatorial orbits.

$$\Delta\phi_{stop} = \pm\left(1-a^2\right)\frac{\Gamma\left[\frac{1}{4}\right]^{\frac{8}{3}}}{2^{\frac{7}{3}}\pi^2\lambda^{\frac{1}{6}}}\left(\frac{E_{initial}}{T^4}\right)^{\frac{1}{3}} \tag{5.2.1}$$

The stopping angle in the frame corotating with the rotating conformal fluid is reduced. One can see that when $a = 0$ the angle returns to the planar black hole results as expected. The correction occurs at quadratic order in a. This is also seen in [AS10] for heavy quarks travelling along equatorial $\theta = \frac{\pi}{2}$ trajectories.

It would be interesting to see the more general trajectory along the sphere. Since some of the symmetry is lost in this system, one needs to use alternative methods such as the Hamilton-Jacobi method to solve for these trajectories.

The final model of interest is the shearing plasma solution discussed by Brett McInnes in [McI14] and [MT14]. The models are based of particular toroidal black hole solu-

tions. By taking large mass and large angular momentum limits correctly, these black hole solutions are planar and asymptotically the space-time invokes a shearing motion. The authors use this solution as a model of plasma shearing. Whilst this solution appears unstable, for small enough values of the shearing parameter a, the decay time is large, and thus it is useful to study light probe jet quenching within this limit. Since the QGPs created by heavy ion collisions are known to exhibit pressure gradients and shearing for some time before reaching isotropy, it would be interesting to investigate how this model affects jet quenching.

In conclusion, there are still interesting avenues to which the finite end point momentum strings can be applied, both in extending the work we have done in this thesis, but also in other applications such as the rotating and shearing plasmas.

Appendix A

Sakai-Sugimoto model

In this Appendix, the basic features of the Sakai-Sugimoto model is described. This model is a holographic dual to a $4D$ gauge theory, without supersymmetry and conformal symmetry. The system also naturally contains a confinement/deconfinement transition, without having to include a hard infra-red wall by hand. Finally, the introduction of chiral quarks, through probe D_8 branes, lead to the manifestation of spontaneous chiral symmetry breaking and restoration, as observed in QCD.

The canonical AdS/CFT duality considers stacks of N_c D_3 branes. The identification of black p-branes and D_p branes is used to obtain an equivalence between the low energy Supersymmetric theory of the D_3 branes, and Type II Supergravity in $AdS_5 \times S^5$. In this case, the starting point is a stack of D_4 branes instead. The first feature to notice is that the dual theory should live on a $5D$ background. In the low energy limit, the boundary of the non-compact part of the black 4-brane is five dimensional, and one may naively exclude this system from any sort of gauge theory model of use.

However, a modification of the D_4 brane can be performed in order to removed this problem. Rather than consider the normal D_4, it is more accurate to use the so called D_4 soliton. This involves compactifying one of the 4 spatial direction parallel

to the branes. In order to see this more clearly, let us write out the metric for the black 4-soliton solution.

$$\begin{aligned} ds^2 &= \left[\frac{r}{L}\right]^{\frac{3}{2}}\left[-dt^2+dx^2+dy^2+dz^2+f(r)d\tau^2\right]+\left[\frac{L^2}{r}\right]^{\frac{3}{2}}\left[\frac{dr^2}{f(r)}+r^2d\Omega_4\right] \\ f(r) &= 1-\frac{r_{KK}^3}{r^3} \qquad\qquad e^{\phi}=g_s\left(\frac{r}{L}\right)^{\frac{3}{4}} \end{aligned} \tag{A.0.1}$$

It is important to note that the function $f(r)$ introduces a conical singularity at $r = r_{KK}$, and this forces τ to become compact with periodicity given by:

$$\delta\tau = \frac{4\pi}{3}\frac{L^{\frac{3}{2}}}{r_{KK}^{\frac{1}{2}}} \tag{A.0.2}$$

The dual theory is clearly no longer conformal; the internal $SO(d+2, d+1)$ symmetry, that exists in the D_3 case, does not hold. However, the system retains Poincaré symmetry and also the $SO(5)$ R-symmetry dual to the isometry group of the S^4.

The periodicity of the τ co-ordinate defines the Kaluza-Klein mass scale. This scale defines the non-zero mass scale in the spectrum of the compactified dual $4D$ theory. For energies below this scale, only zero modes survive and pure Yang-Mills gauge theory is the final dual gauge theory.

$$\begin{aligned} M_{KK} &= \frac{2\pi}{\delta\tau} \\ &= \frac{3}{2}\frac{r_{KK}^{\frac{1}{2}}}{L^{\frac{3}{2}}} \end{aligned} \tag{A.0.3}$$

In order to connect this gravitational theory to the gauge theory, one needs to relate

the gravitational parameters to the gauge field couplings. The following relationships make these connections:

$$\begin{aligned} L^3 &= \frac{1}{4}\frac{g^2 N_c \alpha^{'}}{M_{KK}} \\ g_s &= \frac{1}{4\pi}\frac{g^2}{M_{KK}\sqrt{\alpha'}} \end{aligned} \tag{A.0.4}$$

where g is the $4D$ gauge theory coupling, obtained after the dimensional reduction. It is important to note that the convention chosen in Eq. (A.0.4) is not the one canonically used in the context of holography. In [SS05b], the convention chosen is given by $g_{YM}^2 = \frac{1}{2}g^2$. The reason for choosing such a convention is that it reflects QCD properly, such that the strong coupling α_S relates to the gauge theory coupling through [Reb14]:

$$\alpha_S = \frac{g^2}{4\pi} = \frac{g_{YM}^2}{2\pi} \tag{A.0.5}$$

The dimensionless coupling constant, defining the large N_c expansion, is defined to be $\lambda = g^2 N_c$. This is akin to the t'Hooft coupling constant in the D_3 case. Much like the D_3 case, the classical gravity description corresponds to the large N_c, $\frac{1}{g} \gg 1$, strong coupling $\lambda \gg 1$ limit on the gauge theory side. Given this convention, the t'Hooft like coupling can be written in terms of the gravitational parameters as following:

$$\lambda = \frac{4 M_{KK} L^3}{\alpha^{'}} \tag{A.0.6}$$

At $r = r_{KK}$, a soft IR cutoff exists for this theory. This IR cutoff manifests as an indicator of confinement. The Wilson loop describing heavy static quarks can be

computed by considering static string within the background [Mal98b]. The energetically favourable string is one that starts at the boundary, drops to the cut off, and rises back to the boundary. It can be shown the string tension for this solution approaches a constant in this background, indicating an area law for the Wilson loop, and hence a confining phase.

As noted above, fundamental representation quarks are introduced into the system through probe $D_8/\bar{D}_8$ branes into the gravitational system. The probe brane dynamics are described in Appendix D. The particular configuration of probe branes, that are energetically favourable, are shown to induce chiral symmetry breaking in the dual theory. This is very much an observed phenomenon in QCD and is another admirable feature of this model.

The meson spectrum of the dual theory may be computed, by considering normalisable excitations of the fields living on the probe branes. By identifying the lowest meson mode with the ρ meson and finding the pion decay constant f_π, one can obtain values for the parameters of the gravitational theory. The parameters obtained when using this method are [SS05a], [SS05d]:

$$M_{KK} = 949MeV \qquad \lambda = 33.26 \tag{A.0.7}$$

In [Reb14], these parameters are used to compute the string tension σ, for the heavy quark string used to compute the Wilson loop. To be more precise, the ratio $\frac{m_\rho}{\sqrt{\sigma}}$ is considered. It is found that the model under predicts the ratio compared to large N_c lattice calculations [Bal+13].

Rather than use m_ρ and f_π, using m_ρ and $\frac{m_\rho}{\sqrt{\sigma}}$ leads to a smaller value for λ:

$$M_{KK} = 949MeV \qquad \lambda = 25.1 \tag{A.0.8}$$

This smaller λ is preferable as is closer to values of the strong coupling obtained using perturbative methods. It also leads to the value of $\alpha_S = 0.66$, which is closer to the values used when analysing data from RHIC and LHC in [Bur+14] and [CLQW18].

The model undergoes a phase transition at the critical temperature $T_c = \frac{M_{KK}}{2\pi}$. Above this temperature, the thermodynamically stable solution to the gravitational equations of motion is given by:

$$\begin{aligned} ds^2 &= \left[\frac{r}{L}\right]^{\frac{3}{2}} \left[-f(r)dt^2 + dx^2 + dy^2 + dz^2 + d\tau^2\right] + \left[\frac{L^2}{r}\right]^{\frac{3}{2}} \left[\frac{dr^2}{f(r)} + r^2 d\Omega_4\right] \\ f(r) &= 1 - \frac{r_H^3}{r^3} \end{aligned} \tag{A.0.9}$$

This introduces a black hole in the background, with an event horizon at $r = r_H$. The temperature of the black hole is defined in the canonical way, by removing the conical singularity at the horizon in the Euclidean section.

$$T = \frac{3}{4\pi} \left[\frac{r_H}{L^3}\right]^{\frac{1}{2}} \tag{A.0.10}$$

The Wilson loop calculation in this background leads to a very different physical picture. The energetically favourable heavy quark strings do not connect in the bulk, and fall directly into the black hole. This leads to a zero string tension, and hence the Wilson loop follows a perimeter law behaviour associated to deconfinement.

The probe $D_8/\bar{D}_8$ branes behave in a very different way. The full embeddings

are described in Appendix D. It is shown that up to a certain critical temperature, the probe branes describe a spontaneous chiral symmetry breaking phase. Above this temperature, a phase transition occurs and the chiral symmetry is restored. It is this chiral restoration phase that shall be of interest in our discussion of light probe energy loss, in the context of the QGP.

Appendix B

$\mathcal{N} = 2$ R-Charged STU Black Holes

The canonical holographic correspondence is between Type IIB supergravity on $AdS_5 \times S^5$ and $\mathcal{N} = 4$ super Yang-Mills. In order to perform computations, one usually compactifies over the S^5. The result of the compactification is $5D$ $\mathcal{N} = 8$ gauged supergravity, where the gauge group is $SO(6)$. It is of interest to consider the minimal truncation of this theory, $\mathcal{N} = 2$ supergravity in $5D$.

Let us focus on the bosonic sector of this theory. The field content of the truncation are two scalars and three $U(1)$ gauge fields that are coupled to gravity. These three gauge fields span the Cartan of the full $SO(6)$ gauge group. The action is given by:

$$\begin{aligned} S &= -\frac{1}{16\pi G_5}\int d^5x\sqrt{-G}\Bigg[R + \frac{2}{L^2}\mathcal{V} - \frac{1}{2}G_{ij}F^i_{\mu\nu}F^{j\mu\nu} - G_{ij}\partial_\mu X^i \partial^\mu X^j \\ &+ \frac{1}{24\sqrt{-G}}\epsilon^{\mu\nu\rho\sigma\lambda}\epsilon_{ijk}F^i_{\mu\nu}F^j_{\rho\sigma}A^k_\lambda\Bigg] \end{aligned} \tag{B.0.1}$$

where

$$G_{ij} = \frac{1}{2}\text{diag}\left[\left(\frac{1}{X^1}\right)^2, \left(\frac{1}{X^2}\right)^2, \left(\frac{1}{X^3}\right)^2\right] \tag{B.0.2}$$

$$\mathcal{V} = 2\sum_i (X^i)^{-1} \tag{B.0.3}$$

The two scalars are written in terms of three scalars X^i $(i = 1, 2, 3)$, which are subject to the constraint $X^1X^2X^3 = 1$.

In [BCS99], Behrndt, Cvetič and Sabra found the STU asymptotically AdS five dimensional solution to gauged $\mathcal{N} = 2$ SUGRA. The solution is given by the metric:

$$ds^2 = -(H_1H_2H_3)^{-\frac{2}{3}} f dt^2 + (H_1H_2H_3)^{\frac{1}{3}}(f^{-1}dr^2 + r^2 d\Omega_{3,k}) \tag{B.0.4}$$

where

$$f = k - \frac{m}{r^2} + \frac{r^2}{L^2} H_1H_2H_3, \quad H_i = 1 + \frac{q_i}{r^2}, \quad i = 1, 2, 3 \tag{B.0.5}$$

The scalar fields X^i and three $U(1)$ fields A^i_t are given by:

$$X^i = \frac{(H_1H_2H_3)^{\frac{1}{3}}}{H_i}, \qquad A^i_t = \sqrt{\frac{(kq_i + m)}{q_i}}(1 - H_i^{-1}) \tag{B.0.6}$$

In these co-ordinates, the boundary is approached as $r \to \infty$ and the parameters m and q_i are related to the temperature, and three charges of the black hole. The spatial curvature k shall be set to 0, such that $d\Omega_{0,3}$ is just $\mathbb{R}^3$, and hence the conformal boundary is Minkowski space-time.

It is important to note that this solution can be obtained directly from the full $10D$ theory - see [CG99] and [Cve+99]. The solution of interest is the $10D$ rotating D_3 brane. These branes rotate in three independent directions on the S^5 transverse to the branes. Upon compactification of the near horizon limit, one obtains the $5D$ charged black hole described above. The three parameters, describing the angular

momentum in these directions, are related to the charges of the black hole.

The horizon is defined canonically by the co-ordinate singularity $g_{rr}^{-1} = 0$ and one can invert this to write:

$$m = \frac{(q_1 + r_H^2)(q_2 + r_H^2)(q_3 + r_H^2)}{L^2 r_H^2} \tag{B.0.7}$$

The existence of the horizon is required in order to avoid naked singularities. This provides an important constraint on the parameters. In [BCS99], the following function $x^2 f(x)$ is considered:

$$x^3 + (q_1 + q_2 + q_3)x^2 + \Big(q_1q_2 + q_1q_3 + q_2q_3 - L^2m\Big)\, x + q_1q_2q_3 = x^2 f(x) \tag{B.0.8}$$

Note that $x = r^2$. Now the function and second derivative is positive at $x = 0$ as $q_i \geq 0$. This means the derivative at $x = 0$ must be negative for a positive solution of x, which is required for a real horizon. So, one can write down the following:

$$\Big(q_1q_2 + q_1q_3 + q_2q_3 - L^2m\Big) < 0 \tag{B.0.9}$$

Since one requires there to be at least one horizon, the function must approach a minimum at or below the x-axis. It is also important to note that there are two turning points, and one must be at negative x. The naked singularity is thus avoided by the following constraint:

$$x_+^2 f(x_+) \leq 0 \tag{B.0.10}$$

where x_+ is the location of the positive x turning point.

One can also re-express this condition through Eq. (B.0.7). Charged and rotating black holes have multiple horizons. Each of these horizons map to the mass via Eq. (B.0.7). For the existence of more than one horizon, $m(r_H)$ must have at least one turning point. The branches connecting each turning point maps a particular horizon to the mass. Since our interest is the outer horizon and m increases as $r_H \to \infty$, there must exist a minimum which represents the extremal black hole. The outer horizon must be larger than this value by definition. So one obtains the following constraint:

$$2r_H^6 + r_H^4(q_1 + q_2 + q_3) - q_1 q_2 q_3 \geq 0 \tag{B.0.11}$$

This is verified by the requirement of positivity for the temperature of the black hole.

The gauge field is written in a gauge such that its norm is not well defined at the horizon. One can perform a gauge transformation:

$$A^i \to \mu_i - A^i \tag{B.0.12}$$

where the chemical potentials are given by:

$$\mu_i = \sqrt{\frac{m}{q_i}} \left[1 - H_i^{-1}(r_H)\right] \tag{B.0.13}$$

The temperature is obtained by removing the conical singularity at the horizon and is given by:

$$T = \frac{1}{4\pi} \sqrt{\frac{g'_{tt}(r_H)}{g'_{rr}(r_H)}} \tag{B.0.14}$$

$$= \frac{2r_H^6 + r_H^4(q_1+q_2+q_3) - q_1q_2q_3}{2\pi L^2 r_H^2 \sqrt{(q_1+r_H^2)(q_2+r_H^2)(q_3+r_H^2)}} \tag{B.0.15}$$

Before looking at the thermodynamics of the system, there is one particular choice of charge that is of interest. If one chooses all three charges to be equal i.e. $q_1 = q_2 = q_3 = q$, the solution is in fact the AdS_5 Reissner-Nordström black hole. This of course is just the solution to the Einstein-Maxwell action with negative cosmological constant. The single gauge field is obtained by changing basis in the gauge field vector space. The following choice of basis makes this clearer:

$$A'^1_\mu = \frac{1}{\sqrt{3}}\left(A^1_\mu + A^2_\mu + A^3_\mu\right)$$

$$A'^2_\mu = \frac{1}{\sqrt{2}}\left(A^2_\mu - A^3_\mu\right)$$

$$A'^3_\mu = \frac{1}{\sqrt{6}}\left(A^2_\mu + A^3_\mu - 2A^1_\mu\right) \tag{B.0.16}$$

This gives an orthonormal basis, where A'^2_μ and A'^3_μ both vanish for the STU solution Eq. (B.0.6). The scalars X^i reduce to 1, and this reduces the action to exactly the Einstein-Maxwell action with negative cosmological constant. The metric, however, does not look like the AdS_5 Reissner-Nordstöm solution in canonical form. First, let us perform the following co-ordinate transformation:

$$r = \sqrt{r'^2 - q^2} \tag{B.0.17}$$

In addition to this transformation, one needs to set $Q^2 = mq$ in order for the metric and gauge field A'^1_μ to obtain a canonical form.

Now, let us compute the Euclidean action and hence obtain the thermodynamic

properties of the black hole. This was performed for the $k=1$ case in [CG99]. Let us use the counter term method used in [CCS07]. Whilst the background subtraction method gives a finite result, this scheme gives us non-linear terms. These terms lead us to some inconsistencies with the laws of black holes e.g. the area law is violated. The details of the counter term are given in [LS05]. So we obtain[1]:

$$S_E = \frac{V\left(q_1+r_H^2\right)\left(q_2+r_H^2\right)\left(q_3+r_H^2\right)}{16\pi G_5 L^5 r_H^2 T} \tag{B.0.18}$$

$$\Rightarrow F = -\frac{\left(q_1+r_H^2\right)\left(q_2+r_H^2\right)\left(q_3+r_H^2\right)}{16\pi G_5 L^5 r_H^2} \tag{B.0.19}$$

The black hole is locally stable subject to the following condition, obtained by ensuring the appropriate Hessian matrix is positive definite:

$$2r_H^6 - r_H^4(q_1+q_2+q_3) + q_1q_2q_3 > 0 \tag{B.0.20}$$

Finally, let us consider the global stability of the system. If one performs a background subtraction with respect to the AdS_5 vacuum, it is well known that the black hole is the preferred phase for all values of the parameters. By introducing an IR cutoff in the vacuum solution, a phase transition appear [CCS07]. This can be used to model the confinement/deconfinement phase transition in the dual theory. The change in free energy is given by:

$$\Delta F = -\frac{q_1\left(q_2+r_H^2\right)\left(q_3+r_H^2\right)+r_H^2\left(q_2\left(q_3+r_H^2\right)+q_3r_H^2-2r_{IR}^4+r_H^4\right)}{16\pi G_5 L^5 r_H^2}$$

$$\Rightarrow \quad q_1\left(q_2+r_H^2\right)\left(q_3+r_H^2\right)+r_H^2\left(q_2\left(q_3+r_H^2\right)+q_3r_H^2-2r_{IR}^4+r_H^4\right)$$

[1]Note that F is the free energy density for the planar black holes.

$$\leq \quad 0 \tag{B.0.21}$$

The second line describes the condition for stability of the black hole phase. The cut off can be set by matching to the experimental zero charge phase transition temperature. Let us set this to $170MeV$. Then $z_{IR} = \frac{L^2}{r_{IR}} = \frac{2^{1/4}}{170\pi}(MeV)^{-1}$, where the inverse radial co-ordinate is being used for convenience.

B.0.1 Higher Derivative Correction

Higher derivative corrections are of natural interest in the context of holography. The higher order terms in the $\frac{\alpha'}{L^2}$ expansion for the effective theories of string theory, correspond to the large λ expansion of the gauge theory. Thus, these terms give us an indication of corrections to the stopping distance at next order. The following terms are the next gravitational terms to the pure Einstein-Hilbert Lagrangian.

$$\mathcal{L}_{\mathcal{GB}} = (\alpha_1 R^2 - \alpha_2 R_{\mu\nu} R^{\mu\nu} + \alpha_3 R_{\mu\nu\rho\sigma} R^{\mu\nu\rho\sigma}) \tag{B.0.22}$$

Whilst in principle one could assign three independent coefficients to each term, the particular choice of $\alpha = \alpha_1 = \frac{\alpha_2}{4} = \alpha_3$ is a common choice as it avoids ghosts. This is the so-called Gauss-Bonnet gravitational theory.

In [Jam09] and [CHLS09], the authors looked to find the corrections to the minimal truncation of $\mathcal{N} = 2$ gauged $5D$ SUGRA. In principle, one may compute from the full string theory and then compactify. However, supersymmetry itself poses constraints on the terms allowed in the Lagranigan. The authors use the so called superconformal approach, whereby higher derivative contributions in the superconformal case are considered. The conformal symmetry is then broken, leaving the higher derivative supergravity terms.

The system studied is the pure supergravity case, where the gravitational hyper-

multiplet is not coupled to chiral multiplets. One enforces the pure case through setting the scalars in Eq. (B.0.1) to constants, subject to specific constraints (see [CHLS09]). The three gauge fields are related to a single field through the scalar fields, and hence there is only one photon in this case. The uncorrected Lagrangian is given by:

$$\frac{\mathcal{L}_0}{\sqrt{-G}} = R + \frac{12}{L^2} - \frac{1}{4}F_{\mu\nu}F^{\mu\nu} + \frac{1}{12\sqrt{3}}\frac{1}{\sqrt{-G}}\epsilon^{\mu\nu\rho\sigma\lambda}F_{\mu\nu}F_{\rho\sigma}A_\lambda \tag{B.0.23}$$

This is just the AdS_5 Einstein-Maxwell action, and thus the AdS_5 Reissner-Nordstroöm or equal charge ($q_1 = q_2 = q_3 = q$) three charged black hole (see Eq. (B.0.4) is a solution of this theory. The first order higher derivative corrections to this action are given by S_1:

$$\frac{\mathcal{L}_1}{\sqrt{-G}} = \frac{\lambda_D}{24}\alpha'^2\left[\frac{1}{576}(F^2)^2 - \frac{1}{48}RF^2 - \frac{1}{3\sqrt{3}L^2}\frac{1}{\sqrt{-G}}\epsilon^{\mu\nu\rho\sigma\lambda}F_{\mu\nu}F_{\rho\sigma}A_\lambda\right] + \mathcal{L}_1^{ungauged} \tag{B.0.24}$$

where

$$\begin{aligned}
\frac{\mathcal{L}_1^{ungauged}}{\sqrt{-G}} &= \lambda_D\frac{\alpha'}{24}\Bigg[\frac{1}{16\sqrt{3}}\frac{1}{\sqrt{-G}}\epsilon^{\mu\nu\rho\lambda\sigma}A_\mu R_{\nu\rho}{}^{\delta\gamma}R_{\lambda\sigma\delta\gamma} + \frac{1}{8}C^2 + \frac{1}{16}C_{\mu\nu\rho\lambda}F^{\mu\nu}F^{\rho\lambda} \\
&- \frac{1}{3}F^{\mu\rho}F_{\rho\nu}R^\nu_\mu - \frac{1}{24}RF^2 + \frac{1}{2}F_{\mu\nu}\nabla^\mu\nabla_\rho F^{\mu\rho} + \frac{1}{4}\nabla^\mu F^{\nu\rho}\nabla_\mu F_{\nu\rho} \\
&+ \frac{1}{4}\nabla^\mu F^{\nu\rho}\nabla_\nu F_{\rho\mu} + \frac{5}{64}F_{\mu\nu}F^{\nu\rho}F_{\rho\lambda}F^{\lambda\mu} - \frac{5}{256}\left(F^2\right)^2
\end{aligned}$$

$$+ \quad \frac{1}{32\sqrt{3}}\frac{1}{\sqrt{-G}}\epsilon^{\mu\nu\rho\lambda\sigma}F_{\mu\nu}\left(3F_{\rho\lambda}\nabla^{\delta}F_{\sigma\delta}+4F_{\rho\delta}\nabla^{\delta}F_{\lambda\sigma}+6F_{\rho\delta}\nabla_{\lambda}F_{\sigma}{}^{\delta}\right)\Bigg] \tag{B.0.25}$$

The total Lagrangian is given by $\mathcal{L}=\mathcal{L}_0+\mathcal{L}_1$. λ_D is a dimensionless parameter characterising the higher derivative terms, and $C_{\mu\nu\rho\sigma}=R_{\mu\nu\rho\sigma}-\frac{2}{3}\left(G_{\mu[\rho}R_{\sigma]\nu}-G_{\nu[\rho}R_{\sigma]\mu}\right)+\frac{1}{6}RG_{\mu[\rho}G_{\sigma]\nu}$. It is important to note that the higher derivative theory, that this action reduces to when the gauge field is turned off, is not the Gauss-Bonnet gravity theory. One can see this from the fact that the C^2 term exists in $\mathcal{L}_1^{ungauged}$. This is a different combination of the α_1, α_2 and α_3 parameters in Eq. (B.0.22) to the Gauss-Bonnet combination.

Let us now consider the R-charged black hole solution Eq. (B.0.24).

$$ds^2=-H^{-2}fdt^2+H(f^{-1}dr^2+r^2d\Omega_{3,k}) \tag{B.0.26}$$

The solution for the uncorrected action Eq. (B.0.23) is given by:

$$\begin{aligned} H_0 &= 1+\frac{q}{r^2} \\ A_0 &= \left(\mu-\sqrt{\frac{3\left(kq+m\right)}{m}}\left[1-\frac{1}{H_0}\right]\right)dt \\ f_0 &= k-\frac{\mu}{r^2}+\frac{r^2}{L^2}H^3 \end{aligned} \tag{B.0.27}$$

As noted above, this is the Reissner-Nordström black hole, which can also be obtained by considering the R-charged black hole with equal charges. Now, let us look

at the corrected solution:

$$\begin{aligned} H &= H_0 - \lambda_D \frac{\alpha'}{24}\left[\frac{q(kq+m)}{3r^6 H_0^2}\right] \\ f &= f_0 + \lambda_D \frac{\alpha'}{24}\left[\frac{m^2}{4r^6 H_0} - \frac{8q(kq+m)}{3r^2 L^2}\right] \\ A &= A_0 + \lambda_D \frac{\alpha'}{24}\frac{\sqrt{3q(kq+m)}}{2r^8 H_0^4}\left[2(kq+m)r^2 - mr^2 H_0\right] \end{aligned} \tag{B.0.28}$$

Once more, let us consider the flat $k = 0$ case. The horizon of the black hole to first order is defined by:

$$m = \frac{\left(q + r_H^2\right)^3}{L^2 r_H^2} + \lambda_D \frac{\alpha'}{288 L^4 r_H^6}\left[3q^2 - 26qr_H^2 + 3r_H^4\right]\left[q + r_H^2\right]^3 \tag{B.0.29}$$

One can see that the zeroth order term reduces to Eq. (B.0.7) for $q_1 = q_2 = q_3 = q$. The extremal black hole occurs at the minimum of $m(r_H)$. Thus, the conditions for the existence of the horizon is given by:

$$r_H \geq \frac{1}{96L^2}\sqrt{\frac{q}{2}}\left[96L^2 - 7\lambda_D \alpha'\right] \tag{B.0.30}$$

Once more, it is obvious that this correctly reduces to Eq. (B.0.11) for $\lambda_D = 0$.
Let us now consider the temperature of the black hole. To first order in λ_D, the temperature is given in terms of r_H and q:

$$T = \frac{\sqrt{q + r_H^2}}{2\pi L^2 r_H^2}\left[\left(2r_H^2 - q\right) + \lambda_D \frac{(14q^2 r_H^2 + 29qr_H^4 - 6r_H^6 - 3q^3)}{288 L^2 r_H^4}\alpha'\right] \tag{B.0.31}$$

Finally, the chemical potential μ is obtained by taking the limit $\lim_{r\to\infty} A_0$:

$$\mu = \frac{\sqrt{q(q+r_H^2)}}{Lr_H}\left[\sqrt{3} + \frac{\lambda_D}{192\sqrt{3}L^2 r_H^4}\left(3q^2 - 14qr_H^2 - 9r_H^4\right)\alpha'\right] \tag{B.0.32}$$

Appendix C

Near Boundary Limit of Integrals

Throughout this work, one has to evaluate integrals in order to compute stopping distances, geodesic trajectories or the evolution of energy. These integrals are non-trivial and in general cannot be written in terms of closed analytic forms. In the simple *AdS*-Schwarzchild and Sakai-Sugimoto cases, one can re-express them in terms of special functions, such as Elliptic integrals or hypergeometric functions. These functions simplify elegantly upon evaluating at specific points of interest, and also upon taking the near boundary limit $\frac{r_0}{r_H} \to \infty$[1]. In practice, this limit is obtained by taking large r_0 and holding r_H fixed, for the physical reason that the intrinsic thermodynamic properties of the plasma e.g. T, μ etc, that determine r_H, are finite.

In some cases, there is no obvious relationship between these integrals and special functions, or it is non-trivial to obtain these relationships. However, the integrals often have particular structure, that allow us to extract the leading order contribution in the near boundary expansion. Since this is the contribution we are most interested in, it is sufficient to do this.

[1]This is in co-ordinates where the boundary is located when $r \to \infty$.

C.1 Stopping Distance

Let us first consider the integrals involved in obtaining the stopping distance and the energy

$$\int_1^{\omega} d\hat{r} f(\hat{r}, r_H, \omega) = \int_1^{r_H\omega} d\hat{r} \sum_{i=0}^{\infty} f_i(\hat{r}, r_H)\omega^{l_i} \tag{C.1.1}$$

where $\omega = \frac{r_H}{r_0}$. The form of this integral is usually obtained after scaling the radial co-ordinate $r \to \hat{r}r_0$. The integrand has been expanded in powers of ω labelled l_i. It is naive to expect the leading contribution of this integral to be obtained by integrating the $i = 0$ term from 0 to 1. This is true if the integral of all terms in the series for $i > 0$, contributes a power l_i' such that $l_i' + l_i > l_0$. Let us expand by differentiating under the integral sign:

$$g_i(\omega) = \int_1^{\omega} d\hat{r} f_i(\hat{r}, r_H) \tag{C.1.2}$$

$$= \int_1^{0} d\hat{r} f_i(\hat{r}, r_H) + f_i(0, r_H)\omega + \frac{1}{2} f_i'(0, r_H)\omega^2 + \mathcal{O}(\omega^3) \tag{C.1.3}$$

This expansion is only valid if $f_i(r, r_H)$ and its derivatives are non-singular for $r \to 0$. The expansion adds positive powers only, and hence $l_i' + l_i > l_0$ as required. Hence, one can integrate the leading term in the series:

$$\int_1^{\omega} d\hat{r} f(\hat{r}, r_H, \omega) \approx \int_1^{0} f_0(r, r_H)\omega^{l_0} dr \tag{C.1.4}$$

C.2 Shooting Strings

Now, let us consider the shooting string integrals. The shooting string endpoint trajectory, for backgrounds with reflection symmetry $x \to -x$, is given by:

$$x(r) = x_t(r_*) - x_t(r) \tag{C.2.1}$$

$$x_t(r) = \int_1^{\frac{r\omega}{r_H}} d\hat{r} f(\hat{r}, r_H, \omega)$$

$$= \int_1^{\frac{r\omega}{r_H}} \sum_{i=0}^{\infty} d\hat{r} f_i(\hat{r}, r_H) \omega'^{l_i} \tag{C.2.2}$$

Once more, let us assume that the function is analytic at $r = 0$. This means that each $f_i(r, r_H)$ is also analytic at $r = 0$, and so one can expand each integral by differentiating under the integral sign.

Let us define $g_i(\omega)$ as:

$$g_i(\omega) = \int_1^{\frac{r\omega}{r_H}} d\hat{r} f_i(\hat{r}, r_H) \tag{C.2.3}$$

$$= \int_1^0 d\hat{r} f_i(\hat{r}, r_H) + f_i(0, r_H) \frac{r}{r_H} \omega + \frac{1}{2} f_i'(0, r_H) \left[\frac{r}{r_H}\right]^2 \omega^2$$

$$+ \mathcal{O}(\omega^3) \tag{C.2.4}$$

The leading term in $g_i(\omega)$ is given by the leading term of $g_0(\omega)$. The expansion in Eq. (C.2.4) shows that this leading term is always independent of r, and hence this term does not contribute to $x(r)$ because it cancels -(see Eq. (C.2.2)). The first contribution with non-trivial r dependence is $f_0(0, r_H) \frac{r}{r_H} \omega$. One can then write:

$$x_t(r) = C + f_0(0, r_H) \frac{r}{r_H} \omega^{l_0+1} + ... \tag{C.2.5}$$

where C is the constant term arising from the 0th order term in $g_0(\omega)$. Substituting into Eq. (C.2.2), the final string trajectory is given by:

$$x(r) = \frac{f_0(0, r_H)}{r_H} \omega^{l_0+1} (r_* - r) \tag{C.2.6}$$

It is important to note that this is only correct if $f_0(0, r_H)$ is non-zero. One needs to explore further terms in the near boundary expansion, should this term vanish.

Appendix D

Flavour Probe Brane embeddings

Let us consider the flavour probe branes that introduce matter multiplets into the dual field theory. In the probe limit $N_f << N_c$, the flavour branes are described by the DBI action. The bosonic part of the $N_f = 1$ action is given by:

$$S_{DBI} = -N_f T_{p+1} \int d\lambda^{p+1} e^{-\phi} \sqrt{\det \left[G_{\mu\nu} \frac{dX^\mu}{d\lambda_\alpha} \frac{dX^\nu}{d\lambda_\beta} + 2\pi F_{\alpha\beta} \right]} \tag{D.0.1}$$

where $G_{\mu\nu}$ is the background metric, X^μ describe the embedding of the probe branes, ϕ is the background dilaton field and F_{ab} is the field strength tensor for the $U(1)$ gauge field. It is important to note that the Chern-Simmons terms are not relevant for the solutions discussed. The constant in front of the field strength tensor imposes unconventional dimensions to the gauge field. This choice is made in the context of the strings attached to the probe branes. It is convenient for the gauge field to have mass dimension 1, because factors of α' cancel neatly in the string end point equation of motion.

It is well known that the mass of stretched string states is determined by the separation of the branes. This is shown by quantising strings, whose endpoints end on two separated branes. When the low energy limit is taken on the field theory side, this is seen explicitly in the action, through mass terms for the matter field

that have been introduced as a result of the probe branes. It is these stretched string states that are represented by the matter fields at low energy.

On the gravity side, the mass provides the boundary condition for the solution of the DBI action. The asymptotic behaviour of the brane embeddings is how one arrives at this conclusion [KK02]. The brane embeddings can be redefined in such a way that the function is just a scalar field; the DBI action, in terms of this re-defined field, looks like a normal scalar field. One can then use the holographic dictionary, which maps the scalar to a particular operator based on the asymptotic behaviour of the field. The operator dual to this scalar is found to have mass dimension 3, which is identified as the fermionic mass term $\bar{\psi}\psi$. The standard holographic operator/field correspondence states that this mass term is sourced by the coefficient to the non-normalisable term of the dual gravitational field, near the boundary. So the constant, chosen for the boundary condition of the brane embedding, sources the mass term in the dual theory. This is of course just the mass itself.

Alternatively, one can understand this by a more intuitive reasoning. The gravitational background tends to flat space-time in the near boundary limit. One can naively map the near boundary brane separation to the field theory brane separation, since the gravitation effects are negligible in this limit. Since the separation in the field theory is directly related to the masses of the flavour quarks, the separation at the boundary in the gravity theory is also related to the masses of the quarks in the dual field theory.

In this appendix, the embeddings of the probe branes in both the $D3/D7$ and $D4/D8$ (Sakai-Sugimoto) model are found. This is done for both low and high temperatures, with the high temperature restoration phase being of interest in the context of falling strings.

D.1 D_3/D_7 System Embedding

D.1.1 Low Temperature

Let us first consider the D_3/D_7 system at low temperature. The embedding prescription will follow the conventions of [KK02]. By defining $r^2 = x_4^2+x_5^2+x_6^2+x_7^2+x_8^2+x_9^2$, one can write the $AdS_5 \times S_5$ metric as:

$$\begin{aligned} ds^2 &= \frac{r^2}{L^2}\Big(-dt^2 + dx_1^2 + dx_2^2 + dx_3^2\Big) + \frac{L^2}{r^2}\Big(dx_4^2 + dx_5^2 + dx_6^2 + dx_7^2 + dx_8^2 + dx_9^2\Big) \\ &= \frac{r^2}{L^2}\Big(-dt^2 + dx_1^2 + dx_2^2 + dx_3^2\Big) + \frac{L^2}{r^2}\Big(d\rho^2 + \rho^2 d\theta^2 + \rho^2\cos^2\theta d\phi_1^2 + dx_8^2 + dx_9^2\Big) \\ &+ \rho^2\sin^2\theta d\phi_2^2 \end{aligned} \tag{D.1.1}$$

The last line is obtained by writing the $\mathbb{R}^4$ defined by $dx_4^2 + dx_5^2 + dx_6^2 + dx_7^2$ in the following co-ordinates:

$$x_4 = \rho\ \cos\theta\ \cos\phi_1 \tag{D.1.2}$$

$$x_5 = \rho\ \cos\theta\ \sin\phi_1 \tag{D.1.3}$$

$$x_6 = \rho\ \sin\theta\ \cos\phi_2 \tag{D.1.4}$$

$$x_7 = \rho\ \sin\theta\ \sin\phi_2 \tag{D.1.5}$$

The D_7 embeddings can be written by mapping the co-ordinates on the brane as described by Table D.1.

The background D_3 solution has the well established isometries of the field theory $SO(2,4) \times SO(6)$. The inclusion of the D_7 branes, as prescribed above, breaks this

	t	x_1	x_2	x_3	ρ	θ	ϕ_1	ϕ_2	x_8	x_9
D_3	×	×	×	×						
D_7	×	×	×	×	×	×	×	×		

Table D.1: Table showing the D_3/D_7 embedding. The symbol × marks directions parallel to the branes.

symmetry to $SO(2,4) \times SO(4) \times SO(2)$.

In our discussion, electric gauge fields are of interest, and hence need to be included. The symmetries of the system allow us to reduce dependencies on ρ only, and thus we can write $A = A_0(\rho)dt$, where the Coulomb gauge has been chosen. The symmetries also allow similar ρ dependency for the embedding co-ordinates x_8 and x_9. In order to simplify the system, let us choose $x_9 = 0$, noting that the $SO(2)$ symmetry in the $x_8 - x_9$ plane may be used to obtain all other solutions.

$$S_{D_7} = -2\pi^2 N_f T_8 e^{-\phi} \int dx^4 d\rho \rho^3 \sqrt{1 + [x_8'(\rho)]^2 - 4\pi^2 [A_0'(\rho)]^2} \tag{D.1.6}$$

Thus, the equations of motion for x_8 and A_0 are given by:

$$\frac{d}{d\rho}\left[\frac{2\pi^2\rho^3 x_8'(\rho)}{\sqrt{1 - 4\pi^2[A_0'(\rho)]^2 + [x_8'(\rho)]^2}}\right] = 0 \tag{D.1.7}$$

$$\frac{d}{d\rho}\left[\frac{8\pi^4\rho^3 A_0'(\rho)}{\sqrt{1 - 4\pi^2[A_0'(\rho)]^2 + [x_8'(\rho)]^2}}\right] = 0 \tag{D.1.8}$$

Integrating Eq. (D.1.8), one obtains:

$$x_8'(\rho) = \frac{2\pi C_1}{\sqrt{C_2^2 - 4\pi^2\left(C_1^2 - 4\pi^4\rho^6\right)}} \tag{D.1.9}$$

$$A_0'(\rho) = \frac{C_2}{2\pi\sqrt{C_2^2 - 4\pi^2 C_1^2 + 16\pi^6\rho^6}} \tag{D.1.10}$$

The solution describing the brane is the so called Minkowski solution. The brane does not fill the whole space-time but ends at some finite ρ. The tension of the brane balances the gravitational forces pulling the brane into the small ρ region of the background. One can see from the denominator of Eq. (D.1.10) that $x_8'(\rho)$ diverges at $C_2^2 - 4\pi^2\left(C_1^2 - 4\pi^4\rho^6\right) = 0$. This is the point at which the brane stops, because reducing ρ further leads to an imaginary $x_8'(\rho)$.

The fact that the brane ends like this is not physical because the brane is open. It is possible to construct a physical embedding by extending this solution. By choosing another embedding that smoothly connects to the initial solution at the cutoff ρ, one obtains a fully physical solution. Fig. D.1 shows this solution explicitly and one can see that the brane intersects the boundary at two points. Since the intersection has opposite orientations, the interpretation is that both a D_7 and an anti-D_7 is the physically realised solution.

The denominator of the gauge field equation would also diverge at the same point in ρ, which is clearly not physical. So C_2 must vanish and the gauge field is a trivial constant. The holographic dictionary allows us to identify this constant to the dual chemical potential. It is important to note the fact that the number density is necessarily zero means that this solution is not valid in the canonical ensemble, except for zero density [Kob+07]. On the other hand, the solution is perfectly valid for the fixed chemical potential grand canonical ensemble case.

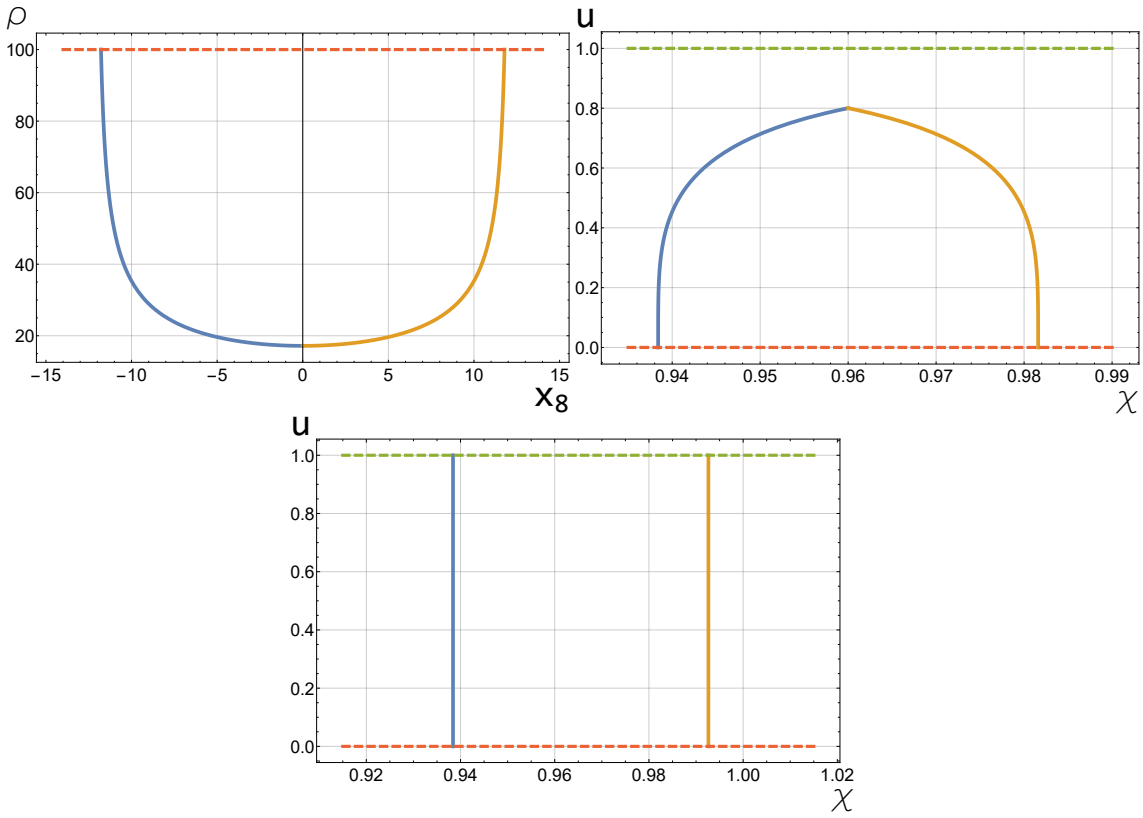

Figure D.1: This shows the plots of the low and high temperature embeddings for the D_3/D_7 system. The top left plot is for the low temperature system. The top right plot shows the Minkowski embedding for the high temperature case. Finally, the bottom plot shows the black hole embedding for the high temperature case. The Blue and Orange lines show the brane embeddings, the dashed Green line represents the horizon and the dashed Red represents the boundary.

D.1.2 High Temperature

Let us now consider the high temperature phase. At large temperatures, the Hawking-Page phase transition occurs and the non-extremal D_3 metric is the thermodynamically stable background. In order to compute the embedding, the radial component is re-scaled to a dimensionless co-ordinate $u = \frac{r_H}{r}$. The near boundary metric is given by:

$$\begin{aligned} ds^2 &= \frac{r^2}{L^2}\Big[-\left(1-\frac{r_H^4}{r^4}\right)dt^2+dx^2+dy^2+dz^2\Big]+\frac{L^2}{r^2}\frac{1}{\left(1-\frac{r_H^4}{r^4}\right)}dr^2+L^2d\Omega_5^2 \\ &= \left(\frac{r_H}{uL}\right)^2\left(-\left(1-u^4\right)dt^2+dx^2+dy^2+dz^2\right)+\frac{L^2}{u^2(1-u^4)}du^2+L^2d\Omega_5^2 \end{aligned} \tag{D.1.11}$$

In order to define the embedding co-ordinates, the S^5 is written in terms of an S^3. The S^5 metric is given by:

$$d\Omega_5 = d\theta_1^2+\sin^2\theta_1 d\theta_2^2+\cos^2\theta_1 d\phi_1^2+\sin^2\theta_1\cos^2\theta_2 d\phi_2^2+\sin^2\theta_1\sin^2\theta_2 d\phi_3^2 \tag{D.1.12}$$

$$= d\theta_1^2+\sin^2\theta_1 d\Omega_3+\cos^2\theta_1 d\phi_1^2 \tag{D.1.13}$$

The metric is obtained by considering the following co-ordinates:

$$x_1 = \cos\theta_1\,\cos\phi_1 \tag{D.1.14}$$

$$x_2 = \cos\theta_1\,\sin\phi_1 \tag{D.1.15}$$

$$x_3 = \sin\theta_1\,\cos\theta_2\,\cos\phi_2 \tag{D.1.16}$$

$$x_4 = \sin\theta_1\,\cos\theta_2\,\sin\phi_2 \tag{D.1.17}$$

$$x_5 = \sin\theta_1\,\sin\theta_2\,\cos\phi_3 \tag{D.1.18}$$

$$x_6 = \sin\theta_1\,\sin\theta_2\,\sin\phi_3 \tag{D.1.19}$$

where x_i denote the co-ordinates for $\mathbb{R}^6$ in which S^5 is embedded in. The embedding for the probe brane is shown in Table D.2:

	t	x_1	x_2	x_3	u	θ_1	ϕ_1	θ_2	ϕ_2	ϕ_3
D_3	×	×	×	×						
D_7	×	×	×	×	×			×	×	×

Table D.2: Table showing the D_3/D_7 embedding. The symbol × marks directions parallel to the branes.

This embedding follows the conventions of [MMMT07] and [Kob+07]. The authors also define $\chi = \cos\theta_1$ and $\phi_1 = 0$. This convention is also followed here. As in the low temperature case, the Coulomb gauge is once more used to describe the gauge field, and the symmetry of the action restricts dependence on the radial co-ordinate only. Substituting into the DBI action, one obtains:

$$\begin{aligned}\frac{S_{D_7}}{2\pi^2 N_f T_8 e^{-\phi}} &= -\int dx^4 du \frac{r_H^3}{u^5}\left[\left[1-\chi(u)\right]^2\right]^{\frac{3}{2}} \\ &\times \left[\frac{r_H^2 u^2\left(1-u^4\right)}{\left[1-\chi(u)\right]^2}\left[\chi'(u)\right]^2 + r_H^2 - 4\pi^2 u^4\left[A_0'(u)\right]^2\right]^{\frac{1}{2}} \end{aligned} \quad \text{(D.1.20)}$$

The equations of motion obtained from this action are given by:

$$\begin{aligned}\frac{2\pi^2 r_H^5\left(1-u^4\right)\left(1-\left[\chi(u)\right]^2\right)\chi'(u)}{u^3\sqrt{r_H^2\left[u^2\left(1-u^4\right)\left[\chi'(u)\right]^2+1-\left[\chi(u)\right]^2\right]-4\pi^2u^4\left(1-\left[\chi(u)\right]^2\right)\left[A'(u)\right]^2}} &= C_1 \\ \frac{8\pi^4 r_H^3\left(1-\left[\chi(u)\right]^2\right)^2 A'(u)}{u\sqrt{r_H^2\left[u^2\left(1-u^4\right)\left[\chi'(u)\right]2+1-\left[\chi\right]^2\right]-4\pi^2u^4\left(1-\left[\chi\right]^2-1\right)A'(u)^2}} &= C_2 \end{aligned} \quad \text{(D.1.21)}$$

It is noted in [MMT07] and [MMT06] that in general there are two classes of solution for the finite temperature system . The Minkowski embeddings are those that do not fall into the black hole. The radius of the S^3 is given by $\sin^2\theta_1$, and the

Minkowski embeddings are defined by the reduction of the sphere radius to zero outside the black hole. To be more precise, at $u = u_0 < 1$, $\chi = 1$ and $\frac{d\chi}{du} = 0$. Fig. D.1 shows the Minkowski embedding for the black hole high temperature background.

The black hole embeddings are those which fall into the black hole i.e at $u = 1$, $\chi = \chi_0$ and $\frac{d\chi}{du} = 0$. The authors of [MMT07] and [MMT06] considered the case with no gauge field, and showed that the transition between embeddings occurs discontinuously as one increases the temperature. At very low/high temperatures, the only solutions available are Minkowski/black hole embeddings. At temperatures near the so called critical solution, where the embedding just touches the black hole horizon, both Minkwoski and black hole solutions exist. Free energy minimisation determines which embedding is physical for the given temperature and mass, and hence a 1st order phase transition occurs. A key physical property, which distinguishes both embeddings, are the mass spectra of the mesons formed from these quarks. The Minkowski embeddings give rise to a discrete spectrum of mesons, whilst the black hole embeddings give a continuous spectrum. The phase transition describes the so called melting of mesons that is observed in QCD.

The case involving a non-zero gauge field was studied in [MMMT07] and [Kob+07]. In the former, finite non-zero number density was studied i.e. the system is analysed in the canonical ensemble. The Minkowski embedding solutions with gauge field do not allow for non-trivial gauge field profiles; the solutions are of the form $A_0(u) = \mu$, and thus Minkowski embeddings are not allowed for the fixed number density case. One can see this physically by considering the electric field lines which have no place to end.

The system at finite chemical potential is considered in [MMMT07]. Since the chemical potential and not the number density is being fixed, the grand canonical ensemble is the distribution of interest. The Minkowski embedding is now allowed

and a phase transition to the black hole embedding occurs at for some set of values (μ, T).

For our study of light quarks, it is the massless limit $\frac{m}{T} \to 0$ that is of interest. The only physical solution is the black hole embedding given by $\chi = 0$. One can now solve Eq. (D.1.21) for the gauge field, imposing the boundary conditions when $u = 1$, $A_0(u) = 0$. The gauge field solution is given by:

$$\begin{aligned} A_0'(u) &= -\frac{dr_H u}{\sqrt{4\pi^2 d^2 u^6 + 1}} \\ \Rightarrow A_0(u) &= \frac{1}{2} dr_H \left[{}_2F_1\left[\frac{1}{3}, \frac{1}{2}; \frac{4}{3}; -4d^2\pi^2\right] - {}_2F_1\left[\frac{1}{3}, \frac{1}{2}; \frac{4}{3}; -4d^2\pi^2 u^6\right] u^2 \right] \end{aligned} \tag{D.1.22}$$

C_2 has been set to $8\pi^4 d r_H^3$, where d is a dimensionless constant. The chemical potential is obtained by taking the limit $u \to 0$, and dividing through by α'. This is in order to account for the dimensional conventions chosen for the gauge field initially. Taking the limit, one obtains:

$$\mu = \frac{dr_H}{2\alpha'} {}_2F_1\left[\frac{1}{3}, \frac{1}{2}; \frac{4}{3}; -4d^2\pi^2\right] \tag{D.1.23}$$

$$\Rightarrow \frac{\mu}{T\sqrt{\lambda}} = \frac{d\pi}{2} {}_2F_1\left[\frac{1}{3}, \frac{1}{2}; \frac{4}{3}; -4d^2\pi^2\right] \tag{D.1.24}$$

$$\approx \frac{d\pi}{2} - \frac{1}{4}\pi^3 d^3 + \frac{3}{7}\pi^5 d^5 + \mathcal{O}(d^7) \tag{D.1.25}$$

The dimsionless constant d is related to the expectation value of the number density n through:

$$n = \frac{N_f N_c \lambda^{\frac{1}{2}} \pi}{2^{\frac{3}{2}}} T^3 d\alpha' \tag{D.1.26}$$

D.2 Sakai-Sugimoto D_4/D_8 System Embedding

D.2.1 Low Temperature

In this section, the probe $D_8/\bar{D}_8$ brane embeddings are computed. The confining low temperature system is considered first. The D_4 soliton describing this low temperature background is given as follows:

$$ds^2 = \left(\frac{r}{L}\right)^{\frac{3}{2}} \left(-dt^2 + dx^2 + dy^2 + dz^2 + f(r)d\tau^2\right) + \left(\frac{L}{r}\right)^{\frac{3}{2}} \left(\frac{dr^2}{f(r)} + r^2 d\Omega_4\right) \tag{D.2.1}$$

where $f(r) = 1 - \left(\frac{r_{KK}}{r}\right)^3$. The periodicity of the τ co-ordinate, required to remove the conical singularity in $\tau - r$ space is given by $\delta\tau = \frac{4\pi}{3} \frac{L^{\frac{3}{2}}}{r_{KK}^{\frac{1}{2}}}$. This is related to the Kaluza-Klein mass scale, obtained by compactifying over the compact τ direction. So, one can relate r_{KK} to the mass scale by:

$$r_{KK} = \frac{4}{9} L^3 M_{KK} \tag{D.2.2}$$

The dilaton field associated with this solution is given by:

$$\phi(r) = g_s \left(\frac{r}{L}\right)^{\frac{3}{4}} \tag{D.2.3}$$

The manner in which the probe branes are embedded in the background is given by Table D.3. Given this choice of embedding, let us solve for the embedding using the DBI action.

	t	x_1	x_2	x_3	r	$\theta 1$	$\theta 2$	ϕ_1	ϕ_2	τ
D_4	×	×	×	×	×					
D_8	×	×	×	×	×	×	×	×	×	

Table D.3: Table showing the D_4/D_8 embedding. The symbol × marks directions parallel to the branes.

$$S_8 = -\frac{4\pi^2}{3g_s} N_f T_9 \int r^{5/2} \sqrt{4\pi^2 L^3 A'(r)^2 + \frac{L^3 r^3}{r^3 - r_{KK}^3} + \tau'(r)^2 \left(r^3 - r_{KK}^3\right)} \qquad \text{(D.2.4)}$$

Extremising the action, one obtains the following equations of motion:

$$\frac{r^{5/2}\tau'(r)\left(r^3 - r_{KK}^3\right)}{\sqrt{4\pi^2 L^3 A'(r)^2 + \frac{L^3 r^3}{r^3 - r_{KK}^3} + \tau'(r)^2 \left(r^3 - r_{KK}^3\right)}} = C_1 \qquad \text{(D.2.5)}$$

$$\frac{r^{5/2} A'(r)}{\sqrt{4\pi^2 L^3 A'(r)^2 + \frac{L^3 r^3}{r^3 - r_{KK}^3} + \tau'(r)^2 \left(r^3 - r_{KK}^3\right)}} = C_2 \qquad \text{(D.2.6)}$$

One can see from the denominator of the embedding equation of motion, that there is a fixed $r_0 \geq r_{KK}$, where the brane must terminate; the denominator of $\tau'(r)$ diverges at this value of r and $\tau'(r)$ becomes imaginary for small values of r. Once more, the open ended nature of the brane is unphysical. As in the D_3/D_7 case Sub. D.1.1, the physical solution is obtained by smoothly connecting this solution to another D_8 embedding that tends to the boundary - (see Fig. D.2). The solution intersects the boundary at two points with different orientations, representing D_8 and anti-D_8 branes.

The branes and the anti-branes curve into the bulk from the boundary and connect at the cutoff radial value. The configuration of the branes can be shown to break the $U(N_f)_L \times U(N_f)_R$ chiral symmetry, as one would expect from QCD [SS05b]. The authors show this by perturbing the probe brane fields about this stable solution.

The gauge field cannot be non-trivial. The denominator of $A'(r)$ diverges at the radial cut of r_0. This is not physical as the electric field clearly diverges in this case. Hence, the gauge field takes a trivial form $A(r) = \mu\alpha'$, where μ is the dual chemical potential.

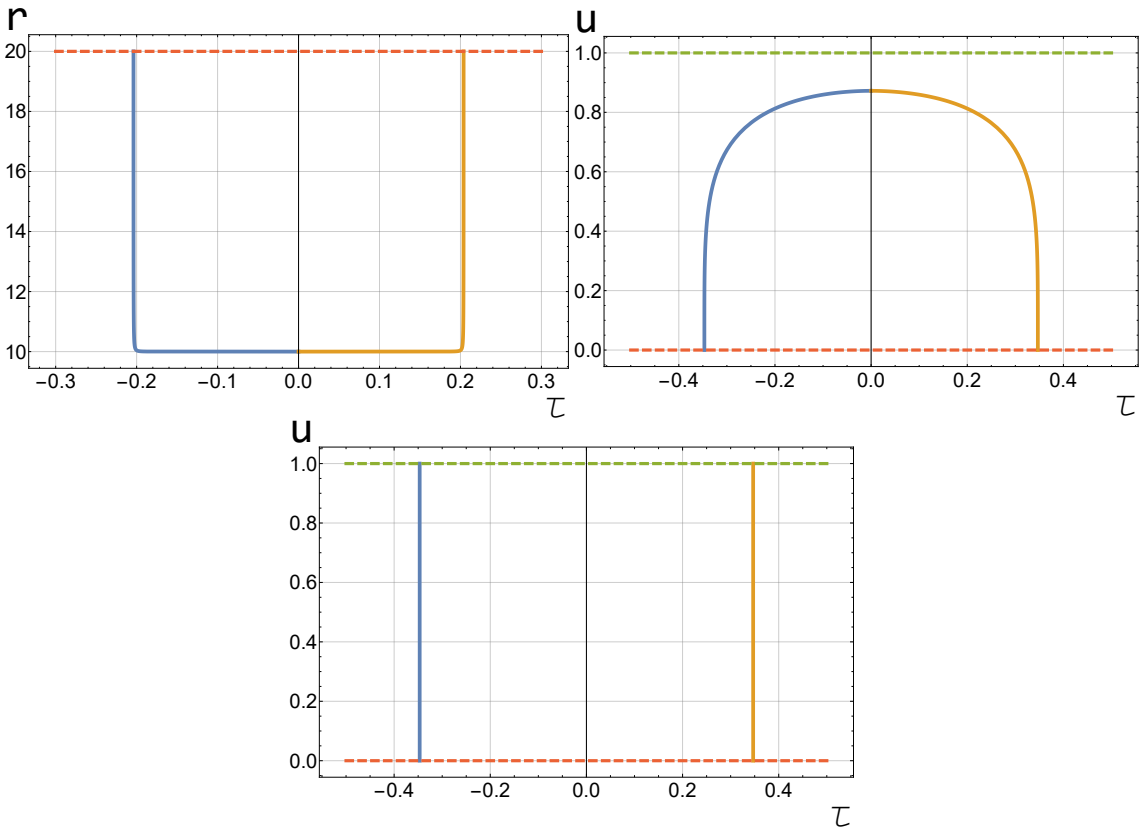

Figure D.2: This shows the plots of the low and high temperature embeddings for the D_4/D_8 Sakai-Sugimoto system. The top left plot is for the low temperature system. The top right plot shows the Minkowski embedding for the high temperature case. Finally, the bottom plot shows the black hole embedding for the high temperature case. The Blue and Orange lines show the brane embeddings, the dashed Green line represents the horizon and the dashed Red represents the boundary.

D.2.2 High Temperature

Let us now consider the high temperature case. At large enough temperatures, the background undergoes a Hawking-Page like phase transition and a black hole appears in the background. On the dual field theory side, this describes the confine-

ment/deconfinement phase transition. The metric is given by:

$$ds^2 = \left(\frac{r}{L}\right)^{\frac{3}{2}}\left(-\tilde{f}(r)dt^2+dx^2+dy^2+dz^2+d\tau^2\right)+\left(\frac{L}{r}\right)^{\frac{3}{2}}\left(\frac{dr^2}{\tilde{f}(r)}+r^2d\Omega_4\right) \quad \text{(D.2.7)}$$

$$= \left(\frac{r_H}{Lu}\right)^{\frac{3}{2}}\left(-\tilde{f}(u)dt^2+dx^2+dy^2+dz^2+d\tau^2\right)+\left(\frac{Lu}{r_H}\right)^{\frac{3}{2}}\left(\frac{r_H^2}{u^4}\frac{du^2}{\tilde{f}(u)}+\frac{r_H^2}{u^2}d\Omega_4\right) \quad \text{(D.2.8)}$$

where $\tilde{f}=1-\left(\frac{r_h}{r}\right)^3=1-u^3$ and $u=\frac{r_H}{u}$. The periodicity of the τ co-ordinate is now imposed and set to that of the low temperature case. The time co-ordinate must be periodic in the Euclidean section in order to remove the conical singularity, as is usual for black hole solutions.

The embedding for the high temperature case is given in the same way as the low temperature case - (see Tab. D.3). In other words, the only direction transverse to the probe brane is the compact τ-direction. Given this choice of embedding, the DBI action can be written as :

$$S_8=\frac{4\pi^2 r_H^{\frac{5}{2}}N_f T_9}{3g_s}\int du\left[\frac{1}{u}\right]^{\frac{17}{4}}\sqrt{r_H^2\left[L^3-r_H u\left(u^3-1\right)\left[\tau'(u)\right]^2\right]-4\pi^2L^3u^4A'(u)^2} \quad \text{(D.2.9)}$$

Using Eq. (D.2.9), one can now find the equations of motion for $\tau(u)$ and the gauge field $A(u)$.

$$\frac{\left(1-u^3\right)\tau'(u)}{\sqrt{u^7\left[r_H^2\left[L^3+r_H u\left(1-u^3\right)\left[\tau'(u)\right]^2\right]-4\pi^2L^3u^4A'(u)^2\right]}} = C_1$$

$$-\frac{A'(u)}{u\sqrt{\left[r_H^2\left[L^3+r_H u\left(1-u^3\right)\left[\tau'(u)\right]^2\right]-4\pi^2L^3u^4A'(u)^2\right]}} = C_2 \quad \text{(D.2.10)}$$

In a similar way to the D_3/D_7 case, there are the two types of solution for the probe D_8 branes. Fig. D.2 shows both the Minkwoski and black hole branes for the Sakai-Sugimoto model. Again, there is a phase transition,where the Minkowski branes dominate for lower temperatures and the black hole branes dominate for high temperatures.

As noted in the low temperature case, the Minkowski branes are the gravitational representation of chiral symmetry breaking, whilst the black hole branes do not break the symmetry. This phase transition represents the chiral restoration phase transition that occurs in QCD [SS05b]. This transition occurs with or without the gauge field turned on [HT07].

Since it is the restoration phase that is of interest in the context of energy loss of light probes, let us compute the gauge field for this case. The black hole embedding is given by the trivial solution $\tau'(u) = 0$. This is equivalent to setting $C_1 = 0$. Given this constant choice and the boundary condition $A(u = 1) = 0$, one obtains the following expression for the gauge field:

$$\begin{aligned} A'(u) &= -\frac{d^2 r_H \sqrt{u}}{\sqrt{1 + 4\pi^2 d^4 u^5}} \\ \Rightarrow A(u) &= \frac{2}{3} d^2 r_H \left[{}_2F_1\left[\frac{3}{10}, \frac{1}{2}; \frac{13}{10}; -4d^4\pi^2\right] - u^{\frac{3}{2}}\, {}_2F_1\left[\frac{3}{10}, \frac{1}{2}; \frac{13}{10}; -4d^4\pi^2 u^5\right]\right] \end{aligned} \tag{D.2.11}$$

In order to simplify the solution, the choice $C_2 = \frac{d^2}{L^{\frac{3}{2}}}$ has been made for the constant and d is a dimensionless constant. The chemical potential is obtained by taking the limit $u \to 0$.

$$\begin{aligned}\mu &= \frac{2}{3}d^2 r_H\, {}_2F_1\left[\frac{3}{10},\frac{1}{2};\frac{13}{10};-4d^4\pi^2\right] \\ &\approx \frac{12}{23}\pi^4 d^{10} r_H - \frac{4}{13}\pi^2 d^6 r_H + \frac{2d^2 r_H}{3} + \mathcal{O}(d^1 4) \qquad \text{(D.2.12)}\end{aligned}$$

Appendix E

Finite Temperature Anisotropic Gravitational Dual

In this section, the finite temperature dual to the anisotropic plasma, as found in [MT11], is described. The solution is a deformation of the canonical $\mathcal{N} = 4$ Super Yang-Mills case. To be specific, the field theory is deformed by a space dependent $\theta(z)$ term. In particular, the θ term depends on one of the three spatial directions chosen to be z. The solution of interest will thus have rotational symmetry in the $x - y$ plane; the element of anisotropy is introduced in this chosen direction. The action is given by:

$$S_{Aniso.} = S_{\mathcal{N}=4} + \frac{1}{8\pi}\int \theta(z)\mathrm{Tr}F \wedge F \tag{E.0.1}$$

The solution of interest is given by choosing $\theta(z) = 2\pi n_{D7} z$. Whilst it may seem as though this term breaks translation invariance, it can be shown by integration by parts that this is not the case. In fact, the solution directly shows this through its independence of z. The action clearly introduces anisotropy.

Space-time dependent θ terms are of interest in the context of the QCD phase transition. The introduction of the θ term induces meta-stable P and CP-violating

QCD vacuum states. These P and CP-odd vacuum domains, known as 'bubbles', have been studied at the RHIC, because it is thought they are relevant to the QCD phase transition in the Early Universe - see [KZ07] and [KPT98].

Having established the field theory action of interest, let us introduce the gravitational dual. The existence of the θ term introduces a non-zero axion term in the dual gravitational description of the system. The axion χ is a pseudo-scalar derived from the closed string zero mass Kalb-Rammond field $B_{\mu\nu}$. The following expression defines the axion in the Einstein frame:

$$\partial_\mu \chi = \frac{1}{6} e^{-2\phi} \sqrt{-\det [G]} \epsilon_\mu{}^{\nu\rho\sigma} H_{\nu\rho\sigma} \tag{E.0.2}$$

where ϕ is the Einstein frame dilaton and $H_{\mu\nu\rho}$ is the field strength three form associated with $B_{\mu\nu}$. The source of the axion field are D_7 branes, which are dissolved into the background and are not probes [ALT09].

The full 5D Einstein frame gravitational action, including the axion and dilaton, is given by:

$$S^E_{Axion} = \frac{N_c^2}{8\pi^2 L^3} \int dx^\mu du \sqrt{-G} \left(R + \frac{12}{L^2} - \frac{1}{2} (\partial\phi)^2 - \frac{1}{2} e^{2\phi} (\partial\chi)^2 \right) \tag{E.0.3}$$

The static asymptotically AdS_5 black hole solution can be written by reducing the unknowns to four function[1]:

$$ds^2_{Aniso.} = \frac{L^2 e^{\frac{1}{2}\phi(u)}}{u^2} \left(-f(u)b(u)dt^2 + dx^2 + dy^2 + h(u)dz^2 + \frac{du^2}{f(u)} \right) \tag{E.0.4}$$

$$\chi(z) = az$$

[1]The radial co-ordinate u is the inverted co-ordinate, where the boundary is define by $u \to 0$.

$$h(u) = e^{-\phi(u)}$$

$$\phi = \phi(u)$$

It is important to note that this 5D metric is part of the full 10D metric given by $ds^2_{Aniso.} \times S^5$. The D_7 branes sourcing the axion field wraps the S^5 and are embedded in the four gauge theory directions. The branes are spread evenly across the z direction with density n_7. The parameter a, which parametrises the anisotropy, is related to the density via $a = \frac{\lambda n_7}{4\pi N_c}$. One can explicitly see the anisotropy comes from the G_{zz} term in Eq. (E.0.4). Similarly, the retention of rotational symmetry in the $x - y$ plane is evident.

The functions $f(u)$, $h(u)$, $b(u)$ and $\phi(u)$ are solved, by substituting Eq. (E.0.4) into the equations of motion obtained from the action Eq. (E.0.1). However, the system is not solvable exactly for arbitrary a. Instead, the authors in [MT11] use numerical techniques to obtain the solution over a finite domain of a. A small a perturbative solution is found and it is this solution that is used in the analysis of the light probe energy loss.

It is important to note that the action is invariant under the transformation $a \to -a$, due to the quadratic nature of the axion kinetic term. This means the perturbative expansion contains only even terms only.

$$f(u) = 1 - \frac{u^4}{u_H^4} + a^2 f_2(u) \tag{E.0.5}$$

$$b(u) = 1 + a^2 b_2(u) \tag{E.0.6}$$

$$\phi(u) = a^2\phi_2(u) \tag{E.0.7}$$

In this case, u_H is the horizon radius[2]. The corrections are found by substituting into the equations of motion. The final forms are given by:

$$\begin{aligned} f_2(u) &= \frac{1}{24u_H^2}\Bigg[8u^2(u_H^2-u^2) - 10u^4\log 2 \\ &+ (3u_H^4+7u^4)\log\left(1+\frac{u^2}{u_H^2}\right)\Bigg] \end{aligned} \tag{E.0.8}$$

$$b_2(u) = -\frac{u_H^2}{24}\left[\frac{10u^2}{u_H^2+u^2} + \log\left(1+\frac{u^2}{u_H^2}\right)\right] \tag{E.0.9}$$

$$\phi_2(u) = -\frac{u_H^2}{4}\log\left(1+\frac{u^2}{u_H^2}\right) \tag{E.0.10}$$

In [MT11], the authors compute the next a^4 correction term. For the purposes of this investigation, the first correction term is enough.

The temperature of this black hole solution is computed in the canonical way; finding the required periodicity of the Euclidean time required to remove the conical singularity at the horizon. The temperature is given by:

$$T = \frac{1}{\pi u_H} + a^2\frac{u_H}{48\pi}\left(\log 32 - 2\right) \tag{E.0.11}$$

The entropy and energy densities of the plasma can be computed from the free energy density f, which is found by evaluating the partition function. As a function

[2]The correction does not affect the horizon radius by the boundary condition $f_2(u_H) = 0$.

of temperature, these are given by:

$$\begin{aligned} s &= \frac{3N_c^2\pi^2T^4}{8} + a^2\frac{N_c^2T^2}{32} \\ \epsilon &= \frac{N_c^2\pi^2T^4}{2} + a^2\frac{N_c^2T}{16} \end{aligned} \tag{E.0.12}$$

An important feature of this system is the fact that it is non-conformal. The deformation away from $\mathcal{N} = 4$ Super Yang-Mills is marginally relevant, and this can be seen explicitly from the non-zero trace of the stress-tensor [MT11]. The system is now dependent on a renormalisation scale μ. Since a has dimensions of energy, the small a limit, that is being taken in this expansion, is more precisely defined by both $\frac{a}{T} \ll 1$ and $\frac{a}{\mu} \ll 1$.

Bibliography

[ABS06] A. Andronic, P. Braun-Munzinger and J. Stachel. 'Hadron production in central nucleus–nucleus collisions at chemical freeze-out'. In: *Nuclear Physics A* 772.3 (2006).

[AC07] Nils Andersson and Gregory L. Corner. 'Relativistic fluid dynamics: Physics for many different scales'. In: *Living Rev. Relativity* 10 (2007).

[ACX10] Pete Arnold, Sean Cantrell and Wei Xiao. 'Stopping distance for high energy jets in weakly coupled quark-gluon plasmas'. In: *Phys. Rev. D 81, 045017* (2010).

[Ada+05a] J. Adams, M. M. Aggarwal, Z. Ahammed, J. Amonett, B. D. Anderson, D. Arkhipkin, G. S. Averichev and S. K. Badyal. 'Experimental and theoretical challenges in the search for the quark–gluon plasma: The STAR Collaboration's critical assessment of the evidence from RHIC collisions'. In: *Nuclear Physics A* 757.1 (2005). First Three Years of Operation of RHIC.

[Ada+05b] J. Adams, M. M. Aggarwal, Z. Ahammed, J. Amonett, J. D. Anderson and D. Arkhipkin. 'Azimuthal anisotropy in Au+Au collisions at $\sqrt{s_{NN}} = 200$ GeV'. In: *Phys. Rev. C* 72 (1 July 2005), p. 014904.

[Ada+08] A. Adare et al. 'Quantitative constraints on the transport properties of hot partonic matter from semi-inclusive single high transverse momentum pion suppression in Au+Au collisions at $\sqrt{s_{NN}} = 200$ GeV'. In: *Phys. Rev. C* 77 (6 June 2008), p. 064907.

[Adc+05] K. Adcox et al. 'Formation of dense partonic matter in relativistic nucleus–nucleus collisions at RHIC: Experimental evaluation by the PHENIX Collaboration'. In: *Nuclear Physics A* 757.1 (2005). First Three Years of Operation of RHIC.

[AEM06] Néstor Armesto, José Daniel Edelstein and Javier Mas. 'Jet quenching at finite 't Hooft coupling and chemical potential from AdS/CFT'. In: *Journal of High Energy Physics* 2006.09 (2006), p. 039.
9.

[ALT09] Tatsuo Azeyanagi, Wei Li and Tadashi Takayanagi. 'On string theory duals of Lifshitz-like Fixed Points'. In: *JHEP 0906:084,2009* (2009).

[And14] Anton Andronic. 'An overview of the experimental study of quark–gluon matter in high-energy nucleus–nucleus collisions'. In: *International Journal of Modern Physics A* 29.22 (2014), p. 1430047.

[Ars+05] I. Arsene, I. G. Bearden, D. Beavis, C. Besliu, B. Budick, H. Boggild, C. Chasman and C. H. Christensen. 'Quark–gluon plasma and color glass condensate at RHIC? The perspective from the BRAHMS experiment'. In: *Nuclear Physics A* 757.1 (2005). First Three Years of Operation of RHIC.

[AS10] A.rdian Nata Atmaja and Koenraad Schalm. 'Anisotropic drag force from 4D Kerr-AdS Black Holes'. In: *arXiv:1012.3800* (2010).

[ASRS08] Mark G. Alford, Andreas Schmitt, Krishna Rajagopal and Thomas Schäfer. 'Color superconductivity in dense quark matter'. In: *Rev Mod. Phys.* 80 (4 Nov. 2008), pp. 1455–1515.

[AV10] Peter Arnold and Diana Vaman. 'Jet quenching in hot strongly coupled gauge theories revisited: 3-point correlators with gauge-gravity duality'. In: *J. High Energy. Phys.* 27 (2010).

[AV11] Peter Arnold and Diana Vaman. 'Jet quenching in hot strongly coupled gauge theories simplified'. In: *J. High Energy. Phys.* 99 (2011).

[Bac+05] B. B. Back, M. D. Baker, M. Ballintijn, D. S. Barton, B. Becker, R. R. Betts, A. A. Bickley and R. Bindel. 'The PHOBOS perspective on discoveries at RHIC'. In: *Nuclear Physics A* 757.1 (2005). First Three Years of Operation of RHIC.

[Bai+97] R. Baier, Yu. L. Dokshitzer, A. H. Mueller, S. Peigné and D. Schiff. 'Radiative energy loss and p_T-broadening of high energy partons in nuclei'. In: *Nuclear Physics B* 484.1 (1997).

[Bal+13] Gunnar Bali, Francis Bursa, Luca Castagnini, Sara Collins, Luigi Del Debbio, Biagio Lucini and Marco Panero. 'Mesons in large-N QCD'. In: *JHEP* (2013).

[Ban06] Vishnu M. Bannur. 'Strongly coupled quark gluon plasma (SCQGP)'. In: *Journal of Physics G: Nuclear and Particle Physics* 32.7 (2006), p. 993.

[Ban95] Vishnu M. Bannur. 'Equation of state for a non-ideal quark gluon plasma'. In: *Physics Letters B* 362.1 (1995).

[BBHP76] William A. Bardeen, Itzhak Bars, Andrew J. Hanson and R. D. Peccei. 'Study of the longitudinal kink modes of the string'. In: *Phys. Rev. D* 13 (1976).

[BCH73] J. M. Bardeen, B. Carter and Stephen W. Hawking. 'The four laws of black hole mechanics'. In: *Communications in Mathematical Physics* (1973).

[BCS99] K. Behrndt, M. Cvetič and W. A. Sabra. 'Non-extreme black holes of five-dimensional $\mathcal{N} = 2$ AdS supergravity'. In: *Nuclear Physics B* 553.1 (1999), pp. 317–332.

[Bec14] Francesco Becattini. 'The Quark Gluon Plasma and relativistic heavy ion collisions in the LHC era'. In: *Journal of Physics: Conference Series* 527.1 (2014), p. 012012.

[Ben09] Jacob Sonnenschein Benjamin A. Burrington. 'Holographic Dual of QCD from Black D5 Branes'. In: *JHEP 0908:057* (2009).

[Bha+14] Tanmoy Bhattacharya, Michael I. Buchoff, Norman H. Christ, Rajan Gupta and Chulwoo Jung. 'QCD Phase Transition with Chiral Quarks and Physical Quark Masses'. In: *Physical Review Letters* (2014).

[Bha14] Rajeev S. Bhalerao. 'Relativistic heavy-ion collisions'. In: *CERN TIFR-TH-14-11* (Apr. 2014).

[BHB10] M. Bonitz, C. Henning and D. Block. 'Complex plasmas: a laboratory for strong correlations'. In: *Reports on Progress in Physics* 73.6 (2010), p. 066501.

[BL07] Piyabut Burikham and Jun Li. 'Aspects of the screening length and drag force in two alternative gravity duals of the quark-gluon plasma'. In: *Journal of High Energy Physics* 2007.03 (2007), p. 067.

[BLLM08] Sayantani Bhattacharyya, Subhaneil Lahiri, R. Loganayagam and Shiraz Minwalla. 'Large rotating AdS black holes from fluid mechanics'. In: *Journal of High Energy Physics* 054 (2008).

[Blo+69] E. D. Bloom et al. 'High-Energy Inelastic $e - p$ Scattering at 6° and 10°'. In: *Phys Rev. Lett.* 23 (16 Oct. 1969), pp. 930–934.

[Bre+69] M. Breidenbach, J. I. Friedman, H. W. Kendall, E. D. Bloom, D. H. Coward, H. DeStaebler, J. Drees, L. W. Mo and R. E. Taylor. 'Observed Behavior of Highly Inelastic Electron-Proton Scattering'. In: *Phys Rev. Lett.* 23 (16 Oct. 1969), pp. 935–939.

[Bur+14] Karen M. Burke et al. 'Extracting the jet transport coefficient from jet quenching in high-energy heavy-ion collisions'. In: *Phys. Rev. C* 90 (1 July 2014), p. 014909.

[BVS06] D. Boyanovsky, H.J. de Vega and D.J. Schwarz. 'Phase Transitions in the Early and Present Universe'. In: *Annual Review of Nuclear and Particle Science* 56.1 (2006), pp. 441–500.

[CCS07] Rong-Gen Cai, Li-Ming Cao and Ya-Wen Sun. 'Hawking-Page phase transition of black D_p-branes and R-charged black holes with an IR cutoff'. In: *JHEP 0711 (2007) 039* (2007).

[CEJM99] Andrew Chamblin, Roberto Emparan, Clifford V. Johnson and Robert C. Myers. 'Charged AdS black holes and catastrophic holography'. In: *Phys. Rev. D 60, 064018* (1999).

[CFMT12a] Mariano Chernicoff, Daniel Fernández, David Mateos and Diego Trancanelli. 'Drag force in a strongly coupled anisotropic plasma'. In: *J. High Energy. Phys.* 100 (2012).

[CFMT12b] Mariano Chernicoff, Daniel Fernández, David Mateos and Diego Trancanelli. 'Jet quenching in a strongly coupled anisotropic plasma'. In: *Journal of High Energy Physics* 2012.8 (Aug. 2012), p. 41.

[CG99] Mirjam Cvetic and Steven S. Gubser. 'Phases of R-charged black holes spinning branes and stronly coupled gauge theories'. In: *JHEP04(1999)* (1999).

[Cha+12] S. Chatrchyan, V. Khachatryan, A. M. Sirunyan, A. Tumasyan, W. Adam and T. Bergauer. 'Azimuthal Anisotropy of Charged Particles at High Transverse Momenta in Pb-Pb Collisions at $\sqrt{s_{NN}}$=2.76 TeV'. In: *Phys Rev. Lett.* 109 (2 July 2012), p. 022301.

[CHLS09] Sera Cremonini, Kentaro Hanaki, James T. Liu and Phillip Szepietowski. 'Black holes in five-dimensional gauged supergravity with higher derivatives'. In: *JHEP 12 (2009) 045* 2009.12 (2009), p. 045.

[CJK09] Paul M. Chesler, Kristian Jensen and Andreas Karch. 'Jets in strongly-coupled N=4 super Yang-Mills theory'. In: *Phys.Rev.D79:025021* (2009).

[CJKY09] Paul M. Chesler, Kristian Jensen, Andreas Karch and Laurence G. Yaffe. 'Light quark energy loss in strongly-coupled N=4 supersymmetric Yang-Mills plasma'. In: *Phys.Rev.D79:125015* (2009).

[CKY14] Elena Caceres, Arnab Kundu and Di-Lun Yang. 'Jet quenching and holographic thermalization with a chemical potential'. In: *Journal of High Energy Physics* 2014.3 (Mar. 2014), p. 73.

[CLQW18] Shanshan Cao, Tan Luo, Guang-You Qin and Xin-Nian Wang. 'Heavy and light flavor jet quenching at RHIC and LHC energies'. In: *Physics Letters B* 777 (2018).

[CM98] Curtis G. Callan and Juan M. Maldacena. 'Brane dynamics From the Born-Infeld action'. In: *Nucl. Phys. B513* (1998).

[Col12] Cms Collaboration. *Nuclear modification factor of high transverse momentum jets in PbPb collisions at* $\sqrt{s_{NN}} = 2.76TeV$. 2012.

[Col18] Atlas Collaboration. *Measurement of the nuclear modification factor for inclusive jets in Pb+Pb collisions at* $\sqrt{s_{NN}} = 5.02TeV$ *with the ATLAS detector*. 2018.

[COOT99] Csaba Csáki, Hirosi Ooguri, Yaron Oz and John Terning. 'Glueball mass spectrum from supergravity'. In: *Journal of High Energy Physics* 1999.01 (1999), p. 017.

[COV05] Norman Cruz, Marco Olivares and Jose R. Villanueva. 'The geodesic structure of the Schwarzchild Anti-de Sitter black hole'. In: *Class. Quant. Grav* 22 (2005), pp. 1167–1190.

[CP75] J. C. Collins and M. J. Perry. 'Superdense Matter: Neutrons or Asymptotically Free Quarks?' In: *Phys Rev. Lett.* 34 (21 May 1975), pp. 1353–1356.

[Cve+99] M. Cvetic, Michael J. Duff, P. Hoxha, James T. Liu, H. Lu and R. Martinez-Acosta. 'Embedding *AdS* black holes in ten and eleven Dimensions'. In: *Nucl. Phys. B558 96-126* (1999).

[DKK99] Ulf H. Danielsson, Esko Keski-Vakkuri and Martín Kruczenski. 'Vacua, propagators, and holographic probes in AdS/CFT'. In: *Journal of High Energy Physics* 1999.01 (Jan. 1999), pp. 002–002.

[DNSS08] Adrian Dumitru, Yasushi Nara, Björn Schenke and Michael Strickland. 'Jet broadening in unstable non-Abelian plasmas'. In: *Phys. Rev. C* 78 (2 Aug. 2008), p. 024909.

[EEKT07] Johanna Erdmenger, Nick Evans, Ingo Kirsch and Ed Threlfall. 'Mesons in Gauge/Gravity duals a review'. In: *http://arxiv.org/abs/0711.4467* (2007).

[FG14] A. Ficnar and S. S. Gubser. 'Finite momentum at string endpoints'. In: *Phys. Rev. D 89, 026002* (2014).

[FGG14] Andreij Ficnar, Steven S. Gubser and Miklos Gyulassy. 'Shooting string holography of jet quenching at RHIC and LHC'. In: *Physics Letters B* (2014).

[FM18] Kazem B. Fadafan and Razieh Morad. 'Jets in a strongly coupled anisotropic plasma'. In: *Eur. Phys. C* 78:16 (2018).

[FPS11] K. Bitaghsir Fadafan, B. Pourhassan and J. Sadeghi. 'Calculating the jet-quenching parameter in STU background'. In: *J. Eur. Phys. J. C* (2011).

[Gel64] M. Gell-Mann. 'A schematic model of baryons and mesons'. In: *Physics Letters* 8.3 (1964).

[GGPR08] Steven S. Gubser, Daniel R. Gulotta, Silviu S. Pufu and Fábio D. Rocha. 'Gluon energy loss in the gauge-string duality'. In: *Journal of High Energy Physics* 2008.10 (2008), p. 052.

[GH76] Gary W. Gibbons and Stephen W. Hawking. 'Action integrals and partition functions in quantum gravity'. In: *Phys. Rev. D 15, 10* (1976).

[Gia12] Dimitrios Giataganas. 'Probing strongly coupled anisotropic plasma'. In: *Journal of High Energy Physics* 2012.7 (July 2012), p. 31.

[GK97] Steven S. Gubser and Igor R. Klebanov. 'Absorption by branes and Schwinger terms in the world volume theory'. In: *Physics Letters B* 413.1 (1997).

[GKP02] Steven S. Gubser, Ivan T. Klebanov and Alexander M. Polyakov. 'A semi-classical limit of the gauge/string correspondence'. In: *Nucl.Phys. B636 (2002) 99-114* (2002).

[GKP98] Steven S. Gubser, Ivan Klebanov and Alexander Polyakov. 'Gauge theory correlators from non-critical string theory'. In: *Phys. Lett.* B428 (1998).

[GKT97] Steven S. Gubser, Igor R. Klebanov and Arkady A. Tseytlin. 'String theory and classical absorption by three-branes'. In: *Nuclear Physics B* 499.1 (1997).

[GM70] R. J. Glauber and G. Matthiae. 'High-energy scattering of protons by nuclei'. In: *Nuclear Physics B* 21.2 (1970).

[GN08] Steven S. Gubser and Abhinav Nellore. 'Mimicking the QCD equation of state with a dual black hole'. In: *Phys. Rev. D* 78 (8 Oct. 2008), p. 086007.

[GPR08] Steven S. Gubser, Silviu S. Pufu and Fábio D. Rocha. 'Bulk viscosity of strongly coupled plasmas with holographic duals'. In: *Journal of High Energy Physics* 2008.08 (2008), p. 085.

[Gub06] Steven S. Gubser. 'Drag force in AdS/CFT'. In: *Phys.Rev.D74:126005* (2006).

[Gub07] Steven S. Gubser. 'Comparing the drag force on heavy quarks in $\mathcal{N} = 4$ super-Yang-Mills theory and QCD'. In: *Phys. Rev. D* 76 (12 Dec. 2007), p. 126003.

[Gub99] Steven S. Gubser. 'Thermodynamics of spinning D3-branes'. In: *Nucl. Phys. B551* (1999).

[GXZ06] Yi-hong Gao, Wei-shui Xu and Ding-fang Zeng. 'Jet quenching parameters of Sakai-Sugimoto Model'. In: (Dec. 2006).

[Haw71] Stephen H. Hawking. 'Gravitational radiation from colliding black holes'. In: *Phys. Rev. Lett. 26, 1344* (1971).

[Haw75] Stephen H. Hawking. 'Particle creation by black holes'. In: *Communications in Mathematical Physics* (1975).

[Her+06] Christopher P. Herzog, Andreas Karch, Pavel Kotvun, Pavel Kotvun, Can Kozcaz and Laurence G. Yaffe. 'Energy loss of a heavy quark moving through N = 4 supersymmetric Yang-Mills plasma'. In: *JHEP 0607 (2006) 013* (2006).

[Her07] Christopher P. Herzog. 'Holographic prediction for the deconfinement temperature'. In: *Phys. Rev. Lett* 98 (9 Feb. 2007), p. 091601.

[HG11] W. A. Horowitz and Miklos Gyulassy. 'The surprising transparent sQGP at LHC'. In: *Nucl. Phys. A872* (2011).

[HHT99] Stephen W. Hawking, C. J. Hunter and M. M. Taylor-Robinson. 'Rotation and the AdS/CFT correspondence'. In: *Phys.Rev.D59:064005* (1999).

[HK83] P. Hasenfratz and F. Karsch. 'Chemical potential on the lattice'. In: *Physics Letters B* 125.4 (1983).

[Hoo74a] G.'t Hooft. 'A planar diagram theory for strong interactions'. In: *Nuclear Physics B* 72.3 (1974).

[Hoo74b] Gerrard 't Hooft. 'A planar diagram theory for strong interactions'. In: *Nuclear Physics* B72 (1974).

[HT07] Norio Horigome and Yoshiaki Tanii. 'Holographic chiral phase transition with chemical potential'. In: *JHEP* (2007).

[Jam09] Phillip Szepietowski James T. Liu. 'Higher Derivative Corrections to R-charged AdS_5 black holes and field redefinitions'. In: *Phys. Rev. D 79, 084042* (2009).

[JM10] Ricardo Jorge and Ferreira Monteiro. 'Classical and thermodynamic stability of black holes'. PhD thesis. University of Cambridge, 2010.

[KK02] Andreas Karch and Emanuel Katz. 'Adding flavor to AdS/CFT'. In: *JHEP 06 (2002)* (2002).

[Kle97] Igor R. Klebanov. 'World-volume approach to absorption by non-dilatonic branes'. In: *Nuclear Physics B* 496.1 (1997).

[Kob+07] Shinpei Kobayashi, David Mateos, Shunji Matsuura, Robert C. Myers and Rowan M. Thomson. 'Holographic phase transitions at finite baryon density'. In: *JHEP 0702:016, 2007* (2007).

[KPT98] Dmitri Kharzeev, Robert D. Pisarski and Michel H. G. Tytgat. 'Possibility of Spontaneous Parity Violation in Hot QCD'. In: *Phys Rev. Lett.* 81 (3 July 1998), pp. 512–515.

[KSH00] Peter F. Kolb, Josef Sollfrank and Ulrich Heinz. 'Anisotropic transverse flow and the quark-hadron phase transition'. In: *Phys. Rev. C* 62 (5 Oct. 2000), p. 054909.

[KZ07] Dmitri Kharzeev and Ariel Zhitnitsky. 'Charge separation induced by P-odd bubbles in QCD matter'. In: *Nuclear Physics A* 797.1 (2007).

[LM06] Feng-Li Lin and Toshihiro Matsuo. 'Jet quenching parameter in medium with chemical potential from AdS/CFT'. In: *Physics Letters B* 641.1 (2006).

[LRW06] Hong Liu, Krishna Rajagopal and Urs Achim Wiedemann. 'Calculating the Jet Quenching Parameter'. In: *Phys Rev. Lett.* 97 (18 Nov. 2006), p. 182301.

[LRW07] Hong Liu, Krishna Rajagopal and Urs Achim Wiedemann. 'Wilson loops in heavy ion collisions and their calculation in AdS/CFT'. In: *Journal of High Energy Physics* 2007.03 (2007), p. 066.

[LS05] James T. Liu and W. A. Sabra. 'Mass in anti-de Sitter spaces'. In: *Phys. Rev. D 72, 064021* (2005).

[LYY17] Meng-Wei Li, Yi Yang and Pei-Hung Yuan. 'Approaching confinement structure for light quarks in a holographic soft wall QCD model'. In: *Phys. Rev. D* 96 (6 Sept. 2017), p. 066013.

[Mal98a] Juan Maldacena. 'The large N Limit of Superconformal field theories and Supergravity'. In: *International Journal of Theoretical Physics* 38.4 (1998), pp. 1113–1133.

[Mal98b] Juan Maldacena. 'Wilson loops in large N field theories'. In: *Phys. Rev. Lett. 80, 4859* (1998).

[McI14] Brett McInnes. 'Shearing black holes and scans of the quark matter phase diagram'. In: *Classical and Quantum Gravity* 31.2 (2014), p. 025009.

[MMMT07] David Mateos, Shunji Matsuura, Robert C. Myers and Rowan M. Thomson. 'Holographic phase transitions at finite chemical potential'. In: *JHEP 0711:085, 2007* (2007).

[MMT06] David Mateos, Robert C. Myers and Rowan M. Thomson. 'Holographic phase transitions with fundamental matter'. In: *Phys. Rev. Lett 97, 091601* (2006).

[MMT07] David Mateos, Robert C. Myers and Rowan M. Thomson. 'Thermodynamics of the brane'. In: *JHEP Issue 05* (2007).

[MS81] Larry D. McLerran and Benjamin Svetitsky. 'Quark liberation at high temperature: A Monte Carlo study of SU(2) gauge theory'. In: *Phys. Rev. D* 24 (2 July 1981), pp. 450–460.

[MT11] David Mateos and Diego Trancanelli. 'Thermodynamics and Instabilities of a Strongly Coupled Anisotopic Plasma'. In: *JHEP 1107:054* (2011).

[MT14] Brett McInnes and Edward Teo. 'Generalized planar black holes and the holography of hydrodynamic shear'. In: *Nuclear Physics B* 878 (2014).

[MY13] Berndt Müller and Di-Lun Yang. 'Light probes in a strongly coupled anisotropic plasma'. In: *Phys. Rev. D* 87 (2013).

[Pan08] Yi Pang. 'Tranverse momentum broadening of heavy quark and gluon energy loss in Sakai-Sugimoto model'. In: *JHEP* (2008).

[Pat74] A. Patrascioiu. 'Quantum dynamics of a massless relatavistic string'. In: *Lettere al Nuovo Cimento* 10 (1974), pp. 676–680.

[PF71] Roger Penrose and R. M. Floyd. 'Extraction of rotational energy from a black hole'. In: *Nature 229* (1971).

[Pło09] Mateusz Płoskoń. 'Inclusive cross section and correlations of fully reconstructed jets in sNN=200 GeV Au + Au and p+p collisions'. In: *Nuclear Physics A* 830.1 (2009). Quark Matter 2009.

[Pol95] Joseph Polchinski. 'Dirichlet Branes and Ramond-Ramond Charges'. In: *Phys Rev. Lett.* 75 (26 Dec. 1995), pp. 4724–4727.

[PRW84] M. Plümer, S. Raha and R. M. Weiner. 'How free is the quark-gluon-plasma?' In: *Nuclear Physics A* 418 (1984).

[PS13] B. Pourhassan and J. Sadeghi. 'STU–QCD correspondence'. In: *Canadian Journal of Physics* 91.12 (2013), p. 995.

[PŠ17] Roman Pasechnik and Michal Šumbera. 'Phenomenological Review on Quark–Gluon Plasma: Concepts vs. Observations'. In: *Universe* 3.1 (2017).

[Reb14] Anton Rebhan. 'The Witten-Sakai-Sugimoto model: A brief review and some recent results'. In: *3rd International Conference on New Frontiers in Physics, Kolymbari, Crete*. 2014.

[Reg59] Tullio Regge. 'Introduction to complex angular momentum'. In: *Il Nuovo Cimento Series 10* 14 (1959), p. 951.

[RFFN16] Romulo Rougemont, Andrej Ficnar, Stefano I. Finazzo and Jorge Noronha. 'Energy loss, equilibration, and thermodynamics of a baryon rich strongly coupled quark-gluon plasma'. In: *Journal of High Energy Physics* 2016.4 (Apr. 2016), p. 102.

[Ris+92] Dirk H. Rischke, Mark I. Gorenstein, Andreas Schäfer, Horst Stöcker and Walter Greiner. 'Non-perturbative effects in the SU(3) gluon plasma'. In: *Physics Letters B* 278.1 (1992).

[Rom07] Paul Romatschke. 'Momentum broadening in an anisotropic plasma'. In: *Phys. Rev. C* 75 (1 Jan. 2007), p. 014901.

[RY01] Soo-Jong Rey and Jung-Tay Yee. 'Macroscopic strings as heavy quarks in large N gauge theory and Anti-de Sitter Supergravity'. In: *Eur.Phys.C22:379-394* (2001).

[Sch10] John H. Schwarz. 'Status of superstring and M-theory'. In: *International Journal of Modern Physics A* 25.25 (2010).

[SDNS08] Björn Schenke, Adrian Dumitru, Yasushi Nara and Michael Strickland. 'QGP collective effects and jet transport'. In: *Journal of Physics G: Nuclear and Particle Physics* 35.10 (2008), p. 104109.

[Shu09] Edward Shuryak. 'Physics of strongly coupled quark–gluon plasma'. In: *Progress in Particle and Nuclear Physics* 62.1 (2009).

[Sir+18] A. M. Sirunyan, A. Tumasyan, W. Adam, E. Asilar, T. Bergauer, J. Brandstetter and E. Brondolin. 'Azimuthal anisotropy of charged particles with transverse momentum up to 100 GeV/c in PbPb collisions at $sNN = 5.02\ TeV$'. In: *Physics Letters B* 776 (2018).

[SS05a] Tadakatsu Sakai and Shigeki Sugimoto. 'Low energy hadron Physics in holographic QCD'. In: *Progress of Theoretical Physics* 113.4 (2005).

[SS05b] Tadakatsu Sakai and Shigeki Sugimoto. 'Low energy hadron physics in holographic QCD'. In: *Prog. Theor. Phys. 113:843-882,* (2005).

[SS05c] Tadakatsu Sakai and Shigeki Sugimoto. 'More on a holographic dual of QCD'. In: *Progress of Theoretical Physics* (2005).

[SS05d] Tadakatsu Sakai and Shigeki Sugimoto. 'More on a holographic dual of QCD'. In: *Progress of Theoretical Physics* 114.5 (2005).

[SS06] Dam T. Son and Andrei O. Starinets. 'Hydrodynamics of R-charged black holes'. In: *JHEP03(2006)* (2006).

[SSPH09] J. Sadeghi, M. Setare, B. Pourhassan and S. Hashmatian. 'Drag force of moving quark in STU background'. In: *Eur Phys. J. C* (2009).

[Wit98a] Edward Witten. 'Anti-de Sitter space and holography'. In: *Adv Theor. Math. Phys.* 2 (1998).

[Wit98b] Edward Witten. 'Anti-de Sitter space, thermal phase transition, and confinement in gauge theories'. In: *Adv. Th. and Math. Phys.* 2.3 (1998).

[WW16] Luying Wang and Shang-Yu Wu. 'Holographic study of the jet quenching parameter in anisotropic systems'. In: *The European Physical Journal C* 76.11 (Oct. 2016), p. 587.

[XLG16] Jiechen Xu, Jinfeng Liao and Miklos Gyulassy. 'Bridging soft-hard transport properties of quark-gluon plasmas with CUJET3.0'. In: *Journal of High Energy Physics* 2016.2 (Feb. 2016), p. 169.

[ZHR13] Zi-qiang Zhang, De-fu Hou and Hai-cang Ren. 'The finite 't Hooft coupling correction on the jet quenching parameter in a $\mathcal{N} = 4$ super Yang-Mills plasma'. In: *Journal of High Energy Physics* 2013.1 (Jan. 2013), p. 32.

[ZP07] Marija Zamaklar and Kasper Peeters. 'The string/gauge theory correspondence in QCD'. In: *45th Winter School on Theoretical Physics*. 2007.

[Zwe64] G. Zweig. 'An SU_3 model for strong interaction symmetry and its breaking'. In: *CERN-TH-412* (Feb. 1964), p. 80.